

Multi-color time-resolved laser-induced incandescence for the measurement of soot and nanoparticle aerosols

Von der Fakultät für Ingenieurwissenschaften,
Abteilung Maschinenbau und Verfahrenstechnik
der Universität Duisburg-Essen

zur Erlangung des akademischen Grades
eines
Doktors der Ingenieurwissenschaften
– Dr.-Ing. –

genehmigte Dissertation

von

Raphael Andreas Mansmann
aus
St. Wendel

Gutachter: Prof. Dr. Christof Schulz
 Prof. Dr. Kyle Daun

Tag der mündlichen Prüfung: 28. März 2019

DuEPublico

Duisburg-Essen Publications online

UNIVERSITÄT
DUISBURG
ESSEN

Offen im Denken

ub | universitäts
bibliothek

Diese Dissertation wird über DuEPublico, dem Dokumenten- und Publikationsserver der Universität Duisburg-Essen, zur Verfügung gestellt und liegt auch als Print-Version vor.

DOI: 10.17185/duepublico/70080

URN: urn:nbn:de:hbz:464-20190404-140909-8

Alle Rechte vorbehalten.

ABSTRACT

Time-resolved laser-induced incandescence (TiRe-LII) is an optical *in situ* diagnostics method for particle-size determination of gas-borne nanoparticles that has been established over the last decades. Recent inter-laboratory comparisons have shown that there are unresolved issues concerning measurement artifacts and noise, and discrepancies exist in reported results from similar measurement conditions. Moving from the established two-color technique (for pyrometric temperatures determination) to spectrally resolved (and multi-color) measurements reveals additional open questions.

The difficulty in LII science is that in literature, a wide range of different LII models and corresponding materials properties is available, and often, for new application cases, new models are composed from various published LII models to match the results from literature or *ex situ* determined quantities (e.g., particle-size distributions). In addition, signal shapes that cannot be explained by previously published LII models lead to the adjustment of the physical models and properties instead of focusing on technical issues of the LII signal acquisition. The variation in calibration, measurement and analysis procedures across the LII community motivates for the development towards standardization of LII signal acquisition and processing to increase the quality of signals that can then later be used as input for future LII model developments.

This work focuses on practical aspects of multi-color TiRe-LII as detector performance/calibration, experimental design, and signal acquisition and on the improvement of the robustness of the measurement technique using multiple detection channels. In the scope of this work, a multi-color LII device was developed along with a software solution for data acquisition and signal processing. Modular and flexible components in the setup and the analysis help to broaden the way for the application of LII on various materials systems and processes, and can build a foundation for future inter-laboratory comparisons.

For multi-color LII techniques, proper detector performance and calibration is essential to produce data that can be used as input for further processing. The detector performance is investigated for photomultiplier tubes (PMT) using pulsed and continuously operated light-emitting diodes at similar light levels as typical LII experiments. The influence of non-linear behavior during LII measurements is demonstrated for different two-color ratios and the importance of linearity as detector requirement is shown. The mathematical description for the calibration of PMTs in the context of LII is presented along with a detailed methodology for the calibration of all components within a typical LII detection system. For this purpose, the suitability of different calibration light sources is assessed and additional measurement issues that could affect the signal quality are discussed. For data acquisition and processing of LII data, a software solution was developed, following a modular approach, making it suitable for the application on various materials systems and with individual processing steps. The software is published as open-source software to allow transparency and adjustments by other researchers. In order to improve the LII signal acquisition further, a new sequential detection technique was developed that takes advantage of gated photomultiplier tubes and is capable to increase the dynamic range of the LII technique.

Having resolved many of the above-mentioned issues is an important step towards harmonization of the experimental procedure, calibration, measurement and interpretation of data.

ZUSAMMENFASSUNG

Zeitaufgelöste laser-induzierte Inkandeszenz (TiRe-LII) ist eine optische In-Situ-Messmethode zur Partikelgrößenbestimmung gasgetragener Nanopartikel, die sich über die letzten Jahrzehnte bewährt hat. Laborvergleiche haben jedoch gezeigt, dass es bisher ungelöste Probleme in Bezug auf Messartefakte und -rauschen gibt, und Unstimmigkeiten zwischen publizierten Ergebnissen zu ähnlichen Messbedingungen existieren. Der Übergang von der etablierten Zweifarben-Technik (für die pyrometrische Temperaturbestimmung) zu spektral aufgelösten (und Mehrfarben-) Messungen führt zu zusätzlichen offenen Fragen.

Die Schwierigkeit in der LII-Wissenschaft besteht darin, dass in der Literatur ein breites Spektrum an unterschiedlichen LII-Modellen und dazugehörigen Materialeigenschaften verfügbar ist und oft für neue Anwendungsfälle neue Modelle aus verschiedenen veröffentlichten LII-Modellen zusammengestellt werden, um gleiche Ergebnisse wie die Literatur zu erhalten oder Ex-Situ-bestimmten Größen (z.B. Partikelgrößenverteilungen) zu entsprechen. Darüber hinaus führen Signalformen, die nicht durch zuvor veröffentlichte LII-Modelle erklärt werden können, zu einer Anpassung der physikalischen Modelle und Eigenschaften, anstatt sich auf technische Probleme der LII-Signalerfassung zu konzentrieren. Die unterschiedlichen Kalibrierungs-, Mess- und Analyseverfahren motivieren zur Entwicklung einer Standardisierung der LII-Messwerterfassung und -verarbeitung, um die Qualität der Signale zu erhöhen, die dann später für zukünftige LII-Modellentwicklungen verwendet werden können.

Diese Arbeit konzentriert sich auf die technischen Aspekte von Mehrfarben-TiRe-LII wie Detektorverhalten/-kalibrierung, experimentelle Auslegung und Signalerfassung, sowie auf die Verbesserung der Stabilität der Messtechnik mit mehreren Detektionskanälen. Im Rahmen dieser Arbeit wurde ein Mehrfarben-LII-Gerät zusammen mit einer Softwarelösung zur Datenerfassung und Signalverarbeitung entwickelt. Modulare und flexible Komponenten im Setup und in der Analyse helfen, den Einsatz von LII auf unterschiedliche Materialsysteme und -prozesse zu erweitern und eine Grundlage für zukünftige Laborvergleichsstudien zu schaffen.

Bei Mehrfarben-LII-Techniken ist ein einwandfreies Ansprechverhalten und Kalibrierung der Detektoren essentiell, um Daten zu erzeugen, die als Grundlage für weitere Signalverarbeitungsschritte verwendet werden können. Das Detektorverhalten wird für Photomultiplier-Röhren (PMT) mit gepulsten und kontinuierlich betriebenen Leuchtdioden bei ähnlichen Lichtstärken wie bei LII-Experimenten untersucht. Der Einfluss von nichtlinearem Verhalten während LII-Messungen wird für verschiedene Zweifarbenverhältnisse demonstriert und die Wichtigkeit von Linearität als Detektoranforderung gezeigt. Die mathematische Beschreibung für die Kalibrierung von PMTs im Zusammenhang mit LII wird zusammen mit einer detaillierten Methodik für die Kalibrierung aller Komponenten innerhalb eines typischen LII-Detektionsystems präsentiert. Zu diesem Zweck wird die Eignung verschiedener Kalibrierlichtquellen bewertet und weitere Messprobleme werden diskutiert, die die Signalqualität beeinflussen können. Für die Signalerfassung und -verarbeitung von LII-Daten wurde eine Softwarelösung nach einem modularen Ansatz entwickelt, die sich für den Einsatz für eine große Bandbreite an Materialsystemen und mit individuellen Verarbeitungsschritten eignet. Die Software wurde als Open-Source-Software veröffentlicht, um Transparenz sowie Anpassungen durch andere Forscher zu ermöglichen. Um die LII-Signalerfassung weiter zu verbessern, wurde eine neue sequenzielle Detektionstechnik entwickelt, die Photomultiplier-Röhren mit ansteuerbarem Detektions-Zeitfenster nutzt und in der Lage ist, den dynamischen Bereich der LII-Technik zu erweitern.

Die Klärung vieler der oben genannten Themen ist ein wichtiger Schritt zur Harmonisierung des experimentellen Verfahrens, der Kalibrierung, Messung und Interpretation von Daten.

TABLE OF CONTENTS

ABSTRACT	I
ZUSAMMENFASSUNG	II
TABLE OF CONTENTS.....	III
LIST OF SYMBOLS.....	VII
1 INTRODUCTION.....	1
2 LASER-INDUCED INCANDESCENCE.....	3
2.1 Spectroscopic model	5
2.2 Heat transfer model	9
2.3 Experimental layout	10
2.3.1 Excitation.....	10
2.3.2 Detection.....	11
2.4 Applications.....	12
3 OBJECTIVE AND CONCEPTS.....	13
3.1 Design requirements for the experimental setup.....	13
3.2 Experimental design and modifications.....	16
3.2.1 Laser system.....	16
3.2.2 Detection system	21
3.2.3 Electronic control of experimental parameters.....	23
3.2.4 Software for data acquisition and analysis	24
3.3 Research focus	25
4 PERFORMANCE OF PHOTOMULTIPLIERS IN THE CONTEXT OF LASER-INDUCED INCANDESCENCE.....	27
4.1 Introduction	28
4.2 Experiment.....	30
4.2.1 Light sources	31
4.2.2 Detection.....	33
4.3 Methodology.....	34
4.3.1 Linearity measurements using light superposition.....	34
4.3.2 Linearity measurements using ND filters	36

4.4	Results	38
4.4.1	Linearity measurements for continuous and pulsed light.....	38
4.4.2	Linearity of pulsed operation in presence of background radiation	40
4.4.3	Quantifying the influence of non-linearity on two-color pyrometric temperature measurements	41
4.5	Conclusions.....	43
5	DETECTOR CALIBRATION AND MEASUREMENT ISSUES IN MULTI-COLOR TIME-RESOLVED LASER-INDUCED INCANDESCENCE.....	45
5.1	Introduction.....	46
5.2	Theory.....	47
5.2.1	Detector requirements and measurement issues in LII	47
5.2.2	Photomultiplier tubes.....	49
5.2.3	Calibration procedures	50
5.2.4	Spectroscopic model	56
5.2.5	Statistical considerations.....	57
5.3	Experiment	59
5.3.1	Calibration light sources	59
5.3.2	Detector arrangement.....	61
5.3.3	Laminar diffusion flame.....	62
5.4	Methodology and results	62
5.4.1	Calibration	62
5.4.2	Reference LII experiment	69
5.5	Additional measurement issues	71
5.6	Conclusions.....	74
6	LIISIM – A MODULAR SIGNAL PROCESSING TOOLBOX FOR LASER-INDUCED INCANDESCENCE MEASUREMENTS.....	75
6.1	Introduction.....	76
6.1.1	Laser-induced incandescence.....	76
6.1.2	Models	76
6.1.3	Software	76
6.2	Models implemented in LIISim	78
6.2.1	Spectroscopic models.....	78
6.2.2	Heat transfer models.....	79
6.3	Implementation.....	80
6.3.1	Software architecture.....	80
6.3.2	Data structure.....	80

6.3.3	Materials database.....	.81
6.3.4	Numerical procedures.....	.81
6.3.5	Modules83
6.4	Application cases.....	.88
6.4.1	Application 188
6.4.2	Application 292
6.5	Software availability and documentation95
6.6	Summary95
7	SEQUENTIAL SIGNAL DETECTION FOR HIGH DYNAMIC RANGE TIME-RESOLVED LASER-INDUCED INCANDESCENCE97
7.1	Introduction98
7.2	Method.....	.100
7.3	Experiment103
7.4	Results103
7.5	Conclusions105
8	OUTLOOK.....	.107
9	SUMMARY109
APPENDIX.....		.113
Appendix A	Linearity measurements113
Appendix B	Signal bias and artifacts117
Appendix C	LIISim – Levenberg–Marquardt algorithm.....	.119
Appendix D	LIISim – Implemented heat transfer models121
Appendix E	LIISim – Example for heat transfer model implementation133
BIBLIOGRAPHY137
PUBLICATIONS.....		.149
ACKNOWLEDGMENTS.....		.153

LIST OF SYMBOLS

This section summarizes the symbols used in the following chapters, but does not contain symbols or constants for the heat transfer models implemented in the LIISim software. A summary of these symbols and corresponding LIISim variable names can be found in Appendix D. The location of symbol occurrence in the chapters and appendices is indicated in the last column of the following tables.

Latin symbols

Symbol	Description	Chapter
a	Coefficient in LIISim property functions	6
\mathbf{a}	Vector of parameters	C
A	Gain calibration coefficient	5, 6
\mathbf{b}	Vector of data	5, C
B	Gain calibration coefficient	5
B_λ	Optical efficiency of the detection system	2, 5
c_0	Speed of light in vacuum	2, 4, 5, 6, 7
c_p	Specific heat capacity	6
C	Intensity scaling factor	6
$C_{\lambda,\text{abs}}$	Absorption cross section	2, 5, 6
$C_{\lambda,\text{ext}}$	Extinction cross section	2
$C_{\lambda,\text{scat}}$	Scattering cross section	2
d_p	Particle diameter	2, 5, 6
D	Relative sensitivity calibration factor (scaled)	5
D^*	Relative sensitivity calibration factor	5
\bar{D}	Relative sensitivity calibration factor (mean)	5
\mathbf{D}	Curvature matrix	C
$E(\mathbf{m}_\lambda)$	Absorption function	2, 4, 5, 6, 7
E	Irradiance	5
E_λ^{ref}	Reference spectral irradiance	5
f_V	Volume fraction	2, 5, 6
G	Gain correction function	5
G_λ	Scaling factor for geometry and optical efficiency of the detector	6
h	Planck constant	2, 4, 5, 6, 7
i	Imaginary unit	2
i^a	Anode current	5
$i^{a,\text{ref}}$	Reference anode current	5
I	Intensity	4

Symbol	Description	Chapter
I_λ	Spectral intensity	2, 4, 5, 6, 7
J_λ	Spectral irradiance	2
J_λ^{exp}	Calibrated spectral irradiance	2, 5
J_λ^{mod}	Simulated spectral irradiance	2, 5
\mathbf{J}	Jacobian matrix	C
k	Extinction coefficient	2
k_B	Boltzmann constant	2, 4, 5, 6, 7
\mathbf{L}	Lower triangular matrix	C
m_p	Particle mass	2, 6
\mathbf{m}_λ	Complex index of refraction	2, 5
n	Refractive index	2
p	Probability density	2, 5
p	Posterior probability	5
p_{like}	Likelihood function	5
p_{pri}	Prior probability	5
\dot{Q}	Heat transfer rate	2, 6
$Q_{\lambda,\text{abs}}$	Absorption efficiency	2
r	Radius	2
S	Signal	4
S_{flame}	Signal contributed from flame	7
S_{probe}	Signal contributed from probe volume	7
S_{total}	Signal contributed from total volume	7
ΔS_p	Difference in signal amplitude between two pulses	4
t	Time	2
T	Temperature	2, 6, 7
T_{gas}	Gas temperature	7
T_p	Particle temperature	2, 4, 6, 7
$T_{p,\text{eff}}$	Effective temperature of nanoparticle ensemble	2, 5
\dot{u}	Mass loss due to evaporation/sublimation	2, 6
U_{Internal}	Internal energy	2
V	Volume	2
V_{baseline}	Baseline signal voltage	5
V_{meas}	Measured signal voltage	5
V_{gain}	Gain voltage	5
$V_{g,\text{ref}}$	Reference gain voltage	5
x	Size parameter	2
x	Gain voltage	6

Symbol	Description	Chapter
x	Ratio of probe volume to total measurement volume	7
\mathbf{x}	Data vector	C
y	Gain correction factor	6
\mathbf{y}	Data vector	C

Greek symbols

Symbol	Description	Chapter
β	Coefficient in empirical $E(\mathbf{m}_\lambda)$ formula	6
δ	Half bandwidth of bandpass filter	5
η	Instrument calibration factor	5
θ	Spectral sensitivity of the LII system	5
$\boldsymbol{\theta}$	Vector of nuisance parameters	5
λ	Detection wavelength	2, 4, 5, 6, 7
λ	Damping factor	C
λ_c	Center wavelength	5
Λ	Intensity scaling factor	2, 5
μ_θ	Expected value of nuisance parameter	5
ξ	Coefficient in empirical $E(\mathbf{m}_\lambda)$ formula	6
σ	Standard deviation	5, C
τ	Transmission	4, 5
ϕ	Efficiency of the collection optics	5

Subscripts

Subscript	Description	Chapter
abs	Absorption	2, 4, 5
B	Broadband	4
BB	Blackbody	2, 5
cond	Conduction	6
cw	Continuous wave	4
eff	Effective	2, 5
evap	Evaporation	6
ext	Extinction	2
LED	Light-emitting diode	4
like	Likelihood	5

Subscript	Description	Chapter
mod	Modeled	C
p	Particle	2, 4, 6
p	Pulse	4
pri	Prior	5
rad	Radiation	6
ref	Reference	4, 6
scat	Scattering	2

Superscripts

Superscript	Description	Chapter
a	Anode	5
exp	Experimental	2, 5
meas	Measured	5
mod	Modeled	2, 5
ref	Reference	5

Abbreviations

Abbreviation	Description
2C	Two-color
2D	Two-dimensional
AC	Auto-compensating
ADC	Analog-to-digital converter
BB	Blackbody
BET	Brunauer-Emmett-Teller
BP	Bandpass
CARS	Coherent anti-Stokes Raman spectroscopy
CLiiME	Community laser-induced incandescence modeling environment
CSV	Comma-separated values
DC	Direct current
DM	Dichroic mirror
DOE	Diffractive optical element
FW	Filter wheel
FWHM	Full width at half maximum
GPL	General Public License
GUI	Graphical user interface

Abbreviation	Description
HAB	Height above burner
HDR	High dynamic range
IS	Integrating sphere
LDLS	Laser-driven light source
LED	Light-emitting diode
LIBS	Laser-induced breakdown spectroscopy
LIDAR	Light detection and ranging
LII	Laser-induced incandescence
LOSA	Line-of-sight attenuation
MA	Multi-alkali
MAP	Maximum a posteriori
MDK	Model development kit
MPoint	Measurement point (LII ^{Sim} signal container)
MRun	Measurement run (LII ^{Sim} signal container)
Nd:YAG	Neodymium-doped yttrium aluminum garnet
ND	Neutral density
ODE	Ordinary differential equation
PIV	Particle image velocimetry
PMT	Photomultiplier tube
SBA	Super bi-alkali
SEM	Scanning electron microscopy
SLS	Stabilized light source
SNR	Signal-to-noise ratio
SPAD	Single-photon avalanche diodes
T	Temperature trace (LII ^{Sim})
TCSPC	Time-correlated single-photon counting
TEM	Transmission electron microscopy
TEW	Two-excitation wavelength
TiRe	Time resolved
TRLS	Time-resolved luminescence spectroscopy
UV	Ultraviolet
VA	Variable aperture
WALS	Wide-angle light scattering

1 INTRODUCTION

Nanoparticles are ultrafine particles having a size below one hundred nanometers in all three spatial dimensions and with special physical and chemical properties that can differ from those of macroscopic materials. They can be found as an unwanted by-product in many practical processes (e.g., soot particles in combustion exhaust or metal particles in welding fumes), but they are also synthesized to take advantage of their large surface-area-to-volume ratio and their size-dependent properties [1]. Nanomaterials are used in the fields of electronics, biotechnology, chemistry, energy technology, and materials science (e.g., highly efficient catalysts or storage material in high-capacity batteries).

Nanoparticle formation processes can generally be divided into *top-down processes*, where the particle size is reduced through mechanical, chemical or thermal influence, and *bottom-up processes* that are based on formation and growth of particles from basic chemical components. Two important bottom-up processes are combustion and gas-phase synthesis of nanoparticles. In order to design or improve such processes, it is essential to understand the particle formation mechanisms and conditions that lead to a certain particle size. For the determination of particle sizes and size distributions, particles are usually sampled in or on a medium. These samples are then analyzed using *ex situ* techniques such as transmission electron microscopy (TEM), scanning electron microscopy (SEM), or nitrogen adsorption analysis (Brunauer-Emmett-Teller, BET, method). The disadvantage of *ex situ* approaches is that, usually, only the final stage of the particulate material can be assessed and, moreover, sampled particles can oxidize or change their structure during the sampling, and therefore, they are potentially no longer representative for the measurement position in the formation process. When representative information is needed, non-intrusive *in situ* methods are required, where information about size, morphology, aggregation, composition, or concentration can be obtained at defined positions in the processes.

Optical diagnostic techniques are considered as non-intrusive methods and can be used if an optical access to the process is available. Laser-induced incandescence (LII) is one such diagnostic technique that is commonly used to obtain *in situ* information about particle size and concentration in aerosols [2, 3]. It is based on pulsed laser heating of gas-borne particles within a defined measurement volume and the observation of the thermal emission (incandescence) of the particles during the cooling process. Typical applications range from soot diagnostics in flames, to engine exhaust and, most recently, synthetic nanoparticle processes [3]. In the case of time-resolved LII (TiRe-LII), information about the particle size is obtained through evaluation of the temporal cooling behavior of the particles (as small particles cool faster than large particles). While the technique is already widely used, there remain many open questions related to optical and physical properties of the investigated materials systems, influence of particle size distributions, chemical composition, morphology, and aggregation. Though these topics are considered primary research tasks within the LII community, only few studies exist that focus on practical aspects such as detection, calibration, and signal processing [4-11].

The difficulty for current research is that LII signal acquisition and analysis is not standardized, and the calibration and processing techniques, as well as physical properties used in the data evaluation models

vary from study to study. In order to make the early stage of LII signal processing more reliable, it is important to improve the quality of the measured raw data and thus to provide clear definitions how signal acquisition and calibration can be improved. One possible improvement is to increase of the number of detection wavelengths. While two-color techniques are considered as standard technique for time-resolved LII, three- [11] and four-color techniques [12] as well as spectrally resolved measurements [12, 13] already showed the potential for improved quality of measurement data because they can more easily detect deviations from the expected spectral characteristics and thus indicate signal interference and non-ideal detector behavior.

This thesis deals with the questions how a measurement setup for the multi-color TiRe-LII technique should be designed and how it can be improved to increase the quality of LII measurements and thus the robustness and reproducibility of the technique. Chapter 2 introduces the basic principle of LII, explains how a typical experimental apparatus is structured, and summarizes typical LII applications. Chapter 3 defines the requirements for an experimental LII setup and shows general concepts of the experimental design to increase the quality of the measurement. Chapter 4 deals with the response of the most common detector type in LII: photomultiplier tubes (PMT). The performance of PMTs with respect to detector linearity is investigated and recommendations for the design and operation are given. The detector calibration methodology and common measurement issues that could occur during LII measurements are presented in chapter 5, including an error analysis of the calibration procedure. Chapter 6 demonstrates the signal processing toolbox LIISim that builds on previous experience [14, 15], but has been developed as a new framework during the last years as an open-source software solution for the LII community. Chapter 7 presents a new method for increasing the dynamic range of LII measurements that enables to increase the signal-to-noise ratio in the later part of the LII signal trace. The outlook and summary are presented in the last chapters (Chapter 8 and 9) followed by the appendices and bibliography.

2 LASER-INDUCED INCANDESCENCE

Laser-induced incandescence is an optical non-intrusive *in situ* diagnostics technique based on laser heating of gas-borne nanoparticles and the observation of the temporal variation of radiation emitted by the particles to conclude on their volume fraction and particle sizes [2, 3].

The earliest observations that light emission of small gas-borne particles heated by a pulsed laser may be correlated with particle size were reported in the 1970's by Weeks and Duley [16], and Eckbreth [17]. A few years later, Melton [18] published first equations describing the energy transfer between laser-heated particles and the surrounding gas. This model connected the magnitude and temporal variation of the incandescence to the particle number density and particle size, which laid a foundation for future heat-transfer models [19]. The measurement equations are derived using an energy- and mass-balance including the most relevant heat transfer mechanisms as summarized in Figure 2-1.

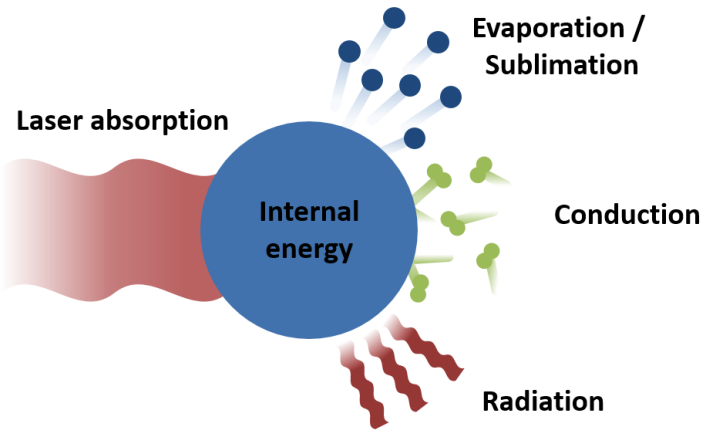


Figure 2-1 Heat transfer mechanisms relevant for laser-induced incandescence.

LII techniques can be broadly categorized as intensity-based LII to measure volume fractions, and time-resolved LII (TiRe-LII) to measure the particle size.

The intensity-based LII technique investigates the magnitude of the LII signal either at the signal peak (also known as "Prompt LII") or with a short delay after the signal peak [20-23]. The measurement method is capable for making relative conclusions on volume fraction as the intensity of the heated particle cloud is correlated with the volume fraction of particles in the detection volume [22-24]. This technique does not require high temporal resolution of the LII signal, and thus gated cameras can be used to obtain spatially resolved measurements of volume fraction, e.g., in engines [25-31] or flames [20, 22-24, 32-35]. Some of these studies combine the intensity-based LII technique with the time-resolved LII technique [21, 27, 30, 34].

Time-resolved LII uses information about the temporal variation of the incandescence and takes advantage of the particle-size dependent surface-to-volume ratio of the particles. For particles in the na-

nometer range, one can assume that the laser light is absorbed throughout the entire volume of the particle, instantly heating the particle to a homogeneous temperature. While during the subsequent cooling process, the heat transfer rate of the particle to the surroundings depends on the surface area and thus can be related to the diameter of the particle. Figure 2-2 shows example particle-temperature decay curves for soot particles in a flame environment for various nanoparticle diameters after laser heating at $t = 0$.

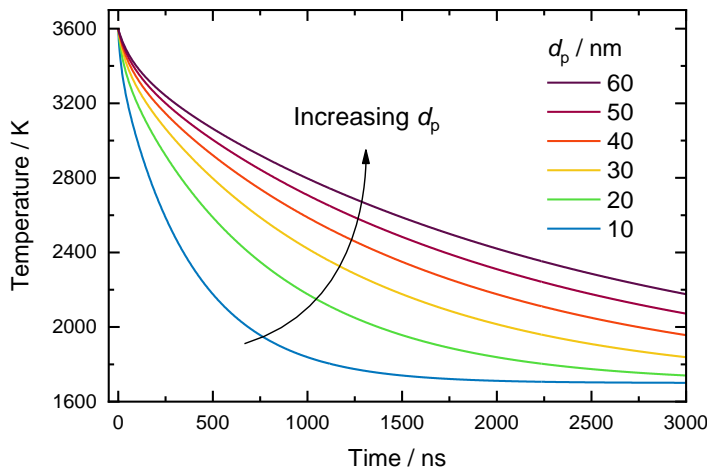


Figure 2-2 Simulated LII temperature decay traces for various particle diameters (soot particles in flame environment at 1700 K ambient gas temperature after heating by a pulsed laser to 3600 K at $t = 0$).

In the early stage of LII science, *single-color* TiRe-LII techniques were common using only one detector. The first quantitative measurements of single-color TiRe-LII were published by Will *et al.* [36], and Roth and Filippov [37]. For the single-color technique, LII signals are normalized to the peak intensity and the slope of the intensity decay is interpreted to determine the mean particle size in the detection volume. For the analysis of such signals, the heating and cooling mechanisms are modeled using the laser fluence, absorption cross-section, and local gas temperature as variable parameters, and are then compared to the normalized signal. As the values of these parameters can be affected by large uncertainties, quantitative interpretation is not recommended, but the technique can still be used for qualitative measurements (e.g., how soot primary particle size changes with location in a flame).

Subsequently, pyrometric techniques have been developed to directly determine temperature traces from LII signals collected at two different detection wavelength bands. The *two-color* TiRe-LII technique was first mentioned by Rohlfing and Chandler [38] who performed 2D-imaging two-color measurements on laser-heated carbon-black particles. Some years later, two-color time-resolved LII was used in several studies and was proven to increase the robustness of the LII analysis [9, 39-42]. McManus *et al.* [43] presented first spectrally resolved LII measurements using a monochromator with an intensified optical multichannel array in gated operation. The drawback of this approach is that the temporal decay of the LII trace needs to be resolved in multiple measurements (as the gate delay with 30 ns exposure time needs to be shifted along the signal trace). With new technologies available, recent studies presented time-resolved *multi-color* techniques by using multiple detectors at three [11] and four [12] detection wavelength bands, or even spectrally/temporally resolved measurements using a spectrometer coupled with a streak camera [12, 13].

The signal analysis for TiRe-LII is commonly split into two major parts: (i) the spectroscopic model that connects the incandescence emitted by the particles in the probe volume with their effective temperature; and (ii) the heat transfer model that simulates the temperature variation of the particles that is then compared against the temperature trace from the spectroscopic model. The variation of modeling parameters yields information about the particle size through least-squares minimization of the residual between simulated and measured data.

In the following sections, the spectroscopic model and the basic energy and mass balances of the heat transfer model are described. Then, a basic experimental layout for LII measurements is presented along with a summary of typical components used in such a setup. The last section gives an overview of the wide range of application cases for the laser-induced incandescence technique.

2.1 Spectroscopic model

The term “pyrometry” covers all techniques that characterize the thermal radiation emitted by an object to determine its temperature. In the context of LII, it is used to determine the temperature of an ensemble of laser-heated nanoparticles in a measurement volume using two or more wavelength bands. This section presents the derivation of the spectroscopic model for multi-color analysis that can be used to simulate the expected incandescence emitted by a nanoparticle for a given wavelength and temperature.

The spectroscopic LII model is derived subject to several key assumptions:

- (i) The particle size is much smaller than the light wavelength (Rayleigh approximation)
 - (ii) The temperature distribution within the particle is homogeneous.
 - (iii) The particles are approximated as spherical with a monodisperse size distribution.
- (i) For sufficiently small particles, the Rayleigh limit of Mie theory can be used to describe the optical properties of a particle with the radius r . If the particle size is much smaller compared to the wavelength, i.e., $x = 2\pi r/\lambda \ll 1$ and $|\mathbf{m}_\lambda| x \ll 1$, the absorption efficiency can be described as [44, 45]

$$Q_{\text{abs},\lambda} = 4x \operatorname{Im} \left\{ \frac{\mathbf{m}_\lambda^2 - 1}{\mathbf{m}_\lambda^2 + 2} \right\}, \quad (2-1)$$

where $\mathbf{m}_\lambda = n + ik$ is the complex index of refraction of the particle. Further, the absorption cross-section $C_{\lambda,\text{abs}}$ is proportional to the cross-sectional area of the particle and the absorption efficiency $Q_{\text{abs},\lambda}$

$$C_{\lambda,\text{abs}} = \pi r^2 Q_{\text{abs},\lambda}. \quad (2-2)$$

For the Rayleigh approximation, light scattering can be neglected and the extinction cross-section $C_{\lambda,\text{ext}}$ can be approximated by the absorption cross-section $C_{\lambda,\text{abs}}$ [44, 45]

$$C_{\lambda,\text{ext}} = C_{\lambda,\text{scat}} + C_{\lambda,\text{abs}} \approx C_{\lambda,\text{abs}}. \quad (2-3)$$

Equation (2-1) and (2-2) can then be summarized as

$$C_{\lambda,\text{abs}} = \frac{8\pi^2 r^3}{\lambda} \text{Im} \left\{ \frac{\mathbf{m}_\lambda^2 - 1}{\mathbf{m}_\lambda^2 + 2} \right\} = \frac{4}{3} \pi r^3 \frac{6\pi}{\lambda} \text{Im} \left\{ \frac{\mathbf{m}_\lambda^2 - 1}{\mathbf{m}_\lambda^2 + 2} \right\}. \quad (2-4)$$

The absorption function $E(\mathbf{m}_\lambda)$ is a common parameter in LII research and describes the optical absorption properties of the material that is investigated by the LII technique

$$E(\mathbf{m}_\lambda) = \text{Im} \left\{ \frac{\mathbf{m}_\lambda^2 - 1}{\mathbf{m}_\lambda^2 + 2} \right\} = \frac{6nk}{(n^2 - k^2 + 2)^2 + 4n^2k^2}. \quad (2-5)$$

$E(\mathbf{m}_\lambda)$ can be calculated from the complex index of refraction \mathbf{m}_λ or it is experimentally determined using the relationship from equation (2-3) with extinction measurements [46] or spectrally-resolved line-of-sight attenuation (LOSA) [12, 47, 48]. Equation (2-5) assumes the material is homogeneous and \mathbf{m}_λ is known, which is not the case for soot. In these cases, $E(\mathbf{m}_\lambda)$ is considered an “effective” parameter, which is often solved for in LII analysis [39, 49, 50].

With the definition of the volume of the particle, $V = 4/3\pi r^3$, and the absorption function, $E(\mathbf{m}_\lambda)$, equation (2-4) becomes

$$C_{\lambda,\text{abs}} = V \frac{6\pi}{\lambda} E(\mathbf{m}_\lambda). \quad (2-6)$$

The wavelength-dependent absorption cross section $C_{\lambda,\text{abs}}$ can then be used in the spectroscopic model to account for the absorption and emission of nanoparticles within the Rayleigh regime.

(ii) For the *laser-heating process*, the Rayleigh limit of Mie theory is used to describe the light–particle interaction allowing the assumption that the laser energy is absorbed by the total volume of the particle [44, 45] and thus the particle can be considered as instantly heated to homogeneous temperatures.

The volume effect of nanoparticles assumes that the proportion of the surface atom mass is large compared to the total particle mass [1]. This means that *during the cooling process*, which is a surface-controlled process, the temperature gradient within the particle can be neglected and therefore the temperature distribution can be considered homogeneous.

(iii) In a real system, particles are not necessary spherical, but can have a fractal structure or can be aggregated. Several studies have investigated the influence of aggregation and morphology on LII analysis [51–58]. While the influence of these effects can be significant, it also adds much to the complexity of LII models and therefore further increases the uncertainty of results. As this work focuses on the technical aspects of the LII analysis, the following description of the spectroscopic model is therefore limited to spherical particles with a monodisperse size distribution.

Building up on the prior assumptions, the incandescence of a single nanoparticle can be described based on the blackbody spectral intensity $I_{\lambda, \text{BB}}$, which is given by Planck's distribution as a function of wavelength and temperature

$$I_{\lambda, \text{BB}}(T) = \frac{2hc_0^2}{\lambda^5} \left[\exp\left(\frac{h c_0}{k_B \lambda T}\right) - 1 \right]^{-1}, \quad (2-7)$$

where h denotes the Planck constant, c_0 the speed of light in vacuum, k_B the Boltzmann constant, λ the wavelength, and T the blackbody temperature.

The incandescence I_λ , emitted by a single particle, can then be expressed as

$$I_\lambda(T_p) = C_{\lambda, \text{abs}} I_{\lambda, \text{BB}}(T_p) = \frac{\pi^2 d_p^3}{\lambda} E(\mathbf{m}_\lambda) I_{\lambda, \text{BB}}(T_p). \quad (2-8)$$

During an LII measurement, usually the incandescence from an ensemble of nanoparticles within the detection volume is measured as an incident spectral irradiance on the detector J_λ . The irradiance is proportional to the integrated intensities over the particle-size distribution using the probability density of the particle diameters $p(d_p)$, and is scaled by the volume fraction within the detection volume f_V and the optical efficiency of the detection system B_λ

$$J_\lambda(T_p) \propto f_V B_\lambda \int_0^\infty p(d_p) C_{\lambda, \text{abs}}(d_p) I_{\lambda, \text{BB}}[T_p(d_p)] dd_p. \quad (2-9)$$

To simplify the analysis, often a monodisperse particle-size distribution is assumed and the temperature in the calculations is considered being an “effective” temperature $T_{p, \text{eff}}$ of the particles in the detection volume, which simplifies equation (2-9) to

$$J_\lambda(T_{p, \text{eff}}) \propto f_V B_\lambda C_{\lambda, \text{abs}} I_{\lambda, \text{BB}}(T_{p, \text{eff}}), \quad (2-10)$$

Equation (2-10) can then be further simplified by summarizing all wavelength-independent properties in a general scaling factor Λ leading to

$$J_\lambda(T_{p, \text{eff}}) \propto \Lambda \frac{E(\mathbf{m}_\lambda)}{\lambda} \frac{2hc_0^2}{\lambda^5} \left[\exp\left(\frac{h c_0}{k_B \lambda T_{p, \text{eff}}}\right) - 1 \right]^{-1}. \quad (2-11)$$

Equation (2-11) can be used as a foundation for the spectroscopic model of multi-color LII techniques. In case of two detection wavelengths, an analytical formula can be derived from equation (2-11), while for more detection wavelengths, the equation system is overdetermined and least-squares methods are needed.

Ratio pyrometry is based on the ratio of the experimentally determined spectral irradiance $J_{\lambda,i}^{\text{exp}}$ at two wavelength bands λ_i

$$\frac{J_{\lambda,1}^{\text{exp}}}{J_{\lambda,2}^{\text{exp}}} = \frac{E(\mathbf{m}_{\lambda_1}) \lambda_2^6}{E(\mathbf{m}_{\lambda_2}) \lambda_1^6} \left[\frac{\exp\left(\frac{h c_0}{k_B \lambda_2 T_{\text{p,eff}}}\right) - 1}{\exp\left(\frac{h c_0}{k_B \lambda_1 T_{\text{p,eff}}}\right) - 1} \right]. \quad (2-12)$$

Using the Wien approximation for small wavelengths (< 1000 nm) and temperatures lower than 4000 K, i.e.,

$$\exp\left(\frac{h c_0}{k_B \lambda T_{\text{p}}}\right) - 1 \approx \exp\left(\frac{h c_0}{k_B \lambda T_{\text{p}}}\right), \quad (2-13)$$

the analytical formula of the two-color pyrometry can be derived by solving equation (2-12) for $T_{\text{p,eff}}$

$$T_{\text{p,eff}} = \frac{h c_0}{k_B} \left(\frac{1}{\lambda_2} - \frac{1}{\lambda_1} \right) \left[\ln \left(\frac{J_{\lambda,1}^{\text{exp}} E(\mathbf{m}_{\lambda_2}) (\lambda_1)^6}{J_{\lambda,2}^{\text{exp}} E(\mathbf{m}_{\lambda_1}) (\lambda_2)^6} \right) \right]^{-1}. \quad (2-14)$$

The formula is commonly used in various LII studies to determine a temperature trace from two calibrated LII signals collected at two different detection wavelengths [9, 40, 41].

When two or more detection channels are available, the experimentally determined spectral irradiance $J_{\lambda,i}^{\text{exp}}$ with standard deviation σ_i for the i^{th} channel can be compared to the simulated irradiance $J_{\lambda,i}^{\text{mod}}$ from equation (2-11) using least-squares minimization

$$T_{\text{p,eff}} = \underset{T_{\text{p}}, \Lambda}{\operatorname{argmin}} \left\{ \sum_i \left(\frac{J_{\lambda,i}^{\text{exp}} - J_{\lambda,i}^{\text{mod}}(T_{\text{p}}, \Lambda)}{\sigma_i} \right)^2 \right\}. \quad (2-15)$$

Theoretically, only two detection wavelengths are needed to determine the particle temperature. Practically, the signals are always affected by noise or signal bias. This is usually not a problem in ratiometric methods if both detection channels are equally affected, but if a single channel is biased more strongly, the calculation would lead to wrong temperatures (see section 4.4.3). Increasing the number of detection channels over-determines the calculation and adds information that can make the measurements more robust. A statistical analysis of the spectroscopic model is provided in chapter 5 along with the description of the calibration procedures for the LII signals.

2.2 Heat transfer model

The pyrometrically determined temperature trace of laser-heated particles can be used to describe the heat exchange of the particle to the surroundings. As small particles cool faster than large particles, the slope of the temperature trace allows conclusions on the mean particle diameter in the detection volume.

Two differential equations are formulated to describe the temporal change of the internal energy during the cooling process and the mass change due to evaporation [3, 19]. The energy balance around the particle surface can be described with

$$\frac{dU_{\text{Internal}}}{dt} = \dot{Q}_{\text{Absorption}} - \dot{Q}_{\text{Evaporation}} - \dot{Q}_{\text{Conduction}} - \dot{Q}_{\text{Radiation}}, \quad (2-16)$$

where U_{Internal} is the internal energy and \dot{Q} the heat transfer rates for absorption, evaporation, conduction and radiation. Usually, heat transfer by radiation is small compared to the other phenomena and can be neglected, but it can still play a role in extreme applications with low pressure and high gas temperatures. Sometimes, additional effects are incorporated in submodels such as thermionic emission [19, 43, 59, 60], oxidation [59, 61, 62], photodesorption [62], or annealing [62].

For LII measurements at high laser fluences, the mass loss of the particles due to evaporation, $\dot{m}_{\text{Evaporation}}$, becomes important in which case the evolving particle mass, m_p , must be solved using

$$\frac{dm_p}{dt} = -\dot{m}_{\text{Evaporation}}. \quad (2-17)$$

The coupled energy and mass balances are usually solved using an ordinary differential equation (ODE) solver for given initial conditions (i.e., particle temperature, gas temperature, laser fluence) and varied over the parameter of interest (i.e., particle size). The key outcome from this step are simulated temperature traces that can be compared with the experimentally determined temperature trace from the spectroscopic model.

For single-color LII, usually the laser absorption is modeled and used to estimate the LII peak temperature. This approach requires accurate knowledge of laser fluence, absorption cross-section and local gas temperature, which is rarely known with a high degree of certainty.

For multi-color LII, the particle temperature can be determined without knowledge of the laser energy and the laser absorption is usually excluded from the modeling. The heat transfer model is solved shortly after the temperature peak, when the process of laser heating is finished.

It needs to be noted that the LII signal decay can be influenced by non-homogeneous laser heating of the particles caused by polydispersity [51, 63-65], aggregation and morphology [52-57, 66], or by practical issues such as non-uniform laser-beam profiles [67-70].

This thesis focuses on the early stage of LII-signal processing to increase the robustness of the obtained temperature traces from the spectroscopic model and therefore, the heat transfer model is not discussed in detail. For the LIISim application cases in chapter 6, three previously published heat transfer models [19] have been implemented in the LIISim software and the corresponding formulas and properties are summarized in Appendix D.

2.3 Experimental layout

Conceptually, an LII apparatus can be split into two major parts: particle excitation and signal detection. Figure 2-3 shows a basic setup for LII including the laser system that is used for heating the particles in the LII probe volume, and a detection system consisting of collection optics, a neutral density (ND) filter wheel, and two photomultipliers equipped with bandpass filters to detect light reflected and transmitted by a dichroic mirror in two different wavelength bands.

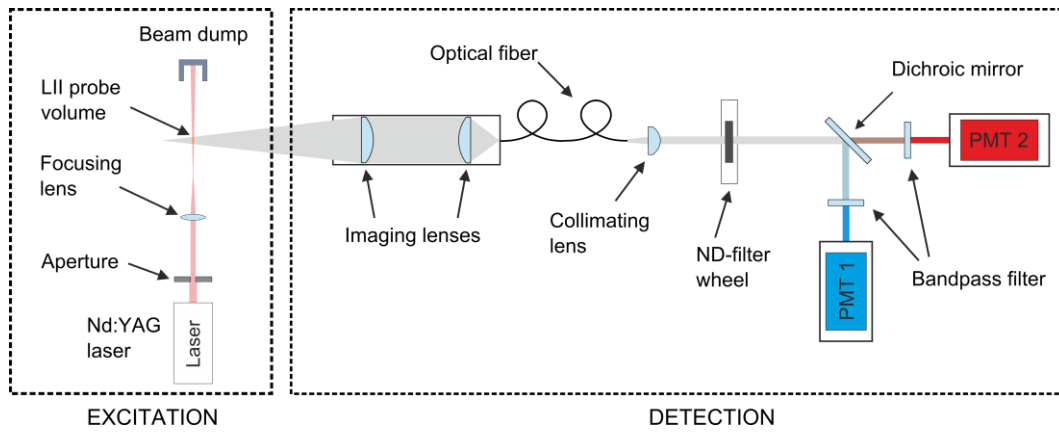


Figure 2-3 Schematics of two-color laser-induced incandescence measurements with a fiber-coupled detector.

For the particle heating, a pulsed laser system, typically an Nd:YAG laser, is used, either with a wavelength of 532 nm, or 1064 nm and with a pulse width of several nanoseconds. The laser-beam profile is shaped using an aperture and then imaged into the position where the incandescence will be analyzed. For the detection, it is desired to spatially limit the detection volume. This is usually done using imaging lenses and a spatial filter as pinhole, an optical fiber, or an aperture. The cross-sectional volume of laser-beam and collection angle defines the probe volume. Particles in this volume are heated to incandescent temperatures and the emission is then measured as the LII signal.

2.3.1 Excitation

For the laser heating, it is important that the laser pulse is significantly shorter than the investigated LII decay duration. Typical laser systems that are used for LII experiments provide pulses with a duration of less than 10 ns at a repetition rate between 1 and 20 Hz. The excitation wavelengths should be selected according the absorption spectrum of the material. Some oxides and non-metals, e.g., SiO_2 , TiO_2 , or sulfates may not absorb laser light in the visible range [10]. Excitation wavelengths that can cause spectral interferences such as fluorescence or phosphorescence should be avoided, which makes visible or near-infrared wavelengths preferable [10]. Common laser wavelengths are the fundamental Nd:YAG wavelength of 1064 nm or the frequency-doubled wavelength of 532 nm. However, the latter might interact with LII detection wavelengths and further optics need to be included in the detection system to discriminate against elastically scattered light. There are also some studies that take advantage of multiple harmonics of Nd:YAG systems to obtain information about the optical properties of the particles. The two-excitation-wavelength LII (TEW-LII) technique [71-73] has been used for inferring the soot absorption function from the ratio of measurements at different excitation wavelengths and is used in recent studies [57, 74, 75].

To ensure equally heating of all particles in the probe volume, the spatial uniformity of the laser-beam profile is essential. While the standard profile of most laser systems is Gaussian, beam shaping towards a top-hat profile can significantly improve the LII signal quality. Various studies investigated the influence of spatially non-uniform laser beam profiles previously [67-69]. In applications with strongly absorbing media (e.g., at high pressure and high concentrations), the laser-beam profile changes as the beam propagates through the medium. For these conditions, the influence of laser-beam geometry on the fluence-dependent peak LII intensity was described by several studies [24, 76, 77].

The laser fluence, needed for an LII experiment, depends on the initial particle temperature and on the absorption efficiency of the material. This means that particles that are in a high-temperature flame environment need less energy to reach the same post-laser-pulse temperatures compared to cold soot from exhaust systems. It was observed that for some materials (e.g., synthesized silicon nanoparticles), a laser fluence ten times greater than normally used for soot measurements was necessary to achieve the same LII signal amplitude [13]. It also should be noted that a high excitation intensity can cause morphology changes of aggregates or affect the internal structure of primary particles (e.g., graphitization) as demonstrated in double-pulse experiments by Vander Wal and Jensen [6].

2.3.2 Detection

The detection system mainly consists of collection optics, optical filters, beam splitter, and the detectors. Different detector types are used depending on the focus of the respective study. While photomultiplier tubes are the most common detector type as they provide fast temporal response and high sensitivity, measurements using intensified cameras can achieve a higher spatial resolution at the expense of temporal resolution. Gated spectrometers can provide a high spectral resolution, but multiple measurements are needed to resolve the full temporal decay. As such subsequent measurements can be time consuming, they are only applicable to perfectly stationary environments. Streak cameras provide both high spectral and temporal resolution, but require a strong LII signal and thus cannot be used in applications with low particle concentrations or low laser fluence.

For time-resolved LII, the accuracy of the inferred aerosol parameters is predicated on obtaining an accurate pyrometric temperature decay. Increasing the number of detection wavelength bands improves the robustness of the measurement [11, 12]. For the selection of detection wavelength bands, the sensitivity range of the detector as well as the potential for spectral interference from fluorescence must be considered. Liu *et al.* [78] presented a study investigating the sensitivity of various two-color ratios on pyrometric temperature determination, suggesting to use detection wavelengths with large gaps, preferably towards longer wavelengths. In the case of soot measurements, there are several studies reporting interference with C₂ emission in flames at very high fluences (i.e., > 2 mJ/mm²) [4, 79-81]. For other, less investigated, materials systems, careful selection of the detection wavelength bands is essential and should be approved with additional spectrally resolved measurement methods (e.g., gated spectrometer, streak camera) [12, 82-84]. In contrast to the regular two-color approach, Flügel *et al.* [85] presented a broad-band two-color LII approach in which the two bandpass filters were replaced with short and long-pass filters, respectively, to achieve higher sensitivity. While this approach can increase the signal-to-noise ratio, accurate knowledge of wavelength dependencies of the involved experimental parameters (i.e., optical efficiencies of the detector, optical properties of the materials system, etc.) is crucial, which is only rarely the case for typical LII experiments.

Further aspects of detection and a literature review about detector performance, detector requirements, and calibration are presented in detail in chapter 4 and 5.

2.4 Applications

Traditional applications of LII focus on determining soot concentrations and particle sizes in flames. The technique was later applied to combustion-based processes such as engine and exhaust measurements. With the recently rising awareness of health, safety, and environmental risks for combustion processes, the research field for atmospheric or environmental measurements keeps growing.

LII applications can be generally split into combustion-based processes and synthetic nanoparticle processes. For the first group the particles are usually an unwanted by-product and the understanding of the formation processes can help to improve these processes towards a desired minimum particle concentration, certain size or morphology. The second group that summarizes applications on synthetic nanoparticle processes is mostly interested in the product from these processes. The knowledge about the particle formation can help to design and improve such processes to yield tailor-made particle properties and to make the process more efficient.

Soot particles in flame environments are a common measurement object in combustion science. Many flames can be operated stably and by using standardized “benchmark” flames operating at standard conditions, the measurements can then be compared to those of other researchers. Several studies applied LII on a wide range of flames as laminar diffusion flames [23, 24, 86-89], laminar premixed flames [14, 20, 77, 90-96], and turbulent flames [24, 32, 97, 98]. But also various other processes as droplet combustion [99], engines / exhaust [100-102], shock tubes [103], and atmospheric / environmental conditions [104, 105] have been investigated in the past.

The transition to the second group becomes smooth, when engineered carbon-black particles are investigated, synthesized by vaporization from graphite by a laser [38], in an arc discharge [106], or behind a shock tube [107], or in exhaust from industrial carbon black processes [108, 109]. Other studies investigated synthesized carbon nanotubes and nanofibers [110], commercially available carbon nanotubes suspended by a piezoelectric disk [111], or various furnace blacks that are suspended in liquids and dispersed by sonication [112].

A wide range of synthetic nanoparticles has been investigated with LII. This covers many metals, such as copper [12], iron [42, 82, 113-116], molybdenum [82, 83, 116-119], silver [116], titanium [82], and tungsten [82] and metal oxides, such as aluminum oxide [120], iron oxide [40], manganese oxide [40], titanium nitride [121], and titanium dioxide [84, 122].

The production of semiconducting nanomaterials and the understanding of their formation mechanisms have become a growing research topic [123]. Silicon nanoparticles have been investigated by LII in several studies [12, 13, 124-126] and LII studies on germanium nanoparticles [127] is topic of ongoing research.

The wide range of different applications demonstrates the need of flexible LII detection systems that are compatible with a preferably large number of materials systems and process conditions.

3 OBJECTIVE AND CONCEPTS

The motivation for the present work is to enable the laser-induced incandescence measurement technique for comparative studies on various materials systems and processes and further, to increase the quality of the generated data. The following section describes some key attributes for LII measurements and the consequences on the quality of the measurement result. These points define the specifications for the design of the experimental setup. Some aspects are of higher importance and will be investigated as self-contained research articles in the following chapters.

3.1 Design requirements for the experimental setup

For the design of the experimental setup for multi-color time-resolved LII measurements, several specifications need to be defined. The objective is to design a mobile measurement system that is capable to handle flexible operation in different lab environments and on different processes. These processes could contain nanoparticles from different materials systems and different process conditions. Results from the analysis should be reproducible, comparable and it should be possible to install the experimental setup on any process without major modifications. In the following, some key specifications are defined that determine the design of an experimental setup:

Laser beam uniformity and stability

The shape and the stability of the laser beam profile is crucial for LII measurements. A non-uniform beam profile can lead to an inhomogeneous temperature distribution of the laser-heated particle ensembles and thus to wrong assumptions of their cooling behavior [67, 69]. The adjustment of the laser fluence (i.e., mean energy per area) is used to control the heat transferred to the particles. When the fluence is changed, the energy distribution in the beam profile should remain spatially homogeneous to ensure that the particles are equally heated throughout the probe volume. In some applications, averaging of signals from multiple laser pulses is required to improve the signal-to-noise ratio. In these cases, the laser energy and temporal jitter over several hundred laser pulses should not deviate too strongly from the mean to avoid temporal blurring effects.

Detector sensitivity, dynamic range and linearity

The sensitivity of the measurement system needs to be sufficiently high to generate an electrical signal that can be measured with an oscilloscope. The LII signal scales with the particle concentration of the aerosol and the laser fluence. This requires the detector to cover a wide dynamic range from weak signals (for low concentrations, low laser fluence) to strong signals (for high concentrations, high fluence). At the same time linearity must be ensured, which means that the electrical signal must be proportional to the optical signal during the full signal trace. If the signal response is linear, the slope of a measured LII signal can be connected to a physical model.

Multiple detection wavelengths

The optical properties of the materials investigated by LII can vary with wavelength, but also with particle composition and physical state. For temperature determination, these wavelength-dependent optical properties are an important input for the spectroscopic model, but at the same time, there is not much information available in literature. Especially for emerging technologies as the formation of synthetic nanoparticles, information about the optical properties at elevated temperatures is rarely available. This requires increasing the robustness of the pyrometry by additional detection wavelengths, to compensate for the uncertainty in the optical properties and to provide additional information that can be used for model validations. Another motivation for additional detection channels is the occurrence of signal interferences affecting one or more detection channels. In this case, the two-color pyrometry using two detectors could still provide plausible results, but pyrometrically inferred temperatures could significantly deviate from the actual temperatures. Additional detection wavelength bands over-determine the pyrometric analysis and help to reveal deviations from the expected spectral characteristics.

Detector calibration

For the pyrometric determination of LII temperature traces based on ratiometric signal analysis, the detectors need to be calibrated relative to each other to generate physical signals that can be used as input for the spectroscopic model. It needs to be validated that the calibration procedure is not affected by the choice of light sources and light levels. Also, variable optical components and detector parameters (i.e., gain) need to be calibrated, so that the same experimental conditions can be measured at different detection settings and always give the same result.

Signal quality

Measurement noise is always present during LII measurements, but needs to be reduced to a minimum level. Equipment in the lab can cause signal bias and measurement artifacts that can influence the LII analysis. It is important to identify and avoid noise in the signal and distinguish physical effects from noise. This is especially important for the development of LII models that can otherwise lead to faulty and more complex models. Noise components can be introduced by the laser unit, power supplies, pulse generator, oscilloscope, or other electronics components. Careful wiring and shielding of all electrical components and usage of power supplies with low ripple noise needs to be considered.

Software for data acquisition and analysis

The processing chain from data acquisition to interpretation of the analysis result involves many steps from export of the data, conversion of the data format, basic signal processing, and comparison with a customized LII model. Usually, individual source code is developed for specific research tasks. A modular structure of the scripts for LII analysis should allow using the same framework for different research projects. The software should be applicable to different materials systems using various heat transfer models and numeric routines.

Reproducibility and standardization

When LII measurements are performed on different materials systems, it can be necessary to move and install the LII setup on another experimental table. A rigid mechanical design of the detection setup is important to achieve reproducible measurements when the setup is moved. Opto-mechanical mounts such as filter wheels with snap-in mechanisms can ensure that optical components retain in the same

positions and angles when they are switched. For the variation of experimental parameters, it is important that especially sensitive settings (i.e., laser energy and detector gain) can be reproducibly changed. This can be achieved by electronic control of set values using analog input/output devices. A standardized file format can help to exchange measurement data between researchers.

Mobility and flexibility of the setup

The measurement system should be portable and compact so that it can be used for the investigation of different particle formation processes in different laboratories. The optical access to the measurement position of the LII experiment is often limited and space/distances available for the collection optics can vary. This makes it desirable to have small collection optics with variable focal lengths that are flexibly connected to the detection device. The particle concentration in the aerosol for different process conditions can vary and the optical properties of the investigated materials systems can influence the magnitude of the LII signal amplitude. Optical components with variable transmission (i.e., ND filter) and variable detector settings (i.e., PMT gain) allow the adjustment of the signal amplitude/light level for a range of measurement conditions. The variable experimental LII parameters (i.e., laser energy, ND filter transmission, and detector gain) should be adjustable without the need for interrupting the particle formation process.

3.2 Experimental design and modifications

This section addresses solutions for the defined requirements and gives recommendations for the experimental design and customization of four major parts: (i) laser system, (ii) detection system, (iii) electronics for the control of experimental parameters, and (iv) software for data acquisition and analysis.

3.2.1 Laser system

The laser energy stability for multiple laser pulses can only be controlled to a certain extend by the experimentalist. Usually, parameters for the laser operation (e.g., flash lamp voltages, Q-switch delay) are set to values recommended by the laser-system manufacturer to achieve high stability of energy and pulse duration, but at the same time, it limits the range of possible laser energies. For many LII experiments, an important variable experimental parameter is the laser fluence that is used to control the particle heating to different peak temperatures and thus determines which heat transfer phenomena are dominant. This requires evaluating different options for experimental control of the laser fluence during an LII experiment without significantly affecting the energy stability, the beam profile, and the temporal profile.

When Q-switched lasers are used, the laser fluence can be varied by varying the Q-switch delay time. With increasing delay, the energy is reduced, but at the same time, the spatial beam profile is distorted. The influence of Q-switch delay variation was investigated using a double pulse Nd:YAG system (Big Sky Laser – CFR200 PIV) for Q-switch delays and corresponding energies of 210 µs (100 mJ), 260 µs (70 mJ), and 310 µs (25 mJ) at a repetition rate of 10 Hz. The beam profile was measured using a wedged beamsplitter in the optical path of the laser beam and recording the spatial energy profile of the reflection with a beam profiler (Coherent – LaserCam-HR). Figure 3-1 shows the measured beam profile distortion for the double-pulse laser system with increasing Q-switch delay.

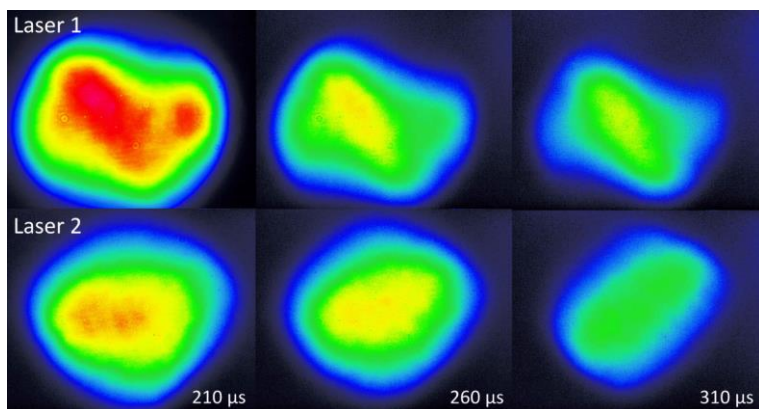


Figure 3-1 Laser-beam profile distortion with increasing Q-switch delay for two identical lasers in a double-pulse system: 210 µs (100 mJ), 260 µs (70 mJ), and 310 µs (25 mJ).

Instead of changing the pulse energy via the Q-switch timing, a possible other solution is using a set of ND filters or a variable energy attenuator. The set of ND filters has the disadvantage of being sensitive to overheating and it needs to be arranged in a certain angle to avoid back reflections. This limits its applicability to low repetition rates and low-energy measurements. An alternative is a continuously variable attenuator that consists of two opposing dielectrically coated plates. The angle between the incident laser beam and the plates determines the ratio of reflected and transmitted light. The symmetric design with a second plate corrects for the beam displacement of the first plate. If strong laser energy attenuation is

needed (e.g., high-power laser is used for low-fluence measurements), the angle of incidence becomes large, and consequently, the laser beam can be distorted.

Variable laser pulse energy attenuator

A well-established solution for achieving a distortion free energy variation in LII setups is the half-wave plate polarizer arrangement that requires linearly polarized laser light (see Figure 3-2). A common setup is a thin-film polarizer arranged at Brewster's angle θ , which reflects only s-polarized light, while p-polarized light is transmitted. The rotation of the half-wave plate changes the polarization state and thus the portion of light reflected and transmitted by the polarizer. The advantage of this strategy is that the spatial energy distribution is not affected when the mean energy is changed. An additional, but optional, element is a quartz plate of the same thickness as the polarizer to compensate for beam displacement.

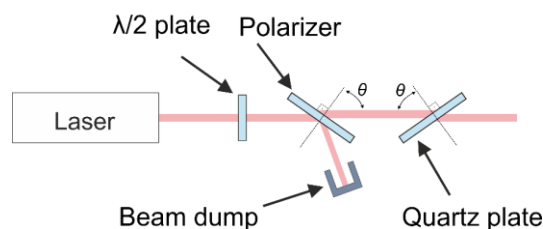


Figure 3-2 Optical arrangement for the variable energy attenuator. The $\lambda/2$ plate is mounted on a rotatable mount to change the polarization state. The polarizer and quartz plate are placed at Brewster's angle θ for optimal transmission.

A very small rotation of the half-wave plate can already cause a strong change in laser energy. This complicates the reproducible adjustment of the laser energy during a running experiment. To solve this issue, the laser-system of the Artium LII device was extended by a newly designed motorized wave-plate rotation unit with a transmission ratio of 1:430. A potentiometer provides the current position and is connected to an analog I/O board extended by a motor-driver board (Faulhaber MCDC3002 S) that was programmed to control the movement of the wave plate via LabVIEW or through the NI-Daqmx driver. Figure 3-3 shows the modified laser unit (Artium/Quantel) including the motorized rotation unit, the polarizer and a quartz plate for beam displacement correction. Additional beam dumps are installed for ghost and back reflections.

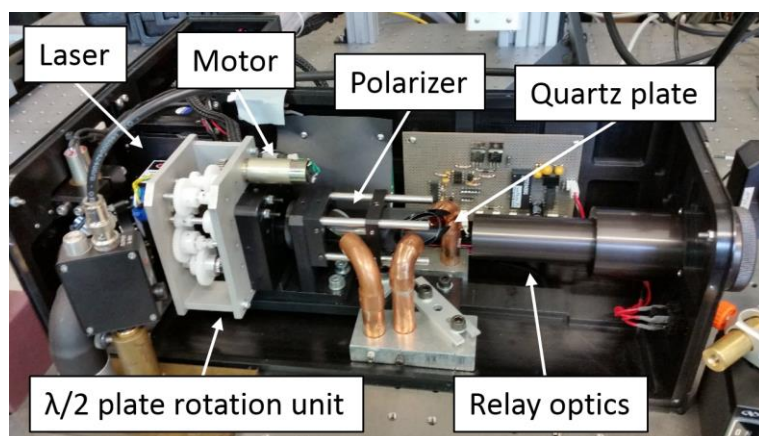


Figure 3-3 Laser unit (Artium modular LII system with Quantel – UL120F11 laser) modified with a newly designed variable laser pulse energy attenuator.

The laser energy can be measured prior the experiment and the wave-plate position and the corresponding laser energy is saved in a lookup table that can then be used during an experiment to set the desired laser energy. To avoid hysteresis errors due to the backlash of the rotation unit, the positions should always be approached from the same direction.

Laser beam relay imaging

The laser beam profile at the laser output is usually of Gaussian shape, which can cause particles across the probe volume to be heated to different temperatures. To ensure a homogeneous energy distribution, an aperture in combination with relay imaging can be used. The aperture size is selected smaller than the original beam diameter and the most uniform area is selected by adjusting the aperture position.

Figure 3-4 shows three possible configurations for beam shaping using (a) one convex lens, (b) two convex lenses and (c) a combination of three convex lenses with a diffractive optical element (DOE).

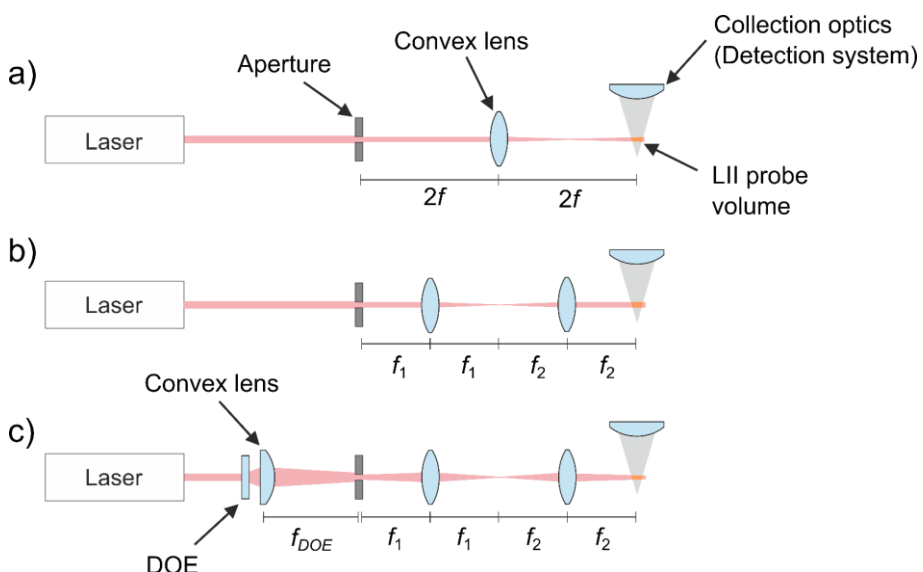


Figure 3-4 Beam shaping using imaging with (a) one lens, and relay imaging with (b) two lenses and (c) two lenses combined with a diffractive optical element (DOE).

While the simplest configuration (a) produces already acceptable results (Figure 3-5), the sharpness of the beam profile can be further improved by using the relay configuration (b) with two lenses.

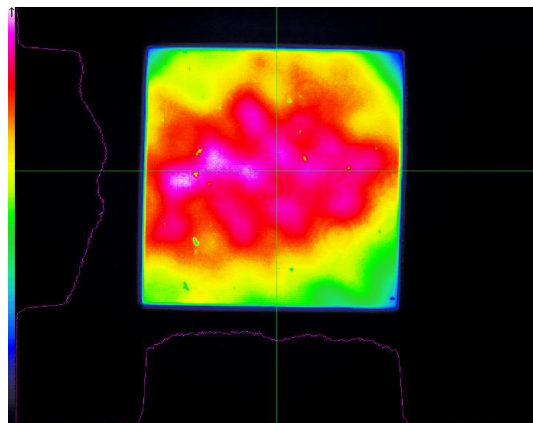


Figure 3-5 Laser profile ($2.4 \times 2.4 \text{ mm}^2$) with nearly top-hat profile, imaged into measurement position using an aperture and a single lens (Quantel – UL120F11).

The beam profile uniformity can be even further improved by diffractive elements in the beam path to smooth the beam profile. Diffractive optical elements (DOE) transform the laser beam into a predefined and uniform shape. They are usually mounted directly at the laser beam output, and are combined with a focusing lens. The beam profile as shown in Figure 3-1 (Laser 1, 210 μs) is used as input for this configuration and Figure 3-6 shows the resulting beam profile without (left) and with (right) an aperture. The aperture is used to increase the sharpness of the profile edges and to select the most homogenous part of the laser beam profile generated by the DOE.

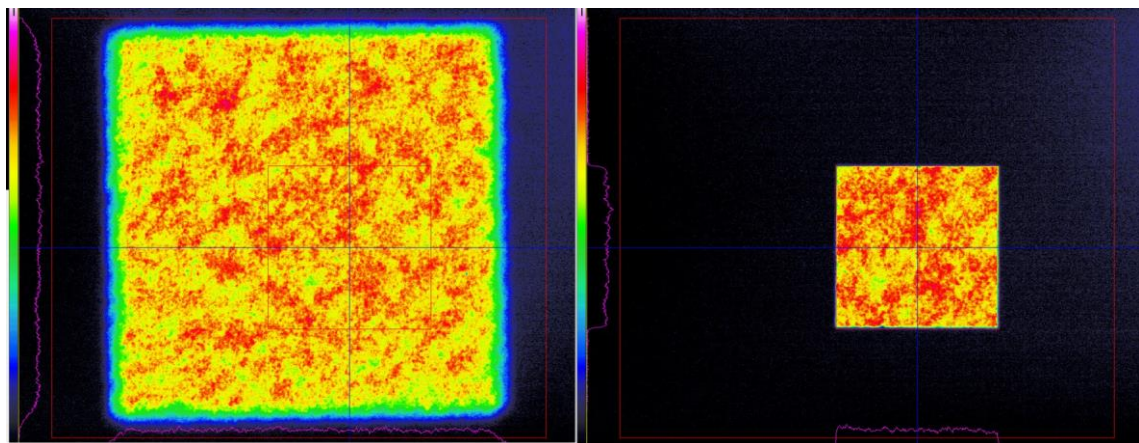


Figure 3-6 Beam profile; relay imaged using a DOE without (left; $9.5 \times 9.5 \text{ mm}^2$) and with aperture (right; $4 \times 4 \text{ mm}^2$) (Big Sky Laser – CFR200 PIV).

The beam profile modified by a DOE imaged into the measurement position is shown in Figure 3-7 for a range of distances relative to the measurement position using two 450 mm focal length lenses for the relay imaging.

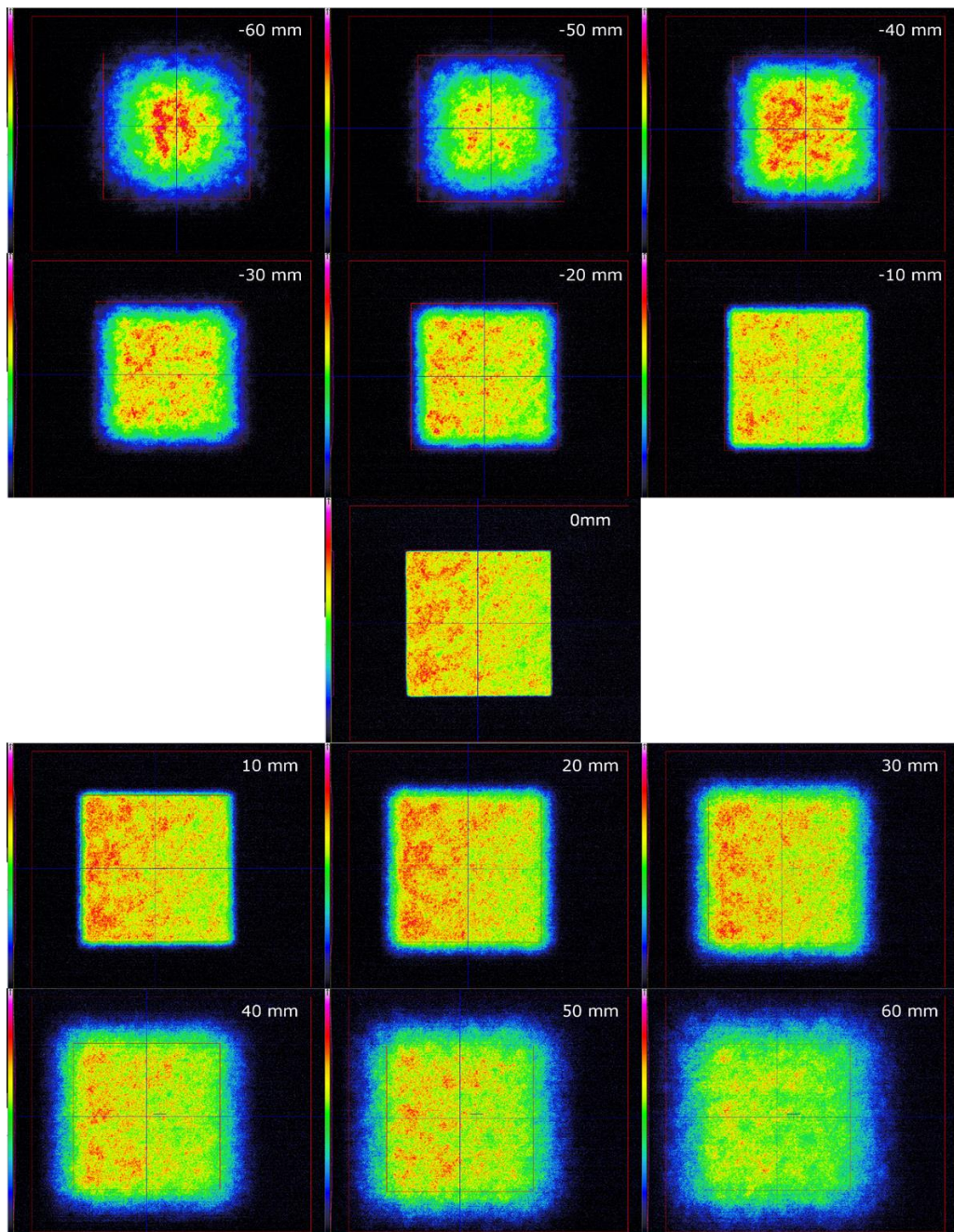


Figure 3-7 Laser profile ($4 \times 4 \text{ mm}^2$) formed by a diffractive optical element (DOE) and aperture, and relay imaged into the probe volume position (0 mm). Images are measured at various distances (-30 mm to 60 mm) to the actual probe volume along the propagation direction of the laser beam (Big Sky Laser – CFR200 PIV).

Optical triggering using a fast photo diode

For time-resolved measurements, the reproducible determination of $t = 0$ is critical. In case LII signals are averaged over multiple laser shots, temporal jitter caused by a variation of the electronic trigger transmission can lead to temporal blurring of the LII signal trace. Depending on the laser system, the trigger for the signal acquisition relative to the laser pulse can be achieved on different ways. The flash lamp and Q-switch timing of the laser unit can be coupled with a pulse generator or with the oscilloscope trigger input (using the Q-switch timing is by far preferred). Alternatively, the laser pulse onset can be detected

by collecting scattered laser light with a fast photo diode coupled to the oscilloscope trigger input causing the jitter being reduced drastically. This requires pre-trigger sampling functionality, which is supported by most digital storage oscilloscopes and which allows recording the signal preceding the trigger moment.

3.2.2 Detection system

The basic design of the LII apparatus used in this work consists of four detection channels and variable fiber-coupled collection optics (Figure 3-8). This setup is modified for the research studies presented in the following chapters and detailed information about modifications and components are described in the corresponding chapters.

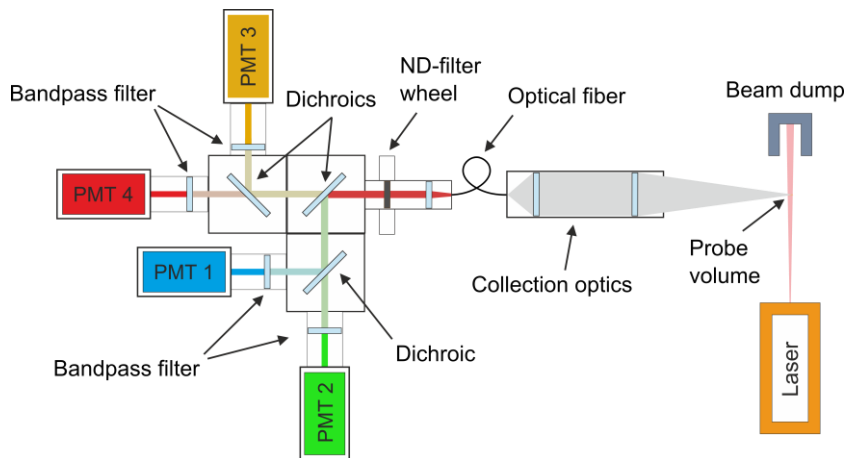
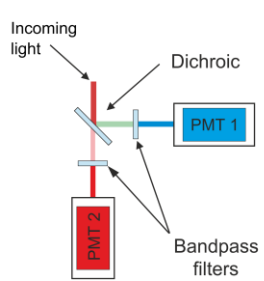


Figure 3-8 Basic LII design with four detectors and fiber-coupled collection optics.

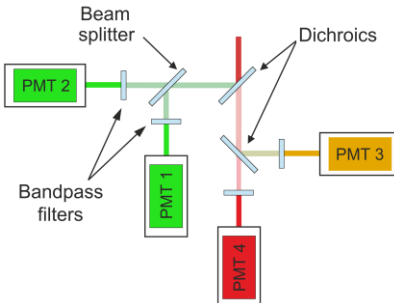
Multiple detection channels

The most basic detection setup for LII is a single-color arrangement, using only one PMT equipped with a bandpass filter. To be able to determine pyrometric temperatures, the incoming light needs to be spectrally separated with a dichroic mirror and then detected with at least two detectors equipped with different bandpass filters. Figure 3-9 shows three possible configurations for multi-color LII that are used in this work.

a) Two color



b) Three color



c) Four color

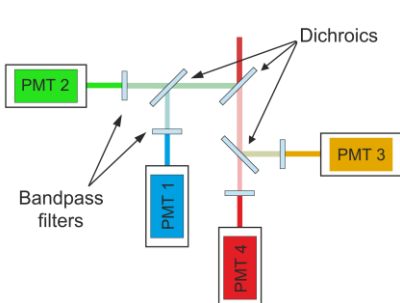


Figure 3-9 Three possible LII detector configurations for (a) two-color LII, (b) three-color LII with four detectors and (c) four-color LII.

The bandpass filters and dichroic mirrors in these configurations need to be selected to match the detector sensitivity range, their transmission ranges need to be sufficiently distant to each other, and the total

transmission should be maximized. For the selection of components, several hundred online-available filter transmission curves were downloaded from the website of two manufacturers (i.e., Semrock, Chroma) and then loaded into MATLAB. The spectral transmission curves of dichroic mirrors (DM) and bandpass filters (BP) were used as an input for a selection algorithm to find four bandpass filters and three dichroic mirrors that are most suitable as detection wavelengths. For this purpose, a MATLAB selection algorithm was implemented to make a pre-selection for most suitable components according several criteria:

1. Match the sensitivity range of available PMTs (i.e., between 350 and 850 nm)
2. Full width at half maximum (FWHM) of BP between 10 and 50 nm
3. Minimal width of the rising edge (DM)
4. Maximal distance of BP transmission spectrum from the DM edge wavelength
5. Maximal mean transmission (BP)
6. Maximal mean transmission at BP spectrum (DM)
7. Minimal mean reflection at BP spectrum (DM)
8. Available shape, dimensions and price

The transmission curves of the selected bandpass filters and dichroic mirrors are presented in Figure 3-10. At this point, it needs to be noted that the selection algorithm does not account for spectral interference due to fluorescence and phosphorescence, which depends on the investigated materials system (cf. section 2.3.2).

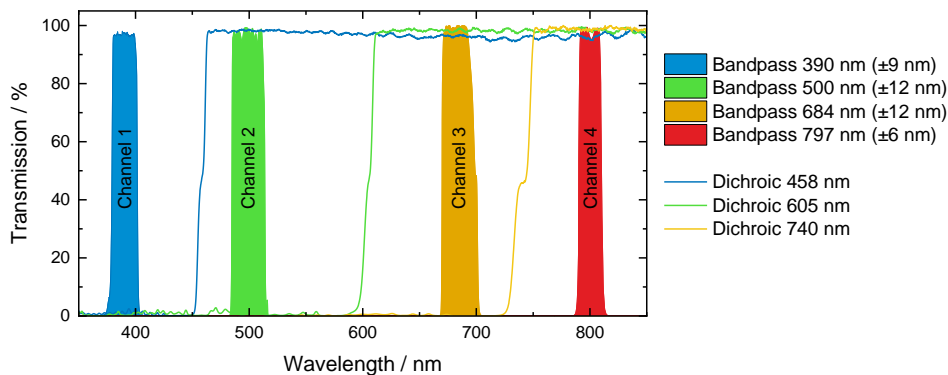


Figure 3-10 Transmissions of the selected bandpass filters and dichroic mirrors based on the data provided by the manufacturer.

With the initial four-color design, the light intensity of the available calibrated light source was not sufficient to calibrate channel 1. Therefore, the dichroic mirror at 458 nm was replaced by a 50%/50% beam splitter and the bandpass filter of channel 1 by the same type as channel 2 (i.e., 500 nm), respectively. This configuration has an advantage for the linearity measurements in chapter 4, as two different photocathode types could be investigated at the same wavelength band and conclusions on the influence of the photocathode material on linearity can be made.

Variable fiber-coupled collection optics

In some applications, it is required to change the focal lengths of the collection optics, or to reach measurement positions that are difficult to access (e.g., if the space around the optical access is limited by other devices or infrastructure). To achieve highest flexibility, the LII detection system is connected to the

collection optics by an optical fiber. This modification has two purposes: (i) the fiber acts as a spatial filter and limits the size of the LII probe volume, and (ii) increases flexibility of the position of the collection optics and the LII detection system in the lab. This means that the focal lengths of the optical tube can be selected according the distance and available space for the optical access and the fiber provides a flexible optical connection to the LII detection device that can then be placed in a free area in the lab. It is important to pay attention to chromatic aberrations introduced by the collection optics as these can strongly influence the spectral response (cf. chapter 5.4.1.3). Achromatic lenses as collection optics can reduce this influence, but they are also only designed for a limited wavelength range.

Mobile rack for the detection setup

A main research field of the institute is the characterization of nanoparticle formation of various materials systems. Usually, multiple measurement techniques are applied to a reaction system to investigate different particle properties. Using the LII technique as a supplementary technique to obtain information about particle size is therefore often desired. For this purpose, the detection setup was mounted to a mobile rack that can be placed directly beneath the reactor of interest. The mobile setup is shown in Figure 3-11. The laser unit is separated from this setup and only connected by cables for the laser trigger and control of the variable energy attenuator.

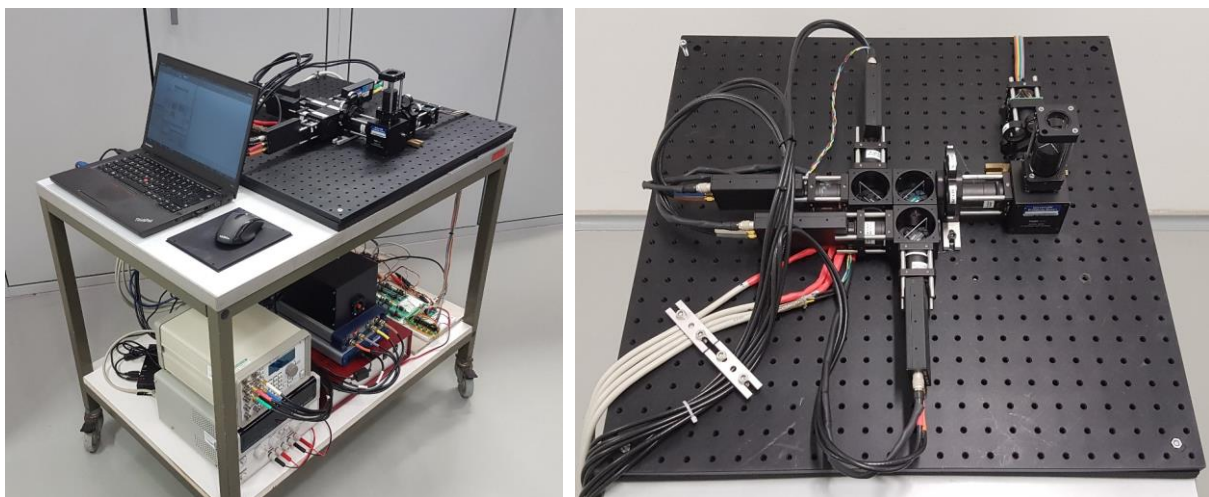


Figure 3-11 Detection setup mounted on a mobile rack including oscilloscope, digital delay generator, power supply and computer.

3.2.3 Electronic control of experimental parameters

Most lab-scale processes used for nanomaterials synthesis are considered quasi-steady, which means the system can be assumed as steady within a short time period of several minutes, but on a longer time scale the process could change due to clogging (e.g., particle filter, piping in closed systems) or by heating-up of the components/environment (e.g., for high-power burners or reactors). When such a process is investigated, it is desired to change experimental parameters as the laser fluence or PMT gain within a short time to preset values so that the measurements are not affected by the temporal drift of the process. An analog I/O device is used to control various experimental parameters as for example the control voltage for the PMT gain or the position of the motorized laser-energy attenuator (cf. previous sections). The analog I/O device can be controlled by LabVIEW or using the instrument drivers with a self-written source code. This allows the easy implementation of automation algorithms for the LII system (i.e., automated

gain calibration sequences), but also process-related automation that helps to keep the process conditions stable (i.e., PID controller for pressure regulation). Further advantage is that process conditions as pressure, flow rates, and temperature, etc. can be logged and saved together with the LII data. For complex experimental matrices, the automation can further be used to predefined process conditions and perform a range of LII measurements for example at predefined laser fluences.

3.2.4 Software for data acquisition and analysis[†]

For data acquisition and analysis, a modular software concept (LII-Sim) was developed that allows flexible adjustment of the signal processing steps and materials systems without the need of changing the source code. This software concept is described in detail in a previous publication shown in chapter 6, but some modifications have been made since the respective paper has been published to extend the software's functionalities by a data acquisition module. The module enables direct communication with the oscilloscope and analog I/O devices. This allows direct storage of metadata (PMT gain, ND filters, laser fluence, experimental conditions, comments, etc.) with the signal data, but can also be used to automate data collection (e.g., for the gain calibration, cf. section 5.4.1.5) or to control the laser fluence via the NI-DAQmx driver and the setup as shown in Figure 3-3. Usually, data collection and analysis are two independent processes and require different software. With the integrated solution, data analysis becomes more efficient as it can be performed quickly during the experiments. Problems with the signal quality or measurement artifacts can so be discovered early and the measurements can be repeated immediately. The user interface of the data acquisition module is shown in Figure 3-12.

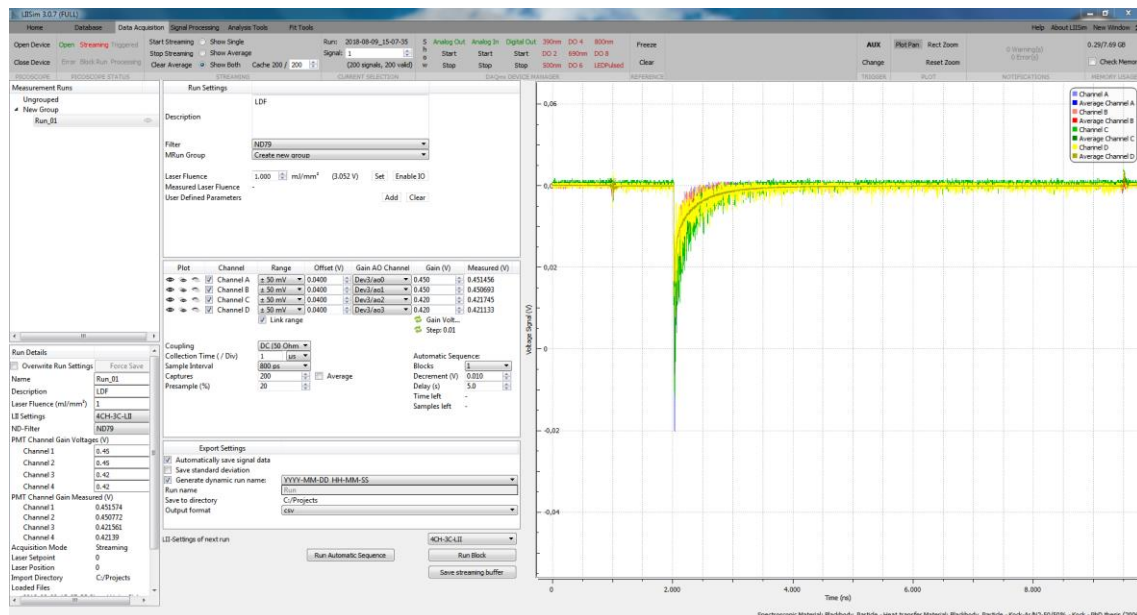


Figure 3-12 Graphical user interface of the data acquisition module of the LII-Sim software.

[†] The LII-Sim data acquisition module is not part of the official pre-compiled LII-Sim version as available through the LII-Sim website. Interested researchers can compile the published source code according to the instructions in the LII-Sim developer guide to obtain full functionalities.

3.3 Research focus

In the following chapters, some of the aspects introduced in the previous sections are investigated in more detail in self-contained research tasks that have previously been published/submitted as individual peer-reviewed journal articles. This includes linearity measurements of PMTs in typical configurations and conditions for LII, detector calibration for multi-color LII using PMTs, a new software concept for LII signal processing and analysis (LII-Sim), and a new detection method to increase the dynamic range of the LII measurement technique.

The study described in chapter 4 uses light-emitting diodes (LED) as reference light source that can be operated in pulsed and continuous mode to investigate the linearity of PMTs. The motivation is to evaluate the performance of the detectors for similar light levels as they occur during LII measurements or detector calibration. The linearity is an important specification of the detector that can significantly bias the outcome of further analysis. Several strategies are presented to measure the linearity using LEDs and discuss the influence of light level on linearity for different PMT photocathode types and wavelengths. A theoretical study evaluates how non-linearity of a single detection channel in a multi-color LII detection setup would affect the pyrometrically determined temperature that acts as input parameter for the particle sizing.

Chapter 5 deals with the calibration methodology of detectors for multi-color time-resolved LII. The detector calibration is demonstrated using multiple light sources that can be used for the calibration of LII devices. The statistical description of the methodology includes a Bayesian approach to propagate the uncertainty from the calibration procedure into the spectroscopic model to quantify the uncertainty in determined temperatures. The performance of two-color pyrometry compared to multi-color analysis is analyzed for a reference LII measurement on a laminar diffusion flame. Measurement artifacts that could occur during LII measurements are summarized and strategies for identification and prevention are discussed.

In chapter 6, a new software concept for LII signal processing and analysis is presented. The software features modular materials systems that enable the user to adjust materials properties for their purpose. The modular signal-processing concept can be used to compose a processing chain from various built-in processing tools, and several published heat transfer models and materials databases can be applied for the analysis of LII measurement data. The software functionalities are demonstrated by two application cases of multi-color LII and results from the analysis are discussed. The open-source software was recently published on a public website to build the foundation for inter-laboratory comparisons.

Chapter 7 presents a new measurement strategy that enables increasing the dynamic range for LII measurements. The sequential detection technique takes advantage of the gating circuits of PMTs that can be used to suppress the high-intensity part of the LII signal. The subsequent part of the LII signal trace can then be measured with ND filters of lower optical density and increased PMT gain. Beside the basic technique, two advanced techniques using LII devices with three or more channels are presented that can be applied for single-shot measurements. The method can be used to resolve the late part of LII temperature traces and even detect local gas heating caused by the heat exchange of the particle with the surrounding gas.

4 PERFORMANCE OF PHOTOMULTIPLIERS IN THE CONTEXT OF LASER-INDUCED INCANDESCENCE

The content of this chapter was published in Applied Optics:

R. Mansmann, T. Dreier, C. Schulz, "Performance of photomultipliers in the context of laser-induced incandescence". Appl. Optics **56(28), pp. 7849-7860 (2017).**

© 2017 Optical Society of America. Reprinted with permission.

My own contribution included designing the experimental study, building the experimental setup, performing the experiments, analyzing and visualizing the data and writing the manuscript. Thomas Dreier and Christof Schulz helped shaping the research study, contributed to the interpretation of the results, and to the manuscript.

Abstract

Photomultiplier tubes (PMTs) are widely used as detectors for laser-induced incandescence (LII), a diagnostics method for gas-borne particles that requires signal detection over a large dynamic range with nanosecond time resolution around the signal peak. Especially when more than one PMT is used (i.e., for pyrometric temperature measurements) even small deviations from the linear detector response can lead to significant errors. Reasons for non-linearity observed in other PMT measurement techniques are summarized and strategies to identify non-linear PMT operation in LII are outlined. To quantify the influence of the non-linear behavior, experiments at similar light levels as those encountered in LII measurements are carried out, and errors propagated in two-color pyrometry-derived temperatures are determined. As light sources, a calibrated broadband light source and light-emitting diodes (LEDs), centered at the band-pass filter wavelengths of the LII detectors, were used. The LEDs were operated in continuous and pulsed (<300 ns) mode, respectively, to simulate DC background radiation (e.g., from sooting flames) and similar pulsed signal traces as in typical LII measurements. A measured linearity deviation of up to 10% could bias the temperature determination by several hundred Kelvin. Guidelines are given for the design and the operation of LII setups, which allow users to identify and prevent errors.

4.1 Introduction

Time-resolved laser-induced incandescence (TiRe-LII) is a well-established *in situ* measurement method for soot particle concentration and primary particle-sizes [3, 18], that is also in development for diagnostics of inorganic nanoparticles [13, 116, 124]. In this technique, gas-borne particles are heated by a pulsed laser to incandescent temperatures (i.e., higher than 2000 K). The magnitude of the incandescence scales with increasing particle volume fraction in the detection volume and the temporal variation of the particle temperature during cooling can be exploited to derive information about the particle size (as small particles cool more quickly than larger ones). A common technique for deriving particle temperatures is two-color pyrometry based on the ratio of signals measured in two wavelength ranges [9, 41]. For particle size determination, simulated temperature traces for a set of particle sizes are then matched to the measurements in an iterative procedure. The robustness of the measurement technique could be improved by using multiple detectors or spectrally resolved measurements as shown by Goulay *et al.* [11] to cope with signals that deviate from blackbody behavior or that are affected by interfering signals.

To interpret the signals from the detectors correctly, linearity must be ensured and a proper sensitivity calibration is necessary. Usually, a known light source is used to measure the detector response for different instrument settings (i.e., signal amplification, variable filter transmissions, etc.) [9, 41]. These calibration factors could then be used in signal analysis to refer the measured detector response to irradiance, which can then be used in two-color pyrometry to determine the particle temperature [9, 41]. Several recent studies showed that errors resulting from improper calibration and measurement noise have a major influence on volume fraction and particle sizing. Daun *et al.* [128] performed a study that examined measurement noise and how it can affect the inferred properties of soot. Crosland *et al.* [35] advanced the understanding of these uncertainties by performing Monte Carlo simulations propagating uncertainties from the calibration source to uncertainties in the volume fraction. More recently, various studies [13, 116, 124] have applied Bayesian analyses in an attempt to better incorporate uncertainties from measurement noise into TiRe-LII analyses. Hadwin *et al.* [69], in particular, considered the uncertainties introduced through calibration affecting the peak temperature and volume fraction. In this process, they showed that the inferred quantities could be highly susceptible to changes in measured incandescence, with variations in the temperature on the order of hundreds of Kelvin. As a result, to ensure the usefulness of LII for particle characterization, proper calibration is crucial.

Detectors to be used for TiRe-LII measurements need to resolve a very short signal peak (<50 ns) and at the same time, they need to provide a high dynamic range to capture the following signal decay over several orders of magnitude. Photomultiplier tubes (PMTs) are widely used as detectors and have excellent characteristics in terms of sensitivity and temporal response necessary for TiRe-LII measurements. However, they still need to be carefully operated to ensure linear signal response, as already noted by Case and Hofeldt [100]. Three general operating ranges can be distinguished by increasing light level [129, 130]: (i) the linear range, where the detector response is proportional to the incident light flux, is generally assumed by practitioners [11, 131]. (ii) The over-linearity range occurs at higher light levels and results in a detector response that is higher than expected for the incident light flux. (iii) Finally, at even higher light levels, the saturation range is where the detector response is lower than expected. These non-linearity effects of PMTs can mainly be grouped into photocathode resistivity, voltage divider, and space charge density effects [132, 133].

When the photocathode is hit by a high number of photons, local depletion leads to a radial voltage drop and a certain time is needed for the photocathode to recover [132, 134]. This effect mainly occurs with semitransparent photocathodes and not with reflection-mode photocathodes (i.e., side-on type) [132]. If the electron flux from the photocathode is already biased, correction is not possible and the bias will overlay with non-linearity produced in the electron multiplier part of the PMT.

The cause of non-linear behavior by the electron-multiplier part can be distinguished between pulse-mode applications where large current, which flows in the later dynode stages, increases the space charge density and causes current saturation, while for longer pulses and in continuous (DC) mode, the magnitude of the signal current leads to a change in the voltage divider circuit [133]. These changes in the circuit can lead to the so-called “over-linearity range” in which the output signal is larger than the ideal level and if the light level further increases, the signal would be saturated [129, 130].

Non-linearity effects are also observed and discussed in several other applications using PMTs at high luminous flux, that is, scintillation [135], phosphor thermometry [133], time-resolved luminescence spectroscopy (TRLS) [136], and light detection and ranging (LIDAR) [137, 138].

Manufacturers usually do not clearly indicate the linear operating ranges for PMTs. Instead, specifications contain information about maximum ratings for the anode current to prevent damage. This means that for each application, individual linearity test procedures need to be carefully carried out by the experimentalist.

Different measurement methods for detector linearity have been examined in the past. There are more general methods for investigating only the PMT and its components that quantify the linear response for a specific light source, for example, pulsed light sources where the light intensity is varied with neutral density (ND) filters [138, 139] or chopper wheels [140]. Other methods are more specific for the measurement application. Knappe *et al.* [133] developed strategies to take reference phosphorescence decays and identify the linear operating range of the PMT for the specific measurement case.

For LII, PMTs are usually calibrated with continuous light sources, while the measurements deliver pulsed signals with high dynamic ranges and short (nanosecond) high-flux peak signals. The initial signal peak contains key information and any non-linearity or deviation in temporal resolution influences the result of the data analysis when assuming ideal detector behavior. This study deals with how PMT linearity is affected by the type and intensity of the light source (pulsed/continuous) and what influence the observed non-linearity has on derived two-color temperature measurements in LII or the calibration. For our measurements, we used pulsed and continuous light-emitting diodes (LED) to illuminate the PMTs within a typical LII detection device and simulate irradiance that occurs during TiRe-LII experiments. Various ND filters are used to control the total irradiance on the PMTs. If the PMT response is linear, one would expect that the increase in the PMT output is proportional to the total irradiance. Deviation from that behavior can be identified as non-linearity.

4.2 Experiment

The relevance of detector linearity in LII measurements is examined using several light sources (including the LII process itself) and a combination of up to four detectors. Figure 4-1 gives a schematic overview of the experimental setup. The central element is an integrating sphere (diameter 5 cm) with four ports (Thorlabs IS200-4) that ensures reproducible radiance measurements for any combination of light source and detector. A calibrated broadband light source and an LED array (2×3 LEDs) are connected to two ports (see section below). For signal attenuation, a ND-filter wheel (FW1) (100, 79, 63, 50, 40, or 32% transmission) was placed between the LED array and the integrating sphere. An optical fiber can be used for coupling to an LII experiment where the light is collected via fiber-coupled collection optics. Homogenized light from the integrating sphere exits through a pinhole and is collimated before passing another ND-filter wheel (FW2) (100, 79, 50, or 10% transmission), two dichroic beam splitters (FF605-Di02 and FF740-Di01) or a 50:50 beam splitter (Thorlabs BSW10R). The light is then focused on four gated PMTs, three of the multi-alkali (MA) photocathode type (Hamamatsu H11526-20) and one of the super bi-alkali (SBA) photocathode type (Hamamatsu H11526-110), which are arranged for simultaneous measurement in various wavelength regions. PMT identifiers and the respective filters and dichroic beam splitters are indicated in Figure 4-1. For spectral separation, bandpass filters in the spectral ranges often used for two-color LII measurements [78] with center wavelengths of 500 ± 13 nm (PMT1 and PMT2, Semrock FF01-500/24), 684 ± 13 nm (PMT3, Semrock FF02-684/24) and 797 ± 9 nm (PMT4, Semrock FF01-800/12) were attached to the PMTs.

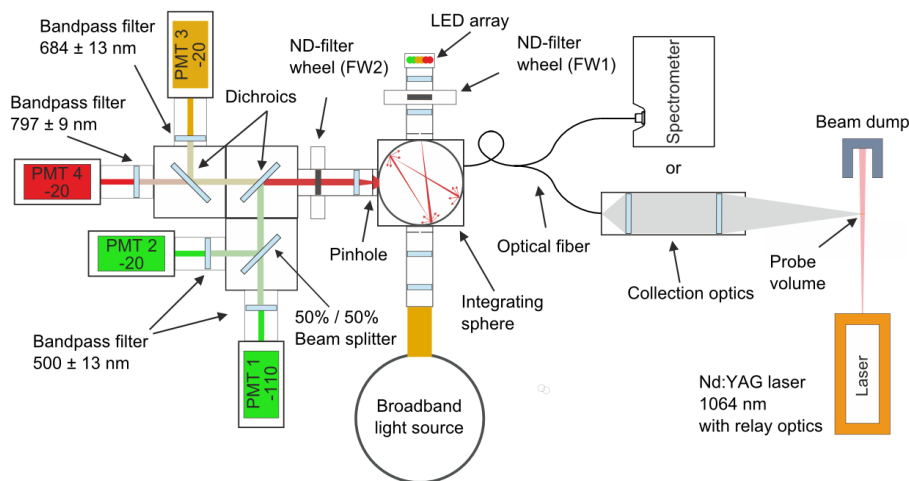


Figure 4-1 4-PMT setup with collecting integrating sphere, LED array and a broadband light source, and a fiber-coupled spectrometer.

The fiber port on the integrating sphere allows the connection of further instruments (e.g., a spectrometer). Here a fiber-coupled spectrometer (Ocean Optics USB-4000) is used to record spectral emission profiles from the attached light sources and to measure the spectral transmission profiles of the ND filters. The detection range is from 350 to 850 nm and it was wavelength calibrated with a pen-ray Hg(Ar) line source (LOT-QuantumDesign LSP035). Internal non-linearity correction of the spectrometer software was used and verified over the sensitivity range using a superposition technique (see section 4.3.1).

4.2.1 Light sources

The reference broadband light source for the measurements consists of three halogen lamps (operated in series) mounted on an integrating sphere (LOT K-150WH) with a laboratory DC power supply (Gossen Metrawatt SLP 120-80). The spectral irradiance of the system was calibrated in the 280–1500 nm range by an external calibration laboratory (opto.cal, Switzerland) just before the measurements. Figure 4-2 shows the calibration spectrum of the light source indicating the wavelength ranges of the respective bandpass filters in front of the PMTs.

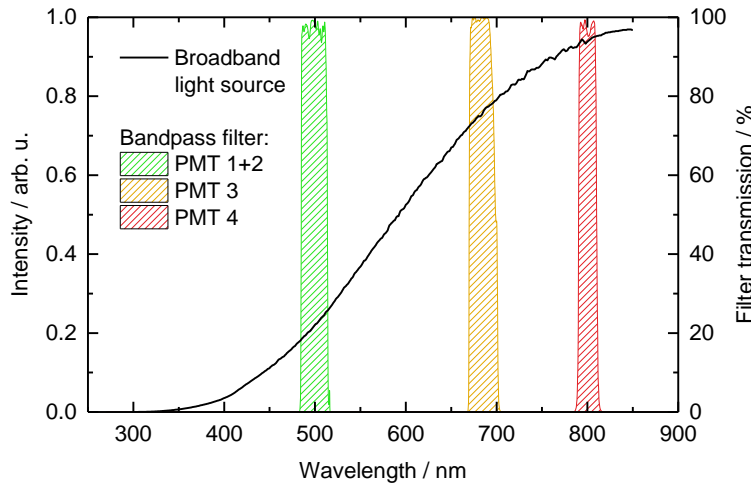


Figure 4-2 Calibration spectrum of the broadband light source. The spectral detection ranges of the bandpass filters in the detection device are also plotted based on the data provided by the manufacturer.

Six LEDs with three different peak emission wavelengths (500, 690, and 819 nm) were selected to match the bandpass filter ranges used in the 4-PMT setup for the LII experiments. The intensity of each LED was adjusted with series resistors to ensure approximately equal intensity levels between the channels. Since the variation of the supply voltage and the resistors could cause a spectral drift of the LED peak wavelength, the operating conditions were maintained as constant throughout all measurements. Long-term measurements of the LED output revealed variations below 0.5% over six hours that were also reproducible on different days. Figure 4-3 shows the spectral intensity of the three continuously operated LEDs measured with the fiber-coupled spectrometer.

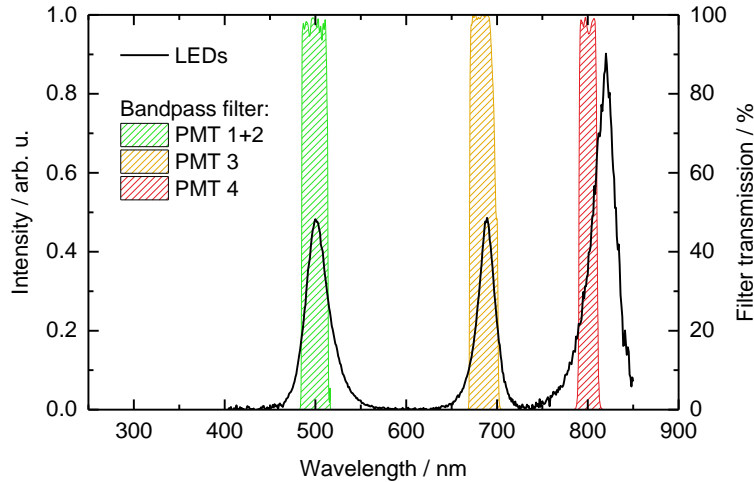


Figure 4-3 Spectra of the continuously operated LEDs.

For pulsed operation, a second set of LEDs (same types as used for cw operation above) can be operated independently or together with the continuously operated LEDs to generate different temporal signal shapes. An electronic circuit as suggested for particle image velocimetry (PIV) measurements by Willert *et al.* [141] was slightly modified and optimized to generate a stable temporal profile of the LED emission with variable pulse durations in the >100 ns range. The continuous and pulsed LEDs were connected to different power supplies to protect them from interference during high-speed switching. The intensities of the pulsed LEDs were kept 6–8 times higher than for the continuously operated LEDs. Figure 4-4 shows the signal waveform for the pulsed 500-nm LED with a full width at half maximum (FWHM) of 160 ns averaged over 200 pulses measured with PMT 1. The reproducibility of the pulsed operation was observed during several hours and fluctuations in the averaged signals have been less than 0.5%. All light sources are operated for at least 30 min before the experiment to ensure that thermal equilibrium is reached.

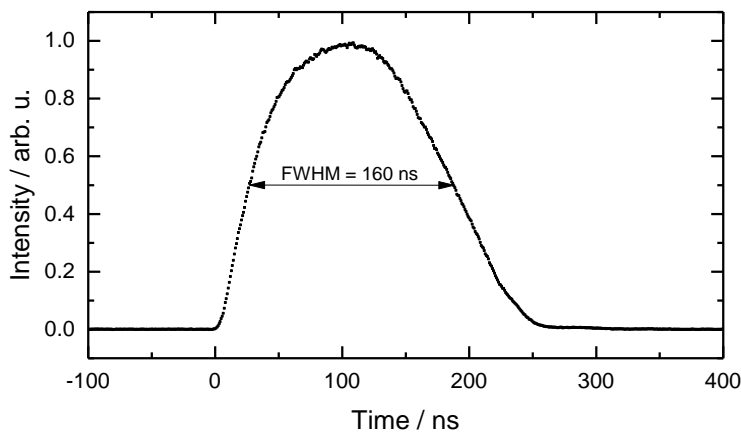


Figure 4-4 Temporal intensity profile (FWHM = 160 ns) of the 500-nm LED measured with PMT 1.

4.2.2 Detection

The rather unconventional usage of an integrating sphere within an LII setup helps to overcome the problem of alignment errors and thus variations in the intensity of the attached light sources. Furthermore, it allows comparing and combining different light sources and detection devices without introducing additional optical elements that could bias the spatial intensity distribution. When the device is used for LII measurements, the LEDs can be used as a permanent inline calibration source with perfect combination of both signal contributions on the detectors. The integrating sphere, however, attenuates the light by a factor of 250–300, compared to direct coupling of the light sources to the detectors, which prevents the application to LII in low-signal situations.

Table 4-1 shows the maximum ratings for the PMT modules used in our experiment. The experimental conditions were chosen, so that half of the maximum rating values indicated by the manufacturer are never exceeded.

Table 4-1 Maximum anode current ratings of Hamamatsu – H11526 PMT modules[‡]

Illumination time	Max. anode output current	Max. output voltage (50 Ω coupling)	Max. repetition frequency
DC	100 μA	5 mV	–
100 μs	1 mA	50 mV	100 Hz
1 μs	10 mA	500 mV	10 Hz
10 ns	100 mA	5 V	1 Hz

For the continuous wave experiments, the PMT gate was opened for 8 μs while never exceeding an anode current of 500 μA. During pulsed operation (FWHM 160 ns; 10 Hz), the anode peak current was kept below 3.2 mA.

[‡] Personal communication with Hamamatsu Photonics (13 July 2015): “The following data shows the rough indication of light amount (by output current) for which the PMT will not be damaged. (The following data is not guaranteed value).”

4.3 Methodology

Two different methods for assessing the linearity of the detector response were used in this study: (i) light superposition of different light sources, which is independent of ND-filter transmissions; and (ii) ND-filter variation, which is independent of the light source, but requires calibrated ND filters.

4.3.1 Linearity measurements using light superposition

The linearity of the fiber spectrometer is validated using a light superposition technique with stable continuous light sources. The spectral transmissions of the ND filters were measured using the validated spectrometer. For measuring the PMT linearity during a pulsed signal in the presence of background radiation, this method can be applied without knowing the ND-filter transmissions.

4.3.1.1 Spectrometer validation

When two light sources are superposed, the expected intensity can be calculated by summing the individual intensities. Linearity is given when the following equation is fulfilled:

$$I_B + I_{LED} = I_{B+LED}, \quad (4-1)$$

where I_B is the intensity from the broadband light source, I_{LED} is the intensity from the LEDs, and I_{B+LED} is the intensity from both light sources at the same time. Figure 4-5 shows the intensities of the continuously operated LEDs (blue line), the broadband light source (orange line), and both (green line) measured with the spectrometer. The ratio between the calculated (black line) and the measured combined intensities (green line) represents the linearity error of the spectrometer (bottom), which could be thus determined to be below 1% within the wavelength ranges of the PMT bandpass filters (see Figure 4-2 and 4-3).

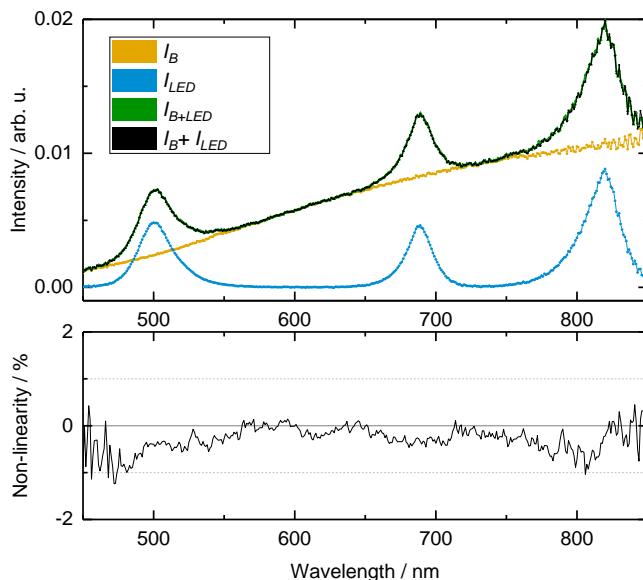


Figure 4-5 (Top) Superposition of the broadband light source (I_B) and the continuous LEDs (I_{LED}) measured with the spectrometer. (Bottom) Deviation between the calculated and measured intensities, indicating non-linear detector behavior.

4.3.1.2 Linearity of pulsed signals in presence of background radiation

In LII measurements performed on particles in a cold gas environment (e.g., aerosols or exhaust gas), the generated signal waveform can be assumed as pulsed-shaped and background free. In contrast, LII signals obtained in hot gases (e.g., in flames) are usually accompanied with continuous background radiation arising from thermal radiation of the particles at the surrounding gas temperature independent of the laser pulse. The background light level during LII measurements is mainly influenced by the temperature and the size of the probe-volume, and its relative contribution to the laser-induced signal varies strongly from experiment to experiment. The combination of continuous and pulsed LED signals (Figure 4-6) was used to simulate a pulsed signal in the presence of continuous background radiation.

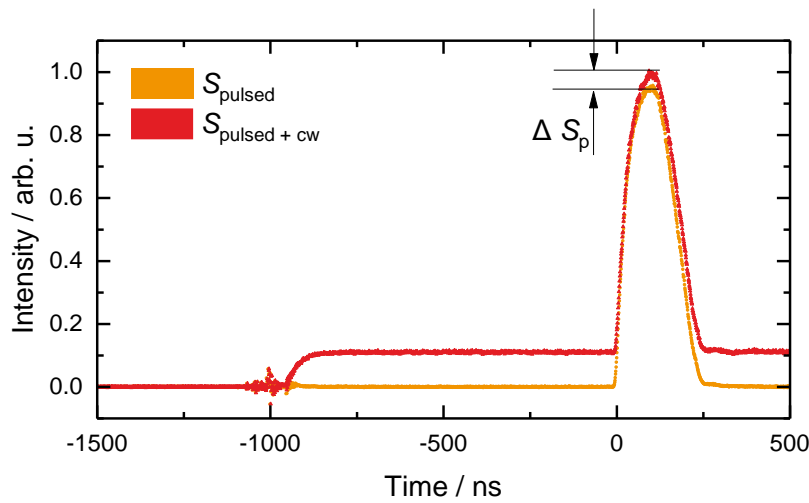


Figure 4-6 Superposition of pulsed and continuous LEDs for PMT 1, both filter wheels at 50% transmission.

For this experiment, the signal of the pulsed LED alone (S_{pulsed}) and the combination of both pulsed and continuous LEDs ($S_{\text{pulsed+cw}}$) was measured for various ND-filter wheel combinations (τ_i). After subtracting the continuous light level signal (S_{cw}), the difference in the signal amplitude of both LED pulses (ΔS_p) provides information about how the background radiation additionally affects the linearity of the pulse detection:

$$\Delta S_p = \left(\frac{S_{\text{pulsed+cw}}(\tau_i) - S_{\text{cw}}(\tau_i)}{S_{\text{pulsed}}(\tau_i)} - 1 \right) \cdot 100\%. \quad (4-2)$$

This method is independent of accurate ND-filter transmission values, but two independent stable light sources are needed. Due to the design of our experiment, we could not vary the intensity ratio between the continuous and pulsed LED while keeping the LED supply voltage constant (because changes in supply voltage would bias the spectral and temporal intensity profile of the LED). Instead, we kept the intensity ratio constant and operated the LEDs at the same light levels as for the linearity measurements using the ND-filter variation.

4.3.2 Linearity measurements using ND filters

The strategy in this experiment is to determine how the temporal shape of light sources (i.e., continuous or pulsed) and the light intensity would affect the PMTs in a typical LII setup. Deviation from linearity can then be used to estimate the error of two-color pyrometry for selected signal ratios.

4.3.2.1 ND-filter calibration

Knowing the ND-filter transmission is very important for these linearity measurements, because errors in the transmission values would lead to under- or overestimation of the linearity. To ensure accurate values, an inline calibration method for filter transmission was chosen, where the PMTs are removed from the setup and a spectrometer was placed at the respective PMT position. The broadband light source was then used to provide a stable reference spectrum. While the spectrometer was mounted at the specific PMT position, the filter wheel (FW2) was rotated, and the intensity for every filter was measured. Referring to the measurements without an ND filter (100% transmission) then provides spectrally resolved transmission values for each ND filter. The procedure was then repeated for the ND-filter wheel (FW1) in front of the LED array with the spectrometer coupled to the integrating sphere as shown in Figure 1. The variation of the spectral filter transmission over the bandpass wavelength range was less than 1%, and therefore, an averaged value over the bandpass filter range could be used in the calculations in this study. In this context, it should be noted that variable ND filters with very low transmissions (i.e., <10%) could introduce a significant error in the LII analysis and should be avoided or be included in the sensitivity calibration by placing them permanently in the LII setup.

In the following experiment, 24 different light levels could be obtained by combining the two ND-filter wheel positions (FW1 and FW2). Figure 4-7 visualizes the resulting 6×4 matrix of overall transmission values for the 500-nm bandpass filter for any ND-filter wheel combination in a linearly interpolated contour plot. The following contour plots were generated from matrices using the built-in functionality of OriginPro2017.

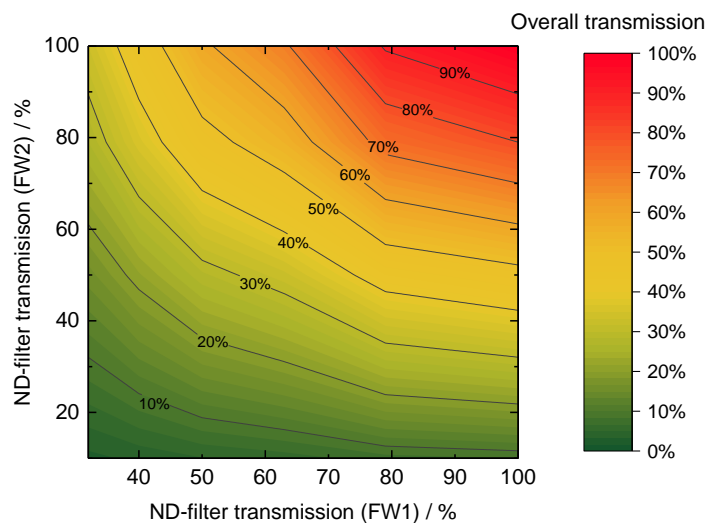


Figure 4-7 Combined transmission of both ND-filter wheels (500-nm bandpass filter).

4.3.2.2 Linearity measurements using the calibrated ND filters

The PMT response for different light levels was measured using continuous and pulsed LEDs. During the experiments, the PMT gain voltage is kept constant at similar values as for LII experiments (400 mV for all PMTs). The inline calibrated ND filters are varied to expose the PMTs to variable light levels. The PMT response was measured at 10 Hz, and 200 signals were collected and averaged for each ND-filter wheel combination. Figure 4-8 indicates the temporal sections of the collected PMT signals, which are used for the analysis. Signal processing was limited to baseline correction (A) before opening the PMT gate and inverting the (negative) signal trace. Deviation from linearity is expressed using the term

$$\left(\frac{S(\tau_i)}{S(\tau_{\text{ref}})} \frac{\tau_{\text{ref}}}{\tau_i} - 1 \right) \cdot 100\%, \quad (4-3)$$

where the temporally averaged signal $S(\tau_i)$ from the continuous (B) and pulsed (C) LEDs is corrected for the ND-filter transmission using the transmission values τ_i from the previous paragraph and then normalized to the lowest light level $S(\tau_{\text{ref}})$. The widths of the temporal sections were arbitrarily chosen as 200 ns (A), 350 ns (B), and 20 ns (C).

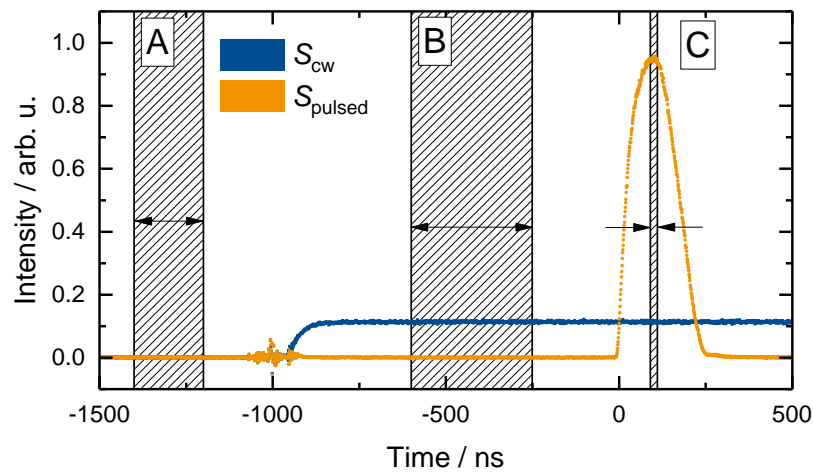


Figure 4-8 Three sections of the PMT response are used in the analysis for the continuous (blue) and pulsed (orange) operation: baseline correction (A) before PMT gate is opened (-1000 ns), and the signal for the continuous (B) and pulsed (C) light sources.

4.4 Results

4.4.1 Linearity measurements for continuous and pulsed light

In this experiment, both ND-filter wheels are varied, while all other parameters (i.e., LED light level and gain voltage) were kept constant. These variations result in 24 ND-filter wheel combinations with different light levels. Figure 4-9 visualizes the measured anode current $S(\tau_i)$ and the corresponding deviation from linearity (Equation (4-3)) for PMT 1 for continuous operation in a linearly interpolated contour plot. Plots for all PMTs can be found in Appendix A in Figure A-1 for continuous operation and in Figure A-2 for pulsed operation.

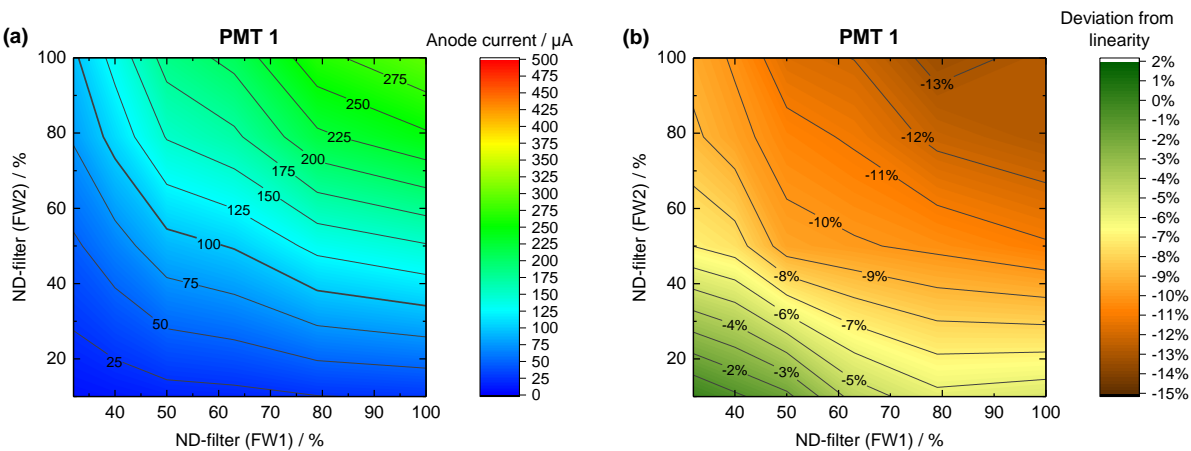


Figure 4-9 ND-filter variation for the continuously operated LEDs; measured anode current (a) and deviation from linearity (b) for PMT 1. For other PMTs and for pulsed operation, see Appendix A.

One dimension of the plots shown in Figure 4-9 can be reduced by calculating the relative light intensity for any ND-filter combination (see Figure 4-7). For every measurement, the deviation from linearity can then be shown as a function of relative light intensity. Results for all PMTs for continuous and pulsed operation are presented in Figure 4-10 and the corresponding anode currents and voltages measured on a $50\text{-}\Omega$ -terminated oscilloscope in Figure 4-11. The repeatability error of the linearity measurements could be determined as less than 2% over several days and could explain some of the fluctuations in the measurements.

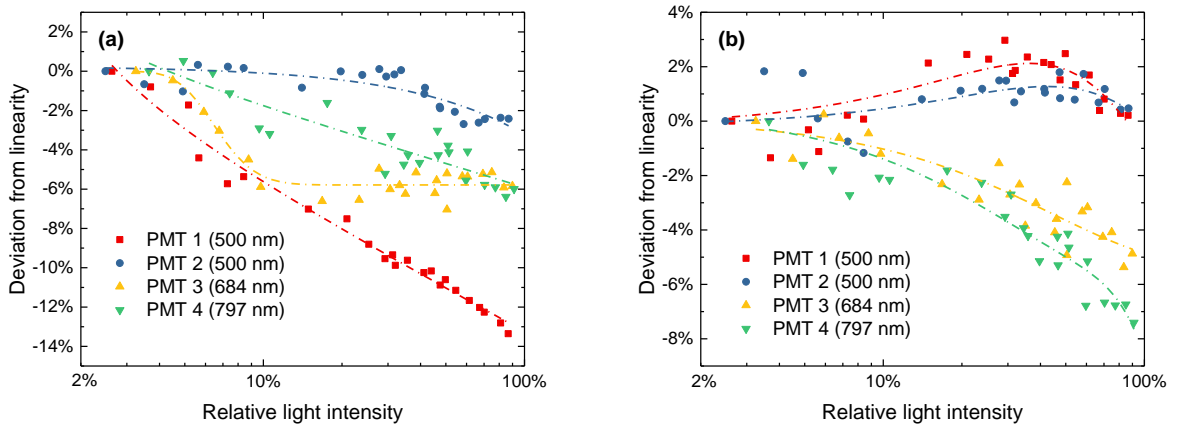


Figure 4-10 Deviation from linearity as a function of light level for continuous (a) and pulsed (b) LED measurements. Lines are added to guide the eye.

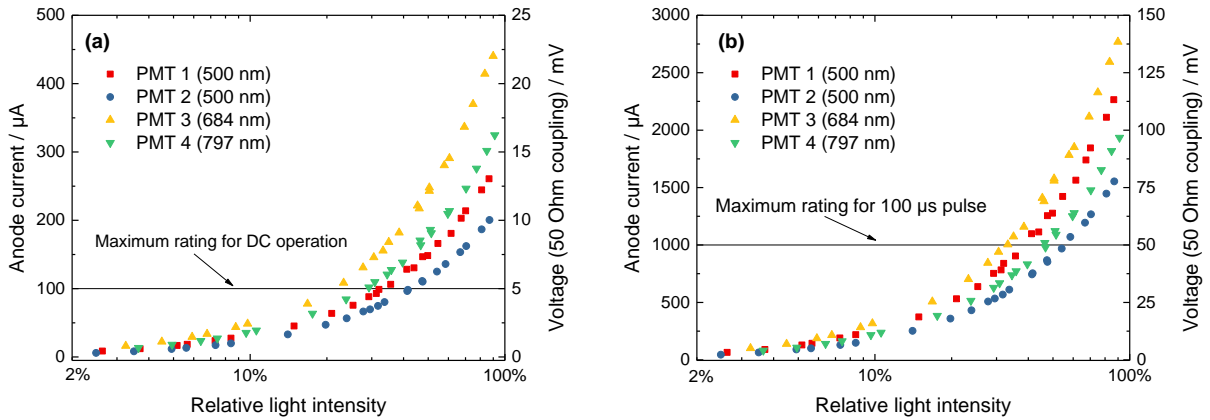


Figure 4-11 Anode current and corresponding voltage ($50\ \Omega$ -coupling) for continuous (a) and pulsed (b) LED measurements; maximum ratings from the PMT specification sheet are indicated by a horizontal line.

The following conclusions on detector linearity can be drawn from these figures:

- PMT 1 (SBA type) shows under-linear behavior for DC measurements (up to 14%), while for pulsed measurements, a slight over-linearity could be observed.
- For DC measurements, PMT 1 (SBA type) deviates much stronger from linearity than PMT 2 (MA type) equipped with the same bandpass filter (500 nm) and similar light levels.
- PMT 2 operated at moderate light levels is least affected during DC and pulsed operation ($\pm 2\%$).
- PMT 3 (high anode current) and PMT 4 (moderate anode current) (MA type) show similar behavior during continuous and pulsed experiments. The deviation increases with the light level and was below 8% for all light levels.
- All PMTs show non-linear behavior much earlier than the maximum anode current indicated by the manufacturer (i.e., at 1 mA for 100-μs pulse duration and 10 mA for 1-μs pulse duration). For

the DC measurements (gated operation with $8\ \mu\text{s}$ gate width), non-linearity in the anode current starts at a factor 10 lower and at a factor 20 lower for the pulsed operation.

Reducing the gate opening time showed no effect on linearity. This could be explained by non-linearity induced mainly by the photocathode, because the PMT gate interrupts only the electron multiplier circuit, not the incident light exposure of the photocathode.

This shows that experimentalists need to be very careful when using a DC light source for gain or sensitivity calibration. Even when the (pulsed) LII measurements are taken under linear conditions, biased calibration factors would systematically affect the determination of temperatures from signal ratios.

4.4.2 Linearity of pulsed operation in presence of background radiation

The same experiment as in the previous section was repeated with the PMTs exposed to a combination of continuous and pulsed LEDs (see Figure 4-6). Every combination of the ND-filter wheels is now compared individually and not normalized on the lowest intensity. Figure 4-12 shows the ratio of the measured signal from pulsed LEDs without and with continuous background for the methodology described in section 4.3.1. Note that this presentation focuses on the (additional) influence of continuous background. Additional non-linearity that might be connected to the detection of the pulsed signal at high light intensities (as measured in section 4.4.1) occurs on top.

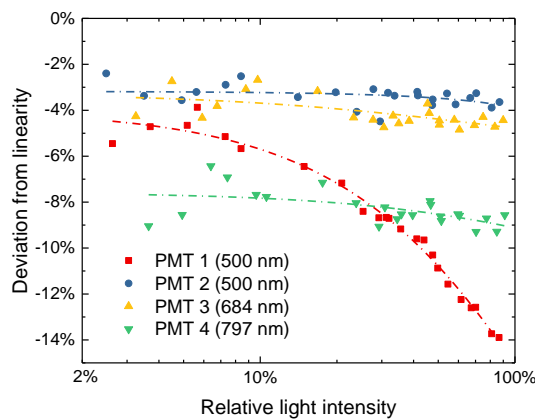


Figure 4-12 Deviation from linearity of the detection of pulsed signal induced by continuous background for various signal levels. Lines are added to guide the eye.

For PMTs 2, 3, and 4 (MA type), a nearly constant deviation for all light levels of the continuous background is observed, while PMT 1 (SBA type) already starts to leave the linear range when exceeding the level of 10% relative light intensity. For LII measurements of soot at high laser fluences, the background radiation light level is usually several orders of magnitude lower than the LII signal, while for measurements with low laser fluences, with materials with low evaporation temperature, and measurements in a hot environment with strong continuous thermal emission, the ratio between the background and signal increases, and the described effects can occur. A strategy to identify the influence of background radiation in a specific experiment would be the repetition of LII measurements with a series of different ND filters. With increasing ND-filter transmission, the signal-to-noise ratio increases, but the deviation from linearity also becomes more likely. The comparison of measurements using multiple ND filters covering a range of

optical densities allows the user to identify the maximum allowable signal intensity that provides the highest signal-to-noise ratio while ensuring linearity.

4.4.3 Quantifying the influence of non-linearity on two-color pyrometric temperature measurements

For the determination of pyrometric temperatures, usually the signals at two or more wavelengths are related to Planck's law. If one of the signals is biased by wrong calibration factors or non-linear detection, this method results in wrong temperatures.

As an example, Figure 4-13 shows the temperatures resulting from the least squares fit of Planck's law for any combination of two PMTs for unbiased data at 3200 K (black) and for a -10% bias of the 500-nm PMT (a) or the 684-nm PMT (b).

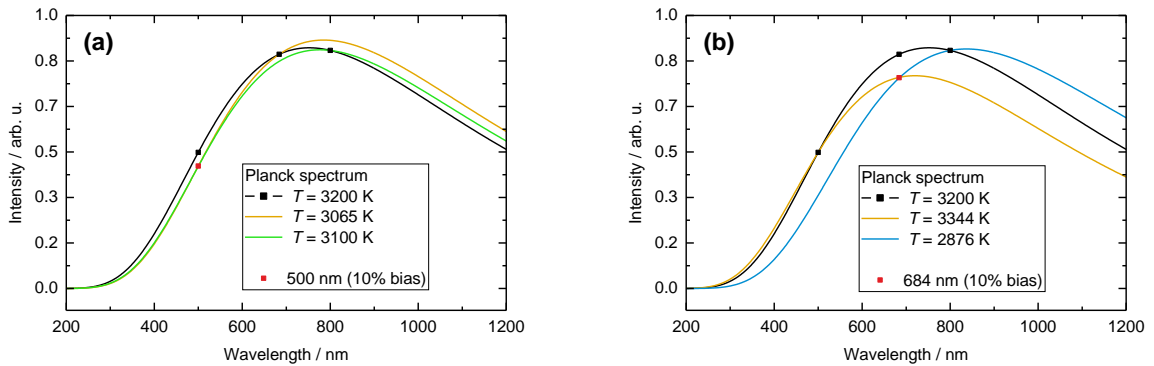


Figure 4-13 Least-squares Planck fit for unbiased intensities (black) and for -10% bias of 500-nm channel (a) and 684-nm channel (b).

At high temperatures around 3200 K or higher, as they occur in LII, the peak of Planck's law could move between the two detection wavelengths, as can be seen in Figure 4-13. In this case, the error introduced by non-linearity of one of the adjacent channels is maximal. Therefore, non-linearity effects during the LII measurements are more likely to occur in the signal peak region and become less so when after the laser pulse, the particle temperature approaches the gas temperature. It can also be seen that the deviation becomes stronger for detection wavelengths that are closer together. Liu *et al.* [78] already showed that the proper selection of detection wavelengths could achieve better accuracy for measurements of the particle temperature and the volume fraction.

In order to quantify the influence of the PMT non-linearity on two-color pyrometry, temperatures were calculated using unbiased intensity ratios. The intensities are then biased by a range of expected non-linearity deviations of (-15% to +5%) to visualize the influence on the initially calculated temperature. For further systematic analysis, the two-color equation according to De Iuliis *et al.* [41] was used:

$$T_p = \frac{h c_0}{k_B} \left(\frac{1}{\lambda_2} - \frac{1}{\lambda_1} \right) \left[\ln \left(\frac{I_\lambda(\lambda_1, T_p)}{I_\lambda(\lambda_2, T_p)} \frac{E(\mathbf{m}_{\lambda_2})}{E(\mathbf{m}_{\lambda_1})} \left(\frac{\lambda_1}{\lambda_2} \right)^6 \right) \right]^{-1}, \quad (4-4)$$

with the particle temperature T_p , the Planck constant h , the speed of light in vacuum c_0 , the Boltzmann constant k_B , the detection wavelengths λ (i.e., the center wavelengths of the detector bandpass filters), and the absolute spectral intensity I_λ .

Figure 4-14 shows the absolute temperature error caused when the absolute spectral intensities $I_\lambda(\lambda_i, T_p)$ are biased by -15% to 5% for a typical LII peak temperature of $T_p = 3200$ K for the center wavelengths λ_i of our detectors compared to a temperature calculated from unbiased intensities.

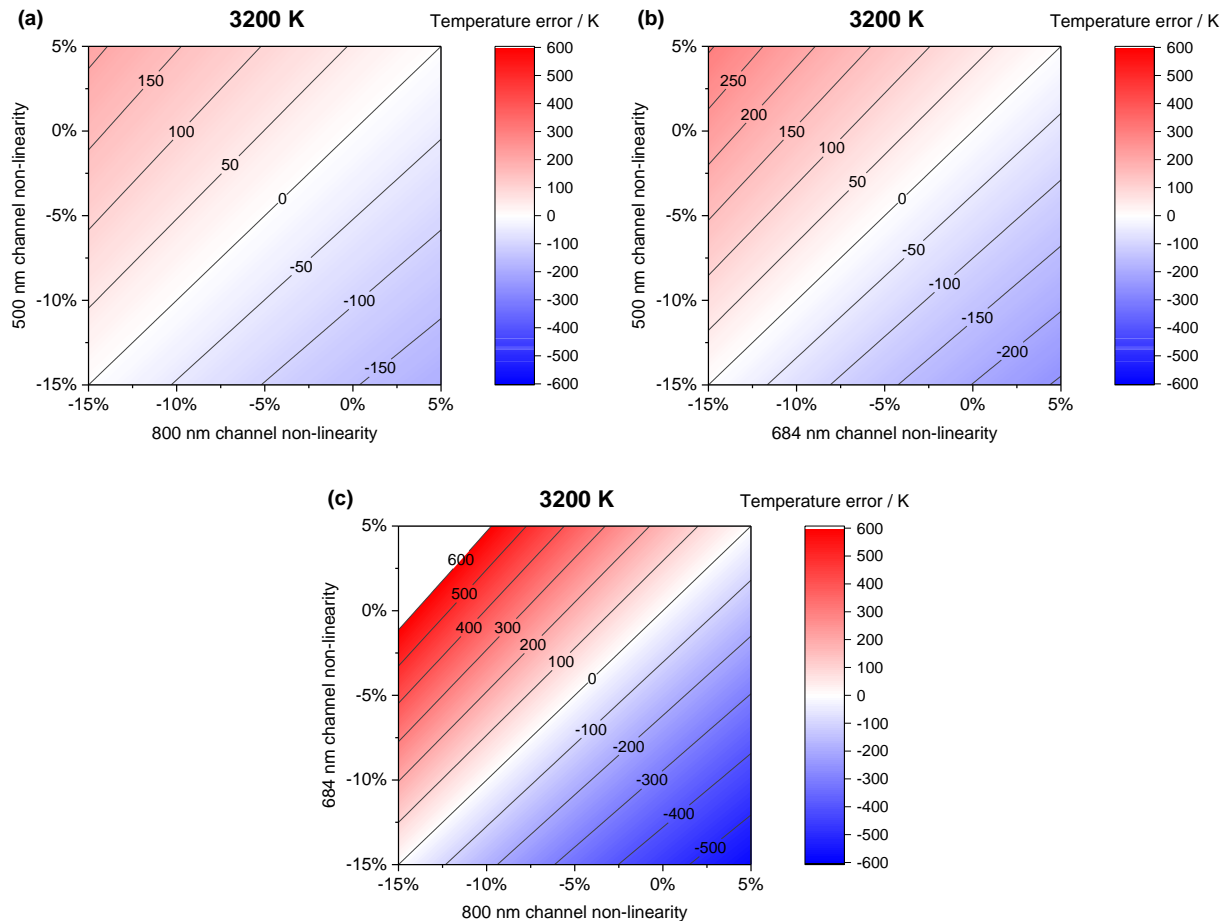


Figure 4-14 Calculated temperature errors for three different combinations of bandpass-filtered signals (2C-ratios) resulting from non-linear PMT behavior between -15% and 5% .

The systematic analysis in Figure 4-14 shows that deviations become stronger if the detection wavelengths are closer together and closer to the Planck's law peak region (c) and less if the gap between the detection wavelengths increases (a and b). The influence of non-linearity during the LII signal decay therefore decreases with decreasing temperature when the peak moves according to Wien's displacement law.

This study comes to the same conclusion as Liu *et al.* [78]: for two-color detection, a larger gap between the detection wavelengths reduces the error in the derived temperature. It needs to be noted that the photocathode material of a PMT usually determines which detection wavelengths can be chosen. While SBA photocathode PMTs are sensitive between 250 and 550 nm, MA photocathode PMTs could be used as detectors between 450 and 800 nm. This causes a dilemma, because the SBA type, which is most affected by linearity errors, would be needed to increase the gap between detection wavelengths to wavelengths below 500 nm.

4.5 Conclusions

This study showed that PMTs can be affected by non-linear behavior of more than 10% during calibration and measurements for typical LII conditions at light levels that lead to detector currents well below the limiting values reported in the manufacturers' specifications. The resulting error propagates from the calibration to the temperature derived from two-color pyrometry measurements. It is influenced by the experimental setup, the calibration light source, the presence of background light, and the light level during the LII measurement.

The photocathode material of the PMT is a critical factor for these kinds of applications. For the same light level, we observed that the super bi-alkali PMT was much more affected by non-linearity than the multi-alkali PMT. The design of the LII apparatus could be optimized by using PMTs with photocathode material that is less sensitive to non-linearity (i.e., multi-alkali) and choosing a wavelength combination with a larger gap between the center wavelengths. This ensures that even if non-linearity occurs, the error in two-color derived temperatures can be minimized already by the design of the apparatus.

For sensitivity calibration of PMTs, normally continuous light sources are used. We showed that PMT signals could already be biased at anode currents much lower than recommended by the manufacturer. In the case of gated PMTs, higher anode currents could be used during the measurements, but still this would not protect the photocathode from depletion and thus cause deviations from linearity. When a calibration factor is biased, multiple experiments can be influenced, even when the actual measurements are performed in the linear operating range. It is recommended to verify the sensitivity calibration by using multiple ND filters covering a range of optical densities.

Two main reasons for non-linear PMT behavior during LII measurements can be identified: too strong LII signal-peak intensities and too high continuous background light levels. A careful design of the LII apparatus should ensure that the general light level is kept low. Signal detection over wide solid angles might therefore be counterproductive. In these cases, a remedy is introducing of ND filters or using a collecting integrating sphere within the setup to artificially reduce the sensitivity of the system.

A comparison of different two-color ratios, from which pyrometric temperatures can be deduced using multispectral LII devices with three or more wavelengths, will help to identify significant deviation from linearity of a single channel. The integration of redundant PMTs of different photocathodes with high and low sensitivity for non-linear behavior within the setup allows the user to recognize early when entering the non-linear regime.

It needs to be noted that the influence of the gain variation was not included in this study due to reasons of complexity and could lead to further linearity problems.

5 DETECTOR CALIBRATION AND MEASUREMENT ISSUES IN MULTI-COLOR TIME-RESOLVED LASER-INDUCED INCANDESCENCE

The content of this chapter was submitted for publication in Applied Physics B:

R. Mansmann, T. A. Sipkens, J. Menser, K. J. Daun, T. Dreier, C. Schulz, “Detector calibration and measurement issues in multi-color time-resolved laser-induced incandescence”. *Appl. Phys. B*, submitted (2018)

© Springer-Verlag GmbH Germany, part of Springer Nature 2018. Reprinted with permission.

My own contribution included designing the experimental study, building the experimental setup, performing the experiments, processing, analyzing and visualizing the data and writing the manuscript. T. A. Sipkens, J. Menser, and K. J. Daun contributed to the discussion of the concepts for the calibration procedures and statistics. T. A. Sipkens, K. J. Daun, T. Dreier and C. Schulz contributed to the discussion of the results, and to the manuscript.

Abstract

Time-resolved laser-induced incandescence (TiRe-LII) is used to infer the size distribution of gas-borne nanoparticles from time-resolved pyrometric measurements of the particle temperature after pulsed laser heating. This study describes a calibration procedure for LII systems, and quantifies the uncertainty in pyrometric temperatures introduced by this procedure. Calibration steps include corrections for: (i) signal baseline, (ii) variable transmission through optical components, and (iii) detector characteristics (i.e., gain and spectral sensitivity). Candidate light sources are assessed for their suitability as a calibration reference and the uncertainty in calculated calibration factors is determined. The error analysis is demonstrated using LII measurements made on a sooting laminar diffusion flame. We present results for temperature traces of laser-heated particles determined using two- and multi-color detection techniques and discuss the temperature differences for various combinations of spectral detection channels. We also summarize measurement artifacts that could bias the LII signal processing and present strategies for error identification and prevention.

5.1 Introduction

Laser-induced incandescence (LII) is a diagnostic for *in situ* nanoparticle size and volume fraction measurements of both soot [2, 3, 142] and inorganic aerosols [13, 40, 82, 84, 116, 118, 121, 124, 143]. The measurement principle is based on pulsed laser-heating of gas-borne nanoparticles within a sample volume. At incandescent temperatures (typically higher than 2,000 K) the spectral incandescence emitted by the nanoparticles at two or more discrete wavelength bands is used to define an instantaneous effective temperature of the ensemble through pyrometry. The particle volume fraction can be inferred from the signal intensity, while the temporal variation of the spectral incandescence (and thus particle temperature) yields the nanoparticle size because small nanoparticles cool more quickly than large ones. Measurements of the decaying incandescence is commonly called time-resolved LII (TiRe-LII) and focuses on the determination of nanoparticle size [9, 40, 144] along with other parameters associated with the heat transfer model. The analysis of TiRe-LII signals is typically split into two major parts: (i) modeling of the spectral characteristics, which describes the nanoparticle–light interaction both for absorption and emission, and relates the observed spectral incandescence to the effective temperature, and (ii) heat transfer modeling, which uses the effective temperature decay to infer the mean nanoparticle diameter.

The incandescence signal is usually measured with fast photomultiplier tubes (PMT) or gated cameras equipped with bandpass filters, gated spectrometers, or streak cameras. The measurement strategy can be classified based on the number of detected discrete wavelength bands, or, in the case of spectrometers and streak cameras, the detection of a nearly continuous emission spectrum. For single-color LII, one PMT equipped with a bandpass filter is used to measure the incandescence decay rate of the laser-heated nanoparticles, which is then compared with simulated incandescence traces generated using a heat transfer model to recover the nanoparticle size. While this approach can be used to make comparative measurements (e.g., how soot primary particle sizes vary within a flame) it is insufficient for absolute size measurements since the peak nanoparticle temperature needed for this calculation must be inferred from the absorption cross-section and the local gas temperature, which are rarely known with a high degree of certainty.

More robust results can be obtained by incorporating additional spectral detection bands, which provides direct access to the particle temperature. For this, at least two detectors equipped with different bandpass filters [9, 40, 41, 101] are required, while more recent work has used three or more wavelengths [11, 145] or a nearly continuous spectra obtained with a spectrometer coupled to a streak camera [12, 13].

All these approaches require the detectors to be calibrated with respect to their relative spectral sensitivity, and to also account for issues of linearity, measurement artifacts, and suppression of interference from other light sources (particularly within flames). Poor calibration practices and poor signal quality can lead to large errors in quantities inferred from LII. This is highlighted by the fact that discrepancies in the temperatures inferred using various two-color LII channel combinations have been reported and that the analysis of temperature traces using different previously published LII models yielded very different particle sizes [145]. Moreover, these errors can also easily be confused as “physical” processes caused by changing thermophysical properties or spectroscopic/transport phenomena, which in turn lead to the development of faulty measurement models.

Discussions during the biennial LII workshop series [146-148] revealed that strategies for detector calibration/operation and signal processing vary widely and, despite their fundamental importance, these topics are rarely addressed in a rigorous manner. This motivates the development of recommended practices

for detector selection, detector calibration, and LII signal processing, as well as a procedure for the early processing steps for LII signal analysis to increase the quality and reproducibility of calibrated LII data across research laboratories.

This work proceeds by defining the requirements for the detection setup and a summary of measurement artifacts that may affect LII signals. This is followed by an overview of photomultiplier characteristics and a mathematical description of the calibration procedures for PMT sensitivity, PMT gain, and variable optical components within an LII setup. The LII signal-processing steps and the spectroscopic model used to determine the temperature are described along with their implementation within the Bayesian framework, which provides an estimate of the uncertainty introduced by the calibration procedures and the measurement.

The subsequent section gives an overview of the experimental apparatus, which consists of four calibration light sources, the LII detection setup and a laminar diffusion flame that is used as a target. The calibration procedures are shown for this setup, and the suitability of various light sources for calibration is evaluated. For the uncertainty analysis, reference measurements are carried out on an ethene-fueled laminar diffusion flame and the inferred temperatures for two-color and multi-color pyrometry are discussed within the context of the Bayesian framework. Finally, important measurement artifacts that can cause a bias during LII signal acquisition are presented along with strategies for error identification and prevention.

5.2 Theory

5.2.1 Detector requirements and measurement issues in LII

The TiRe-LII detection system should be designed, and components should be selected, according to several criteria: (i) absolute and spectral sensitivity; (ii) linearity, gain and dynamic range; (iii) rise- and fall-time characteristics; (iv) reproducibility/drift; and (v) chromatic aberrations of the focusing optics and apertures. Problems with any of these aspects will cause measurement errors that bias the signals and their temporal variation, and consequently the pyrometrically inferred temperature, and thus can strongly influence the derived quantities (e.g., nanoparticle size).

Most detectors exploit the photoelectric effect, through which a material irradiated with photons emits photoelectrons. The number of incident photons reaching the detector depends on the optical collection efficiency, the particle volume fraction within the probe volume, the spectral absorption cross-section of the particulate material, the laser fluence, and the nanoparticle temperature. The detector sensitivity must be high enough to generate a sufficient number of electrons such that amplification within subsequent multiplier stages (i.e., dynode stages, micro channel plate, etc.) results in an adequate signal-to-noise ratio. The signal-to-noise ratio can also be enhanced by improving the collection efficiency, e.g., by using optical components with high optical transmittance and ensuring precise alignment, which is especially important for applications involving weak LII signals (i.e., low fluence, low particle concentrations). On the other hand, in applications with strong LII signals, it is sometimes necessary to reduce the collection efficiency, e.g., via neutral density filters, to avoid detector overload and saturation effects. In the case that the temperature is determined by multi-color pyrometry, the spectral transmittance of the bandpass filters and spectral sensitivity of the photosensitive parts of the detector (e.g., photocathode, photodiode) must also be taken into account.

Linearity of the detection system ensures that the electronic signal generated by the detector is proportional to the irradiance incident on the detector. While most LII studies presume linearity, nonlinear PMT behavior has been reported in some experiments [100, 149] as well as in other applications like laser-induced luminescence [136] and phosphor thermometry [133]. Nonlinear detector behavior biases the signal, consequently introducing large errors into the ratio-based pyrometric temperature. This is particularly challenging for LII experiments since the incandescence signal strength varies by several orders-of-magnitude over a single measurement trace (e.g., five orders of magnitude between 1500 and 4000 K in the visible range). Therefore, the detector must have a large dynamic range to maximize the range of measurable temperatures, which is needed to obtain robust estimates of the aerosol attributes. The dynamic range is limited by the combination of a large temporal signal variation with the finite linear vertical resolution of the oscilloscope, the latter being constrained by the digitization depth of the analog-to-digital converter (usually between 8 and 12 bit). The detector gain can be reduced to prevent damage/saturation or increased to improve the signal-to-noise ratio. The detectors can also be gated by temporally-disabling the gain circuit to avoid saturation by background flame radiation or damage caused by strong excitation light as in the case of double pulse LII [82, 150]. Gated operation can also be used to block a part of the initial LII signal and increase the dynamic range by a sequential detection of parts of the signal trace with adapted gain settings and ND filters [151].

The rise- and fall-time characteristics of the detectors need to be sufficiently fast (< 2 ns rise-time) to resolve the rapidly-varying LII signal. Slow detector response, either caused by a slow detection technology or built-in low-bandwidth electronic components (e.g., low-bandwidth amplifiers), can falsely suggest larger particle sizes in cases with fast signal decay. Bougie et al. [27] introduced a deconvolution algorithm to compensate for slow PMT signal response in fast-decaying LII applications. Charwath et al. [7] investigated the influence of the temporal response of the detector using a streak camera and concluded that parameters inferred through single-color TiRe-LII can be significantly biased by limited temporal response, while those found using two-color TiRe-LII are more robust to this phenomenon. Luo et al. [152] investigated the overshooting behavior of PMTs that can occur for steep signal gradients, as can happen in LII measurements carried out at elevated pressure or with small particles (< 10 nm).

In order to obtain an unbiased pyrometric temperature estimate, multiple detectors (working in different wavelength ranges) must operate reproducibly and must be drift-free. Additionally, the detection system must be calibrated for relative spectral sensitivity. Absolute sensitivity calibration is not required for time-resolved LII but is essential for determining the soot volume fraction using the auto-compensating LII technique [9].

Other detection system issues include chromatic errors through focusing optics and apertures [87], which can be particularly important when using low *f*-number optics [153]. Will et al. [154] noted that a short-pass filter could still show significant transmission in the near IR, which can cause unexpected interference from background radiation.

In summary, it is important to correctly identify common measurement artifacts to distinguish signal bias from effects associated with incandescence from the laser-heated nanoparticles.

5.2.2 Photomultiplier tubes

Most LII detection systems are based on photomultiplier tubes (PMTs). Figure 5-1 shows the schematics of a PMT, consisting of three major parts: photocathode, electron multiplier, and anode. When photons are absorbed by the photosensitive surface of the photocathode, photoelectrons are released and accelerated towards the focusing electrode. Multiple dynode stages generate secondary electrons that amplify the original signal. The electron cloud arriving at the anode induces a current signal that can be measured as a voltage using the internal impedance of the oscilloscope (typically 50Ω).

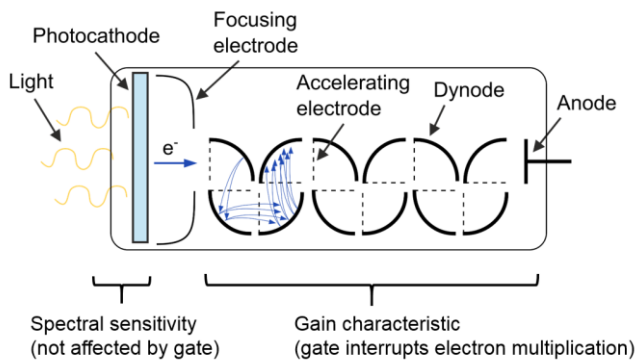


Figure 5-1 Schematics of a photomultiplier tube.

Photocathode materials are chosen based on their cathode quantum efficiency (QE), i.e., the ratio of emitted photoelectrons to incident photons, which is strongly wavelength-dependent. It has been previously observed that bi-alkali photocathodes (SbKCs) are more prone to non-linear behavior than multi-alkali (SbNa₂KCs) photocathodes [149], particularly at high incident light levels. In a PMT, the primary emission (photocathode) and secondary emissions (dynodes) of electrons can both be subject to non-linearity: the photocathode resistivity increases with increasing incident photon flux and thus releases less photoelectrons, while if the electron multiplier gain is too high, space-charge effects at the last dynode stages limit the anode current [129, 130]. The first effect is most likely for semi-transparent photocathodes [130] while the latter effect is most likely to occur at low light levels with high gain [129, 155]. The photon flux during the LII signal peak is usually much higher compared to measurements at lower light levels and non-linearity has been reported for anode current levels lower than the manufacturer-specified limit [149]. It is important to keep this in mind when using gated PMTs as the electrical gate circuit only interrupts the high-voltage power supply of the dynode stages rather than preventing the photocathode from primary photoelectron emissions. Consequently, even when the gate is inactive, the photocathode can be depleted and will affect the linearity of the measurement or calibration.

This study focuses on compact PMT modules with a built-in high-voltage power supply, voltage-divider circuit and gate circuit, which have recently become commercially-available. This leaves the experimentalist with three adjustable operating parameters: (i) the incident light flux, via variable neutral density (ND) filters, (ii) the electron gain by changing the control voltage of the voltage-divider circuit, and (iii) the gate-opening time and duration. The PMT gain characteristics depend on the number and type of dynode stages, the voltage-divider circuit design, and the applied gain voltage. It can be experimentally-determined and approximated by plotting the gain and gain voltage on logarithmic axes [129, 156]. An additional advantage of gated PMTs is that the signal baseline (dark current) can be determined immediately

before the gate opening of each individual signal trace, while for ungated operation the baseline needs to be determined prior the experiment.

5.2.3 Calibration procedures

Calibration can be done directly or indirectly [3, 10]. The indirect approach calibrates an LII-inferred aerosol attribute (e.g., particle volume fraction or particle size) against values obtained from independent measurement techniques, most often extinction measurements [5, 86, 90, 92, 157], gravimetric sampling [158, 159], or transmission electron microscopy (TEM) [13, 160]. Reproducible calibration aerosol sources with properties reported in literature [46, 55, 121, 161], or commercially-available and pre-characterized powders suspended in an aerosol [112, 121, 162] may also be used. For direct calibration, the spectral emission is measured from a known radiance source and the relative instrument sensitivity is obtained from the ratio of the measured spectrum and the reference spectrum. The relative sensitivity calibration of the measurement system is essential when determining the pyrometric temperature from the response of two or more detectors. Through direct calibration the measured signals are directly relatable to a physical quantity (i.e., spectral incandescence), which in turn can be used as input for the LII model, while the indirect approaches simply scale the measured signal to match the expected particle size or volume fraction. The indirect approach has the disadvantage that the calibrated aerosol properties tend to be uncertain (e.g., varying with process condition or time), which can introduce significant uncertainty into the calibration. The remaining discussion therefore focuses on the direct calibration procedure.

Typically, direct calibration is carried out by placing a well-characterized light source at the LII probe-volume position so as to include all optical components in the sensitivity calibration. The most common source is the calibrated tungsten filament lamp [8, 9, 11, 49, 87, 115], which can be approximated as a greybody at temperatures between 2000 and 4000 K, depending on the lamp current, but cannot be modeled as spatially-uniform or diffuse (i.e., the emitted intensity varies with angle and location). Consequently, calibration accuracy depends strongly on the ratio of filament size and LII probe volume, and further optical elements (e.g., a pinhole, a diffuser, or an integrating sphere) may be introduced to account for a non-Lambertian intensity distribution. Ryer et al. [163] used an integrating sphere in combination with a halogen lamp to homogenize the intensity distribution. Smallwood [8] used a calibrated spectrometer attached to an integrating sphere to trace the lamp performance and calculate a reference spectrum. Irradiance standards are light-source systems that are calibrated against an independent standard and optimized for homogeneity and reproducibility with various optical elements. Recent studies used irradiance standards with a calibrated tungsten/halogen lamp with a diffuser system [11, 164] or a quartz halogen lamp scattered off the surface of a Lambertian surface [8]. In contrast, Cenker and Roberts [165] calibrated their detectors for relative sensitivity using incandescence from a well-characterized reference flame. A drawback of this approach is that variations in process conditions could affect the temperature profile of the flame and thus directly affect the calibration. Spectral incandescence at typical flame temperatures (\sim 1600 K) is also quite weak at the shorter detection wavelengths typical in most LII measurements.

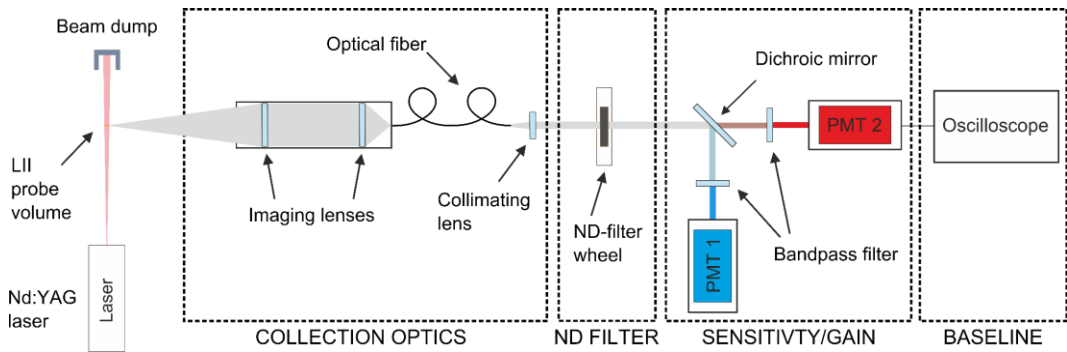


Figure 5-2 Schematics of a typical LII setup indicating the components affected by the individual calibrations. The calibration light source is usually placed at the LII probe-volume position.

The following sections demonstrate the optical sensitivity calibration procedures and error calculation for a multi-wavelength LII device. Before the signals from multiple PMTs can be used for LII signal processing, four calibration steps need to be performed to account for: (i) signal baseline, (ii) relative channel sensitivity, (iii) PMT gain characteristic, and (iv) variable optical components (i.e., neutral-density (ND) filter, collection optics). Figure 5-2 shows the schematics of a typical LII setup and indicates the components affected by the individual calibration steps. The following calibration procedures can be applied to any LII system with two or more PMTs.

5.2.3.1 Baseline correction and signal range

The baseline signal, V_i^{baseline} , is related to the PMT signal measured in a dark environment and represents the reference zero line for all subsequent processing steps. The baseline can be nonzero if thermal noise in the PMT produces a dark current or if the oscilloscope offset is nonzero. Baseline drift can occur if the electronics are not in thermal equilibrium with the surrounding (see section 5.5). The baseline should not be confused with the bias caused by background illumination, e.g., flame radiation along the optical path. For ungated PMTs, the baseline signal level is found using an independent dark measurement, which is later subtracted from the measured signal, while for gated PMTs the signal before the gate opening can be used to obtain a mean baseline signal level. Figure 5-3 illustrates a typical signal obtained from gated PMTs, along with the corresponding signal sections used for various calibration procedures.

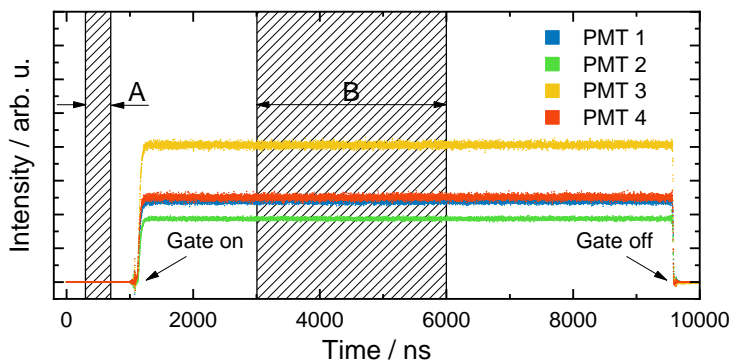


Figure 5-3 Signal trace of a gated PMT. Signal sections A and B are used for the calibration procedure.

Section A is used for baseline correction and section B is averaged to calculate a mean signal and its standard deviation from sufficient large number of signals (> 100). Section B needs to be sufficiently distant ($> 1 \mu\text{s}$) from the PMT gating to avoid any biases introduced by the gating characteristics.

5.2.3.2 Relative PMT-sensitivity calibration

In two- or multi-color LII measurement systems, the PMTs making up the different channels must be calibrated relative to one another. For this purpose, the irradiance of a spectrally-known light source is measured at constant gain voltage, which defines a reference point, $V^{\text{g,ref}}$, that is discussed in section 5.2.3.3. The PMT signal response of all LII channels can then be used to calculate the relative spectral sensitivity of the PMT at this gain voltage. Depending on the light level of the calibration light source or LII signals, it may also be necessary to reduce the light intensity using calibrated ND filters. The spectral transmittance of the ND filter is usually sufficiently flat over the bandpass filter widths so that it can be approximated by a mean transmittance $\tau_{i,j}$ for the i^{th} channel and j^{th} filter. Repeating the sensitivity calibration at various light levels using different ND filters will determine if a PMT and its calibration are affected by non-linearity [149].

Figure 5-4 shows a reference spectrum of an integrating sphere light source and the transmission spectra of the bandpass filters in front of the individual PMTs.

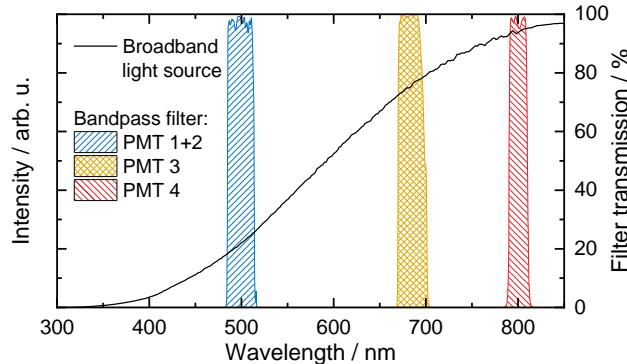


Figure 5-4 Reference spectrum of the integrating sphere broadband light source and the transmission curves of the bandpass filters used in this study.

Let E_{ik} represent the irradiance detected by the i^{th} sensor due to emission from the k^{th} light source. If the detector is equipped with a bandpass filter with center wavelength $\lambda_{c,i}$ and bandwidth $2\delta_i$, E_{ik} can be approximated by integrating the product of the reference spectral irradiance, $E_{\lambda,k}^{\text{ref}}(\lambda)$, and the spectral sensitivity of the LII system, $\theta(\lambda)$, over the spectral width of the bandpass filter. Assuming that the spectral transmittance of the bandpass filter and the spectral sensitivity of the detectors is constant over the narrow filter bandwidth, the spectral sensitivity of the LII system can be approximated at the center wavelengths of the detectors [9, 11], $\theta_i = \theta(\lambda_{c,i})$, to give

$$E_{ik} = \int_{\lambda_{c,i}-\delta_i}^{\lambda_{c,i}+\delta_i} \theta(\lambda) E_{\lambda,k}^{\text{ref}}(\lambda) d\lambda \approx \theta_i E_{ik}^{\text{ref}}, \quad (5-1)$$

where

$$E_{ik}^{\text{ref}} = \int_{\lambda_{c,i}-\delta_i}^{\lambda_{c,i}+\delta_i} E_{\lambda,k}^{\text{ref}}(\lambda) d\lambda. \quad (5-2)$$

The irradiance E_{ik} , can be related to the measured PMT voltage with an additional instrument calibration factor η_i that scales the irradiance measured with a detector to a voltage:

$$V_{ik}^{\text{meas}} - V_i^{\text{baseline}} = \eta_i E_{ik} = \eta_i \theta_i E_{ik}^{\text{ref}}. \quad (5-3)$$

Knowledge of the exact value of $\eta_i \theta_i$ is only needed to measure the particle volume fraction and requires an absolute calibrated light source (see Ref. [9]). For light sources that are only calibrated for relative sensitivity, the true value of $\eta_i \theta_i$ is unknown and a relative sensitivity calibration factor can be defined according to

$$D_i^* \propto \frac{1}{\eta_i \theta_i}. \quad (5-4)$$

For the present analysis, the relative sensitivity calibration factor D_{ijk}^* for the i^{th} PMT channel, j^{th} ND filter, and k^{th} light source is defined from the measured mean signal voltage, the baseline voltage, the ND-filter transmittance, and the reference spectrum:

$$D_{ijk}^* \equiv \frac{\tau_{ij} E_{ik}^{\text{ref}}}{V_{ijk}^{\text{meas}} - V_i^{\text{baseline}}}. \quad (5-5)$$

The calibration sets, resulting from multiple measurements of different light sources and ND filters, can be scaled by their mean value for each light source to allow for comparison between light sources of different intensities:

$$D_{ijk} = \frac{nm}{\sum_i^m \sum_j^n D_{ijk}^*} D_{ijk}^*. \quad (5-6)$$

In general, the calibration factors can be envisioned as normally-distributed random variables due to imperfect knowledge of the reference spectra and variations in measured quantities for which a mean and standard deviation are often known. Consequently, the calibrated LII signals will also follow a normal distribution. In order to quantify the uncertainty associated with the calibration factors, the mean, \bar{D}_i , and standard deviation, σ_{D_i} , of D_{ijk} over the various light sources and ND filters are incorporated in a Bayesian approach within the signal processing presented in the following sections.

5.2.3.3 PMT-gain calibration

The *gain* of a PMT is the ratio of the incident photon flux to the generated anode current, which can be controlled by varying the *gain voltage* of the high-voltage divider circuit in the PMT. Variation of this quantity increases the dynamic range of PMTs and allows measurements over a wide range of light levels. The anode current is usually measured as a voltage signal using the internal impedance of the oscilloscope (typically 50Ω). While neutral density filters reduce the light level only by a fixed factor, the gain can be

used to increase the PMT signal to match the vertical resolution of the oscilloscope in order to make full use of the digitization depth, thereby maximizing the signal-to-noise ratio. In cases where PMT measurements are taken at a range of gain voltages, the calibration coefficient of each channel must additionally be multiplied by a gain correction factor.

The mean baseline-corrected anode current, i_i^a , produced by a PMT can be related to the actual gain voltage, V_i^{gain} , in the linear range of the PMT by

$$\ln(i_i^a) = A_i \ln(V_i^{\text{gain}}) + B_i . \quad (5-7)$$

The coefficient B can be eliminated by normalizing about a reference gain voltage, $V_i^{\text{g,ref}}$, and the corresponding anode current, $i_i^{\text{a,ref}}$

$$\frac{i_i^a}{i_i^{\text{a,ref}}} = \exp \left[A_i \ln \left(\frac{V_i^{\text{gain}}}{V_i^{\text{g,ref}}} \right) \right] = \left(\frac{V_i^{\text{gain}}}{V_i^{\text{g,ref}}} \right)^{A_i} . \quad (5-8)$$

This relationship can be rewritten in terms of the gain correction function,

$$G_i(V_i^{\text{gain}}) \equiv \left(V_i^{\text{gain}} / V_i^{\text{g,ref}} \right)^{-A_i} , \quad (5-9)$$

such that the anode current that would be expected at the reference gain voltage can be calculated from the anode current at any other gain voltage,

$$i_i^{\text{a,ref}} = i_i^a G_i(V_i^{\text{gain}}) . \quad (5-10)$$

The value of A_i can be determined by applying weighted-least squares to Eq. (5-8) using anode currents measured at a range of gain voltages,

$$A_i = \arg \min_A \left\{ \left\| \frac{i_i^a - i_i^{\text{a,ref}} (V_i^{\text{gain}} / V_i^{\text{g,ref}})^A}{\sigma_{i_i^a}} \right\|_2^2 \right\} , \quad (5-11)$$

where $\sigma_{i_i^a}$ is the standard deviation of i_i^a , which can be estimated by making multiple measurements of the anode current. By approximating the problem as locally-linear, uncertainties in A_i can be determined using traditional statistical techniques and propagated through to G using the propagation-of-error formula [166]:

$$\sigma_{G_i} = \sigma_A \left| \frac{dG_i}{dA} \right| = \sigma_A \left| - \left(\frac{V_i^{\text{gain}}}{V_i^{\text{g,ref}}} \right)^{-A} \ln \left(\frac{V_i^{\text{gain}}}{V_i^{\text{g,ref}}} \right) \right| . \quad (5-12)$$

It should be noted that σ_{G_i} goes towards zero when measurements are made at the reference gain voltage (e.g., for the channel-sensitivity calibration described in the previous section). The gain calibration should be repeated with various ND filters to ensure linear operation over the entire range of signal intensities relevant for the experiment [149] and that gain voltages and anode currents remain within the specifications of the manufacturer. Sample PMT signals generated following this procedure are shown in Figure

5-5, including an indication of the temporal range over which the PMT signal is averaged to obtain i_i^a and for which the variance is used to estimate $\sigma_{i_i^a}$. The increase in noise for higher signals is consistent with the standard Poisson-Gaussian noise model [167].

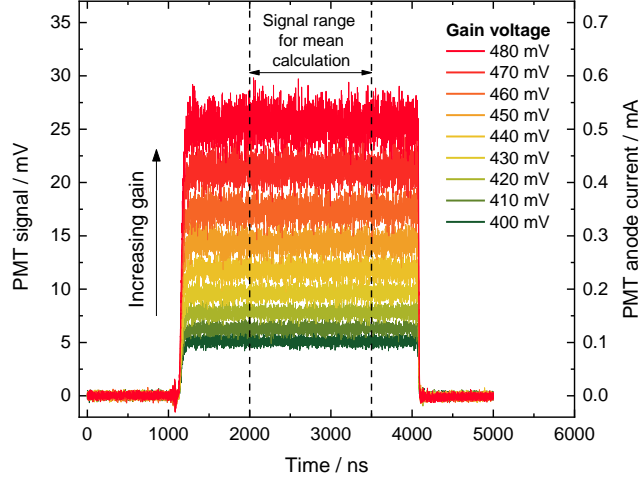


Figure 5-5 Gated PMT signals for 50- Ω coupling and corresponding anode currents for a variation of gain voltages.

5.2.3.4 Correction for variable optical components

For some LII experiments, additional optical components must be introduced to adapt to experimental conditions. For example, variable ND filters may be used to attenuate the light/signal intensity or the collection optics may be adjusted to alter the collection solid angle. Usually, the calibration light source is placed at the LII probe volume position and the efficiency of collection optics is included in the PMT sensitivity calibration. In this study, we use an arrangement based around a collecting integrating sphere in order to separate the collection optics calibration from the PMT sensitivity calibration. The efficiency of the collection optics ϕ and the transmittance of ND filters τ are therefore incorporated as additional factors in the signal processing.

5.2.3.5 Summary of LII signal calibration

By combining the various calibration procedures in the preceding sections, the calibrated relative irradiance $J_{\lambda,i}^{\text{exp}}$ can be calculated from the measured signal response V_i^{meas} of the i^{th} channel at time t according to

$$J_{\lambda,i}^{\text{exp}}(t) = \frac{\bar{D}_i G_i}{\tau_{i,j} \phi_i} [V_i^{\text{meas}}(t) - V_i^{\text{baseline}}]. \quad (5-13)$$

This can act as input to subsequent signal processing.

5.2.4 Spectroscopic model

Following calibration, LII signal processing proceeds with two consecutive steps: (i) calculation of a temperature trace from calibrated LII signals using a spectroscopic model and (ii) inferring the quantities-of-interest (e.g., particle size) by comparing the measured temperature traces to those obtained using a heat transfer model. The spectroscopic model is given by

$$J_{\lambda,i}^{\text{mod}}(T_p) \propto f_V B_\lambda \int_0^\infty p(d_p) C_{\lambda,\text{abs}}(d_p) I_{\lambda,\text{BB}}[T_p(d_p)] dd_p, \quad (5-14)$$

where $I_{\lambda,\text{BB}}$ and $C_{\lambda,\text{abs}}$ are the blackbody spectral intensity and wavelength-dependent absorption cross-section of a particular particle diameter, respectively, which is integrated over the particle size distribution using the probability density of the particle diameter $p(d_p)$, and then scaled by the volume fraction of particles in the measurement volume during the given laser pulse f_V , and the geometry and optical efficiencies of the detection system B_λ . For spherical nanoparticles the spectral absorption cross-section $C_{\lambda,\text{abs}}$ is often calculated assuming the Rayleigh limit of Mie theory [44],

$$C_{\lambda,\text{abs}}(d_p) = \frac{\pi^2 d_p^3}{\lambda} E(m_\lambda), \quad (5-15)$$

provided that $\pi d_p / \lambda \ll 1$ and $|m_\lambda| \pi d_p / \lambda < 1$, where $E(m_\lambda)$ is the absorption function and m_λ is the complex index of refraction. In the current work, a monodisperse particle size distribution is assumed and the temperature is considered as an “effective” temperature of an ensemble of nanoparticles of the same size that is a biased estimate of the true mean particle temperature. Accordingly, equation (5-14) can be written as

$$J_{\lambda,i}^{\text{mod}}(T_{p,\text{eff}}) \propto f_V B_\lambda C_{\lambda,\text{abs}} \frac{2hc_0^2}{\lambda_i^5} \left[\exp\left(\frac{h c_0}{k_B \lambda_i T_{p,\text{eff}}}\right) - 1 \right]^{-1}. \quad (5-16)$$

The wavelength-independent properties of equation (5-15) and (5-16) (i.e., the particle diameter, the particle volume fraction, and the detection efficiency) are combined into Λ , which further simplifies equation (5-15) and (5-16) to

$$\begin{aligned} J_{\lambda,i}^{\text{mod}}(T_{p,\text{eff}}, \Lambda) &\propto \Lambda \frac{E(m_{\lambda_i})}{\lambda_i} I_{\lambda,\text{BB}}[T_p(d_p)] \\ &= \Lambda \frac{E(m_{\lambda_i})}{\lambda_i} \frac{2hc_0^2}{\lambda_i^5} \left[\exp\left(\frac{h c_0}{k_B \lambda_i T_{p,\text{eff}}}\right) - 1 \right]^{-1}. \end{aligned} \quad (5-17)$$

For the calculation of temperature traces from measured irradiances, two methods are widely used: (i) two-color pyrometry and (ii) fitting of the spectral incandescence to two or more spectral measurements bands or to full spectra. The temperature calculation is repeated at each measurement time in order to obtain a temporally-resolved temperature trace that serves as an input to the heat transfer model used in determining the nanoparticle size and other attributes of the aerosol.

Two-color pyrometry (e.g., [9, 40, 41, 101]) requires calibrated LII signals at two independent wavelengths and involves taking the ratio of the spectral irradiance at both wavelengths

$$T_{p,\text{eff}} = \frac{h c_0}{k_B} \left(\frac{1}{\lambda_2} - \frac{1}{\lambda_1} \right) \left[\ln \left(\frac{J_{\lambda,1}^{\text{exp}}(t)}{J_{\lambda,2}^{\text{exp}}(t)} \frac{E(m_{\lambda_2})}{E(m_{\lambda_1})} \left(\frac{\lambda_1}{\lambda_2} \right)^6 \right) \right]^{-1}, \quad (5-18)$$

where $T_{p,\text{eff}}$ is the effective particle temperature, h is the Planck constant, c_0 the speed of light in vacuum, k_B the Boltzmann constant, and λ_i the center wavelength of the detector bandpass filter. This is the default method used by practitioners.

When two or more spectral detection channels are available, the temperature can be inferred through nonlinear least-squares regression to the experimentally-determined calibrated irradiances, $J_{\lambda,i}^{\text{exp}}$:

$$T_{p,\text{eff}} = \arg \min_{T_p, \Lambda} \left\{ \sum_i \left[\frac{J_{\lambda,i}^{\text{exp}}(t) - J_{\lambda,i}^{\text{mod}}(T_p, \Lambda)}{\sigma_i} \right]^2 \right\}. \quad (5-19)$$

For multiwavelength pyrometry using more than two channels, the variance of different channels needs to be considered as standard deviation of the measurement data σ_i . The magnitude of the variance of each channel is related to detector noise, detector sensitivity, and the measured signal intensity and can vary significantly between channels. It can be experimentally determined by pooling the results of multiple laser shots, or estimated using a noise model as outlined in Ref. [167]. Assigning equal influence of all channels by assuming $\sigma_i = 1$ would falsely give more influence to a channel that is affected by higher uncertainty and thus biases the inferred temperatures.

5.2.5 Statistical considerations

There is an increasing trend in the LII community to account for how measurement noise and model-parameter uncertainty affect quantities derived from LII measurements [13, 69, 116, 124, 168]. In this study, the Bayesian approach was used to investigate the influence of calibration parameters and measurement noise on pyrometrically determined temperatures from multi-color LII detection using photomultiplier tubes. The Bayesian approach treats the various quantities as random variables that follow some distribution [169]. The observations contained in \mathbf{b} and the quantities-of-interest (QoI, which is the effective temperature in the current work) are then related by way of a likelihood, $p_{\text{like}}(\mathbf{b}|T_{p,\text{eff}})$, which defines the likelihood of the observed data (spectral incandescence, or, more fundamentally, PMT voltages) occurring for a hypothetical temperature. Assuming that the noise and model errors in \mathbf{b} are independent and normally-distributed, the likelihood can be phrased as a multivariate normal distribution

$$p_{\text{like}}(\mathbf{b}|T_{p,\text{eff}}) = \frac{1}{\prod_i (2\pi)^{1/2} \sigma_{b,i}} \exp \left(-\frac{1}{2} \sum_i \left[\frac{b_i(t) - b_i^{\text{mod}}(T_{p,\text{eff}}, \Lambda)}{\sigma_{b,i}} \right]^2 \right), \quad (5-20)$$

where b_i^{mod} is a model of the measured quantity and $\sigma_{b,i}$ is the standard deviation of the measurement data for the i^{th} channel. Moreover, the maximum of this distribution corresponds to the weighted least-squares solution, that is

$$T_{p,\text{eff}} = \arg \max_{T_{p,\text{eff}}, \Lambda} [p_{\text{like}}(\mathbf{b}|T_{p,\text{eff}})] = \arg \min_{T_{p,\text{eff}}, \Lambda} \sum_i \left[\frac{b_i(t) - b_i^{\text{mod}}(T_{p,\text{eff}}, \Lambda)}{\sigma_{b,i}} \right]^2. \quad (5-21)$$

In the current study, the data is taken as the average signal measured by the PMTs, corrected for the baseline, the transmittance of the ND filters, and the efficiency of the collection optics, which are considered deterministic parameters,

$$b_i(t) = \frac{1}{\tau_{j,i}\phi_i} (\bar{V}_i^{\text{meas}}(t) - V_i^{\text{baseline}}), \quad (5-22)$$

where the overbar indicates an average over multiple shots and i denotes the i^{th} channel. This quantity is normally-distributed according to the central limit theorem, justifying the form chosen for the likelihood. Moreover, in this case, $\sigma_{b,i}$ is the standard deviation of the mean signal, corresponding to the standard deviation over multiple shots reduced by the square root of the number of shots and by $\tau_{j,i}$ and ϕ_i . By this definition, b_i^{mod} is the modeled data evaluated at some hypothetical $T_{\text{p,eff}}$, which incorporates the gain correction function G_i and the relative PMT sensitivity calibration factor D_i . In this study, we focus on the PMT sensitivity calibration and consider only measurements at the gain reference voltage, so that $G_i = 1$. The expected signal for the i^{th} channel is then

$$b_i^{\text{mod}}(T_{\text{p,eff}}, \Lambda) = \frac{1}{D_i G_i} \Lambda \frac{E(m_{\lambda_i}) 2hc_0^2}{\lambda_i^5} \left[\exp\left(\frac{h c_0}{k_B \lambda_i T_{\text{p,eff}}}\right) - 1 \right]^{-1}. \quad (5-23)$$

Unfortunately, this approach neglects the uncertainty introduced through the calibration procedure described above. This can be incorporated by defining the calibration factors as additional *nuisance parameters* to be solved along with the unknown pyrometric temperature, $\boldsymbol{\Theta} = [D_1, D_2, \dots, D_n]^T$. These can be incorporated into the likelihood by adding a conditional, such that

$$p_{\text{like}}(\mathbf{b}|T_{\text{p,eff}}, \boldsymbol{\Theta}) = \frac{1}{\prod_i (2\pi)^{1/2} \sigma_{b,i}} \exp\left(-\frac{1}{2} \sum_i \left[\frac{b_i(t) - b_i^{\text{mod}}(T_{\text{p,eff}}, \Lambda, \boldsymbol{\Theta})}{\sigma_{b,i}} \right]^2\right), \quad (5-24)$$

where b_i^{mod} becomes a function of both $T_{\text{p,eff}}$ and $\boldsymbol{\Theta}$. In considering the nuisance parameters, it is crucial to incorporate prior information known about the nuisance parameters and QoI before a measurement, via the prior probability, $p_{\text{pri}}(\boldsymbol{\Theta})$, in addition to information extracted from the data [169]. The result is the posterior probability, $p(T_{\text{p,eff}}, \boldsymbol{\Theta}|\mathbf{b})$, which is described by Bayes' equation. If the nuisance parameters and QoI are statistically independent before the measurement [69] and no prior information is known about $T_{\text{p,eff}}$ a priori, the posterior is given by

$$p(T_{\text{p,eff}}, \boldsymbol{\Theta}|\mathbf{b}) = \frac{p_{\text{like}}(\mathbf{b}|T_{\text{p,eff}}, \boldsymbol{\Theta}) p_{\text{pri}}(\boldsymbol{\Theta})}{p(\mathbf{b})}, \quad (5-25)$$

where $p(\mathbf{b})$ is the evidence that acts to scale the product of the priors and likelihood so that the Law of Total Probability is satisfied. Information known about the nuisance parameters are also encoded in a normal distribution,

$$p_{\text{pri}}(\boldsymbol{\Theta}) \propto \exp\left\{-\frac{1}{2} \sum_i \left[\frac{\theta_i - \mu_{\theta,i}}{\sigma_{\theta,i}} \right]^2\right\}. \quad (5-26)$$

where $\mu_{\theta,i}$ and $\sigma_{\theta,i}$ are the expected value and standard deviation of each calibration coefficient.

The distribution of the effective temperature alone can then be derived by marginalizing over the nuisance parameters

$$p(T_{\text{p,eff}}|\mathbf{b}) = \frac{1}{p(\mathbf{b})} \int p_{\text{like}}(\mathbf{b}|T_{\text{p,eff}}, \boldsymbol{\theta}) p_{\text{pri}}(\boldsymbol{\theta}) d\boldsymbol{\theta}. \quad (5-27)$$

Moreover, the maximum of the posterior distribution, called the maximum a posteriori (MAP) estimate,

$$\begin{aligned} [T_{\text{p,eff}}, \boldsymbol{\theta}]^{\text{MAP}} &= \arg \max_{T_{\text{p,eff}}, \boldsymbol{\Lambda}, \boldsymbol{\theta}} [p(T_{\text{p,eff}}, \boldsymbol{\theta}|\mathbf{b})] \\ &= \arg \min_{T_{\text{p,eff}}, \boldsymbol{\Lambda}, \boldsymbol{\theta}} \left\{ \sum_i \left[\frac{b_i(t) - b_i^{\text{mod}}(T_{\text{p,eff}}, \boldsymbol{\Lambda}, \boldsymbol{\theta})}{\sigma_{b,i}} \right]^2 + \sum_i \left[\frac{\theta_i - \mu_{\theta,i}}{\sigma_{\theta,i}} \right]^2 \right\}, \end{aligned} \quad (5-28)$$

represents the most probable value of $T_{\text{p,eff}}$ and $\boldsymbol{\theta}$ based on the observed data and priors. The posterior distribution also carries information about how widely the inferred temperatures are spread. This information can then be compared for various channel combinations to evaluate the combined uncertainty introduced by the calibration coefficients and measurement noise.

5.3 Experiment

The presented calibration procedure is applied using a multi-color LII detection setup and various calibration light sources. The derived calibration factors from this procedure and the associated uncertainty are then used for multi-color LII measurements performed on a laminar diffusion flame.

5.3.1 Calibration light sources

For this study, four different light sources are used: (i) halogen lamps built into an integrating sphere (IS), (ii) a laser-driven light source (LDLS), (iii) a stabilized tungsten halogen light source (SLS), and (iv) light-emitting diodes (LED). The IS and the LDLS have been calibrated previously for spectral irradiance by external certified calibration laboratories. The key parameters for all light sources are summarized in Table 5-1. The center wavelengths of the LEDs closely match the detector's bandpass center wavelengths and were used in a previous study to investigate the linearity of PMTs [149]. The characterization procedure of the light sources is described in section 5.4.1.4.

Table 5-1 Light sources used for the calibration procedure in this paper

	IS	LDLS	SLS	LED
Type	Halogen lamps built into an integrating sphere	Laser-driven light source	Stabilized tungsten halogen light source	Light-emitting diodes
Model	K-150WH (LOT-Oriel)	EQ-99X LDLS (Energetiq)	SLS201L (Thorlabs)	EOLD-505-534 EOLD-685-524 EOLD-810-525 (EPIGAP)
Power supply	SLP120-80 (Gossen-Metrawatt)	Internal	Internal	GPS-2303 (GW Instek)
Calibration	Dec. 2016 opto.cal (Switzerland)	Sept. 2017 PTB(Germany)	–	–
Spectrum	Broadband	Broadband	Broadband	Narrow band around center wavelength
Spatial intensity profile	Homogeneous	Spatial intensity profile not homogeneous, coupling with diffuser optics/ integrating sphere recommended		
Advantages	Homogeneous spatial intensity profile, reduces alignment errors	Strong emission from UV to near-infrared enables covering most detection wavelength bands	Compact and low cost	Intensity can be individually controlled for each LED; very low cost
Disadvantages	Weak emission in the UV increases uncertainty of calibration at short detection wavelengths	Xenon plasma atomic emission lines can interfere with detection wavelength bands and introduce errors (very strong > 820 nm)	Weak emission in the UV increases uncertainty of calibration at short detection wavelengths	Center wavelengths should match detection wavelengths, but not all center wavelengths are commercially available
Price	Moderate	High	Low	Very low

5.3.2 Detector arrangement

Figure 5-6 gives a schematic overview of the experimental setup. The central element is an integrating sphere (diameter 5 cm, Thorlabs IS200-4) with four ports that ensures reproducible radiance measurements for any attached light source and detector. The broadband light sources and the LED array (3 LEDs) are connected to two ports and the spectral emission profiles can be observed with a fiber-coupled spectrometer (Ocean Optics USB-4000). As an alternative, an optical fiber (core diameter: 1000 μm) is used for coupling to an LII experiment where the light is collected via fiber-coupled collection optics. The collection optics consists of two achromatic doublets with 100 mm and 150 mm focal lengths. Homogenized light from the integrating sphere exits through a pinhole and is collimated before passing an ND-filter wheel (100, 79, 50, or 10% transmission) and two dichroic beam splitters with edge wavelengths of 605 nm (FF605-Di02) and 740 nm (FF740-Di01), or a 50:50 beam splitter (Thorlabs BSW10R). The light is then focused on four gated PMTs: three with a multi-alkali (MA) photocathode (Hamamatsu H11526-20) and one with a super bi-alkali (SBA) photocathode (Hamamatsu H11526-110).

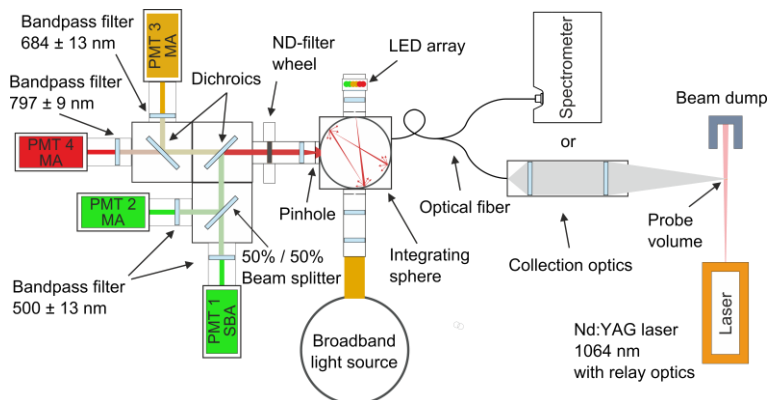


Figure 5-6 Four-PMT setup with collecting integrating sphere, LED array, broadband light source, and a fiber-coupled spectrometer.

For spectral separation, bandpass filters are attached to the PMTs that are specified for the spectral ranges often used for two-color LII measurements [78] with center wavelengths and bandwidths (FWHM) of 500 ± 13 nm (PMT1 and PMT2, Semrock FF01-500/24), 684 ± 13 nm (PMT3, Semrock FF02-684/24), and 797 ± 9 nm (PMT4, Semrock FF01-800/12). For the LII measurements, soot particles are heated by a pulsed (10 ns FWHM) Nd:YAG laser at 1064 nm (Continuum, Powerlite 7000). A circular 3.2-mm aperture is used to shape the laser profile. Signals are collected with a 500-MHz oscilloscope (PicoScope 6404C) with a vertical resolution of 8 bit and 0.8-ns sampling intervals.

The use of an integrating sphere within the LII detection optics makes the system more robust to alignment errors and thus variations in the intensity of the attached light sources. Furthermore, it allows superimposing the light from various sources for linearity measurements and facilitates comparison of detection devices without introducing additional optical elements that could bias the spatial intensity distribution. However, the integrating sphere could introduce a distortion in the temporal intensity measurement that needs to be considered [170]. Multiple reflections within the sphere result in a long light path compared to the nanosecond time-resolution of the detector, which temporally-stretches the signal. This effect can be identified as temporal blurring and the FWHM was determined for this sphere as below 12 ns.

5.3.3 Laminar diffusion flame

Validation measurements were performed using a laminar non-premixed flame [171] that has been the subject of numerous TiRe-LII studies [2]. The burner is operated at its standard conditions of 0.194 standard liters per minute (slm) ethene (C_2H_4) and 284 slm air, and measurements were performed at the standard reference position of 42 mm height above burner (HAB). For this position the gas temperature was previously determined to be 1730 ± 25 K [171] and 1740 K [172], respectively, using Coherent Anti-Stokes Raman Spectroscopy (CARS).

5.4 Methodology and results

The calibration procedure as outlined above is demonstrated with the presented detector arrangement and light sources. The acquired set of calibration factors is then used to calibrate LII signal traces obtained from in-flame measurements and the uncertainty of the calibration factors is propagated through the analysis to evaluate the uncertainty in the inferred temperatures for different channel combinations.

5.4.1 Calibration

The comparison of the calibration procedures can be divided into five steps: (i) spectrometer validation, to ensure linearity and a correct wavelength calibration, (ii) calibration of the transmission through ND filters, (iii) measurement of the spectral transmission through collection optics and sensitivity to chromatic aberration, (iv) light-source characterization for spectral irradiance, and (v) PMT gain and sensitivity calibration.

All light sources are operated for at least 60 minutes before the experiment to ensure thermal equilibration. The intensity of each LED is adjusted with series resistors to ensure approximately equal intensity levels for all channels.

5.4.1.1 Spectrometer validation

A fiber-coupled spectrometer (Ocean Optics USB-4000) is used to record the spectral emission from the attached light sources and to measure the spectral transmission through optical components. The detection range is from 350 to 850 nm, and it is wavelength calibrated with a pen-ray Hg(Ar) line source (LOT-QuantumDesign LSP035). Internal non-linearity correction of the spectrometer software is used and verified over the sensitivity range using a linearity measurement technique as described in Ref. [149].

5.4.1.2 ND-filter calibration

There are two options to account for the ND-filter spectral transmittance within the setup. When the ND-filter transmittance is not known, the ND filter is included in the sensitivity calibration as any other optical element. However, this requires to determine an individual set of sensitivity calibration factors for each ND filter. Alternatively, when the ND-filter transmittances are known, the spectral transmittance for each detection channel can be included as an additional correction factor during LII signal processing. The ND-filter calibration for this setup was described previously in [149].

5.4.1.3 Characterization of collection optics

A configuration of the collection optics with achromatic doublets is compared to the configuration with uncoated plano-convex lenses to investigate the influence of chromatic aberration. For the alignment/focusing of the collection optics, a fiber-coupled diode laser (635 nm) was used. The influence of chromatic aberration is investigated relative to this wavelength.

The spectrometer is attached to the fiber port of the integrating sphere broadband light source (IS) (Figure 5-7 – Position A) and the calibrated spectrum of the light source is recorded as a reference. The spectrometer is then attached to Position B to measure the transmitted light through the collection optics. Dividing the reference spectrum by the attenuated spectrum gives then the spectrally resolved transmittance of the collection optics. To experimentally-identify the influence of chromatic aberration, a variable aperture (VA) is mounted in front of the IS light source and a fiber-coupled diode alignment laser is attached to Position B. The opening diameter of the VA is then reduced to match the fiber core diameter (1000 µm) as visualized by the diode laser.

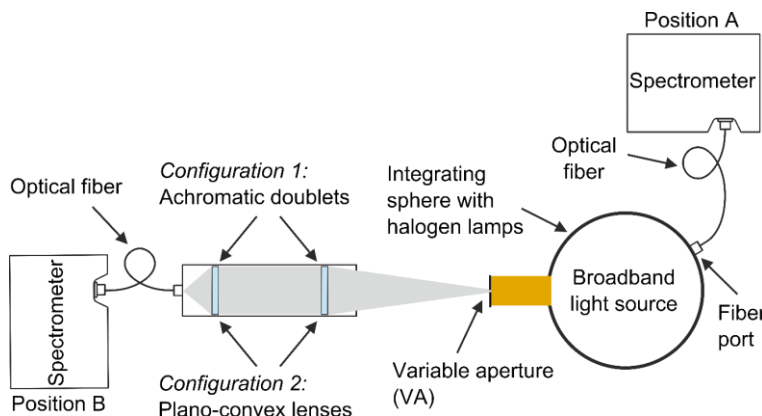


Figure 5-7 Setup for spectrometer calibration and characterization of the collection optics.

Figure 5-8 shows the measured spectra at Position A (blue) and Position B with the variable aperture opened 1 mm (yellow) and opened 4 mm (red) for achromatic doublets (a) and uncoated plano-convex lenses (b).

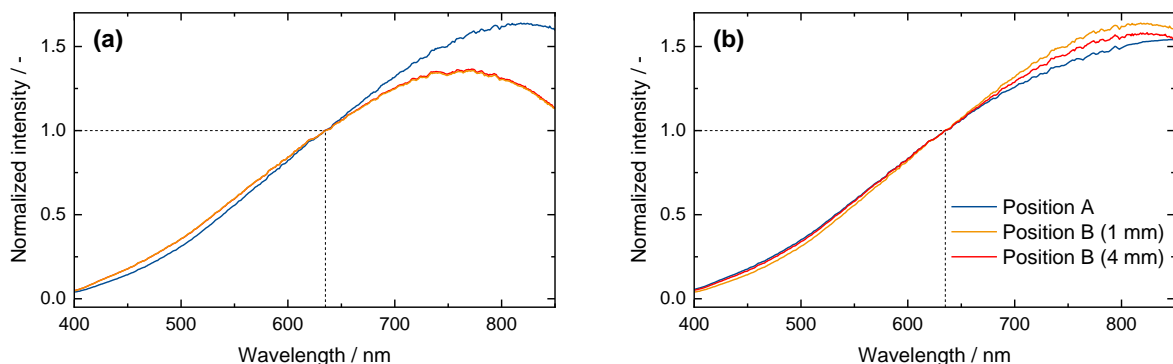


Figure 5-8 Measured spectra of the reference light source at Position A (blue) and Position B with the variable aperture 1 mm opened (yellow) and 4 mm opened (red) for (a) achromatic doublets and (b) uncoated plano-convex lenses.

While the spectra measured with the achromatic lenses show almost no differences between the aperture opening diameters, the normal lenses reveal significant influence of chromatic aberration with decreasing opening diameters. This means that, for wavelengths longer and shorter than the alignment wavelength, the focal length shifts, resulting in less light collected by the fiber. Similar effects are expected when focusing light on the entrance slit of a spectrometer or a pinhole for spatial filtering. For the achromatic lenses, the reduced intensity, measured for wavelengths longer than 700 nm can be explained by the reduced spectral transmittance of the lenses as specified by the manufacturer.

For LII measurements, it is often desired to spatially-limit the detection volume by imaging the signal light through a pinhole, a slit, or by focusing the signal light on the entrance face of a fiber (which then acts as a pinhole). The resulting detection solid angle, combined with the spatial laser profile, defines the probe volume. When these components are used without achromatic optics, chromatic aberration can strongly bias pyrometrically determined temperatures. The comparison of two-color peak temperatures at detection wavelengths of 500 and 800 nm for the conditions described in section 5.4.2, revealed a 500 K lower peak temperature for the lenses affected by chromatic aberration compared to the achromatic doublets. In several recent LII studies, achromatic lenses are already standard components for the collection optics [11, 68, 73]. To account for the transmission through collection optics, a correction for the collection efficiency ϕ_i for each channel i is included in the signal processing. The values for ϕ_i for the achromatic lenses used in this study are 1.0, 0.98, and 0.87 for the 500-, 684-, and 797-nm channel, respectively; they are included in equation (5-13) and (5-22).

5.4.1.4 Characterization of the calibration light sources

The arrangement shown in Figure 5-6 can be used to characterize various light sources and calibrate the PMT setup. For these measurements, the spectral reflectivity of the collecting integrating sphere (IS200-4) was assumed as sufficiently flat ($99 \pm 0.2\%$) between 350 and 850 nm as specified by the manufacturer. For the analysis, the fiber-coupled spectrometer is attached to the fiber port to collect spectra of various light sources (i.e., halogen lamps built into an integrating sphere (IS), laser-driven light source (LDLS), stabilized tungsten halogen lamp (SLS), and the three continuously operated LEDs).

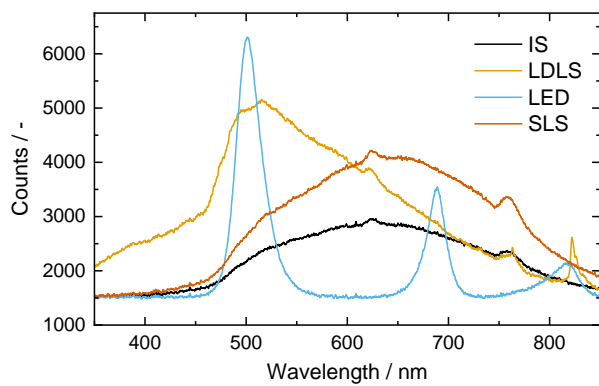


Figure 5-9 Measured uncorrected light source emission intensities convolved with the instrument function of the fiber-coupled spectrometer.

The spectra collected with the spectrometer (Figure 5-9) must be corrected for the dark signal. The spectra of the light sources with known calibration (IS and LDLS) are then used to calculate two independent instrument-sensitivity spectra (Figure 5-10) that can then be used to calibrate other light sources.

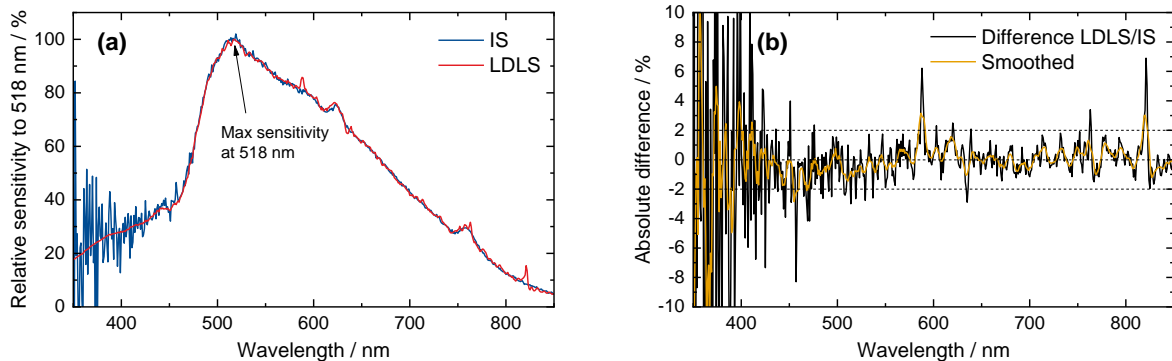


Figure 5-10 (a) Instrument sensitivity calculated from the calibration spectrum of the halogen lamp/integrating sphere light source (IS) and the laser-driven light source (LDLS). (b) Absolute deviation between the two calibrations methods.

The spectrometer sensitivity peaks at 518 nm. The instrument sensitivity spectrum becomes noisier at shorter wavelengths due to the low intensity of the IS below 450 nm, combined with low sensitivity of the spectrometer at these wavelengths. The stronger intensity of the LDLS results in a smoother instrument sensitivity spectrum, particularly at lower wavelengths. Unfortunately, the fluctuating intensity of atomic emission lines from the xenon plasma also results in narrow wavelength-specific anomalies that lead to errors in the LDLS calibration spectrum.

Figure 5-11 shows the relative intensities of all light sources, calculated from the calibration spectra of the IS (a) or the LDLS (b).

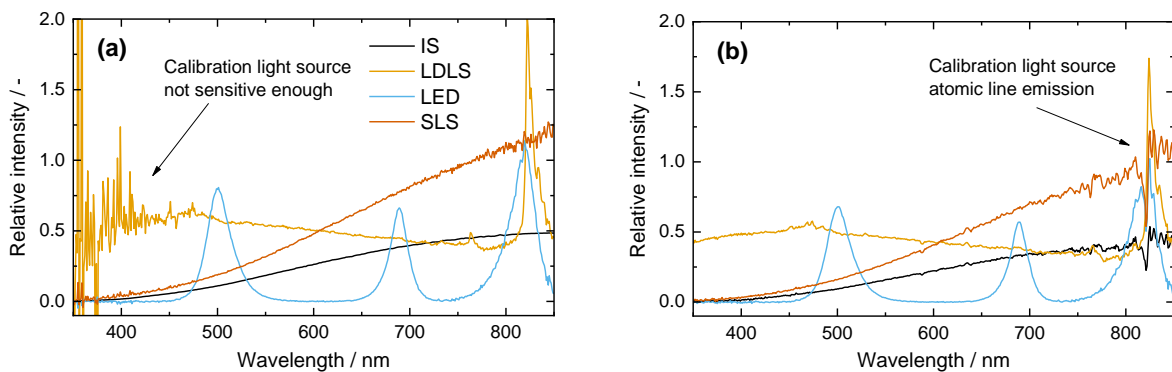


Figure 5-11 Calibrated light source intensity spectra, calculated from (a) the IS calibration and (b) the LDLS calibration.

The intensity of the IS decreases continuously towards the UV and can thus introduce errors in the calibration of shorter wavelengths. The LDLS intensity spectrum is stronger in the near-UV and is therefore suitable for calibration at short detection wavelengths (< 450 nm); however, for wavelengths longer than 820 nm, measurements can be biased by strong atomic emissions caused by the plasma source. The error between the two calibration sources is smaller than 1% for the detection wavelengths used in this study.

Therefore, the IS calibration spectrum is used to calibrate the spectrometer sensitivity in subsequent sections.

The light exiting the pinhole from the collecting integrating sphere is now characterized and can be used for the relative sensitivity calibration of the PMTs. The characterization of the LEDs revealed that the LED peak wavelengths differed slightly from the manufacturer specification and were determined as 500, 689, and 820 nm.

5.4.1.5 PMT calibration

The arrangement shown in Figure 5-6 is used to calibrate the PMTs. The gain correction and sensitivity calibration are related to the same reference voltage (i.e., 450 mV). 200 signals were collected at 10 Hz with a PMT gate time of 8 μ s (same as for the LII measurements). The widths of the temporal sections were arbitrarily chosen as 400 ns (A) and 3000 ns (B) according to Figure 5-3.

PMT-gain calibration

Any stable light source can be used for calibrating the PMT gain. The measurements in this section are performed using the LDLS as its spectral intensity is nearly uniform over the detection spectrum. The gain calibration was performed for gain control voltages between 300 and 550 mV. The maximum gain voltage for each channel was determined so as to ensure that the measured signal does not exceed the vertical range of the oscilloscope. To determine the gain characteristics, the gain voltage was set to the maximum value and decreased in 2 mV steps until reaching a minimum value of 300 mV. The signal response for each voltage was measured after 5 s of stabilization. This sequence was then repeated with 1 mV offset and 2 mV steps to achieve 1 mV total resolution. In case of temporal drifting of the light source, an offset in the data from the two sequences could be identified. To increase reproducibility, a LABVIEW algorithm was used for the automation of the calibration sequence. Figure 5-12 shows the ND-filter-corrected results for PMT 1 and 2 for three ND filters (i.e., 10, 50, and 79% transmission). For PMT 1 (a), the offset between the filter curves can be interpreted as non-linearity for various light levels.

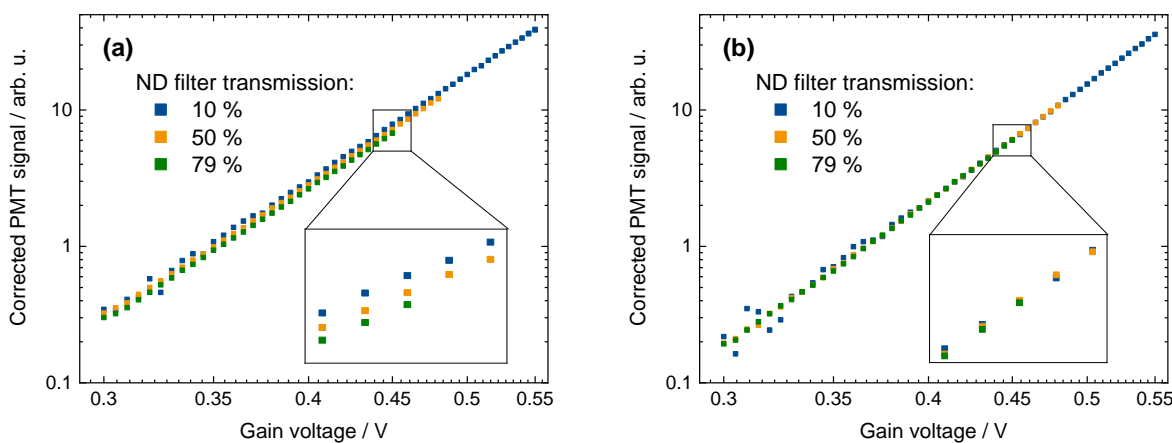


Figure 5-12 Mean signal as a function of gain voltage for (a) PMT 1 and (b) PMT 2 corrected for the respective ND-filter transmission.

The gain correction function is determined for three ND filters and is shown for PMT 2 in Figure 5-13. The result from this analysis is the gain correction function G_i and its standard deviation σ_{G_i} as described in

section 5.2.3.3. The wide spread in signal data for gain voltages below 400 mV indicates unstable behavior of the PMTs and should be avoided.

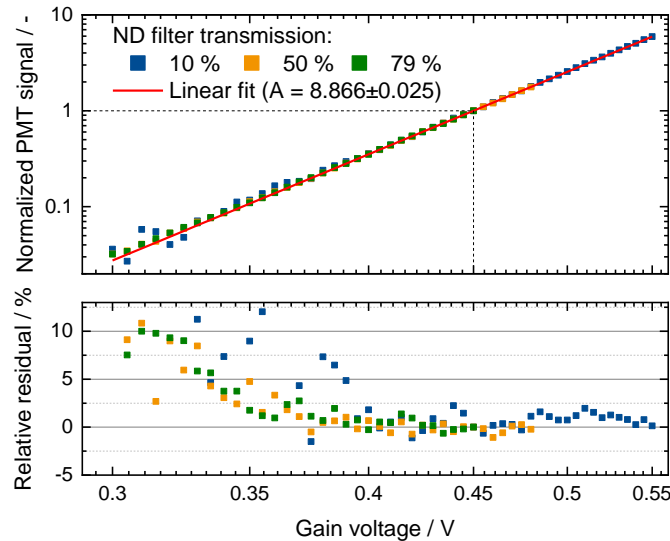


Figure 5-13 Gain-correction function with best fitting coefficient $A = 8.866 \pm 0.025$ for PMT 2 and the residual between the experimentally determined gain correction function and the measurements. The dashed line indicates the gain reference voltage used for the normalization.

Relative PMT-sensitivity calibration

The light sources described in section 5.3.1 are used for the relative PMT-sensitivity calibration. The PMT response is recorded for various ND-filter transmissions and for a constant gain control voltage (i.e., 450 mV) (Figure 5-14). Calibration factors for all channels and light sources can then be calculated according section 5.2.3.2 and the standard deviation from the complete set can be used for the uncertainty analysis of the calibration.

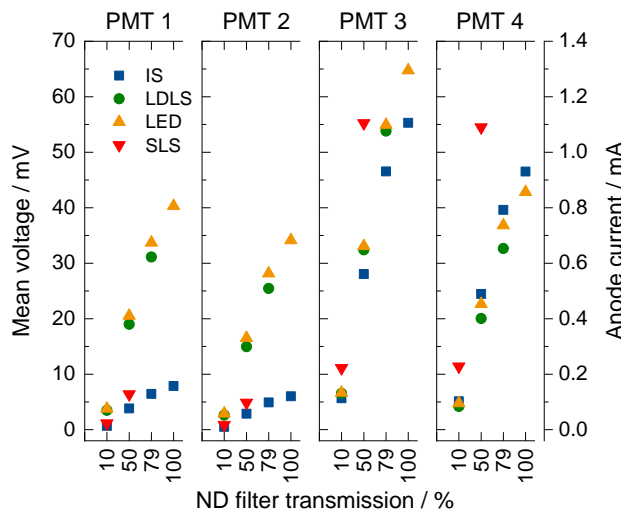


Figure 5-14 Measured anode currents and corresponding signal voltages for 50- Ω coupling for various ND-filter transmissions for IS, LDLS, SLS, and LEDs.

The calculated calibration factors are summarized in Figure 5-15. PMT 1 shows strong non-linear behavior with increasing light level. This causes the calibration factor to increase with increasing light level, while PMT 2 measured at the same wavelength is not affected. This can be traced back to the photocathode material of PMT 1, which is more sensitive to non-linearities [149]. The non-linear behavior can also be observed for PMT 3 and PMT 4 but to a lesser extent.

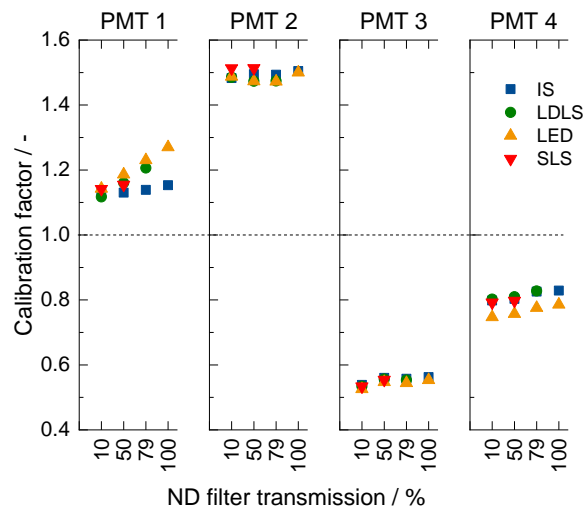


Figure 5-15 Comparison of sensitivity calibration factors from different light sources for various ND-filter transmissions.

For the calibration of PMT 4, an offset between the signal detected with the LEDs and the other light sources is visible. This is attributed to the fact that the detection center wavelength of PMT 4 (i.e., 797 ± 9 nm) is offset from the LED center wavelength (820 nm) by more than the bandpass filter FWHM. The integral calculation method (cf. eq. (5-2)) is more sensitive to intensity fluctuations or wavelength errors when the edge of a narrowband spectrum is analyzed compared to the center region. The mean calibration factors used for the further analysis according section 5.4.1.5 are summarized in Table 5-2.

Table 5-2 Mean calibration factors with standard deviation.

	Channel 1 (500 nm)	Channel 2 (500 nm)	Channel 3 (684 nm)	Channel 4 (797 nm)
\bar{D}_i	1.166	1.490	0.548	0.796
σ_D	0.045	0.015	0.012	0.025

5.4.2 Reference LII experiment

The uncertainty in the calibration is incorporated into the signal processing of the measured data from an LII experiment to determine the uncertainty in the temperature trace. For the present analysis we assume $E(m_\lambda)$ to be wavelength-independent [168]. Measurements are carried out at the gain reference voltage of all PMTs (i.e., 450 mV) to neglect the error introduced by the gain correction function. The laser energy is adjusted to obtain a fluence of 1 mJ/mm², and LII signals for 100 laser shots are acquired. Figure 5-16 shows the baseline-corrected LII signal traces for all four channels. Four data points are selected for further analysis: (A) flame emission without laser interaction, (B) LII signal peak, and the LII signal at (C) 1 μs, and (D) 2.5 μs after the peak.

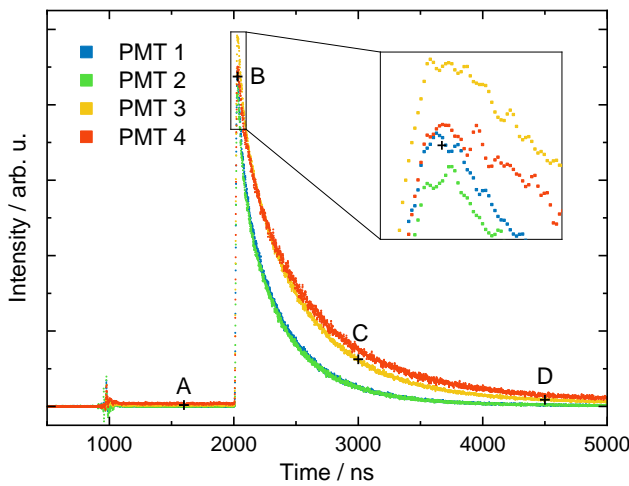


Figure 5-16 LII signal traces for 1 mJ/mm²; Letters A–D indicate points in time used for further analysis.

The spectral fitting is investigated using various channel combinations with regard to uncertainty from the detector calibration and measurement noise. Table 5-3 shows the channel combinations used for the spectral fitting. While T1 represents the spectral fitting of all channels, T2–T6 represent all possible two-color combinations from this configuration.

Table 5-3 LII signal channels used for the calculation of the particle-temperature traces.

Temperature trace	Channel 1 (500 nm)	Channel 2 (500 nm)	Channel 3 (684 nm)	Channel 4 (797 nm)
T 1	x	x	x	x
T 2	x		x	
T 3	x			x
T 4		x	x	
T 5		x		x
T 6			x	x

The standard deviations of the calibration factors, as calculated in section 5.4.1.5, are used as a prior for the uncertainty analysis and the standard deviation from the multi-shot averaging is incorporated in the calculation of the likelihood (cf. section 5.2.5). The credibility intervals in this section represent the interval in which the measurement values lie with a probability of 95%.

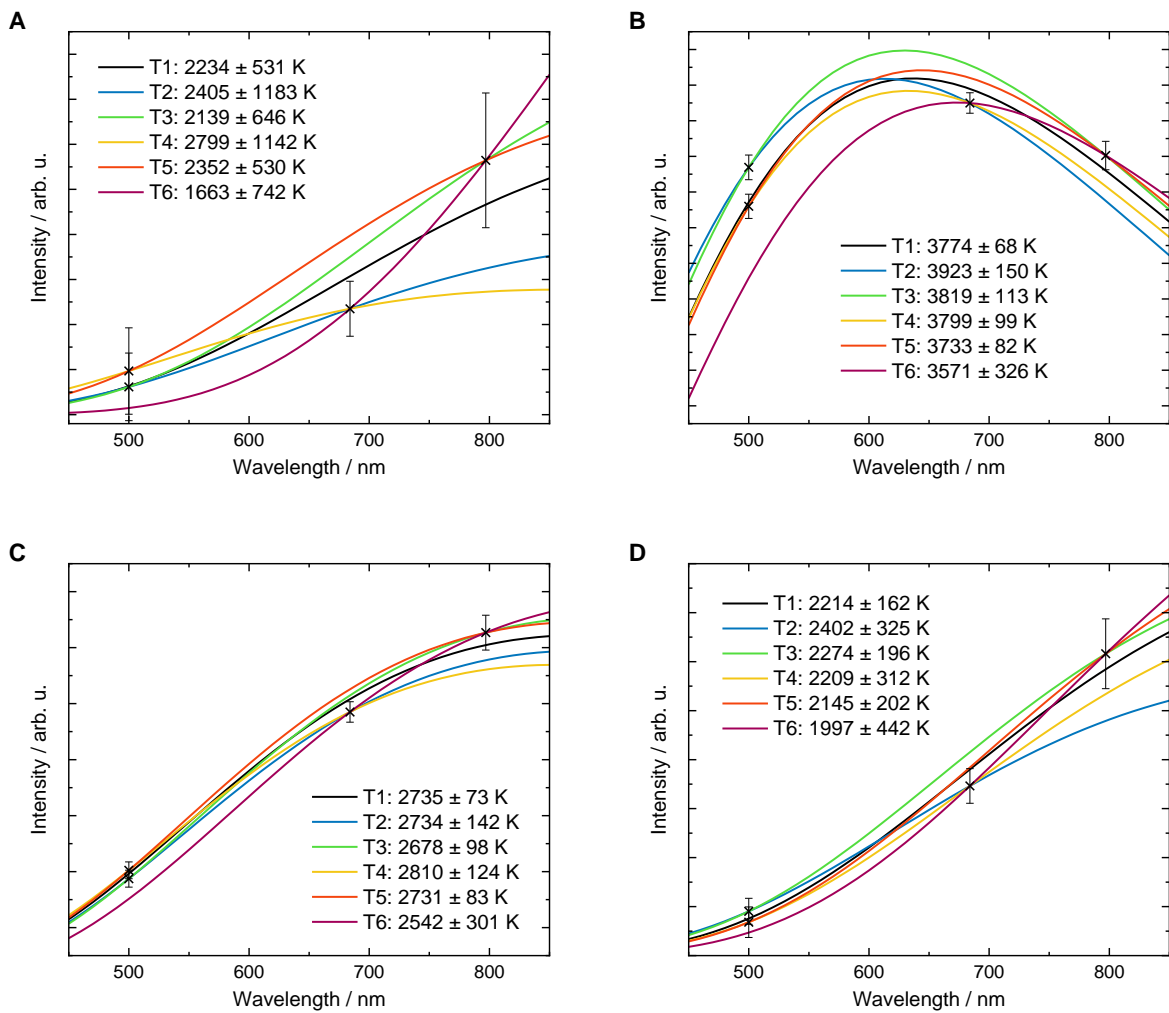


Figure 5-17 Spectral fits of data as indicated in Figure 5-16 for all temperature traces (T1 to T6). Error bars indicate the standard deviation of the measurement for each data point σ_b . (A) flame emission without laser interaction, (B) LII signal peak, and the LII signal at (C) 1 μ s and (D) 2.5 μ s after the peak.

Figure 5-17 shows the spectral fits for all channel combinations for the temporal sections A to D. The temperature differences between the channel combinations cannot be explained by the uncertainty introduced by measurement noise and the calibration. This could indicate that the soot absorption function has some variation with respect to wavelength, or there may be additional chromatic aberrations within the LII setup that were not included in the calibration procedure. The signals of channel 1 and 2 are measured at the same bandpass filter wavelengths and therefore they should match after calibration. However, for a strong signal (B) the signal from channel 1 is higher than channel 2. This is because the calibration of

PMT 1 is strongly affected by non-linearities, which leads to overestimation of the signals in the experiment. This could lead to differences in the evaluated temperatures of 100–200 K. Weak signals (i.e., A and D) are affected by high uncertainty due to the low signal-to-noise ratio and show large discrepancies between the channel combinations.

It can be seen that the temperatures determined by two-color ratios, Eq. (5-17), (T2–T6) are very sensitive to calibration errors. In principle, these estimates can be made more robust by increasing the number of detection wavelengths (T1). However, further error sources should also be considered that can additionally affect the analysis and are not covered within this study. For example, the calibration light source spectrum could have changed due to lifetime drift (i.e., bulb coating, deposits on optical components). Polydispersity [51, 63] or non-uniform laser heating [67, 68] can cause the particles in the probe volume being heated to different temperatures, so that the measured incandescence spectrum is not representative for the mean particle temperature. Probably the leading source of uncertainty remains the radiative properties of the nanoparticles, which, especially in the case of soot, vary with respect to wavelength in an uncertain way.

5.5 Additional measurement issues

Several other commonly-encountered issues, in addition to the calibration errors described above, can introduce errors when interpreting LII measurements. This section therefore summarizes the observed effects and identifies strategies to avoid these anomalies. Further effects are reported in the Appendix B.

Baseline drift

In the first 30 minutes of operation of the PMTs/oscilloscope, the baseline was observed to drift by up to 2% of the oscilloscope vertical range before stabilizing, due to thermal stabilization of the electronics. Meaningful measurements and calibrations should therefore only be carried out after sufficient warm-up times. The manufacturers of the PMTs used in this study recommend allowing a warm-up time of 30 to 60 minutes at similar gain supply voltages and anode currents of several μA [129].

Rise-time differences between channels

Differences in the rise-time of different PMT channels can be caused by different cable lengths, but also by different photocathode materials, gain voltages, and PMT gates. The wavelength-dependence of the photocathode material can only account for rise-time differences of less than 1 ns [173–175]. A more important factor is the PMT gate characteristics, which caused an observable rise-time delay between PMTs containing different photocathode materials. Figure 5-18 shows the PMT gate-opening characteristics for a continuous light source with a 10-ns rise-time difference (A), and for the PMT gate opened 1 μs before a pulsed LED showing no rise-time difference (B). These rise-time differences could strongly influence ratio-pyrometry and lead to nonphysical temperatures, particularly near the peak signal. In this scenario, temporal-alignment of the LII signal peaks or the rising edge of two channels, which is a common procedure among LII practitioners, may introduce a strong bias of calculated temperatures. Instead, it is recommended to use other signal artifacts for alignment (i.e., Q-switch noise patterns, spikes, or PMT gate opening noise) that do not coincide with the peak signal.

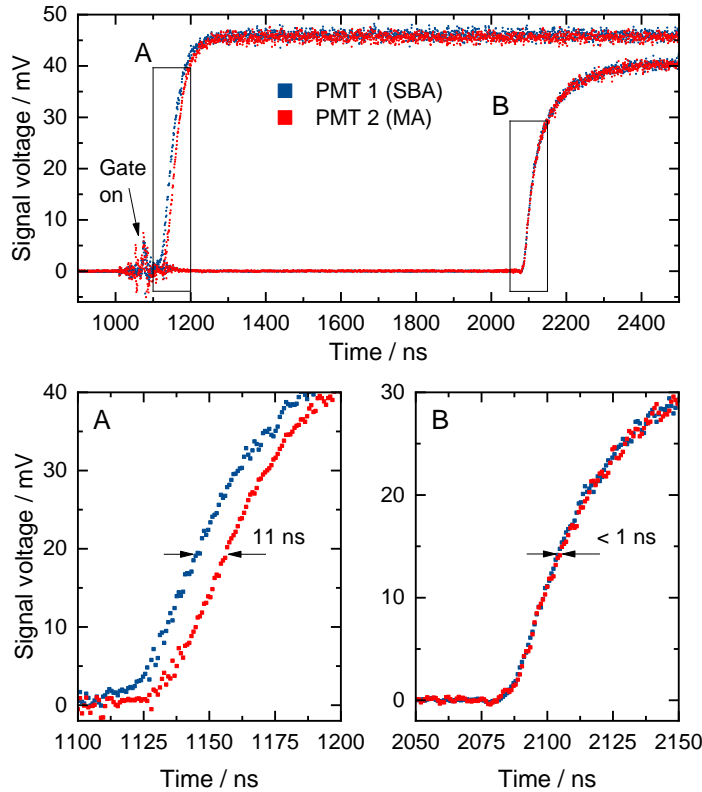


Figure 5-18 Rise-time difference measured with PMTs of different photocathode materials: (A) continuously operated LED and (B) pulsed LED. For the pulsed LED, the rise-time difference was negligible (< 1 ns), while for the continuously operated LED, the gate-opening characteristics lead to a difference of 11 ns.

PMT gain stability/reproducibility

In many PMT configurations, the gain can be controlled by an external control voltage. If this voltage is not set and measured precisely, the resulting error strongly affects the gain-correction calibration. Unstable power supplies for the PMTs/gain control can introduce ripple noise that propagates to the measured LII signal. Setting the gain voltages below the minimum value recommended by the manufacturer can also decrease the reproducibility of the measurements. In case the gain is set too high, the noise component can increase and the measured signals can exceed the vertical range of the oscilloscope. This can cause a bias for very low (i.e., baseline) and high (i.e., LII signal peak) signal levels.

Oscilloscope vertical range overflow

Single-shot LII signals are usually affected by a strong noise component, and, consequently, signals must be averaged over several hundred laser shots to obtain a sufficient signal-to-noise. When the LII signal peak intensity is close to the maximum of the vertical range of the oscilloscope, clipping of single signal maxima can occur, which biases the average. This effect may not be obvious when examining the averaged traces.

Signal overshooting

Signal overshooting (i.e., the signal falls below the baseline) can be caused by the charging of the capacitors in the high-voltage divider circuit of the PMT [152]. The overshooting increases with increasing gain voltages and can be detected by repeating the measurement at various gain voltages. Figure 5-19 (a) shows a PMT signal measured for a pulsed LED while the gain voltage is increased. At the end of the light pulse the signal drops rapidly and the PMT signal becomes negative (b). Figure 5-19 (c) shows the dependence on gain voltage for the section before the signal (A), immediately after the signal (B), and 2 μ s later (C). The bias increases with gain voltage and can persist for several microseconds. This effect can occur for fast-decaying LII signals and significantly biases the temperature determination at later decay times.

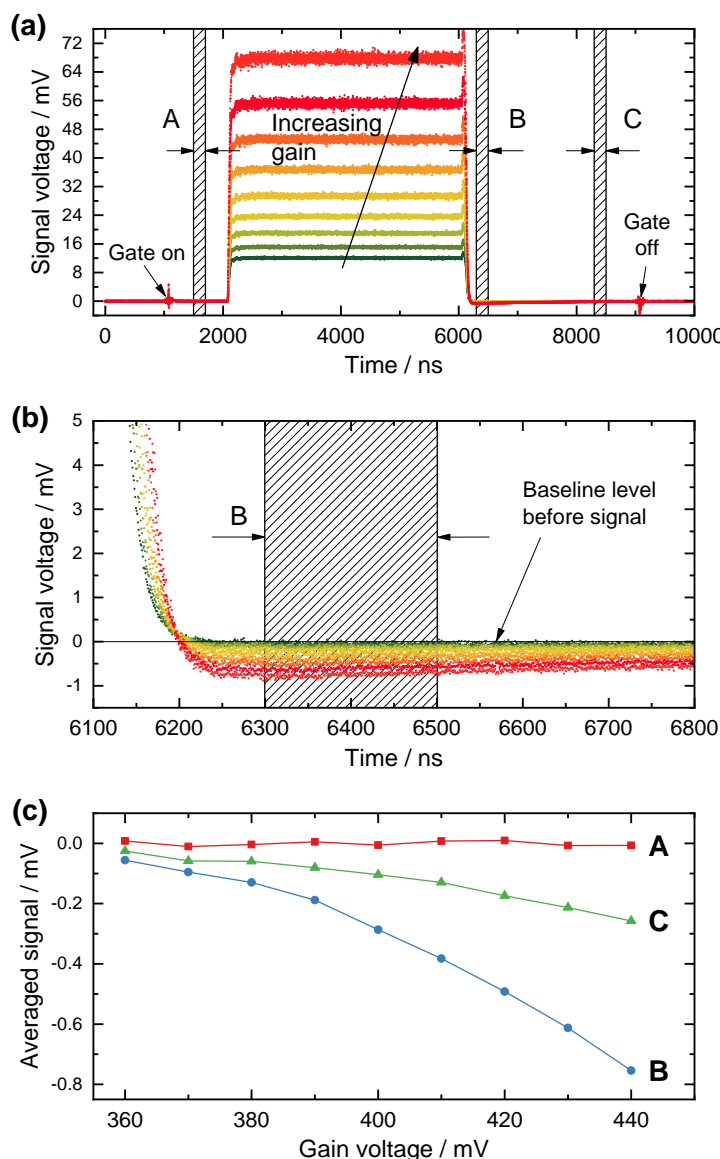


Figure 5-19 PMT signals measured for pulsed LED light for increasing gain voltages (a) and (b). Signal sections A–C are averaged and plotted for all gain voltages in (c).

5.6 Conclusions

This study demonstrates the detector calibration methodology for multi-color time-resolved LII measurements. The calibration procedure consists of: (i) baseline correction, (ii) sensitivity calibration, (iii) gain calibration, and (iv) calibration of variable optical components. Multiple light sources are compared and calibration factors at various light levels were determined. A reference LII experiment is performed on a laminar diffusion flame to quantify the uncertainty introduced by the calibration. A Bayesian approach is used to estimate the uncertainty in LII temperature traces by propagating the uncertainty from the calculation of the calibration factors and the measurement noise to the spectral fitting of LII traces.

When using a light source for calibration, the spectral profile should be compared with the detection wavelength band for lamp artifacts (i.e., atomic plasma emission). For the LEDs, proper selection of the peak wavelengths and bandwidths according the bandpass filter ranges is essential.

PMTs are normally assumed to behave linearly, but, due to the strong dynamic variation of LII signals, the linearity range can easily be exceeded in the initial phase of the signal trace. It was shown that nonlinearity can affect the calibration and this can cause biased calibration factors that can lead to a larger signal amplitude and thus influence the pyrometrically determined temperature. Repeated measurements at different light levels using multiple ND filters can be used to diagnose nonlinear detector response.

Chromatic aberration of the detection optics can introduce significant errors into the detector calibration and the measurement data used in the spectroscopic model. If the system is affected by chromatic aberration, this effect cannot be easily identified during calibration. A fiber-coupled measurement arrangement was presented to identify chromatic errors in the collection optics. This effect can be avoided using achromatic lenses, although these are often optimized over a limited wavelength range.

Apparent particle temperatures were determined for all possible two-color channel combinations and for all four channels using a spectral fit. The temperature values determined from the various two-color ratios differed by up to several hundred Kelvin, highlighting the weakness of two-color ratio pyrometry. The uncertainties were the lowest for spectral fitting using all detection channels and the highest for the two-color ratio using the two longest detection wavelengths (i.e., 684 and 800 nm). Spectral fitting using more than two detection channels improved the robustness of the temperature determination by reducing the uncertainty significantly and are thus recommended. However, additional aspects that can affect the analysis need to be considered such as polydispersity, non-uniform particle heating, and wavelength-dependent optical properties.

6 LIISim – A MODULAR SIGNAL PROCESSING TOOLBOX FOR LASER-INDUCED INCANDESCENCE MEASUREMENTS

The content of this chapter was published in Applied Physics B:

R. Mansmann, T. Terheiden, P. Schmidt, J. Menser, T. Dreier, T. Endres, C. Schulz,
“LIISim: a modular signal processing toolbox for laser-induced incandescence measurements”. *Appl. Phys. B* **124**(4), p. 69 (2018).

© Springer-Verlag GmbH Germany, part of Springer Nature 2018. Reprinted with permission.

For this paper, I designed the software concept and the main software architecture, managed the software development project, implemented the numerical algorithms and LII models, performed the validation experiments and wrote the manuscript. In the programming of the software, I was assisted by Tobias Terheiden and Philip Schmidt. Jan Menser contributed to the discussion of the software concept and the user interface. Thomas Dreier, Torsten Endres, and Christof Schulz provided feedback for the software concept and contributed to the manuscript.

Abstract

Evaluation of measurement data for laser-induced incandescence (LII) is a complex process, which involves many processing steps starting with import of data in various formats from the oscilloscope, signal processing for converting the raw signals to calibrated signals, application of models for spectroscopy/heat transfer and finally visualization, comparison, and extraction of data. We developed a software tool for the LII community that helps to evaluate, exchange, and compare measurement data among research groups and facilitate the application of this technique by providing powerful tools for signal processing, data analysis, and visualization of experimental results. A common file format for experimental data and settings simplifies inter-laboratory comparisons. It can be further used to establish a public measurement database for standardized flames or other soot/synthetic nanoparticle sources. The open-source concept and public access to the software development should encourage other scientists to validate and further improve the implemented algorithms and thus contribute to the project. In this paper, we present the structure of the LIISim software including the materials database concept, signal-processing algorithms, and the implemented models for spectroscopy and heat transfer. With two application cases, we show the operation of the software how data can be analyzed and evaluated.

6.1 Introduction

6.1.1 Laser-induced incandescence

Laser-induced incandescence (LII) is well-established for *in situ* measurements of gas-borne soot particles [2, 3, 142], which is also used in an increasing number of applications for the investigation of gas-borne inorganic nanoparticles [12, 13, 40, 82-84, 116, 121, 124, 143]. In LII, particles are heated by a pulsed laser to incandescent temperatures (i.e., higher than 2000 K). The magnitude of the incandescence at a given heat-up temperature scales with the particle volume fraction in the detection volume and the temporal variation of the particle temperature during cooling can be exploited to derive information about the particle size (as small particles cool more quickly than larger ones). The latter approach is commonly called time-resolved LII (TiRe-LII). Both the integral signal intensity and the temporal decay strongly depend on the heat-up temperature of the particles as well as the temperature of the bath gas. The temperature of the laser-heated particles is commonly determined by pyrometry. Often, two-color pyrometry is used based on the time-resolved signal measured with two fast photomultipliers [9, 144, 176] assuming black- or grey-body characteristics of the particles. If more than two detection wavelengths are available (either through the combination of more than two detectors with respective bandpass filters [11, 149] or through detection with spectrometers and streak-camera systems [11-13, 49]), the measured intensities can be related to spectroscopic models that can incorporate a more complex spectral response.

6.1.2 Models

In LII history, model development is an ongoing process and many research groups have been using their own models. It is a common practice to relate the measured (electrical) signal from a fast detector to another physical quantity using a model that describes the signal generation and detection based on physical principles. This “spectroscopic model” usually consists of a temperature-dependent equation derived from Planck’s law corrected for deviation from blackbody behavior, which relates the measured signal to a temperature. In the early stage of LII, only the normalized signal of a single channel was related to that equation and the absorption of laser energy was used to estimate the LII peak temperature [18]. Later, two detectors were used to increase the robustness of the measurements using two-color pyrometry for the determination of the LII peak temperature [9, 101] or the complete temperature trace [40]. Most recent studies use three or more detectors [11, 149] or streak cameras [12, 13, 176] and apply spectral fitting. The result from the spectroscopic model is usually a temperature trace during and after the laser pulse, which can then be interpreted with a “heat transfer model”. The first effort of model standardization was made in 2007 by ten research groups that published a comparison of their models [19]. All LII models share the same energy- and mass-balance equations, but the submodels describing the heat transfer phenomena and the selected physical properties varied widely.

6.1.3 Software

For the processing of LII signals, usually unpublished source code is used by each research group. They target various purposes. Some software allows familiarizing students and beginning researchers with the complex dependences of LII signals – often with the opportunity to select competing models and submodels. Additionally, there are several in-house codes that are often not published in detail. In a few cases, models (with limited documentation) are incorporated in commercial devices. Within the LII-workshop series (e.g., [146-148]) there has been a continuous effort to provide model data sets to compare the

models in a series of test cases with increasing hierarchy [2, 19]. This led to the desire to make consolidated models available to the entire community. We are aware of two such approaches: (i) The Community Laser-Induced Incandescence Modeling Environment (CLiiME) project, started in 2013, aimed at providing a collaborative model infrastructure for researchers. The concept was based on an agile software development process between scientists and scientific software developers [177, 178]. After the release of the open-source software, different research groups should have been able to extend the CLiiME's functionalities by adding physical models based on new available data. The software is based on FORTRAN and Java; at the time of writing this manuscript, it has not yet been published. (ii) **LIISIM** has been introduced in 2001 as a console application (LIISim 1.5) and has been provided via a web interface (<http://web.liisim.com>) [15]. The console application was written in C and the web interface was based on Perl. Modeling settings and file names for experimental data could be defined in DAT files and after execution of the console application, DAT output files containing the modeling results are created. Later, the console application was extended by a C++ based graphical user interface (GUI) by Tobias Terheiden and Martin Leschowski that allows also the visualization of the modeling results from the DAT files (LIISim Desktop 1.02 and Console 2.14). While the console application was distributed among the community, the desktop version was not published and was only internally used. The software was previously used for soot diagnostics on laminar premixed high-pressure flames [14, 94, 96, 179], on atmospheric pressure laminar non-premixed flames [65] and at Diesel engine conditions [28]. The LIISim web interface has been referenced in recent publications [50, 180].

The new version of LIISim 3.0 presented in this paper, builds on the previous experience but follows a fundamentally different approach: Data analysis in the past has been a static and iterative process starting with modification and execution of processing settings following processing, visualization, interpretation, and extraction of results. The new approach is based on a dynamic evaluation concept using a graphical user interface and modular tools for processing and visualization to get a deeper insight into the data. While in previous versions the processing chain and physical properties were hard-coded, the new concept allows flexible combination and configuration of processing steps within the graphical user interface. Physical properties are now not limited to a single materials system anymore (i.e., soot), but can be provided as any constant or temperature-dependent equation through standardized text files. This allows easy switching between materials systems while keeping the same processing chain. This opens the way for various synthetic nanoparticle applications, such as already available for silicon [13, 124]. Researchers could provide their experimental data from their publications in the LIISim-compatible format including various meta-data (i.e., laser fluence, process pressure, measurement position, etc.). This would be the foundation for a public reference measurement database for standardized flames or synthetic nanoparticle applications, which will simplify the comparison of data and evaluation strategies among research groups. Particularly with regard to the biennial LII workshop, the LIISim format could be used for exchange of data for inter-laboratory comparisons. The new LIISim source code is published under the GNU General Public License (GPL) to provide transparency in all implemented algorithms and allows other researchers to review and modify the source code or add new heat-transfer models.

In this paper, the new LIISim software is presented and its application is demonstrated by two test cases. First, we discuss the implemented spectroscopic and heat transfer models, then the software architecture, data structure, and materials database concept are explained. After describing the main modules for signal processing, data analysis and fitting, we show some of the functionalities by using a published validation data set [11] and recently measured data using a standardized laminar diffusion flame.

6.2 Models implemented in LIISim

Signal processing of experimental LII data can be separated in three consecutive steps: (i) basic signal processing (i.e., baseline correction, calibration, simple arithmetics, etc.); (ii) spectroscopic modeling for calculation of temperature trace from signal data, and (iii) heat transfer modeling for fitting modeled temperature traces to the experimentally determined temperature traces.

6.2.1 Spectroscopic models

For the calculation of temperature traces, two methods are implemented in LIISim: two-color pyrometry and spectral fitting of Planck's law. The two-color pyrometry is commonly used in recent studies [9, 40, 41, 101] and requires calibrated LII signals at two independent wavelengths:

$$T_p = \frac{h c_0}{k_B} \left(\frac{1}{\lambda_2} - \frac{1}{\lambda_1} \right) \left[\ln \left(\frac{I_\lambda(\lambda_1, T_p)}{I_\lambda(\lambda_2, T_p)} \frac{E(\mathbf{m}_{\lambda_2})}{E(\mathbf{m}_{\lambda_1})} \left(\frac{\lambda_1}{\lambda_2} \right)^6 \right) \right]^{-1}, \quad (6-1)$$

where T_p is the particle temperature, h the Planck's constant, c_0 the speed of light in vacuum, k_B the Boltzmann constant, λ_i the bandpass center-wavelength of the detector, I_λ the calibrated intensity, and $E(\mathbf{m}_\lambda)$ the absorption function. It needs to be noted that this formula is derived using the Wien approximation and differentiates in this aspect from a spectral fitting.

When two or more spectral detection channels are available, a spectral fit including all channels can be performed. For this analysis, Planck's law corrected for deviation from blackbody behavior is fitted to the data points of all selected channels. A detailed description of the equation can be found in [167]:

$$I_\lambda(\lambda, T_p) = f_V G_\lambda C_{\lambda, \text{abs}} \frac{2hc_0^2}{\lambda^5} \left[\exp \left(\frac{h c_0}{k_B \lambda T_p} \right) - 1 \right]^{-1}, \quad (6-2)$$

where f_V is the volume fraction during the given laser shot, G_λ scales the emitted intensity based on the geometry and optical efficiencies of the detector, and $C_{\lambda, \text{abs}}$ is the wavelength-dependent absorption cross-section given by the Rayleigh limit of Mie theory [44]

$$C_{\lambda, \text{abs}}(d_p) = \frac{\pi^2}{4} \frac{d_p^3}{\lambda} E(\mathbf{m}_\lambda). \quad (6-3)$$

In LIISim, wavelength-independent properties of equation (6-2) and (6-3) are summarized in a general scaling factor C , which simplifies equation (6-2) to:

$$I_\lambda(\lambda, T_p) = C \frac{E(\mathbf{m}_\lambda)}{\lambda} \frac{2hc_0^2}{\lambda^5} \left[\exp \left(\frac{h c_0}{k_B \lambda T_p} \right) - 1 \right]^{-1}. \quad (6-4)$$

6.2.2 Heat transfer models

The LII technique is based on particle heating by a pulsed laser and the investigation of the subsequent energy transfer to the surroundings. The energy transfer rates depend on the particle size and can be incorporated in heat transfer models. The particle diameter can then be used as a fitting parameter and the residual between the simulated and the measured temperature decay is minimized in a least-squares fitting algorithm.

For determination of particle sizes, various heat transfer models from literature are implemented that share the same equations for the energy- and mass balance. The individual heat transfer rates from published models are described in Appendix D. For the description of particle cooling, the following energy balance is used:

$$\frac{d}{dt}(m_p c_p T_p) = -\dot{Q}_{\text{evap}} - \dot{Q}_{\text{cond}} - \dot{Q}_{\text{rad}}, \quad (6-5)$$

where m_p is the particle mass, c_p the specific heat capacity, and T_p the particle temperature. \dot{Q}_{evap} , \dot{Q}_{cond} , and \dot{Q}_{rad} represent cooling rates for evaporation, heat conduction, and radiation, respectively. These cooling rates are re-implemented in each individual heat transfer model. It needs to be noted that the LIISim energy balance is limited to particle cooling and does not include heat transfer by laser absorption. The mass balance is simplified to

$$\frac{d m_p}{dt} = -\dot{m}_{\text{evap}}, \quad (6-6)$$

which includes only \dot{m}_{evap} , the mass loss due to evaporation, which is also re-implemented in the individual heat transfer models. Michelsen *et al.* [19] summarized different heat transfer models and the physical properties used by various research groups. The following models from this publication are implemented: “Kock”, “Liu” and “Melton (workshop)”. A detailed description of the implemented models and the corresponding physical properties can be found in Appendix D.

6.3 Implementation

6.3.1 Software architecture

The LIISim software is written in object-oriented C++ using the Qt-framework (5.5.0) [181] for the graphical user interface (GUI). For mathematical operations like ordinary differential equation (ODE) stepper and complex data container, the Boost library (1.55) [182] and for visualization of data the Qwt library (6.1.3) [183] was used. The source code can be compiled for 64-bit computer architecture to overcome the 4-GB memory limitation or in case older computers are used for 32-bit architecture. Multi-threading using more than one CPU kernel at a time is implemented for parallel signal processing and fitting, which reduces processing time.

In addition to the C++ software, a model development kit (MDK) was written in MATLAB for comparison and validation of the integrity of the implemented algorithms. For the MDK the same class structure is used and the functionalities are limited to simulation of temperature traces using the previously discussed heat transfer models. The MDK can be used for testing new models before they are integrated in the LIISim framework. The source code of LIISim-MDK can be found on the LIISim project page and is not discussed further.

6.3.2 Data structure

The import of LII signals supports comma-separated values (CSV) or plain text files. File structure and file names are documented within the import tools. For data export, additionally the MATLAB file format can be chosen. The data visualized in every plot can be copied to the clipboard and can so be directly used in any spreadsheet compatible software. Experimental data are stored in a hierarchical data model, which is shown in Figure 6-1.

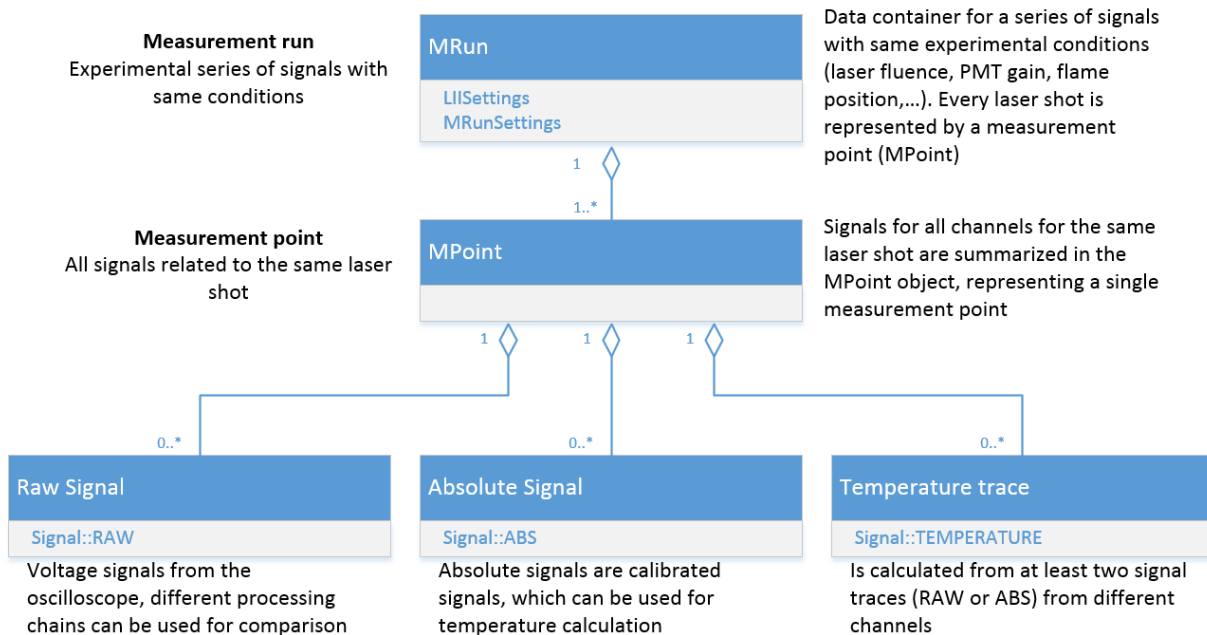


Figure 6-1 Data structure used within the LIISim software.

Three data container classes (i.e., MRun, MPoint, and Signal) connect the single LII signal traces. MRun represents a series of LII signals collected at identical experimental conditions (i.e., laser fluence, PMT gain, flame position, etc.). MPoint stores all signals related to the same laser shot. This means for the same laser shot there could be a “Raw Signal”, a calibrated “Absolute Signal”, and the “Temperature Trace” calculated from the respective signals.

6.3.3 Materials database

Physical properties for materials or gases are usually defined in the source code prior to execution. In LIISim, a modular database approach was chosen that allows to change or to switch properties during runtime. An unlimited number of user-defined database objects (material, gas, gas mixtures, LII settings) can be saved within plain text files that are automatically imported from a database folder. The properties can be defined as constant or as functions of temperature or wavelength according to Table 6-1. The database files can then be selected and combined for heat transfer modeling. The most recent list of available properties and guidelines to create customized property files can be found in the user guide of the respective LIISim version.

6.3.4 Numerical procedures

For data evaluation, the residual between simulated and experimental data is minimized by varying the model parameters using the Levenberg–Marquardt nonlinear least-squares method [184]. The implemented algorithm is loosely based on Numerical Recipes 3rd Edition [185] and is described in detail in Appendix C. All numerical procedures for matrix transformation, integration, solving ordinary differential equations (ODEs) and fitting are summarized in the Numeric Class of the LIISim source code.

Table 6-1 List of available property types and the corresponding temperature- or wavelength-dependent formulae.

LIISim Type	Function	Equation (temperature T , parameter $a_0 \dots a_8$)
const	Constant value	$f(T) = a_0$
case	Piecewise-defined	$f(T) = \begin{cases} a_1, & T \leq a_0 \\ a_2, & T > a_0 \end{cases}$
poly	Polynomial	$f(T) = a_0 + a_1T + a_2T^2 + a_3T^3 + a_4T^4 + a_5T^5 + a_6T^6 + a_7T^7 + a_8T^8$
poly2	Polynomial	$f(T) = a_0 + a_1T + a_2T^2 + a_3T^3 + a_4T^{-1} + a_5T^{-2}$
polycase	Piecewise-defined polynomial	$f(T) = \begin{cases} a_1 + a_2T + a_3T^2 + a_4T^3, & T \leq a_0 \\ a_5 + a_6T + a_7T^2 + a_8T^3, & T > a_0 \end{cases}$
exp	Exponential with Euler number as base	$f(T) = a_0 + a_1 \exp(a_2 + a_3T^{-1} + a_4T)$
expoly	Exponential with polynomial exponent	$f(T) = a_0 + a_1 \exp(a_2 + a_3T + a_4T^2 + a_5T^3 + a_6T^4 + a_7T^5)$
powx	Exponential with parameter as base	$f(T) = a_0 + a_1 a_2^{(a_3 + a_4T^{-1} + a_5T)}$
optics_temp	Wavelength-dependent polynomial provided for each wavelength	$f(\lambda, T) = f(a_0, T) = a_1 + a_2T + a_3T^2 + a_4T^3$
optics_case	Wavelength-dependent piecewise-defined polynomial	$f(\lambda, T) = f(a_0, T) = \begin{cases} a_2, & T \leq a_1 \\ a_3, & T > a_1 \end{cases}$
optics_lambda	Wavelength-dependent polynomial	$f(\lambda) = a_0 + a_1\lambda + a_2\lambda^2 + a_3\lambda^3 + a_4\lambda^4 + a_5\lambda^5 + a_6\lambda^6 + a_7\lambda^7 + a_8\lambda^8$
optics_exp	Wavelength-dependent exponential	$f(\lambda) = a_0 \lambda^{(1-a_1)}$

6.3.5 Modules

The software is structured in four main modules: Database, Signal Processing, Analysis Tools and Fit Tools, which can be accessed through a tab menu. Database visualizes the previously described materials databases and also provides some tools for modifications. Signal Processing is the main module, which allows the processing of raw signals, absolute signals and temperature traces. Analysis Tools provides only visualization functionalities for deeper insight into the processed data and for comparison of multiple measurement runs. Finally, the Fit Tools use the calculated temperature traces for fitting the data to pre-implemented heat transfer models. The graphical user interface for the Signal Processing module is exemplarily shown in Figure 6-2. A detailed description of all functionalities can be found in the user guide.

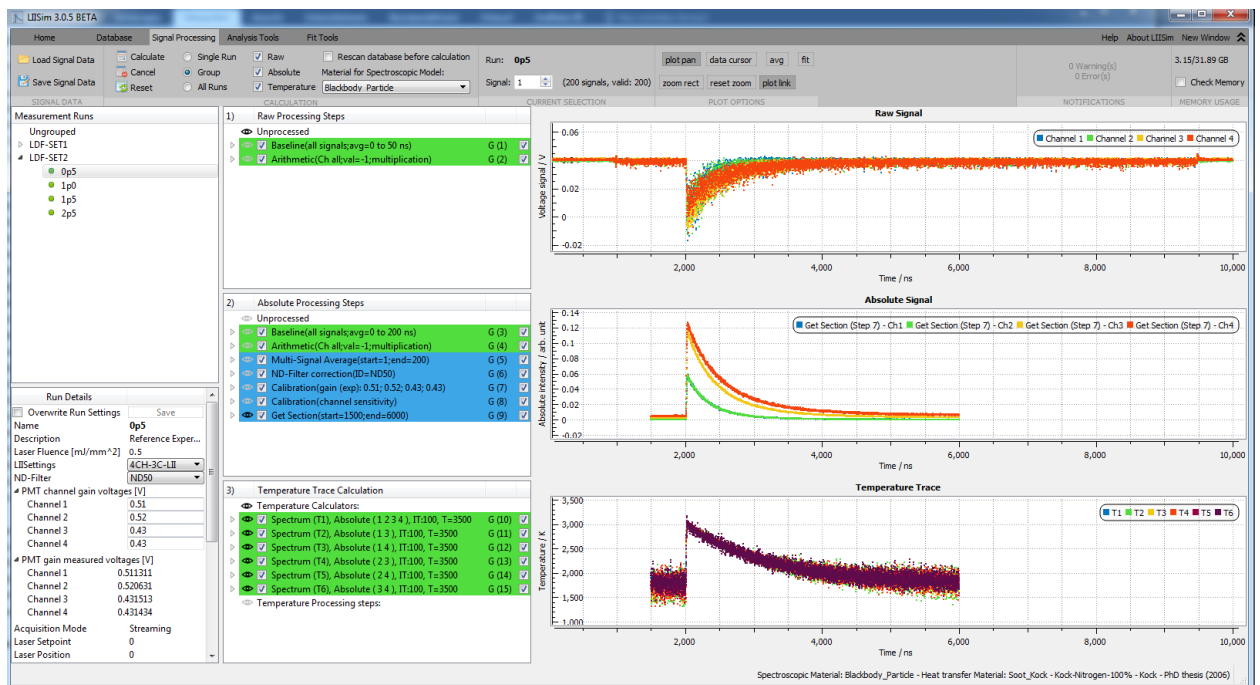


Figure 6-2 Graphical user interface (GUI) for “Signal Processing”.

6.3.5.1 Signal processing

Within the “Signal Processing” module, processing steps can be individually ordered and parameters can be set individually for every measurement run, for a group or globally. This allows the systematic processing of all loaded measurement data. Each signal type (i.e., raw, absolute, temperature) has its own processing chain, which is consecutively executed in the order: raw, absolute, temperature. The following processing plugins are available and can be applied multiple times in a signal processing chain:

- “Baseline” provides two options for signal-offset correction. (i) For gated PMTs: the signal before the gate opening can be used to calculate the offset. This is done by averaging a user-defined signal range and subtract this from the signal. (ii) For ungated PMTs, the baseline offset for each channel can be defined in the LIISettings file. During processing, these values are automatically retrieved and subtracted from the signal trace.
- “Arithmetic” operations (addition, subtraction, multiplication, and division) can be applied on each data point for all or a single channel. Applicable, for example for signal inversion, scaling, offset correction.
- “Normalization” scales the signal according to the signal peak or a user-defined value. The operation can be applied on all or a single channel.
- “Neutral-density (ND) filter correction” uses the transmission values from the current LIISettings according to the selected filter identifier. The identifier can be automatically selected from the measurement run settings file or manually chosen. Each signal trace is divided by the respective filter transmission values.
- “Calibration (gain, channel sensitivity)” takes the channel calibration values for detector gain and sensitivity from the current LIISettings. The gain correction factor y_i for channel i is calculated for “gain (exp)” according to

$$y_i = \exp\left(-A_i \ln\left(\frac{x_i}{x_{i,\text{ref}}}\right)\right), \quad (6-7)$$

and for “gain (log10)” as

$$y_i = 10^{\left(-A_i \log\left(\frac{x_i}{x_{i,\text{ref}}}\right)\right)}, \quad (6-8)$$

where x_i is the channel gain voltage, $x_{i,\text{ref}}$ the gain reference voltage and A_i the gain calibration value for the respective channel. The gain correction factor and channel-sensitivity calibration values are multiplied with the signal traces giving calibrated signal traces.

- “Multi-signal average” calculates an averaged signal from multiple single signals within a measurement run. Subsequent processing steps are then applied only to the averaged signal.

The absolute signal, which is corrected for spectral sensitivity of the detectors, can then be used in the temperature processing chain to calculate temperature traces with the “Two-Color” and “Spectrum” method as described in section 6.2.1. When the “Spectrum” method is used, the fitted spectrum for each iteration and time step can be visualized using the Analysis Tool “Temperature Fit” (see next section).

6.3.5.2 Analysis tools

The analysis tools allow the systematic analysis and comparison of multiple measurement runs. Three tools are available: “Plotter”, “Temperature Fit”, and “Parameter Analysis”. The simplest tool “Plotter” visualizes selected measurement runs and allows comparison of the signal traces.

“Temperature Fit” (Figure 6-3) requires previously calculated temperature traces using the “Spectrum” method in the “TemperatureCalculator”-processing step. This tool allows the comparison of different temperature calculation settings (i.e., spectral fit with various numbers of channels, different initial conditions, or optical properties) and helps making assumptions of the quality of the fitting result or identify any errors within the processing iterations. Figure 6-3 illustrates the GUI with the temperature trace plot (top left) for data point selection, the fitting result at the selected position (top right) and visualization of the fitting iterations with plots (bottom left) and tables (bottom right).

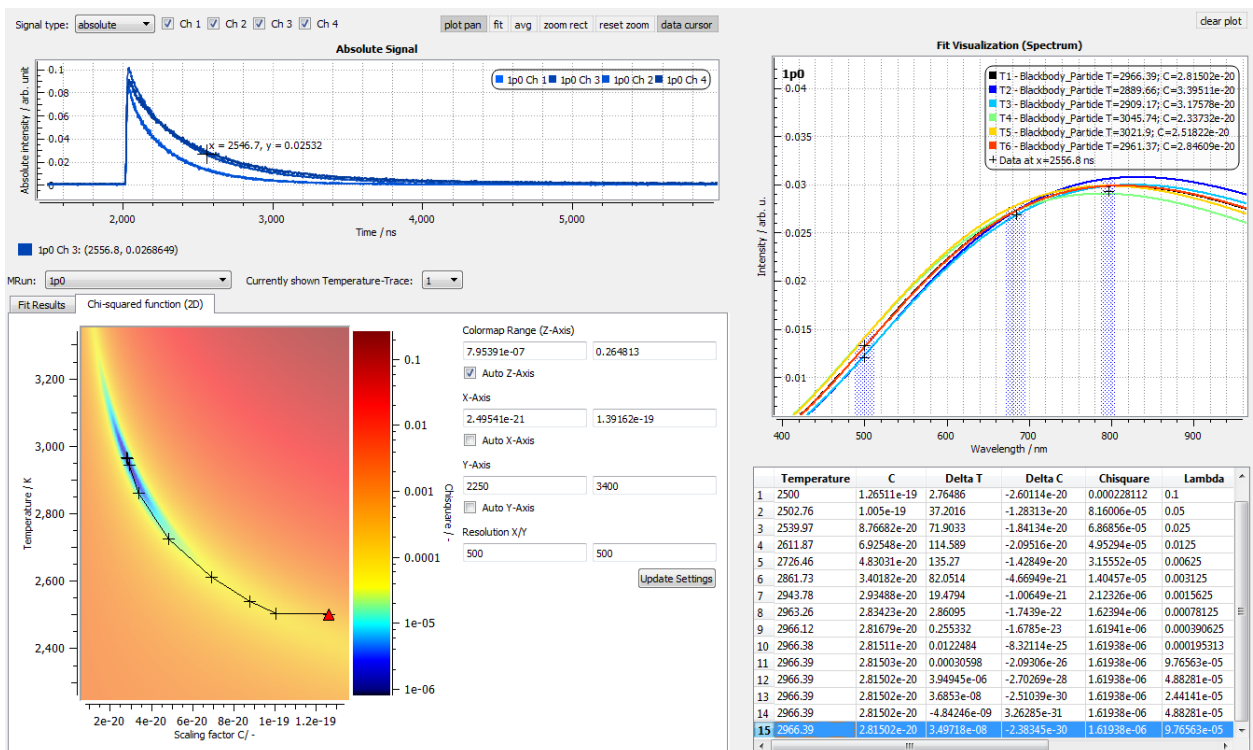


Figure 6-3 GUI for the “Temperature Fit” analysis tool showing the temperature trace and for the selected position, the iterations and the final result of the spectral temperature fit.

For each measurement run, experimental parameters (i.e., laser fluence, ND-filter, PMT gain voltages, etc.) can be stored in the measurement run settings that are accessible in every module. These parameters can be used to compare selected measurement runs in the “Parameter Analysis” tool (Figure 6-4). Available built-in parameters are for example laser fluence, PMT gain, ND-filter, average of signal range, but also user-defined parameters can be added. The GUI shows the signal traces of the selected measurement runs (top left), the experimental parameters curves to be visualized (bottom left) and the result in graphical (top right) and tabular format (bottom right).

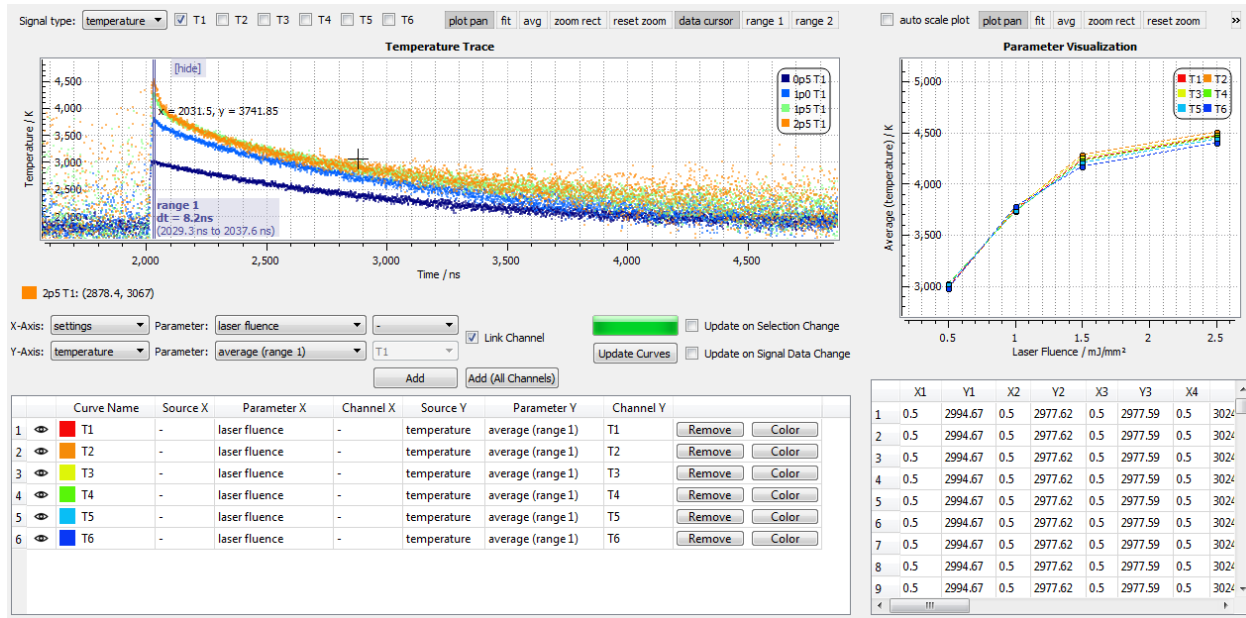


Figure 6-4 GUI for the “Parameter Analysis” tool showing multiple measurement runs with varying laser fluence.

6.3.5.3 Fit tools

After signal processing and analysis of the temperature traces, pre-implemented heat transfer models and materials databases can be used to perform a fit to the data. For this, temperature traces or sections of temperature traces can be selected as data range for the fit. Three fit parameters (i.e., initial particle diameter, gas temperature, and peak temperature) can be set as free or fixed parameters. For solving the ordinary differential equation (ODE) of the selected heat transfer model, the type of ODE solver and the accuracy can be selected. The result of the fit and each iteration can be analyzed using various plots (i.e., heat transfer rates, particle diameter history, fit error, etc.). The GUI of the “Fit Creator” (Figure 6-5) shows the data to be fitted (top left), settings for the fitting (top right), and an overview of the meta data for the performed fitting runs (bottom right). The experimental temperature trace is overlaid with the modeled temperature trace (bottom left). Additional plots provide information about the temporally resolved heat transfer rates, particle size, and fitting parameter changes during the fitting iterations.

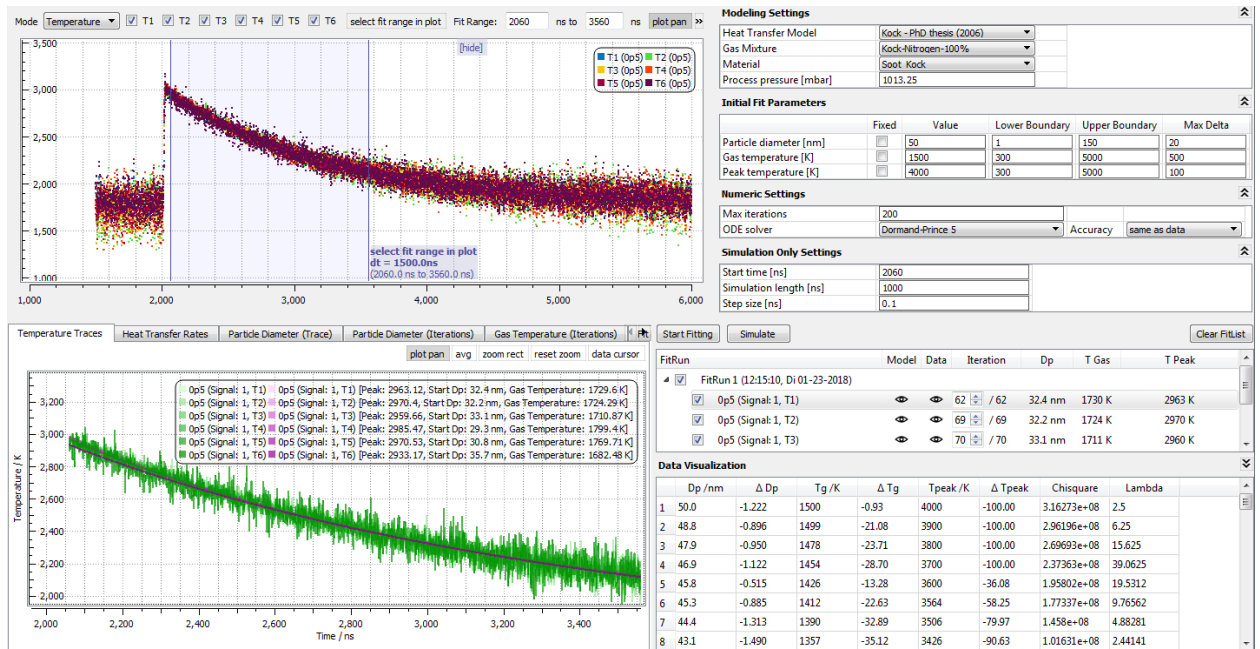


Figure 6-5 GUI for the “Fit Creator” tool showing fits for multiple temperature traces.

6.4 Application cases

Two example cases are used to demonstrate the main functionalities of LIISim. First, the recently published validation dataset by Goulay *et al.* [11] and second, recently collected own unpublished data using the same apparatus as in [149] on a standardized laminar diffusion flame [171]. Both data sets are available online as electronic supplementary material and can be imported within LIISim as benchmark data (for details refer to the user guide on www.liisim.com). For both application cases, the materials database combinations as summarized in Table 6-2 were used.

Table 6-2 Materials database combinations used for the simulations.

	Model 1	Model 2	Model 3
Heat transfer model	Kock	Liu	Melton
Gas mixture	Kock-Nitrogen-100%	Liu-Flame	Melton-Nitrogen-100%
Material	Soot_Kock	Soot_Liu	Soot_Melton (Workshop)

6.4.1 Application 1

We selected the three-channel LII dataset for the Santoro burner [23] provided by Goulay *et al.* [11] to visualize the spectral fitting and heat transfer modeling. The signals are collected at center wavelengths of 451, 682, and 855 nm. The wavelength information is stored in the LIISettings file and is automatically used during analysis. Basic signal processing was not necessary, because the data have already been corrected for background, PMT sensitivity, and neutral-density filter characteristics. To overcome fitting convergence difficulties the data were scaled by a factor of 10^9 . The imported signal traces for a laser fluence of 0.986 mJ/mm^2 and an excitation wavelength of 1064 nm are shown in Figure 6-6.

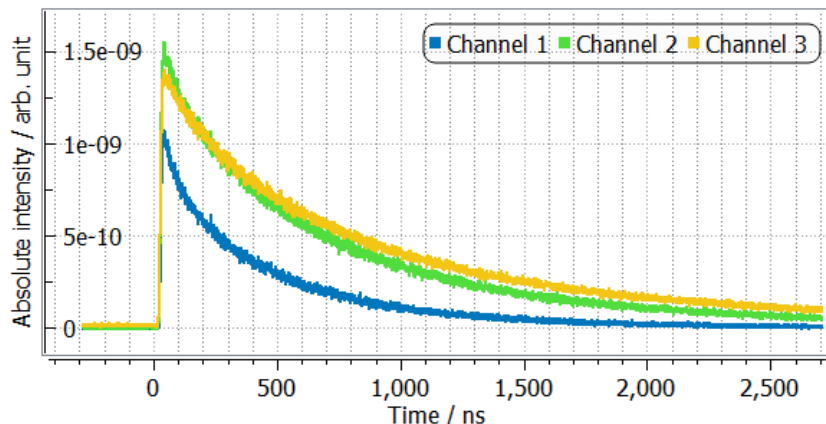


Figure 6-6 Original LII signal traces for three spectral detection channels at a laser fluence of 0.986 mJ/mm^2 (1064 nm).

For the temperature calculation, spectral fits according to equation (6-4) have been performed using the absorption function $E(\mathbf{m}_\lambda)$ suggested by the original publication

$$E(\mathbf{m}_\lambda) = \frac{\lambda^{1-\xi}\beta}{6\pi}, \quad (6-9)$$

which simplifies with the provided values of $\xi = 0.83$ and $\beta = 28.72 \text{ cm}^{-0.17}$ to

$$E(\mathbf{m}_\lambda) = a_0\lambda^{a_1}, \quad (6-10)$$

with $a_0 = 3.333 \text{ m}^{-0.17}$ and $a_1 = 0.17$ and λ in meter. These two parameters are then used within the “optics_exp” equation type (see Table 6-1) through the spectroscopic materials database file.

In a multi-wavelength measurement, temperatures can be derived from various combinations of two (or three) spectral detection channels. If the spectroscopic model is correct and no measurement errors are present, all combinations should lead to the same result. For this dataset, four different temperature traces (T1–T4) have been investigated. The LII signal channels used for the analysis are shown in Table 6-3:

Table 6-3 LII-signal channels used for the calculation of the temperature traces.

Temperature trace	Channel 1 (445 nm)	Channel 2 (682 nm)	Channel 3 (855 nm)
T 1	x	x	x
T 2	x	x	
T 3	x		x
T 4		x	x

After processing, the temperature traces are compared in the same plot. Figure 6-7 shows the calculated temperature traces using the “Spectrum” mode, which reveals some disagreement within the first microsecond after the laser pulse. For further investigation, the analysis tools can be used on the temperature fit to look into the single iteration steps during temperature fitting.

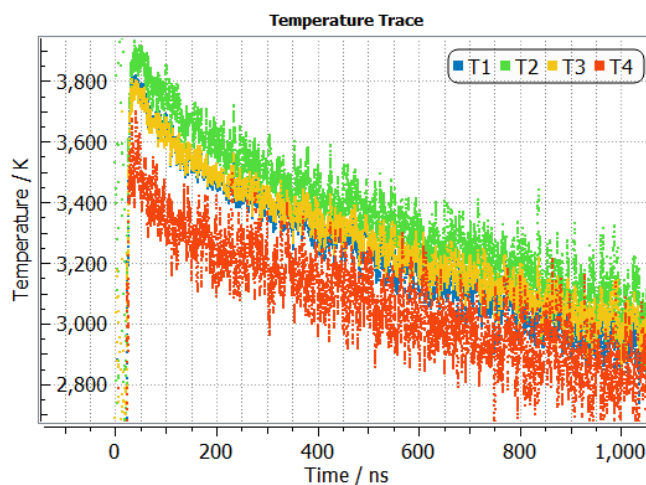


Figure 6-7 Temperature traces calculated using the “Spectrum” method.

In the “Temperature Fit” tool, single data points can be picked from the signal to visualize the fitted temperature spectrum for all four temperature traces (Figure 6-8). It can be seen that for example at 60 ns the solution of the spectral fits approximately matches the data from the selected signal channels, but the temperatures vary from 3527 to 3797 K for different temperature traces (T1–T4). Possible reasons for this discrepancy could be non-linearity affecting one or more of the three channels as demonstrated in [149] or the change of optical properties during particle cooling. To trace down the cause of this effect, further measurements using the same setup would be required.

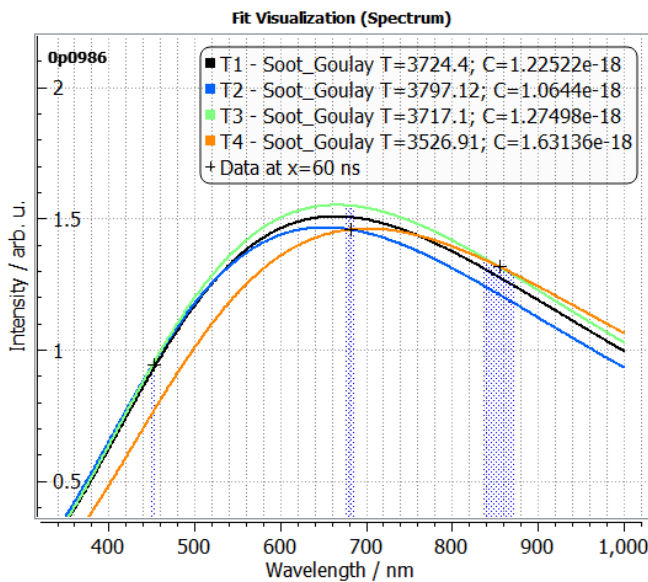


Figure 6-8 Fit for different channel combinations T1–T4 at 60 ns.

For presentation of the particle-sizing feature, we use temperature trace T1 in the FitCreator module, for comparison of selected heat transfer models (Kock, Liu and Melton [19]). For the fitting, the process pressure was set to 1.013 bar (1 atm) and the gas temperature to 1676 K according to the original publication. The range for the fit was set from 60 to 1560 ns and the ODE solver “Dormand-Prince 5” was used (accuracy same as data) [186]. The initial particle diameter and the peak temperature are free parameters and the gas temperature was kept constant. For comparison, the same procedure was applied to the 0.495 mJ/mm² data. The simulated temperature traces for each heat transfer model and the fitting results are displayed in Figure 6-9.

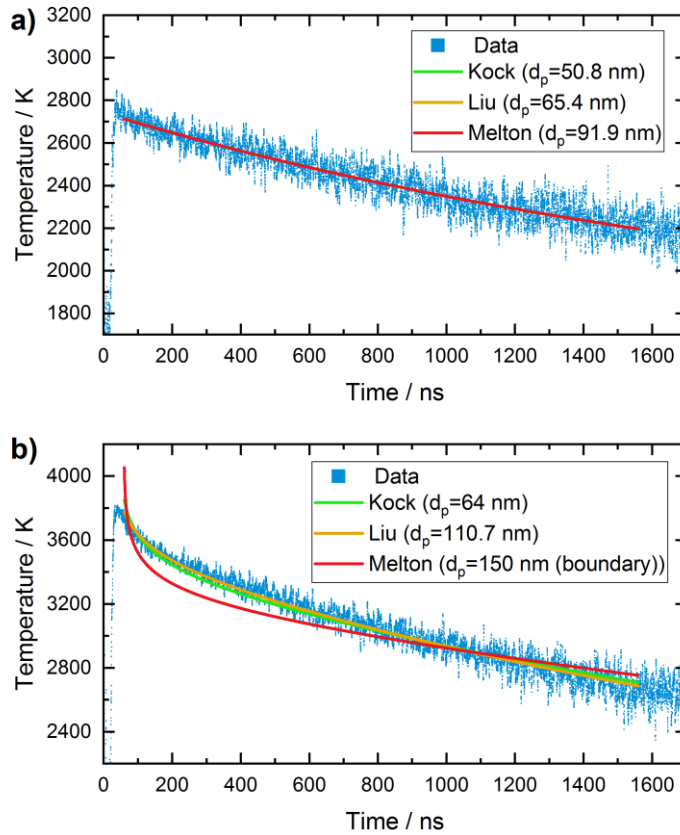


Figure 6-9 Comparison of fitting results from three heat transfer models (range 60 to 1560 ns) for 0.495 mJ/mm^2 (a) and 0.986 mJ/mm^2 (b).

The three modeled traces for the low fluence data (0.495 mJ/mm^2) fit the measured data, but gave initial particle sizes much higher than previously reported values of 33 nm [2]. For the 0.986 mJ/mm^2 data, the Melton model predicted higher values for the particle diameter as the LIISim upper boundary value of 150 nm. This upper boundary should ensure that the range of validity of the physical equations is not exceeded. The fitted values for the particle diameter using the other two pre-implemented models differ also widely from previously reported values. To our knowledge, the only publication using this validation data set for model development was Lemaire and Mobtil [59], who stated they could not find any agreement between their modeled data and the validation data set. With further publications of LII data on this particular flame, data from different groups could be compared to investigate the origin of these discrepancies. This helps to distinguish whether this effect is dependent on the specific experiment or the implemented models.

6.4.2 Application 2

Data have been collected using a four-channel LII device with bandpass center-wavelengths at 500, 684, and 797 nm. A detailed description of the detection device can be found in [149]. A laminar non-premixed flame (Gülder burner), which has been investigated by TiRe-LII previously [2, 9, 151], was operated at its standard conditions of 0.194 slm (standard liters per minute) ethene and 284 slm air and the soot particles are heated by pulses (8 ns FWHM) from an Nd:YAG laser at 1064 nm with a fluence of 0.5 and 1 mJ/mm². Raw LII signals are collected for 200 laser shots and then processed using the following processing chain to generate calibrated averaged signal traces:

1. Baseline correction (using the signal detected before the PMT gate opening averaged for 200 ns)
2. Arithmetic multiplication with -1 for inversion of the signal trace
3. Multi-signal average
4. ND-filter correction
5. Calibration (PMT gain)
6. Calibration (channel sensitivity)
7. Get section (1500 to 6000 ns).

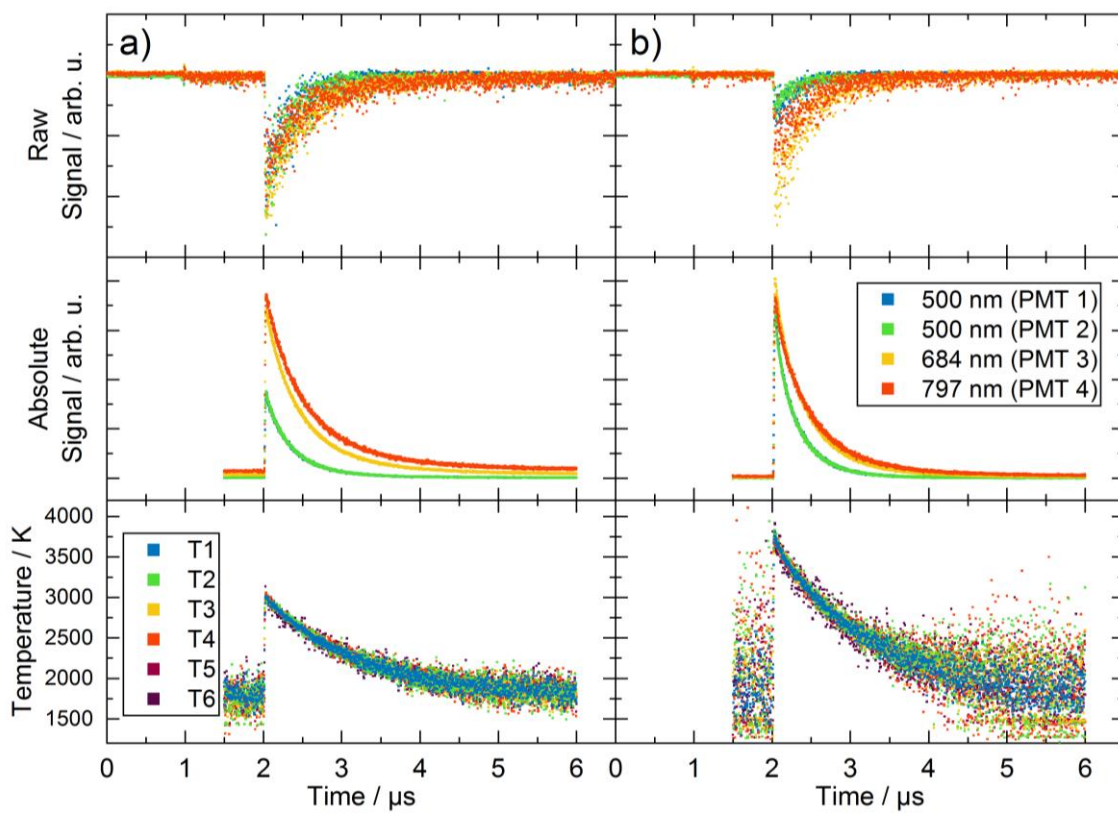


Figure 6-10 Raw LII signals (single shot) collected from the oscilloscope (top row), calibrated and averaged signals (center row), calculated temperature traces from calibrated signals (bottom row) for 0.5 mJ/mm² (a) and 1 mJ/mm² (b).

After signal processing, the calibrated and averaged signals (Figure 6-10 center row) can be used within the temperature processing chain to calculate temperature traces (Figure 6-10 bottom row).

With four available channels at three different wavelengths one temperature trace (T1) was calculated using a spectral fit of all four channels, and for comparison with two-color pyrometry, five temperature traces (T2–T6) were calculated using all possible pairs at independent wavelengths according to Table 6-4. For this analysis, a constant $E(m_\lambda)$ value was used for all channels (using the spectroscopic materials data “Blackbody_Particle”).

Table 6-4 LII signal channels used for the calculation of the temperature traces.

Temperature trace	Channel 1 (500 nm)	Channel 2 (500 nm)	Channel 3 (684 nm)	Channel 4 (797 nm)
T 1	x	x	x	x
T 2	x		x	
T 3	x			x
T 4		x	x	
T 5		x		x
T 6			x	x

Figure 6-10 (bottom row) shows the result of the temperature processing for all six temperature traces, which show good agreement. The spectral fit at 2060 ns was visualized using the temperature fit tool (see Figure 6-11) giving temperatures between 2901 and 2945 K for 0.5 mJ/mm² and between 3637 and 3680 K for 1 mJ/mm².

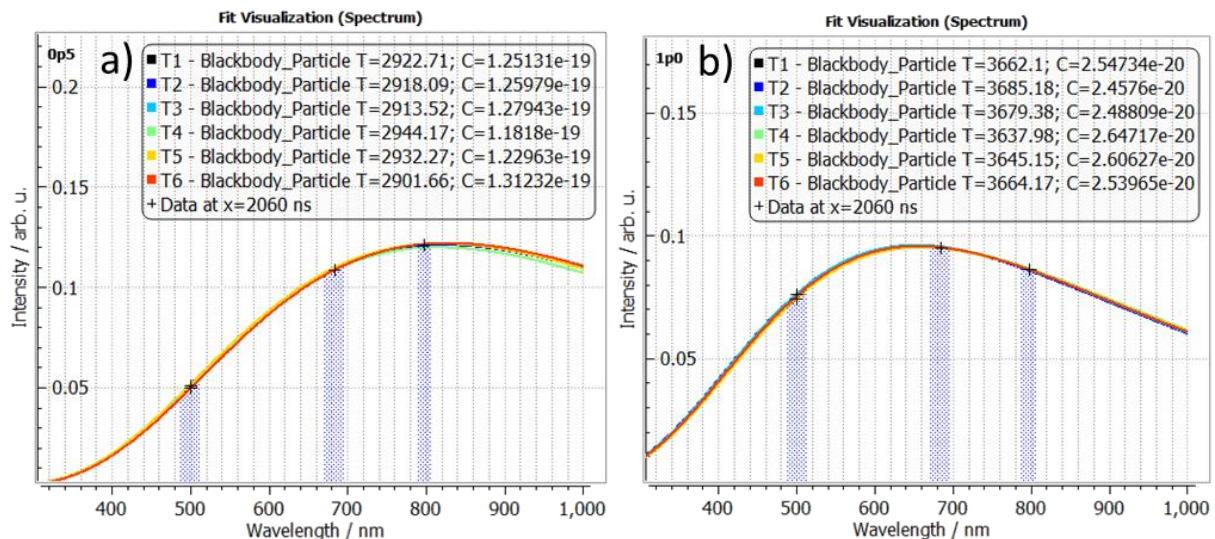


Figure 6-11 Fit for channel combinations T1–T6 at 2060 ns for 0.5 mJ/mm² (a) and 1 mJ/mm² (b).

The same settings as in Application 1 were used except for the gas temperature, which was reported for this laminar diffusion flame as 1730 K [187]. For evaluation, a 1.5- μ s range was selected starting 30 ns after the signal peak to avoid interference with the signal variation during laser heating. The comparison of the fitting results is summarized in Figure 6-12.

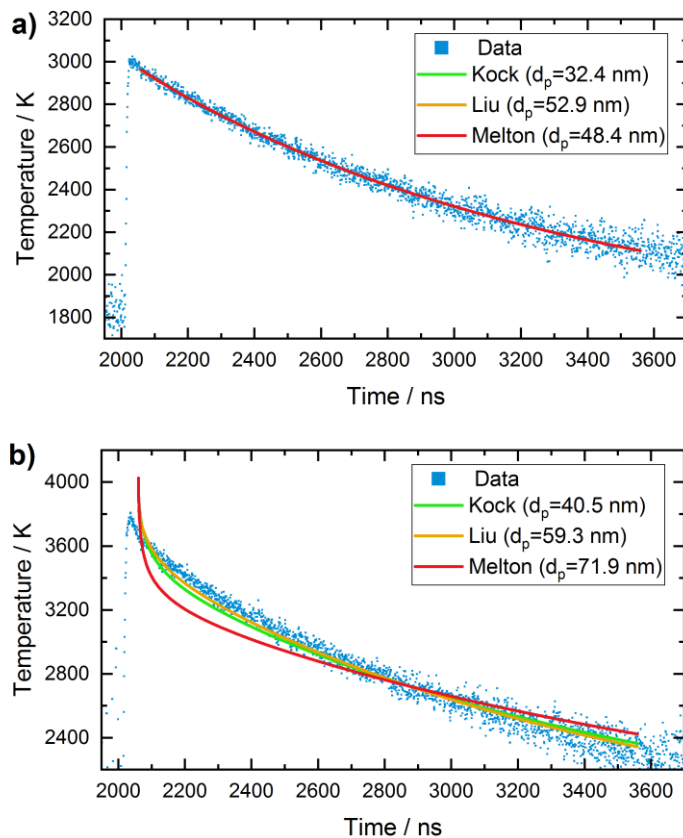


Figure 6-12 Comparison of fitting results from three heat transfer models (2060 to 3560 ns) for 0.5 mJ/mm² (a) and 1 mJ/mm² (b).

All fits for the low fluence of 0.5 mJ/mm² show a good agreement between modeled and calculated temperatures traces and initial particle sizes from the Kock model agree with previously reported values of 29 to 32 nm using LII and TEM [2]. The Liu and Melton model yielded higher particle sizes of 52.9 and 48.4 nm, respectively. For the 1 mJ/mm² fits, the modeled temperature trace shows a much steeper gradient in the beginning of the signal, which indicates over-prediction of the evaporation cooling. Comparison with measurements of the same flame from other groups could help to trace down, whether this is a LII model problem or related to the specific experimental setup.

6.5 Software availability and documentation

As the new LIISim version is a complete rebuild, we want to avoid confusion with earlier LIISim versions and have chosen the version number 3.0 for the first release. For tracking changes of the source code, we are using the public version-control service GitHub (www.github.com/LIISim). Documentation, software releases and further announcements are available through www.liisim.com.

6.6 Summary

The new LIISim is the first open and public software toolbox for signal processing and data analysis of laser-induced incandescence measurement data. It was designed to be user-friendly, freely available for the scientific community, with transparent algorithms and versatile tools for data processing and evaluation. The software targets newcomers in the LII technique, but also experienced researchers who want to compare their signal processing procedures to an open standard. The toolbox provides an easy entrance in this measurement technique with simple and transparent algorithms, built-in example databases and pre-implemented published heat transfer models. Modular materials databases in a standardized file format allow switching physical properties without changing the processing algorithms and allow applications of both, soot and synthetic nanoparticle sources. A common file format can act as a foundation for public reference measurement databases for standardized flames and synthetic nanoparticle source and should enable future inter-laboratory comparison studies in the context of the biennial LII workshop. The source code of the software is published under the GNU General Public License (GPL) to allow further development by all interested researchers within the scientific community.

7 SEQUENTIAL SIGNAL DETECTION FOR HIGH DYNAMIC RANGE TIME-RESOLVED LASER-INDUCED INCANDESCENCE

The content of this chapter was published in Optics Express:

R. Mansmann, K. Thomson, G. Smallwood, T. Dreier, C. Schulz, "Sequential signal detection for high dynamic range time-resolved laser-induced incandescence". Opt. Express **25**(3), p. 2413 (2017).

© 2017 Optical Society of America. Reprinted with permission.

The paper is based on an idea that has occurred to me during my 2014 research visit at the National Research Council of Canada. I was working in the Black Carbon Metrology group lead by Kevin Thompson on a soot LII project using a multi-color LII device with gated photomultiplier tubes. I developed the measurement concept and the methodology, performed the validation experiments and wrote the manuscript. All authors discussed the results and contributed to the manuscript.

Abstract

A new method for collecting time-resolved laser-induced incandescence (TiRe-LII) signals with high dynamic range is presented. Gated photomultiplier tubes (PMT) are used to detect temporal sections of the LII signal. This helps to overcome the limitations of PMTs caused by restricted maximum signal current at the strong initial signal and poor signal-to-noise ratios when the signal intensity approaches the noise level. We present a simple method for increasing the accuracy of two-color pyrometry at later decay times and two advanced strategies for getting high accuracy over the complete temperature trace or even achieve single-shot capability with high dynamic range. Validation measurements in a standardized flame show that the method is sensitive enough to even resolve the local increase in gas temperature as a consequence of heating the soot particles with a laser pulse.

7.1 Introduction

Time-resolved laser-induced incandescence (TiRe-LII) is a well-established *in situ* measurement method for soot particle concentration and primary particle-sizes [3, 18, 176]. Two-color (2C) pyrometry is frequently used for detecting the particle temperature by measuring the ratio of LII signals in two wavelength bands [3, 36, 41, 128, 176]. The signal-to-noise ratio (SNR) of LII measurements strongly decreases with signal duration because of the exponential decay of the signal intensity following the initial heat-up of the gas-borne particles with a pulsed laser. For fast decaying LII signals (e.g., very small particles, elevated pressure, large differences between particle peak temperature and local gas temperature) the dynamic range of the detection system is important for retrieving a temperature trace that can be used for comparison with LII models.

Figure 7-1 gives an example of the strongly varying temperature results at the end of the signal decay period due to low signal levels (middle) and the deviation from a double exponential fit (bottom). The temperature trace was calculated from averaged LII signals (top) over 100 laser shots, further averaging does not provide significant improvement. Analog digital converter (ADC) quantization resolution for 8 bit and 12 bit is indicated for the 800 nm and 500 nm channels, respectively, to demonstrate the limits for single-shot acquisition.

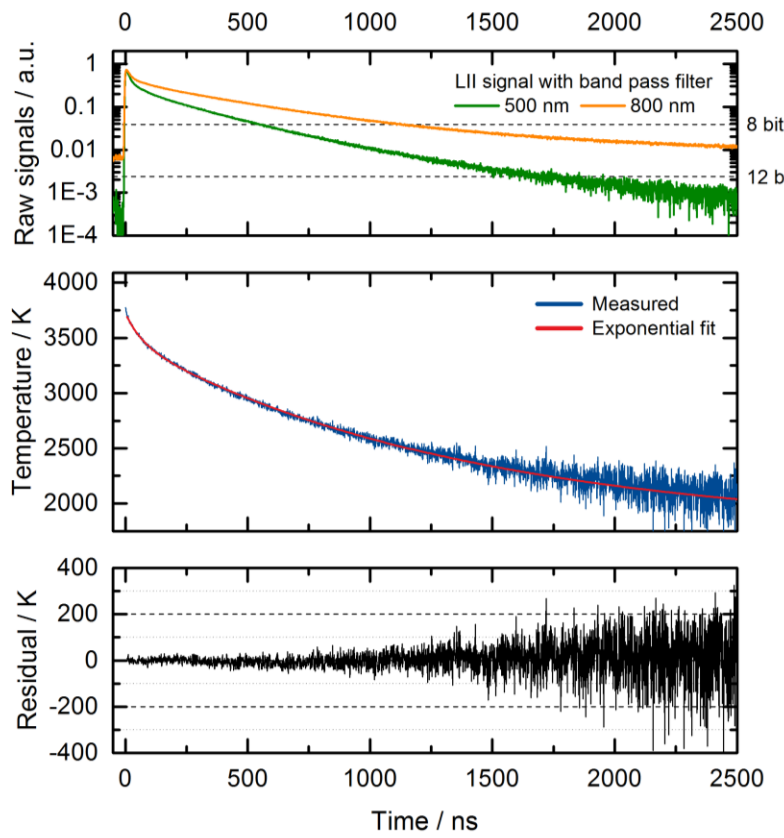


Figure 7-1 Example for a typical temperature trace of LII in-flame measurements starting from the signal peak. Temperatures (blue) are calculated from the ratio of two LII signals in two different wavelength ranges (orange/green) using a relative channel calibration, double exponential regression (red) and the residual between fit and measured data (black).

In TiRe-LII, signals are detected with fast photomultiplier tubes (PMTs, typically < 1 ns response time). The dynamic range relevant in this application needs to be distinguished between the dynamic range for a fixed detector setting and the total dynamic range of the LII setup with detector settings adjusted to the respective signal levels.

When measuring LII signals, the signal peak represents the upper limit of the dynamic range. Due to non-linear behavior and saturation effects, the maximum PMT anode current needs to be limited at this maximum signal value. This can be achieved by attenuation of light by appropriate neutral density filters and adjustment of the PMT gain control voltage.

The lower limit of the dynamic range is the vertical resolution of the analog digital converter of the oscilloscope. As a result, the decreasing signal-to-noise ratio during the (approximately exponential) signal decay limits the detection time despite the fact that the signal intensity at later times is still on a level that could be detected with PMTs. The PMT gain control voltage, however, requires a settling time of 100 ms to 2 s (specified by the manufacturer) and thus cannot be adjusted to the varying signal level during a single signal trace; the same applies for the neutral density filter.

Thus, in the conventional arrangement, only a fraction of the total dynamic range of PMTs can be used. Here, we show that the combination of gated photomultipliers with switching of neutral density filters and gain voltage variation allows one to overcome this limitation, and thus dramatically improve the quality of TiRe-LII measurements.

Tosi *et al.* [188] presented a method to increase the dynamic range in time-correlated single-photon counting (TCSPC) with time-gated single-photon avalanche diodes (SPAD). There, delayed gating of the SPAD was used to prevent the detection of unwanted photons in the initial part of the signal trace thus prolonging the signal recording to later times. There is a fundamental difference compared to the intensity-based measurements presented in the present paper. Single-photon counting techniques rely on high repetition frequencies and large numbers of samples and can work with ultra-low laser powers. LII in contrast requires a minimum laser fluence in the range of 0.5 to 1 mJ/mm² to generate measurable signals and has a long signal lifetime in the range of up to several microseconds. LII is thus not suitable for the high-repetition-rate lasers usually used for TCSPC.

7.2 Method

Gated photomultiplier tubes (PMT) can be triggered with variable delay with respect to the laser pulse to discard the high-intensity portion of the LII signal trace. The low-intensity portion of the signal can then be measured with reduced or no optical signal attenuation and at increased gain, resulting in dramatically increased SNR. The various sections of the LII signal can thus be measured taking advantage of the full dynamic range of the LII setup.

Figure 7-2 (left) illustrates the method starting from the typical LII signal (trace a). From trace b to d (i.e., 2nd to 4th sequence), the PMT gate delay is increased by 500 ns increments and therefore the initial part of the LII signal is suppressed. For each sequence, appropriate neutral density (ND) filters are selected and the gain is adjusted to ensure similar peak signal intensities at the beginning of each signal trace to maximize the SNR. Additional delays can be used until optical signal attenuation is not required anymore and the PMT gain cannot be further increased. The absolute signals (Figure 7-2, right) can then be calculated for each sequence using an absolute light-intensity calibration and gain correction [9]. With this approach, called high-dynamic range TiRe-LII (or HDR-TiRe-LII), the LII signal is detected in multiple segments resulting in a much improved signal quality (Figure 7-2, right).

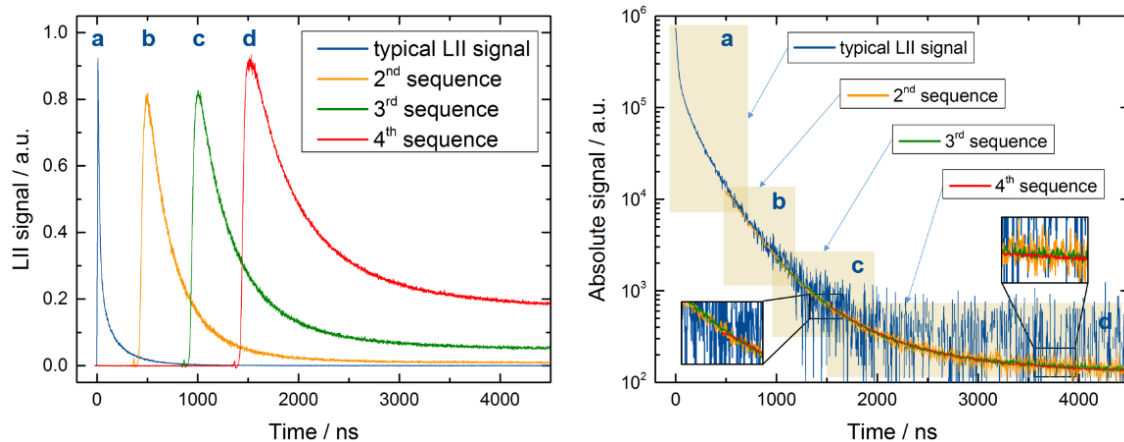


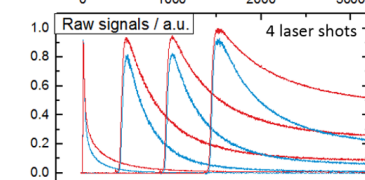
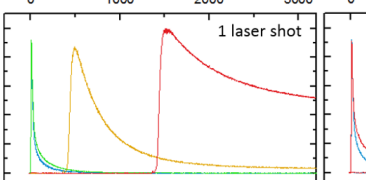
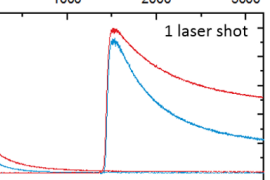
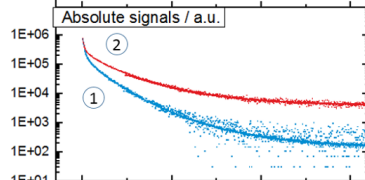
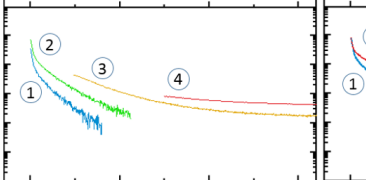
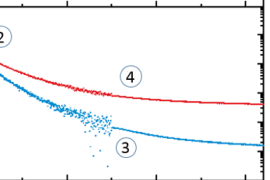
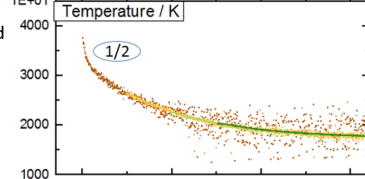
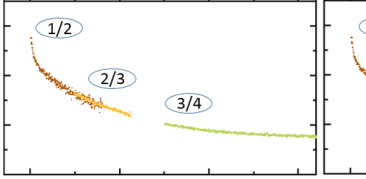
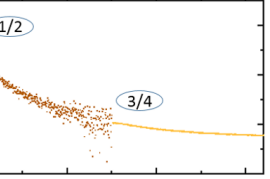
Figure 7-2 Principle of the basic sequential detection technique: Raw signals (left) are used to calculate absolute signals (right); (a) typical LII signal, (b-d) Sequential detection technique applied three times.

Table 1 shows various possible configurations of this detection technique. The basic principle (Table 7-1-A) uses one gated PMT for each of the two colors that are required for two-color LII. A series of subsequent experiments provides the high dynamic range. For each single experiment, the evaluation of signal ratios yields particle temperature traces for a limited part of the decay curve that then can be combined to reconstruct the full temperature trace.

This method can be extended by increasing the number of gated PMTs to provide improved accuracy while maintaining single-shot capability. The scanning and interpolation technique (Table 7-1-B) uses three or more gated photomultipliers in different wavelength bands, which result from the combination of dichroic and bandpass filter transmissions. Two PMTs are used to collect the entire LII signal trace and any additional PMT is delayed to an appropriate later time. The signal of two PMT channels must overlap to allow for temperature detection. Sections where only a single channel is collected can be interpolated

with high fidelity because of the near-exponential characteristics of the LII decay at later times. The wavelength bands should be selected to detect shorter wavelengths at the beginning and longer wavelengths at the later section of the signal according to Wien's displacement law causing a red-shift of the signal with time during particle cooling.

Table 7-1 Schematic comparison of basic (A) and two advanced (B and C) sequential detection techniques: circled numbers denote respective PMT detectors and generated signal (and temperature) traces.

	A) Basic technique	B) Scanning and interpolation	C) Delayed double detection		
Number of gated PMTs	2	3 or more	4		
Minimum laser shots needed	2 or more	1	1		
Number of detection wavelength bands	2	3 or more	2		
Beam splitter	1 dichroic mirror	2 or more dichroic mirrors	1 dichroic mirror, 2 beam splitter		
Method	Absolute signals overlap between measurements. 2C-pyrometry is applied on each overlapping section.	2C-pyrometry is applied on each overlapping section. Missing temperature section is interpolated	Temperature trace is calculated for two sections. Missing temperature section is interpolated		
Application	Steady state particle source	Fluctuating particle source			
Gate delay is increased and gain adjusted	  				
Absolute signals are calculated from raw signals using calibration and gain settings	  				
Temperature is calculated by two-color pyrometry, missing sections are interpolated (circles indicate channel ratios)	  				

The delayed double detection strategy (Table 7-1-C) requires four gated PMTs, two at each of the two detection wavelengths. The LII signal is split by a dichroic mirror and then by two beam splitters on the four detectors. Each wavelength channel is detected by two PMTs with different gate delays. The temperature trace can be collected for two sections and the missing section in between can be interpolated. The beam splitter should be selected so that the PMT with the early gate starting time receives a smaller fraction of the signal, while the PMTs with the later gate starting time capture a larger fraction of the signal (e.g., 10:90 split ratio).

While technique A can only be applied on a steady source where particle size and morphology does not change between laser pulses, such as in steady laminar flames, techniques B and C are instantaneous, and suitable for all sources, including those that are unsteady or turbulent.

When using this technique in flames where the flame temperature is still in the range that can be detected with two-color pyrometry (i.e., >1500 K), the pulsed LII signal is accompanied by a DC signal resulting from flame radiation. Snelling *et al.* [187] presented a method to correct for this bias by splitting the measured radiation into flame radiation and radiation from the probe volume. Because the fraction of the soot radiation that comes from the unheated soot in the probe volume is unknown, an iterative correction procedure is used. In our case with gated PMT detection, the baseline before the gate opening (zero-level) and after gate opening S_{flame} (flame radiation) can be measured. Eq. (7-1) shows how the DC corrected signal S_{probe} can be estimated, which can then be used to determine the unbiased two-color temperature trace. The contribution from flame radiation is subtracted from the measured signal S_{total} and the contributing part from the probe volume S_{probe} is added again.

$$S_{\text{probe}}(\lambda, T) = S_{\text{total}}(\lambda, T) - S_{\text{flame}}(\lambda) + S_{\text{probe}}(\lambda, T_{\text{gas}}) \quad (7-1)$$

Since $S_{\text{probe}}(\lambda, T_{\text{gas}})$ is unknown, we estimate the radiation from the probe volume through the geometrically defined ratio of probe volume to total measurement volume x .

$$S_{\text{probe}}(\lambda, T_{\text{gas}}) = x S_{\text{flame}}(\lambda) \quad (7-2)$$

Figure 7-3 shows temperature traces calculated by sequential signal detection and corrected for different ratios of probe volume and total measurement volume.

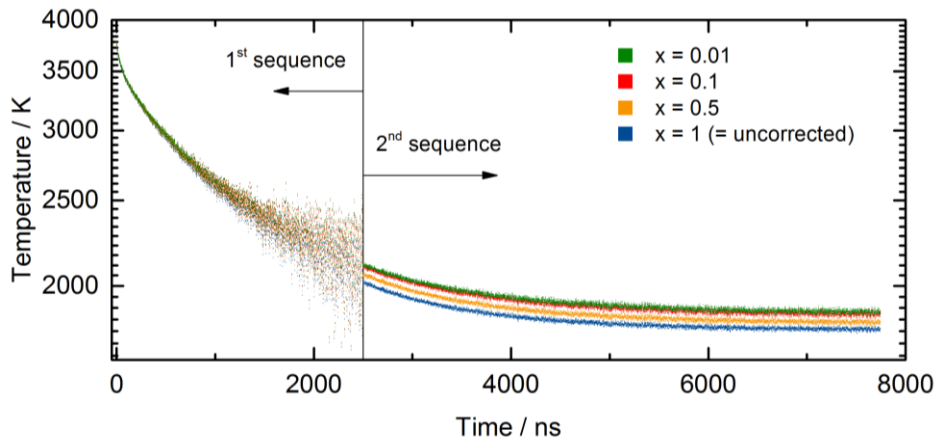


Figure 7-3 Temperature trace (log scale) calculated from two sequences and corrected for flame radiation (1750 K) as a function of probe volume to total measurement volume ratio x .

The strongest deviation occurs for very small probe-volume-to-total-volume ratios and high flame temperatures. For example, when the probe volume is only 1% of the total measurement volume and the flame temperature is 1750 K, the temperature is underestimated up to a maximum of 85 K at later decay times.

7.3 Experiment

Validation measurements were performed using a laminar non-premixed flame (Gülder burner) which has been investigated by TiRe-LII previously [2, 9]. The burner is operated at its standard conditions of 0.194 slm ethene and 284 slm air. The soot particles are heated by pulses (8 ns FWHM) from an Nd:YAG laser at 1064 nm. A square ($2.4 \times 2.4 \text{ mm}^2$) laser beam profile was produced by an aperture and relay-imaged to the measurement position. For all measurements, the laser fluence was set to 1.5 mJ/mm^2 . Two plano-convex lenses were used to image the cylindrical probe volume (1 mm diameter, 2.4 mm length) into a 1-mm diameter fiber. The light exiting the fiber was collimated, split by a dichroic beamsplitter (Semrock FF605-Di02), and focused on two gated PMTs (Hamamatsu H11526-20). Bandpass filters with a center wavelength of 500 nm (Semrock FF01-500/24) and 800 nm (Semrock FF01-800/12) were attached to the two PMTs, respectively. To avoid saturation for the initial high-intensity signals, neutral-density filters were used to attenuate the signal. Signals were collected with a 500-MHz oscilloscope (PicoScope 6404C) with a vertical resolution of 8 bit and 0.8-ns sampling intervals. The triggering of laser and PMT gate time was controlled by a digital delay/pulse generator.

7.4 Results

The basic sequential detection technique (Table 7-1-A) was applied with three gating time steps in the flame at a height above burner of 42 mm. Laser fluence, measurement position and PMT gain were kept constant and the PMT delay was varied. For each sequence, appropriate neutral density filters (transmission of 1, 10, and 79%) were used to prevent saturation of the detectors.

The temperature trace was calculated by applying Eq. (7-3) [187, 189] for each data point assuming a constant ratio of the absorption function $E(\mathbf{m}_{\lambda_1})/E(\mathbf{m}_{\lambda_2}) = 1$,

$$T_p = \frac{hc_0}{k_B} \left(\frac{1}{\lambda_2} - \frac{1}{\lambda_1} \right) \left[\ln \left(\frac{I_\lambda(\lambda_1, T_p)}{I_\lambda(\lambda_2, T_p)} \frac{E(\mathbf{m}_{\lambda_2})}{E(\mathbf{m}_{\lambda_1})} \left(\frac{\lambda_1}{\lambda_2} \right)^6 \right) \right]^{-1}, \quad (7-3)$$

with the particle temperature T_p , the Planck constant h , the speed of light in vacuum c_0 , the Boltzmann constant k_B , the detection wavelengths λ (i.e., the center wavelengths of the 500 and 800 nm bandpass filters), and the absolute spectral intensity I_λ . The sensitivity and error analyses of soot temperature determined by two-color LII were previously published by Liu *et al.* [78].

Figure 7-4 shows a comparison of signal processing results between single-shot (left) and multi-signal average of 100 laser shots (right) starting from the raw signals for three different gate delay times (top). Absolute signals are calculated using the instrument and filter calibrations (middle). The temperature trace (bottom) is calculated by two-color pyrometry using Eq. (7-3). Particles reach a maximum temperature of 3820 K and approach the local gas temperature of 1790 K at about 7 μs after the signal peak.

For the single-shot signals, quantization noise caused by the restricted vertical resolution of the ADC can already be seen after 1 μs in the absolute signals as multiple horizontal lines (blue curve). By using the detector arrangement of technique C (Table 7-1), a full temperature trace can even be measured for a single laser shot.

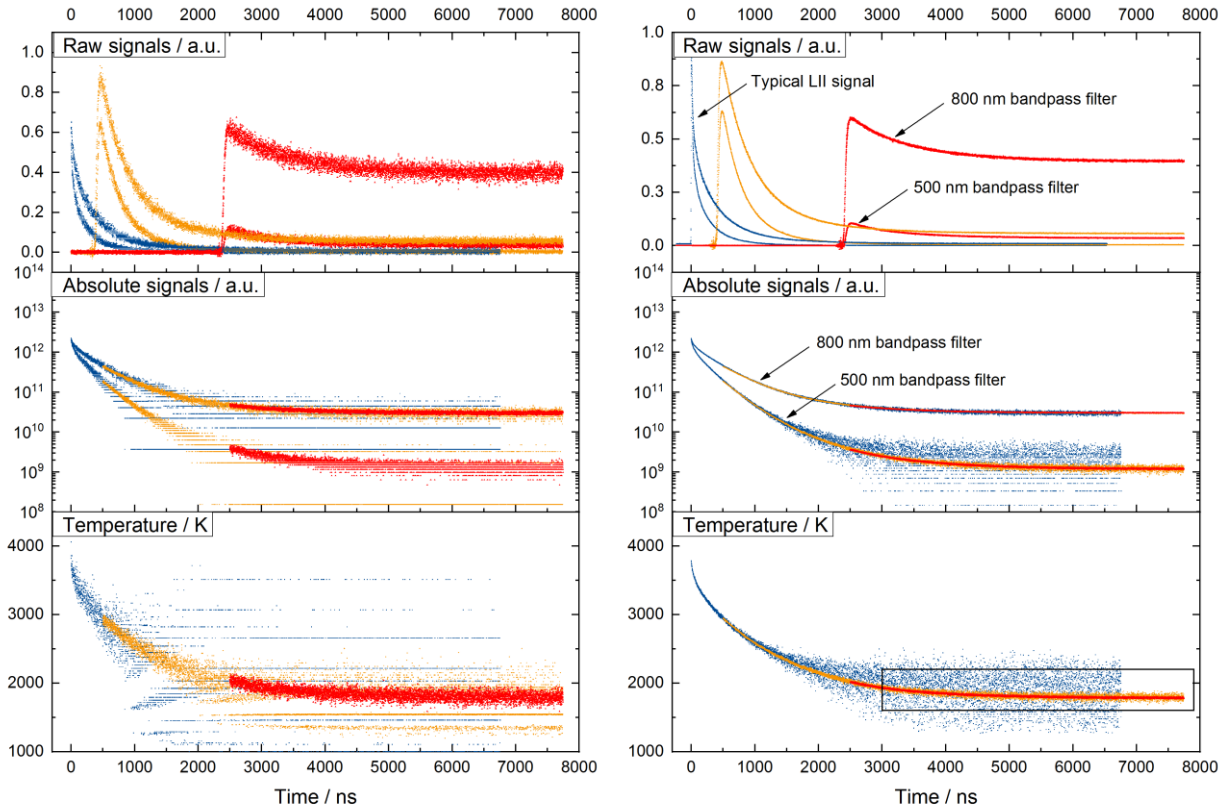


Figure 7-4 Comparison of single-shot (left) and multi-shot analysis (right) (100 laser shots); Absolute signals (middle graphs) are calculated from raw signals (upper graphs) using spectral calibration and gain settings; Temperature (lower graphs) calculated by two-color pyrometry; the portion covered by the rectangle is enlarged in Figure 5. The following ND filters were used: (blue: 1%, orange: 10%, red: 79%).

The improved capability of this technique is demonstrated by measuring the gas heat-up as a consequence of laser-induced particle heating. While LII is considered a non-intrusive technique, recent studies have demonstrated that energy deposition in the probe volume due to laser heating of particles is not negligible and influences the simulation of conduction cooling of the particles [172, 187]. Complex measurements using CARS [172] and extrapolation/modeling techniques [187] confirm evidence of local gas heating. This effect strongly depends on the soot volume fraction and varies with the laser fluence.

HDR-TiRe-LII for the first time allows determination of the temperatures even at very late times when particles are in thermal equilibrium with the surrounding gas. Comparing two-color pyrometry without and with laser heating allows one to measure the heat-up effect (see Figure 7-5). At 6.5 μ s after the laser pulse, the typical LII signals lead to a temperature of 1840 ± 268 K (blue) while the first sequential detection gives 1795 ± 30 K (orange) and the second 1790 ± 10 K (red). The error bars represent the 2σ standard deviation from the mean. For comparison of the (laser-induced) temperature increase, the incandescence was measured for a gate duration of 2 μ s. For the selected measurement position the local gas temperature (without laser-heating) was determined as 1760 ± 10 K (green), which is very close to the previously reported CARS temperatures of 1730 ± 25 K [171] and 1740 K [172].

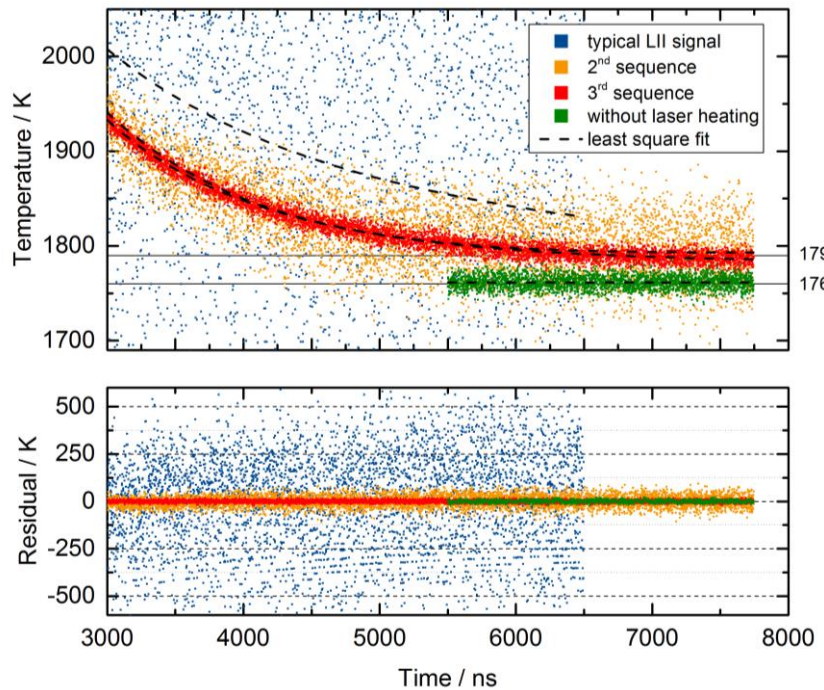


Figure 7-5 Enlarged portion of the temperature trace from Figure 7-3: Temperature traces from the conventional analysis of full LII decays (blue) and results of the sequential detection technique (orange and red) show the dramatic improvement in data quality that now allows to determine the effect of local gas heating (red) compared to measurements without laser heating (green). Residual of least square fit of measured data (bottom). After DC flame radiation correction ($x = 0.24$), local gas heating could be determined as 80 K for these laser settings and flame conditions.

This demonstrates that HDR-TiRe-LII can detect particle temperatures in atmospheric pressure flames even 8 μ s after the laser pulse. As mentioned previously, the asymptotic temperature decay after laser heating and subsequent cooling leads to a particle temperature of 1790 K at 7 μ s after the signal peak. For the DC flame radiation correction, the probe-volume-to-total-measurement-volume ratio in our measurements was geometrically determined as 0.24 that leads to a corrected local gas temperature of 1840 K, indicating an increase in the local gas temperature of 80 K.

7.5 Conclusions

We presented a new method for collecting LII signals with high dynamic range using delayed sequential detection. The suggested two-step approach of gate-delayed voltage switching for blocking the beginning of a LII signal and adjustment of filter/gain settings to an optimum level can be applied in different ways. We have suggested three techniques using gated PMTs to get detailed information of the later temperature decay, two of which provide single shot capability. The method is sensitive enough to measure local gas-heating during LII, which is an uncertainty in research that until now needed to be determined by other—much more complex—measurement techniques (e.g., CARS). Particularly advantageous for very short LII signals such as with small particles or high pressures, this method can be used to collect a larger/longer temperature range and therefore improve data accuracy and model-based evaluation.

8 OUTLOOK

The research presented in this thesis defines guidelines for the experimental design of LII setups and introduces new measurement strategies that should be further explored in the future.

Multi-color time-resolved LII. As part of this work, a multi-color LII device was build that allows measurements with improved spectral quality. Measurements at multiple wavelength bands showed that pyrometrically inferred temperatures are subject to large uncertainties and improvements to this technique should be prioritized. Although measurements at more than two colors over-determine the analysis, it was found that different two-color ratios do not yield the same temperatures as expected. This could be explained by false optical properties, but also by measurement issues as underestimated polydispersity or non-uniform laser-heating. With increased spectral quality of multi-color LII measurements, future spectroscopic models should be extended to cover these effects.

The presented multi-color device was initially equipped with four different bandpass filters, but due to the weak signal intensity in the near-UV of the calibration light sources available at that time, a 390-nm bandpass filter of the first channel was replaced by a 500-nm bandpass filter. The recent availability of new calibrated light sources as the laser-driven light source (LDLS) now enables us to perform a calibration also at wavelengths below 450 nm. This change in design was too late in the advance of this work, but the higher spectral resolution can be beneficial for future LII studies on synthetic nanoparticle applications, for which optical properties are often not available in literature.

LII heat transfer model developments. Parameter studies at multiple detection wavelengths on various measurement targets can help to identify next steps for the development of basic heat transfer models that can be used as the foundation for future model development. With the apparatus and measurement strategies presented in this work, reproducible LII measurements with high signal quality can be performed and, using the LIISim software, these signals can be recorded in a standardized file format including various metadata (i.e., process conditions, laser fluence and detection settings). Screening of the data in respect of parameter variation using the built-in analysis tools of the LIISim software can help to identify potential parameter dependencies that are important for the modeling. The data can be exported from the LIISim software as MATLAB datasets that can then be used in the LIISim-MDK that is written in MATLAB code, or in other customized MATLAB scripts. Having both the raw data and metadata available in the MATLAB environment, facilitates the application of advanced data analysis techniques such as data fusion with supplementary measurement techniques (e.g., laser-induced breakdown spectroscopy (LIBS) [190] or wide-angle light scattering (WALS) [191]) within the Bayesian framework, as well as fluence curve analysis [13, 192], or Bayesian model selection [193].

Combination of LII with other techniques. Comparison of multi-color LII with spectrally- and temporally-resolved LII using a streak camera can be an important and promising approach to gain more information about the temporal blurring and rise-time behavior of different detector types. As the temporal variation is the key parameter in LII analysis, insight into these effects can be very helpful for the understanding of discrepancies between models and data.

Optical properties of many materials are unknown, or the reference conditions in literature (e.g., low temperature, solid) are far away from the conditions during the LII measurement (e.g., high temperature, liquid). Simultaneous measurements with spectrally resolved line-of-sight attenuation (LOSA) or heated-LOSA (i.e., during the LII signal) will help to gain more information to resolve these issues.

LII *Sim* *software development.* The open-source concept and public availability of the software/source code enables other researcher to implement new heat transfer models. The implementation of heat transfer models is outlined in Appendix E and in the developer guide available through the LII*Sim* website. Extension of the materials databases, especially in regard to engineered nanoparticles, can facilitate comparative studies on reactors that can be operated with different precursor materials. Further modules and functionalities could be implemented in the current framework such as combined solution of spectroscopic models and heat-transfer models, but also statistical tools for the systematic analysis of parameter studies.

Standardization and inter-laboratory comparisons. Best-practice guidelines for performing LII experiments are mostly only internally communicated within a research group. The biennial international workshop on LII can act as a platform to establish best-practice standards, increasing the reliability of published data, and enabling comparisons across research groups. Standardization of materials databases and establishing a public database could help to make the best choice of materials properties for the LII modeling. Publicly available lists of published experimental conditions could help identify similar studies that could be used to benchmark ongoing experiments. When databases or conditions are provided, the units of the quantities should be always expressed in base units (i.e., m, kg, K, s, etc.) according the International System of Units (SI) to simplify comparisons and the model implementation. Sharing of calibrated LII signals from various conditions on public platforms could enable open inter-laboratory comparisons that are not linked to a specified timeframe.

9 SUMMARY

Time-resolved laser-induced incandescence (TiRe-LII) is an important optical diagnostics tool for *in situ* measurements of nanoparticle size and volume fraction in aerosols. It can be used to characterize formation processes of nanoparticles and provides valuable information to support simulations or for the design of such processes.

Major challenges for LII science concern the signal acquisition and early stage of signal processing. The LII signals resulting from these two steps are used as input for all subsequent processing and analysis steps. Thus, it is important to achieve a high initial signal quality in order to increase the quality of the analysis. Detector performance and measurement errors have hardly been investigated in the context of LII, but can significantly affect the signal quality. State-of-the-art techniques as two-color pyrometry can be very sensitive to these signal biases and large errors in derived particle temperatures might remain unnoticed. This makes it even more important to have best-practice guidelines for practical procedures as detector calibration and signal acquisition, and further, to investigate new innovative detection and data evaluation concepts that can contribute to establish high-quality measurements. Furthermore, variations in experimental procedures between different research studies reduce the comparability of scientific results. The harmonization of the experimental procedure, calibration, measurement, and interpretation of data is therefore strongly needed.

This work advances in the direction of standardization of the experimental processes and focuses on technical and practical aspects of the multi-color time-resolved LII technique related to the design of an LII setup, detector performance, calibration, and data acquisition/processing. This contributes to a high signal quality for various application cases that can then be used as input for LII model development research.

The first chapters of this work outline the technical and theoretical framework of the LII technique and specify design requirements for a typical LII setup. It was demonstrated that the variation of the laser Q-switch delay, to control the laser fluence in an LII experiment, could affect the spatial intensity profile. A variable laser-energy attenuator can help to keep the spatial energy distribution uniform while the laser energy can be varied. With relatively simple optical arrangements for laser-beam shaping, the beam profile can be conditioned to achieve homogeneous heating of all particles in the measurement volume. Other concepts presented in this thesis address the selection of detection wavelengths, electronic control of experimental parameters, and modifications towards flexibility and mobility of such a setup.

In the context of this work, a multi-color LII detection device was designed and built including four detectors that can be equipped with individual bandpass filters. The extension from two-color to multi-color analysis lowers the degrees of freedom in the spectroscopic modeling of LII signals and yields more reliable particle temperature traces. An additional data acquisition module, implemented in the presented LII-Sim software, can be used to control experimental parameters of the LII setup (i.e., laser fluence, PMT gain, oscilloscope settings) and record LII signals in a standardized file format. The setup is used in several research tasks and technical aspects concerning detector performance and calibration are investigated.

Photomultiplier tubes that are the most common detector types in LII research have been investigated in the context of linearity and experiments using continuously and pulsed operated LEDs have been performed at similar light levels as they occur during LII calibration and measurements. It was shown that in the context of LII, the photocathode is the most sensitive part of a PMT that can be affected by non-linearity. The super bi-alkali (SBA) photocathode showed significant non-linear behavior when exposed to high light levels, while the multi-alkali (MA) type was less affected. In a theoretical study, it was demonstrated that two-color temperature determination could be affected by a bias of a single detection channel. This can cause errors in LII temperature traces of several hundreds of Kelvin.

The calibration of the detectors is essential for multi-color LII analysis, as any subsequent analysis step is based on proper calibrated signals. A detailed study on the methodology of the calibration procedure of the LII detector for individual components within the detection setup was presented. The technical background of detector requirements was explained and a mathematical description of the calibration procedure and error analysis was established. Multiple light sources were investigated for their suitability as calibration light source and, in a comparative study, they have been combined with various neutral-density (ND) filters to achieve different calibration light levels. It was found that the calibration factors have been biased with increasing light levels, especially with the SBA photocathode. Biased calibration factors are usually not questioned in later analysis steps and could systematically affect all subsequent signal-processing steps. Repeating the calibration and measurements at multiple light levels helps to identify operational regimes, which can yield reproducible results. The simplest and fastest method to ensure reproducibility is to measure LII signals twice, with two different ND-filter transmissions.

The new software concept for the LII-Sim software was presented, building on previous experience from a predecessor software, but following a fundamentally different approach. The motivation was to provide a software solution that can accommodate LII measurements for various materials systems, and allows flexible usage on various processes and conditions. For the software structure, a modular approach was chosen, to increase the flexibility by allowing the assembling of individual processing chains from predefined signal-processing steps. The new materials-database concept enables switching between materials systems or different sets of physical properties during the LII analysis. For the data fitting, three published heat transfer models were implemented with the corresponding sets of physical properties. The graphical user interface (GUI) of the software provides flexible tools for data visualization and analysis and enables systematic data comparison for large data sets and parameter studies. In the context of inter-laboratory comparisons, the software can help to analyze and compare data across research labs and the open-source concept allows further developments by the LII community. The object-oriented software architecture helps in this process, as modifications of LII related source code are limited to small parts of the entire source code.

The presented sequential detection technique increases the dynamic range of LII measurements by taking advantage of the detector gate and multi-color detection. The method is demonstrated on a laminar diffusion flame allowing identification of local gas heating by heat exchange of the particles with the surrounding gas. This technique can yield high-resolution LII signal traces that are invaluable for LII model development.

The research presented in this work helps to resolve many questions related to the practical and technical aspects of LII signal acquisition and demonstrates measurement strategies that are a major step towards robust LII measurements. The applicability was demonstrated with a newly built multi-color LII device that

combines reproducible high-quality measurements with flexibility for a wide range of materials and processes. Researchers can adapt the concepts to establish and communicate best-practice procedures and achieve a harmonization of the experimental processes within the community. This significantly increases the comparability of research results between laboratories and the improved data quality will be invaluable for modeling experts for the development of reliable LII models. The open-source software LiISim developed within this thesis integrates this knowledge and provides an important service to the community.

APPENDIX

Appendix A Linearity measurements

The measured anode current and the corresponding deviation from linearity, as described in section 4.4.1, are visualized for all PMTs in an interpolated contour plot. Figure A-1 presents the data for the continuously operated LEDs and Figure A-2 shows that for pulsed LEDs.

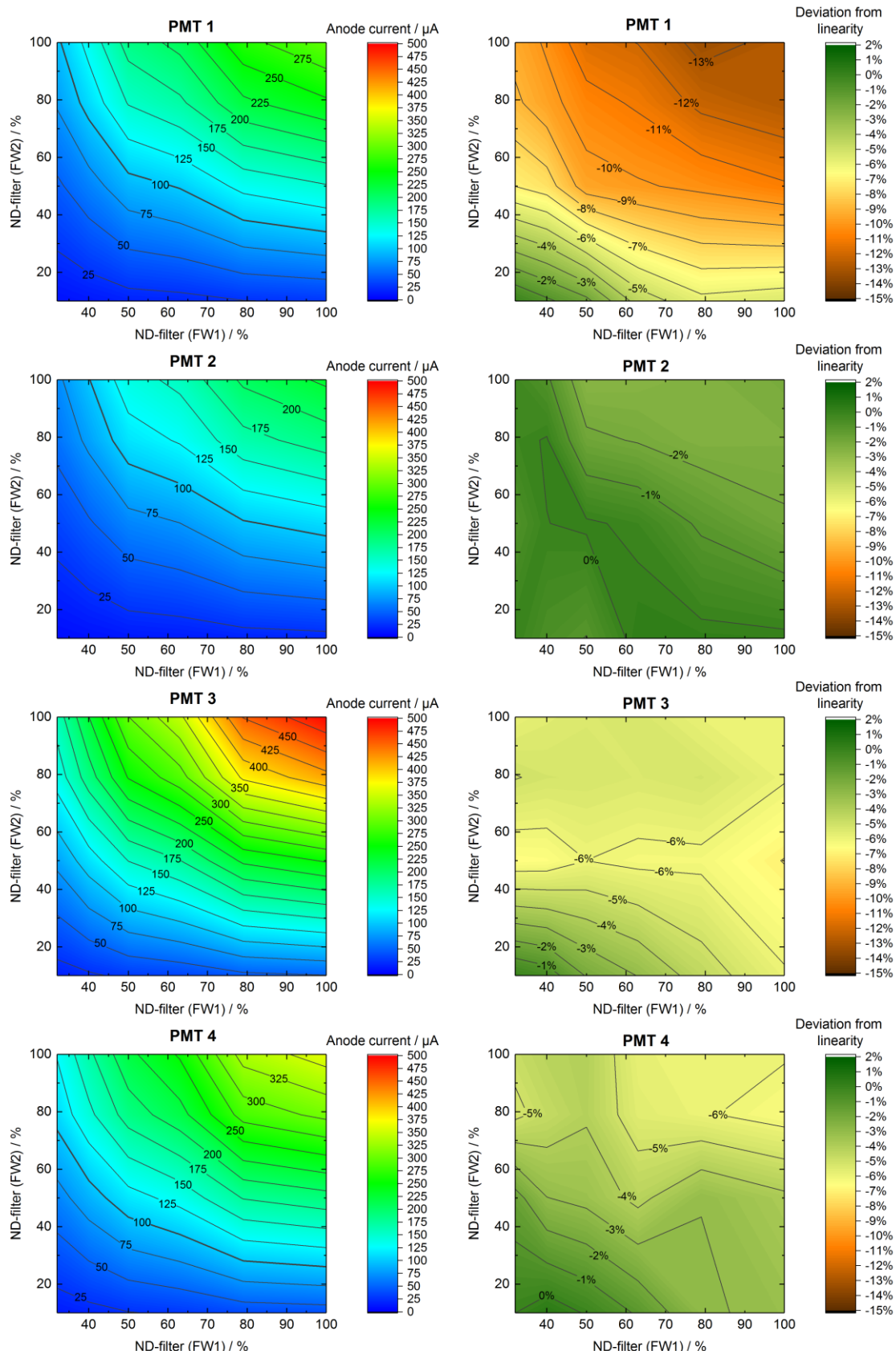


Figure A-1 Linearity measurements with continuously operated LEDs: ND-filter variation; measured anode current (left) and deviation from linearity (right).

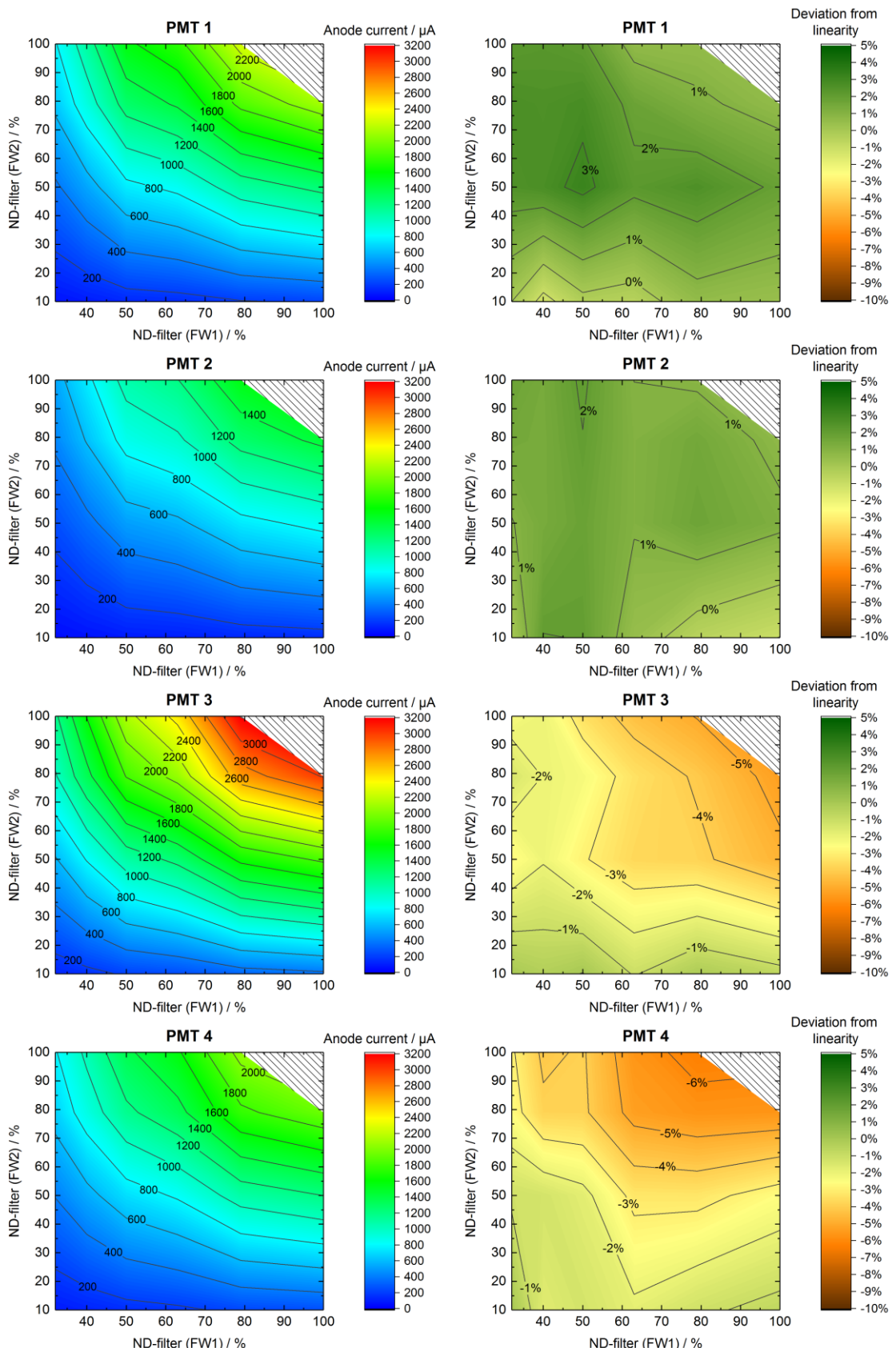


Figure A-2 Linearity measurements with pulsed LEDs: ND-filter variation; measured anode current (left) and deviation from linearity (right).

Appendix B Signal bias and artifacts

Several general measurement artifacts have been observed that are not directly connected to the LII technique, but may also lead to nonphysical results or low signal quality:

- i) Signal ringing can be caused by signal reflection due to an impedance mismatch [194, 195].
- ii) Q-switch noise of the laser-unit can interfere with the LII signal trace and bias the result (Figure B-1). Proper shielding of the electronics or increasing the distance between detection electronics and laser can help to prevent this.

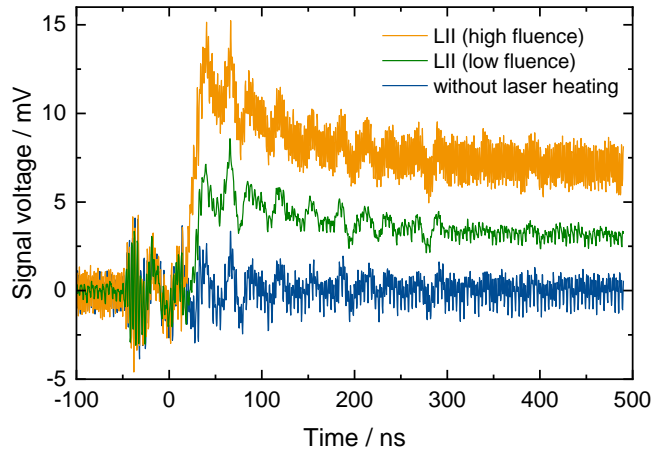


Figure B-1 Q-switch noise interfering with the measured LII signal.

- iii) Crosstalk with other devices connected to the same power circuit can introduce measurement artifacts in the LII traces. Fast-switching electronic circuits (e.g., transistor circuit for shutter, pulsed light sources) for example, often appear as small spikes within the PMT signal traces.
- iv) Incorrect coupling of trigger/timing circuits could induce crosstalk between the oscilloscope channels. Figure B-2 shows the crosstalk between the oscilloscope trigger channel and the oscilloscope signal input for two different coupling settings on the pulse/delay generator. While the spike in the beginning of the LII signal can be neglected (due to high SNR), the drift in the later part of the LII signal could bias temperature determination.

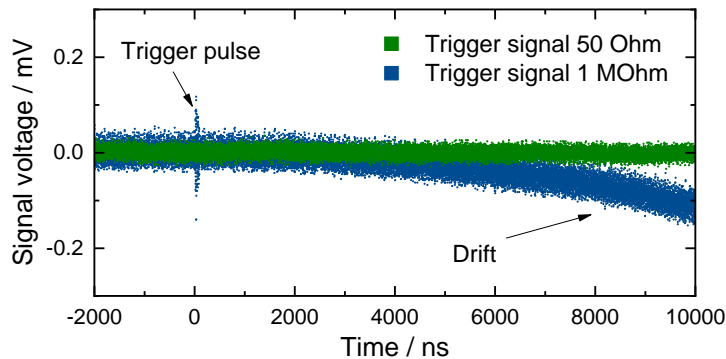


Figure B-2 Signal biased by false coupling of timing circuit (pulse/delay generator).

- v) Low-bandwidth integrated amplifier circuits within the PMT may limit the bandwidth of the measured temporal LII signal profile. Figure B-3 shows the signal response of a pulsed LED (500 nm, 3 μ s FWHM) for a commercially-available PMT system (PMT A) with integrated amplifier circuit (SMT MEA 1030 V8DA with Hamamatsu R7400U) and a directly coupled PMT (PMT B) from this study (Hamamatsu H11526), recorded with the same oscilloscope. The integrated amplifier circuit influences the rise and fall characteristic, which can also bias the LII signal by limiting the temporal resolution.

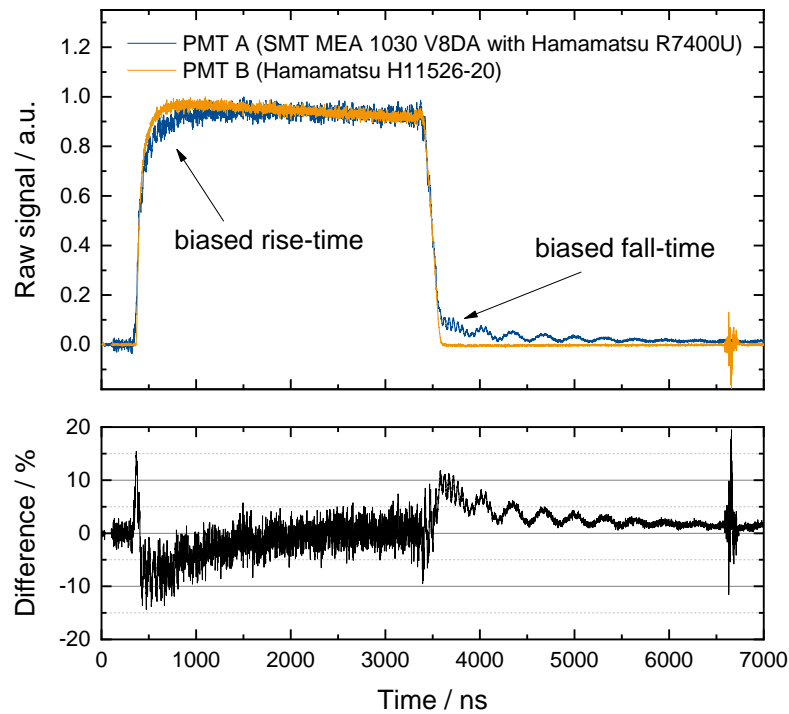


Figure B-3 Comparison of pulsed LED signal response for PMTs with (A) and without (B) integrated amplifier circuit and the difference in percent of the full vertical oscilloscope scale.

Appendix C LIISim – Levenberg–Marquardt algorithm

This section describes the Levenberg–Marquardt algorithm as it is implemented in the LIISim numerical classes.

For a given data vector y of the length m and for n parameters \mathbf{a} and a vector of standard deviations σ_i , the residuals for a given model $y_{\text{mod}}(x_i, \mathbf{a})$ (spectroscopic or heat transfer model) can be described as

$$f_i(\mathbf{a}) = \frac{y_i - y_{\text{mod}}(x_i, \mathbf{a})}{\sigma_i} \quad i = 1, 2, \dots, m, \quad (\text{C-1})$$

and

$$\mathbf{F}(\mathbf{a}) = \begin{bmatrix} f_1(\mathbf{a}) \\ \vdots \\ f_m(\mathbf{a}) \end{bmatrix} \in \mathbb{R}^m. \quad (\text{C-2})$$

The goal is now to minimize the nonlinear least squares problem for the parameters \mathbf{a}

$$\arg \min_{\mathbf{a}} f(\mathbf{a}) \quad (\text{C-3})$$

with

$$f(\mathbf{a}) = \sum_{i=1}^m f_i(\mathbf{a})^2. \quad (\text{C-4})$$

The gradient of $f(\mathbf{a})$ can be written in matrix notation as

$$\nabla f(\mathbf{a}) = 2\mathbf{J}(\mathbf{a})^T \mathbf{F}(\mathbf{a}) \in \mathbb{R}^m, \quad (\text{C-5})$$

where $\mathbf{J}(\mathbf{a})$ is the Jacobian

$$\mathbf{J}(\mathbf{a}) = \begin{bmatrix} \frac{\partial f_1}{\partial a_1} & \dots & \frac{\partial f_1}{\partial a_n} \\ \vdots & \ddots & \vdots \\ \frac{\partial f_m}{\partial a_1} & \dots & \frac{\partial f_m}{\partial a_n} \end{bmatrix} \in \mathbb{R}^{m \times n}, \quad (\text{C-6})$$

and \mathbf{D} half of the Hessian matrix:

$$\nabla^2 f(\mathbf{a}) \approx 2\mathbf{J}(\mathbf{a})^T \mathbf{J}(\mathbf{a}) = 2\mathbf{D}. \quad (\text{C-7})$$

For each iteration, the gradient of the parameters \mathbf{a} can be found by solving [196]:

$$(\mathbf{J}(\mathbf{a})^T \mathbf{J}(\mathbf{a}) + \lambda \mathbf{I}) \Delta \mathbf{a} = -\mathbf{J}(\mathbf{a}^k)^T \mathbf{F}(\mathbf{a}^k), \quad (\text{C-8})$$

which can be transformed using the Cholesky decomposition to the form $\mathbf{L}\mathbf{L}^T\mathbf{x} = \mathbf{b}$ with

$$\begin{aligned}\mathbf{L}\mathbf{L}^T &= (\mathbf{D} + \lambda\mathbf{I}) \\ \mathbf{x} &= \Delta\mathbf{a} \\ \mathbf{b} &= -\mathbf{J}(\mathbf{a}^k)^T \mathbf{F}(\mathbf{a}^k).\end{aligned}\tag{C-9}$$

Now \mathbf{x} can be found by forward $\mathbf{Ly} = \mathbf{b}$ and backward substitution $\mathbf{L}^T\mathbf{x} = \mathbf{y}$, which gives the new parameter approximation for the next iteration k :

$$\mathbf{a}^{k+1} = \mathbf{a}^k + \Delta\mathbf{a}.\tag{C-10}$$

In LII-Sim, the parameters \mathbf{a}^k are visualized for the temperature fit in “AnalysisTools Temperature Fit” and for the heat transfer modeling in the FitCreator module.

Appendix D LIISim – Implemented heat transfer models

This appendix describes the heat transfer models from literature [19] implemented in LIISim. The heat transfer rates are defined in the HeatTransferModel child classes in the calculations/models/ folder of the source code.

Further detailed information for the implementation of heat transfer models can be found in the LIISim developer guide on www.liisim.com.

Summary of available parameters

Property	LIISim variable	Unit	Description
α_T	alpha_T_eff	–	Thermal accommodation coefficient (conduction)
ε	eps	–	Total emissivity for radiation heat transfer
γ	gamma	–	Heat capacity ratio calculated from heat capacity
κ_a	therm_cond	$\text{W m}^{-1} \text{K}^{-1}$	Thermal conductivity of gas molecules
ρ_p	rho_p	kg m^{-3}	Particle density
θ_e	theta_e	–	Thermal accommodation coefficient (evaporation)
$C_{p,\text{mol}}$	C_p_mol	$\text{J mol}^{-1} \text{K}^{-1}$	Molar heat capacity
c_p	c_p_kg	$\text{J kg}^{-1} \text{K}^{-1}$	Specific heat capacity
$E(m)$	Em	–	$E(m)$ absorption function value at wavelength λ
$E(m)$	Em_func	–	$E(m)$ absorption function
ΔH_v	H_v	J mol^{-1}	Enthalpy of evaporation
L	L	m	Mean free path of gas molecules
M	molar_mass	kg mol^{-1}	Molar mass
M_v	molar_mass_v	kg mol^{-1}	Molar mass of vapor species
p_v	p_v	Pa	Vapor pressure function
p_v^*	p_v_ref	Pa	Reference pressure for Clausius-Clapeyron
T_v^*	T_v_ref	K	Reference temperature for Clausius-Clapeyron

Summary of constants

Constant	LIISim variable	Unit	Value (LIISim/NIST)	Description
c_0	c0	m s^{-1}	2.99792458×10^8	Speed of light in vacuum
h	h	Js	$6.62607004 \times 10^{-34}$	Planck constant
k_B	k_B	J K^{-1}	$1.38064852 \times 10^{-23}$	Boltzmann constant
N_A	N_A	mol^{-1}	$6.02214085 \times 10^{23}$	Avogadro constant
R	R	$\text{J mol}^{-1} \text{K}^{-1}$	8.3144598	Molar gas constant
π	pi	-	3.14159265359	Pi
σ	sigma	$\text{W m}^{-2} \text{K}^{-4}$	5.670367×10^{-8}	Stefan-Boltzmann constant
c_1	c_1	W m^2	$c_1 = 2hc_0^2$	First radiation constant for spectral radiance
c_2	c_2	K m	$c_2 = hc_0/k_B$	Second radiation constant

Summary of general properties

The following materials and gas mixture properties are calculated for all models according:

Name	LIISim variable	Symbol (original)	Symbol (LIISim)	Equation	Unit
Specific heat capacity of the particle	c_p_kg	c_s	c_p	$c_p = C_{p,\text{mol}}/M_p$	$\text{J kg}^{-1} \text{K}^{-1}$
Thermal velocity of gas molecules	c_tg	$c_{\text{tg}}(T_g)$	$c_{\text{tg}}(T_g)$	$c_{\text{tg}} = \left(\frac{8 k_B N_A T_g}{\pi M_{\text{mix}}}\right)^{\frac{1}{2}}$	m s^{-1}
Molar heat capacity of gas mixture	C_p_mol	-	$C_{p,\text{mix}}$	$C_{p,\text{mix}} = \sum_i^n x_i C_{p,g,i}$	$\text{J mol}^{-1} \text{K}^{-1}$
Heat capacity ratio	gamma	$\gamma(T_g)$	$\gamma(T_g)$	$\gamma(T_g) = \frac{C_{p,\text{mix}}}{C_{p,\text{mix}} - R}$	-
Molar mass of gas mixture	molar_mass	-	M_{mix}	$M_{\text{mix}} = \sum_i^n x_i M_{g,i}$	kg mol^{-1}

Kock model

Materials properties (Soot_Kock)

Name	Variable	Type	Symbol (original)	Symbol (LiSim)	a_0	a_1	a_2	a_3	a_4	a_5	a_6	a_7	a_8	Unit
Accommodation coefficient	alpha_T_eff	const	α_T	α_T	0.23	-	-	-	-	-	-	-	-	-
Accommodation coefficient	theta_e	const	α_M	θ_e	1.0	-	-	-	-	-	-	-	-	-
Molar heat capacity ^b	C_p_mol	poly2 ^a	-	$C_{p,\text{mol}}$	22.5566	0.0013	-	-	-	-1.8195 $\times 10^6$	-	-	-	J mol ⁻¹ K ⁻¹
Total emissivity	eps	const	ε	ε	1.0	-	-	-	-	-	-	-	-	-
Molar mass	molar_mass	const	W_s	M_p	0.012011	-	-	-	-	-	-	-	-	kg mol ⁻¹
Molar mass of vapor	molar_mass_v	const	W_v	M_v	0.036033	-	-	-	-	-	-	-	-	kg mol ⁻¹
Density	rho_p	const	ρ_s	ρ_p	1860	-	-	-	-	-	-	-	-	kg m ⁻³
Enthalpy of evaporation	H_v	const	ΔH_v	ΔH_v	790776.6	-	-	-	-	-	-	-	-	J mol ⁻¹
Reference pressure ^c	p_v_ref	const	p_{ref}	p_v^*	61.5	-	-	-	-	-	-	-	-	Pa
Reference temperature ^c	T_v_ref	const	T_{ref}	T_v^*	3000	-	-	-	-	-	-	-	-	K

^a $f(T) = a_0 + a_1 T + a_2 T^2 + a_3 T^3 + a_4 T^{-1} + a_5 T^{-2}$

^b Calculated from given c_s

^c Clausius-Clapeyron

Gas mixture properties (Kock-Nitrogen-100%)

Composition

Gas	Variable	Symbol	Fraction
Nitrogen_Kock	x	x	1.0

Gas properties (Nitrogen_Kock)

Name	Variable	Type	Symbol (original)	Symbol (LIISim)	a_0	a_1	a_2	a_3	a_4	a_5	Unit
Molar mass	molar_mass	const	M_g	M_g	0.028014	–	–	–	–	–	kg mol^{-1}
Molar heat capacity ^a	C_p_mol	poly2 ^b	$C_{mp,g}$	$C_{p,g}$	28.58	0.00377	–	–	–	-50,000	$\text{J mol}^{-1} \text{ K}^{-1}$

^a For nitrogen from [102]

^b $f(T) = a_0 + a_1T + a_2T^2 + a_3T^3 + a_4T^{-1} + a_5T^{-2}$

Heat transfer model (HTM_KockSoot)

Evaporation

$$\dot{Q}_{\text{evap}} = - \frac{\Delta H_v}{M_v} \dot{m}_{\text{evap}} \quad (\text{D-1})$$

$$\dot{m}_{\text{evap}} = -\theta_e \frac{1}{4} \pi d_p^2 c_{tv} \rho_v \quad (\text{D-2})$$

$$c_{tv} = \left(\frac{8 k_B N_A T_p}{\pi M_v} \right)^{\frac{1}{2}} \quad (\text{D-3})$$

$$\rho_v = \frac{p_v M_v}{R T_p} \quad (\text{D-4})$$

$$p_v = p_v^* \exp \left(-\frac{\Delta H_v}{R} \left(\frac{1}{T_p} - \frac{1}{T_v^*} \right) \right) \quad (\text{D-5})$$

Conduction

$$\dot{Q}_{\text{cond,fm}} = \frac{\alpha_T \pi d_p^2 p_g c_{tg}}{8} \left(\frac{\gamma + 1}{\gamma - 1} \right) \left(\frac{T_p}{T_g} - 1 \right) \quad (\text{D-6})$$

$$c_{tg} = \left(\frac{8 k_B N_A T_g}{\pi M_{\text{mix}}} \right)^{\frac{1}{2}} \quad (\text{D-7})$$

Radiation

$$\dot{Q}_{\text{rad}} = \pi d_p^2 \varepsilon \sigma (T_p^4 - T_g^4) \quad (\text{D-8})$$

Liu model

Materials properties (Soot_Liu)

Name	Variable	Type	Symbol (original)	Symbol (LiiSim)	a_0	a_1	a_2	a_3	a_4	a_5	a_6	Unit
Accommodation coefficient	alpha_T_eff	const	α_T	α_T	0.37	—	—	—	—	—	—	—
Accommodation coefficient	theta_e	const	α_M	θ_e	0.77	—	—	—	—	—	—	—
Molar heat capacity ^a	C_p_mol	poly ^b	$C_{p,mol}$	3.54288	3.55694 $\times 10^{-2}$	-2.55018 $\times 10^{-5}$	9.83713 $\times 10^{-9}$	-2.10385 $\times 10^{-12}$	2.35752 $\times 10^{-16}$	-1.07879 $\times 10^{-20}$	J mol ⁻¹ K ⁻¹	
Total emissivity	eps	const	ε	ε	0.4	—	—	—	—	—	—	—
Molar mass	molar_mass	const	W_v	M_p	0.012011	—	—	—	—	—	kg mol ⁻¹	
Molar mass of vapor	molar_mass_v	const	W_1	M_v	17.179 $\times 10^{-3}$	6.8654 $\times 10^{-7}$	2.9962 $\times 10^{-9}$	-8.5954 $\times 10^{-13}$	1.0486 $\times 10^{-16}$	—	—	kg mol ⁻¹
Density	rho_p	const	ρ_s	ρ_p	1860	—	—	—	—	—	—	kg m ⁻³
Enthalpy of evaporation	H_v	poly ^a	Δh_v	ΔH_v	2.05398 $\times 10^5$	7.366 $\times 10^2$	-0.40713	1.1992 $\times 10^{-4}$	-1.7946 $\times 10^{-8}$	1.0717 $\times 10^{-12}$	—	J mol ⁻¹
Vapor pressure ^c	p_v	expoly ^d	p_v	p_v	—	101325 (unit conversion)	-122.96	9.0558 $\times 10^{-2}$	-2.7637 $\times 10^{-5}$	4.1754 $\times 10^{-9}$	-2.4875 $\times 10^{-13}$	Pa

^a Valid from 1200 K to 5500 K; calculated from given c_s

^b $f(T) = a_0 + a_1 T + a_2 T^2 + a_3 T^3 + a_4 T^4 + a_5 T^5 + a_6 T^6 + a_7 T^7 + a_8 T^8$

^c Original unit: [atm]; from fits to data

^d $f(T) = a_0 + a_1 \exp(a_2 + a_3 T + a_4 T^2 + a_5 T^3 + a_6 T^4 + a_7 T^5)$

Gas mixture properties (Liu_Flame)

Composition

Gas	Variable	Symbol	Fraction
FlameAir_Liu	x	x	1.0

Properties (manually set for this composition)

Name	Variable	Type	Symbol (original/ LIISim)	a ₀	a ₁	a ₂	a ₃	a ₄	Unit
Heat capacity ratio ^a	gamma_eqn	poly ^b	γ	1.4221163 416	-1.863600 2383 $\times 10^{-4}$	8.0783894 569 $\times 10^{-8}$	-1.642508 2302 $\times 10^{-11}$	1.2750021 975 $\times 10^{-15}$	-

^a For flame mixture from [197]

$$^b f(T) = a_0 + a_1 T + a_2 T^2 + a_3 T^3 + a_4 T^4 + a_5 T^5 + a_6 T^6 + a_7 T^7 + a_8 T^8$$

Gas properties (FlameAir_Liu)

Name	Variable	Type	Symbol (original)	Symbol (LIISim)	a ₀	Unit
Molar mass	molar_mass	const	-	M_g	0.02874	kg mol ⁻¹

Heat transfer model (HTM_Liu)

Evaporation

$$\dot{Q}_{\text{evap}} = -\frac{\Delta H_v}{M_v} \dot{m}_{\text{evap}} \quad (\text{D-9})$$

$$\dot{m}_{\text{evap}} = -\frac{\pi d_p^2 M_v \theta_e p_v}{RT_p} \left(\frac{RT_p}{2\pi M_v} \right)^K \quad (\text{D-10})$$

with $K = 0.5$

Conduction

$$\dot{Q}_{\text{cond}} = \frac{\pi d_p^2 \alpha_T p_0}{2T_g} \sqrt{\frac{RT_g}{2\pi M_{\text{mix}}}} \left(\frac{\gamma^* + 1}{\gamma^* - 1} \right) (T_p - T_g) \quad (\text{D-11})$$

$$\frac{1}{\gamma^* - 1} = \frac{1}{T - T_0} \int_{T_0}^T \frac{1}{\gamma(T') - 1} dT' \quad (\text{D-12})$$

This heat transfer model uses polynomial fitting coefficients for the calculation of $\gamma(T)$. These are provided through the “gamma_eqn” property of the LIISim implementation in the GasMixture database. If $\gamma(T)$ is not defined, the heat capacity of the gas mixture $C_{p,\text{mix}}(T)$ is used to calculate $\gamma(T)$ according to

$$\gamma(T) = \frac{C_{p,\text{mix}}(T)}{C_{p,\text{mix}}(T) - R}. \quad (\text{D-13})$$

Radiation

$$\dot{Q}_{\text{rad}} = \frac{199\pi^3 d_p^3 (k_B T)^5 \epsilon}{h(hc)^3} \quad (\text{D-14})$$

Melton model

Materials properties (Soot_Melton(Workshop))

Name	Variable	Type	Symbol (original)	Symbol (LIISim)	a_0	Unit
Accommodation coefficient	alpha_T_eff	const	α_T	α_T	0.3	—
Accommodation coefficient	theta_e	const	α_M	θ_e	1.0	—
Molar heat capacity ^a	C_p_mol	const	—	$C_{p,\text{mol}}$	22.8	J mol ⁻¹ K ⁻¹
Molar mass	molar_mass	const	W_s	M_p	0.012	kg mol ⁻¹
Molar mass of vapor	molar_mass_v	const	W_v	M_v	0.036	kg mol ⁻¹
Density	rho_p	const	ρ_s	ρ_p	2260	kg m ⁻³
Enthalpy of evaporation	H_v	const	ΔH_v	ΔH_v	7.78×10^5	J mol ⁻¹
Reference pressure ^b	p_v_ref	const	p_{ref}	p_v^*	100000	Pa
Reference temperature ^b	T_v_ref	const	T_{ref}	T_v^*	3915	K

^a calculated from given c_s : $C_{p,\text{mol}} = c_{s,\text{Melton}} M_p$

^b Clausius-Clapeyron

Gas mixture properties (Melton-Nitrogen-100%)

Composition

Gas	Variable	Symbol	Fraction
Nitrogen_Melton	x	x	1.0

Properties (manually set for this composition)

Name	Variable	Type	Symbol (original/ LIISim)	a_0	a_1	Unit (original)	Unit (LIISim)
Thermal conductivity	therm_cond	const	κ_a	0.1068	–	$\text{W cm}^{-1} \text{K}^{-1}$	$\text{W m}^{-1} \text{K}^{-1}$
Mean free path	L	poly ^a	L	–	2.355×10^{-10}	cm	m

$$^a f(T) = a_0 + a_1 T + a_2 T^2 + a_3 T^3 + a_4 T^4 + a_5 T^5 + a_6 T^6 + a_7 T^7 + a_8 T^8$$

Gas properties (Nitrogen_Melton)

Name	Variable	Type	Symbol (original)	Symbol (LIISim)	a_0	Unit
Molar heat capacity ^a	C_p_mol	const	–	$C_{p,g}$	36.0295	$\text{J mol}^{-1} \text{K}^{-1}$

$$^a \text{ calculated from given } \gamma(1800K) = 1.3 = \frac{C_p}{C_p - R} \Rightarrow C_p = \frac{1.3}{0.3} R$$

Heat transfer model (HTM_Melton)

Evaporation

$$\dot{Q}_{\text{evap}} = - \frac{\Delta H_v}{M_p} \dot{u}_{\text{evap}} \quad (\text{D-15})$$

This model uses molar mass of solid species in equation (D-18).

$$\dot{u}_{\text{evap}} = - \frac{\pi d_p^2 M_v \theta_e p_v}{R T_p} \left(\frac{R T_p}{2 M_v} \right)^{0.5} \quad (\text{D-16})$$

$$p_v = p_v^* \exp \left(- \frac{\Delta H_v}{R} \left(\frac{1}{T_p} - \frac{1}{T_v^*} \right) \right) \quad (\text{D-17})$$

Conduction

$$\dot{Q}_{\text{cond}} = \frac{2 \kappa_a \pi d_p^2}{d_p + G L(T_g)} (T_p - T_g) \quad (\text{D-18})$$

$$G = \frac{8f}{\alpha_T(\gamma + 1)} \quad (\text{D-19})$$

$$f = \frac{9\gamma - 5}{4} \quad (\text{D-20})$$

Radiation

Not included in this model.

Appendix E LIISim – Example for heat transfer model implementation

This section demonstrates the simplicity of the implementation or modification of heat transfer models in the LIISim software. While the databases can be easily edited within the graphical user interface, the heat transfer models are individually implemented as subclasses of the “HeatTransferModel” class. The subclass has access to the selected databases through the `material`, or `gasmixture` objects (as a function of temperature) or to the process conditions (e.g., gas temperature and pressure) through `process`. The heat transfer rates can be implemented as functions of particle temperature and diameter, which are used in the heat transfer model main class to solve the system of ordinary differential equations.

A detailed description of all steps and file locations is summarized in the developer guide available through www.liisim.com.

Materials database

Property	Type	a_0	a_1	a_2	a_3	a_4	a_5	a_6	a_7	a_8	Unit	Equation
alpha_T_eff	const	0.23									[-]	$f(T) = \alpha_0$
C_p_mol	poly2	22.5566	0.0013	0	0	0	-1.8195...				[J/mol/K]	$f(T) = \alpha_0 + \alpha_1 T + \alpha_2 T^2 + \alpha_3 T^3 + \alpha_4 T^{-1} + \alpha_5 T^{-2}$
H_v	const	790777									[J/mol]	$f(T) = \alpha_0$
molar_mass	const	0.012011									[kg/mol]	$f(T) = \alpha_0$
molar_mass...	const	0.036033									[kg/mol]	$f(T) = \alpha_0$
rho_p	const	1860									[kg/m^3]	$f(T) = \alpha_0$
theta_e	const	1									[-]	$f(T) = \alpha_0$
p_v	notSet										[Pa]	
p_v_ref	const	61.5									[Pa]	$f(T) = \alpha_0$
T_v_ref	const	3000									[K]	$f(T) = \alpha_0$
eps	const	1									[-]	$f(T) = \alpha_0$
Em_func	optics_lam	1	0	0	0	0	0	0	0	0	[-]	$f(\lambda) = \alpha_0 + \alpha_1 \lambda + \alpha_2 \lambda^2 + \alpha_3 \lambda^3 + \alpha_4 \lambda^4 + \alpha_5 \lambda^5$
omega_p	notSet										[rad/s]	
tau	notSet										[s]	
+ Em												

Calculated properties:			
Property	Value	Unit	Description
<i>vapor pressure is calculated by Clausius-Clapeyron equation ($T^* = 3000\text{ K}$ and $p^* = 61.5\text{ Pa}$) using $H_v(T)$</i>			
vapor_pressure(293 K)	3.83783e-126	[Pa]	Vapor pressure at 293 K
vapor_pressure(1500 K)	1.04832e-12	[Pa]	Vapor pressure at 1500 K
vapor_pressure(3000 K)	61.5	[Pa]	Vapor pressure at 3000 K
vapor_pressure(4000 K)	170204	[Pa]	Vapor pressure at 4000 K
vapor_pressure(5000 K)	1.978e+7	[Pa]	Vapor pressure at 5000 K

Figure E-1 Graphical user interface for editing database properties (Materials).

Name: Nitrogen_Kock File: gases/Nitrogen_Kock.txt Open file
Description: Apply changes

Property	Type	a_0	a_1	a_2	a_3	a_4	a_5	a_6	a_7	a_8	Unit	Equation
alpha_T	notSet										[\cdot]	
C_p_mol	poly2	28.58	0.00377	0	0	0	-50000				[J/mol/K]	$f(T) = a_0 + a_1T + a_2T^2 + a_3T^3 + a_4T^{-1} + \dots$
molar_mass	const	0.028014									[kg/mol]	$f(T) = a_0$
zeta	notSet										[\cdot]	

Figure E-2 Graphical user interface for editing database properties (Gases).

Name: Kock-Nitrogen-100% File: gasmixtures/Kock_N2_100.txt Open file
Description: Apply changes

Gas	Fraction	Unit
Nitrogen_Kock	1	X
+		

Properties (manually set):

Property	Type	a_0	a_1	a_2	a_3	a_4	a_5	a_6	a_7	a_8	Unit	Equation
L	notS										[m]	
gamma_eqn	notS										[\cdot]	
therm_cond	notS										[W/m/K]	

Calculated properties:

Property	Value	Unit	Description
molar_mass	0.028014	[kg/mol]	Molar mass of gas mixture
c_tg(293 K)	470.58	[m/s]	Thermal velocity of gas molecules at 293 K
c_tg(1500 K)	1064.74	[m/s]	Thermal velocity of gas molecules at 1500 K
C_p_mol(293 K)	29.1022	[J/mol/K]	Molar heat capacity at 293 K
C_p_mol(1500 K)	34.2128	[J/mol/K]	Molar heat capacity at 1500 K
c_p_kg(293 K)	1038.84	[J/kg/K]	Specific heat capacity at 293 K
c_p_kg(1500 K)	1221.27	[J/kg/K]	Specific heat capacity at 1500 K
gamma(293 K)	1.39997	[\cdot]	Heat-capacity ratio: gamma(T) = Cp(T) / (Cp(T) - R) at 293 K
gamma(1500 K)	1.32104	[\cdot]	Heat-capacity ratio: gamma(T) = Cp(T) / (Cp(T) - R) at 1500 K

Figure E-3 Graphical user interface for editing database properties (GasMixture).

HeatTransferModel subclass functions (Kock model)

```

/***
 * @brief HTM_KockSoot::calculateEvaporation Heat transfer by evaporation
 * @param T Particle temperature [K]
 * @param dp Particle diameter [m]
 * @return q Heat transfer rate [J/s]
 */
double HTM_KockSoot::calculateEvaporation(double T, double dp)
{
    if(!useEvaporation) return 0.0;

    return -1.0 * material.H_v(T) / material.molar_mass_v(T)
           * calculateMassLossEvap(T, dp);
}

/***
 * @brief HTM_KockSoot::calculateMassLoss Mass loss by evaporation
 * @param T Particle temperature [K]
 * @param dp Particle diameter [m]
 * @return u_evap Mass loss due to evaporation [kg/s]
 */
double HTM_KockSoot::calculateMassLossEvap(double T, double dp)
{
    if(!useEvaporation) return 0.0;

    // Calculate vapor pressure by Clausius-Clapeyron equation
    // Uses molar mass of vapor species (C3)

    double vapor_density = material.vapor_pressure(T)
        * material.molar_mass_v(T)
        / Constants::R
        / T;

    return -0.25 * Constants::pi
           * material.theta_e(T)
           * dp * dp
           * material.c_tv(T)
           * vapor_density;
}

```

```
/***
 * @brief HTM_KockSoot::calculateConduction Heat transfer by conduction
 * @param T      Particle temperature [K]
 * @param dp     Particle diameter [m]
 * @return q     Heat transfer rate [J/s]
 */
double HTM_KockSoot::calculateConduction(double T, double dp)
{
    if(!useConduction) return 0.0;

    double T_g = process.T_g;

    return material.alpha_T_eff(T)
        * Constants::pi
        * dp * dp
        * process.p_g / 8.0
        * gasmixture.c_tg(T_g)
        * (gasmixture.gamma(T_g) + 1.0)
        / (gasmixture.gamma(T_g) - 1.0)
        * (T / T_g - 1.0);
}

/***
 * @brief HTM_KockSoot::calculateRadiation Heat transfer by thermal radiation
 * @param T      Particle temperature [K]
 * @param dp     Particle diameter [m]
 * @return q     Heat transfer rate [J/s]
 */
double HTM_KockSoot::calculateRadiation(double T, double dp)
{
    if(!useRadiation) return 0.0;

    return Constants::pi
        * dp * dp
        * material.eps(T)
        * Constants::sigma
        * (pow(T, 4) - pow(process.T_g, 4));
}
```

BIBLIOGRAPHY

1. Wu, M.K., R.S. Windeler, C.K.R. Steiner, T. Börs, and S.K. Friedlander, *Controlled Synthesis of Nanosized Particles by Aerosol Processes*. Aerosol Science and Technology, 1993. **19**(4): p. 527-548.
2. Schulz, C., B.F. Kock, M. Hofmann, H. Michelsen, S. Will, B. Bougie, R. Suntz, and G. Smallwood, *Laser-induced incandescence: recent trends and current questions*. Applied Physics B, 2006. **83**(3): p. 333-354.
3. Michelsen, H.A., C. Schulz, G.J. Smallwood, and S. Will, *Laser-induced incandescence: Particulate diagnostics for combustion, atmospheric, and industrial applications*. Progress in Energy and Combustion Science, 2015. **51**: p. 2-48.
4. Vander Wal, R.L., *Laser-induced incandescence: detection issues*. Applied Optics, 1996. **35**(33): p. 6548-6559.
5. Choi, M.Y. and K.A. Jensen, *Calibration and correction of laser-induced incandescence for soot volume fraction measurements*. Combustion and Flame, 1998. **112**(4): p. 485-491.
6. Vander Wal, R.L. and K.A. Jensen, *Laser-induced incandescence: excitation intensity*. Applied Optics, 1998. **37**(9): p. 1607-1616.
7. Charwath, M., R. Suntz, and H. Bockhorn, *Influence of the temporal response of the detection system on time-resolved laser-induced incandescence signal evolutions*. Applied Physics B, 2006. **83**(3): p. 435-442.
8. Smallwood, G.J., *A critique of laser-induced incandescence for the measurement of soot*. 2008.
9. Snelling, D.R., G.J. Smallwood, F. Liu, Ö.L. Gülder, and W.D. Bachalo, *A calibration-independent laser-induced incandescence technique for soot measurement by detecting absolute light intensity*. Applied Optics, 2005. **44**(31): p. 6773-6785.
10. Vander Wal, R.L., *Laser-induced incandescence: excitation and detection conditions, material transformations and calibration*. Applied Physics B, 2009. **96**(4): p. 601-611.
11. Goulay, F., P.E. Schrader, X. López-Yglesias, and H.A. Michelsen, *A data set for validation of models of laser-induced incandescence from soot: temporal profiles of LII signal and particle temperature*. Applied Physics B, 2013. **112**(3): p. 287-306.
12. Daun, K., J. Menser, R. Mansmann, S.T. Moghaddam, T. Dreier, and C. Schulz, *Spectroscopic models for laser-heated silicon and copper nanoparticles*. Journal of Quantitative Spectroscopy and Radiative Transfer, 2017. **197**: p. 3-11.
13. Menser, J., K. Daun, T. Dreier, and C. Schulz, *Laser-induced incandescence from laser-heated silicon nanoparticles*. Applied Physics B, 2016. **122**(11): p. 277.
14. Hofmann, A.M., *Laser-induced incandescence for soot diagnostics at high pressure*. 2006, Heidelberg University.
15. Hofmann, M., B. Kock, and C. Schulz. *A web-based interface for modeling laser-induced incandescence (LII-Sim)*. in *Proceedings of the European Combustion Meeting*. 2007. Kreta.
16. Weeks, R.W. and W.W. Duley, *Aerosol - particle sizes from light emission during excitation by TEA CO₂ laser pulses*. Journal of Applied Physics, 1974. **45**(10): p. 4661-4662.

17. Eckbreth, A.C., *Effects of laser - modulated particulate incandescence on Raman scattering diagnostics*. Journal of Applied Physics, 1977. **48**(11): p. 4473-4479.
18. Melton, L.A., *Soot diagnostics based on laser heating*. Applied Optics, 1984. **23**(13): p. 2201-2208.
19. Michelsen, H.A., F. Liu, B.F. Kock, H. Bladh, A. Boiarcicu, M. Charwath, T. Dreier, R. Hadef, M. Hofmann, J. Reimann, S. Will, P.E. Bengtsson, H. Bockhorn, F. Foucher, K.P. Geigle, C. Mounaïm-Rousselle, C. Schulz, R. Stirn, B. Tribalet, and R. Suntz, *Modeling laser-induced incandescence of soot: a summary and comparison of LII models*. Applied Physics B, 2007. **87**(3): p. 503-521.
20. Vander Wal, R.L. and K.J. Weiland, *Laser-induced incandescence: Development and characterization towards a measurement of soot-volume fraction*. Applied Physics B, 1994. **59**(4): p. 445-452.
21. Mewes, B. and J.M. Seitzman, *Soot volume fraction and particle size measurements with laser-induced incandescence*. Applied Optics, 1997. **36**(3): p. 709-717.
22. De Iuliis, S., F. Migliorini, F. Cignoli, and G. Zizak, *2D soot volume fraction imaging in an ethylene diffusion flame by two-color laser-induced incandescence (2C-LII) technique and comparison with results from other optical diagnostics*. Proceedings of the Combustion Institute, 2007. **31**(1): p. 869-876.
23. Quay, B., T.W. Lee, T. Ni, and R.J. Santoro, *Spatially resolved measurements of soot volume fraction using laser-induced incandescence*. Combustion and Flame, 1994. **97**(3): p. 384-392.
24. Ni, T., J.A. Pinson, S. Gupta, and R.J. Santoro, *Two-dimensional imaging of soot volume fraction by the use of laser-induced incandescence*. Applied Optics, 1995. **34**(30): p. 7083-7091.
25. Crua, C., D.A. Kennaird, and M.R. Heikal, *Laser-induced incandescence study of diesel soot formation in a rapid compression machine at elevated pressures*. Combustion and Flame, 2003. **135**(4): p. 475-488.
26. Boiarcicu, A., F. Foucher, C. Mounaïm-Rousselle, and O. Pajot, *Estimate Measurement of Soot Diameter and Volume Fraction Inside the Bowl of a DirectInjection-Compression-Ignition Engine: Effect of the Exhaust Gas Recirculation*. Combustion Science and Technology, 2007. **179**(8): p. 1631-1648.
27. Bougie, B., L.C. Ganippa, A.P. van Vliet, W.L. Meerts, N.J. Dam, and J.J. ter Meulen, *Soot particulate size characterization in a heavy-duty diesel engine for different engine loads by laser-induced incandescence*. Proceedings of the Combustion Institute, 2007. **31**(1): p. 685-691.
28. Cenker, E., K. Kondo, G. Bruneaux, T. Dreier, T. Aizawa, and C. Schulz, *Assessment of soot particle-size imaging with LII at Diesel engine conditions*. Applied Physics B, 2015. **119**(4): p. 765-776.
29. Cenker, E., *Imaging measurements of soot particle size and soot volume fraction with laser-induced incandescence at Diesel engine conditions*, in *Engineering Sciences [physics]*. 2014, Ecole Centrale Paris.
30. Oger, B., *Soot characterisation in diesel engines using laser-induced incandescence*. 2012, University of Brighton.
31. Bakker, P.C., R.C. Willems, and N.J. Dam, *Implementation of High-Speed Laser-Induced Incandescence Imaging in CI Engines*. SAE Technical Paper 2016-01-0725, 2016.
32. Geitlinger, H., T. Streibel, R. Suntz, and H. Bockhorn, *Two-dimensional imaging of soot volume fractions, particle number densities, and particle radii in laminar and turbulent diffusion flames*. Symposium (International) on Combustion, 1998. **27**(1): p. 1613-1621.

33. Snelling, D.R., K.A. Thomson, G.J. Smallwood, and Ö.L. Gülder, *Two-dimensional imaging of soot volume fraction in laminar diffusion flames*. Applied Optics, 1999. **38**(12): p. 2478-2485.
34. Boiarciuc, A., F. Foucher, and C. Mounaïm-Rousselle, *Soot volume fractions and primary particle size estimate by means of the simultaneous two-color-time-resolved and 2D laser-induced incandescence*. Applied Physics B, 2006. **83**(3): p. 413-421.
35. Crosland, B.M., M.R. Johnson, and K.A. Thomson, *Analysis of uncertainties in instantaneous soot volume fraction measurements using two-dimensional, auto-compensating, laser-induced incandescence (2D-AC-LII)*. Applied Physics B, 2011. **102**(1): p. 173-183.
36. Will, S., S. Schraml, and A. Leipertz, *Two-dimensional soot-particle sizing by time-resolved laser-induced incandescence*. Optics Letters, 1995. **20**(22): p. 2342-2344.
37. Roth, P. and A.V. Filippov, *In situ ultrafine particle sizing by a combination of pulsed laser heatup and particle thermal emission*. Journal of Aerosol Science, 1996. **27**(1): p. 95-104.
38. Rohlfing, E.A. and D.W. Chandler, *Two-color pyrometric imaging of laser-heated carbon particles in a supersonic flow*. Chemical Physics Letters, 1990. **170**(1): p. 44-50.
39. Snelling, D.R., F. Liu, G.J. Smallwood, and Ö.L. Gülder, *Determination of the soot absorption function and thermal accommodation coefficient using low-fluence LII in a laminar coflow ethylene diffusion flame*. Combustion and Flame, 2004. **136**(1-2): p. 180-190.
40. Lehre, T., R. Suntz, and H. Bockhorn, *Time-resolved two-color LII: size distributions of nanoparticles from gas-to-particle synthesis*. Proceedings of the Combustion Institute, 2005. **30**(2): p. 2585-2593.
41. De Iuliis, S., F. Cignoli, and G. Zizak, *Two-color laser-induced incandescence (2C-LII) technique for absolute soot volume fraction measurements in flames*. Applied Optics, 2005. **44**(34): p. 7414-7423.
42. Kock, B.F., C. Kayan, J. Knipping, H.R. Orthner, and P. Roth, *Comparison of LII and TEM sizing during synthesis of iron particle chains*. Proceedings of the Combustion Institute, 2005. **30**(1): p. 1689-1697.
43. McManus, K., J. Frank, M. Allen, and W. Rawlins, *Characterization of laser-heated soot particles using optical pyrometry*. 36th AIAA Aerospace Sciences Meeting and Exhibit, AIAA 98-0159, 1998. **36**.
44. Bohren, C.F. and D.R. Huffman, *Absorption and scattering of light by small particles*. 2008: John Wiley & Sons.
45. Mishchenko, M.I., L.D. Travis, and A.A. Lacis, *Scattering, absorption, and emission of light by small particles*. 2002: Cambridge university press.
46. Bescond, A., J. Yon, F.X. Ouf, C. Rozé, A. Coppalle, P. Parent, D. Ferry, and C. Laffon, *Soot optical properties determined by analyzing extinction spectra in the visible near-UV: Toward an optical speciation according to constituents and structure*. Journal of Aerosol Science, 2016. **101**: p. 118-132.
47. Thomson, K.A., M.R. Johnson, D.R. Snelling, and G.J. Smallwood, *Diffuse-light two-dimensional line-of-sight attenuation for soot concentration measurements*. Applied Optics, 2008. **47**(5): p. 694-703.
48. Kempema, N.J., B. Ma, and M.B. Long, *Investigation of in-flame soot optical properties in laminar coflow diffusion flames using thermophoretic particle sampling and spectral light extinction*. Applied Physics B, 2016. **122**(9): p. 232.

49. Goulay, F., P.E. Schrader, and H.A. Michelsen, *Effect of the wavelength dependence of the emissivity on inferred soot temperatures measured by spectrally resolved laser-induced incandescence*. Applied Physics B, 2010. **100**(3): p. 655-663.
50. Maffi, S., S. De Iuliis, F. Cignoli, and G. Zizak, *Investigation on thermal accommodation coefficient and soot absorption function with two-color Tire-LII technique in rich premixed flames*. Applied Physics B, 2011. **104**(2): p. 357-366.
51. Liu, F., M. Yang, F.A. Hill, D.R. Snelling, and G.J. Smallwood, *Influence of polydisperse distributions of both primary particle and aggregate size on soot temperature in low-fluence LII*. Applied Physics B, 2006. **83**(3): p. 383-395.
52. Filippov, A.V., M. Zurita, and D.E. Rosner, *Fractal-like Aggregates: Relation between Morphology and Physical Properties*. Journal of Colloid and Interface Science, 2000. **229**(1): p. 261-273.
53. Liu, F. and G.J. Smallwood, *Effect of aggregation on the absorption cross-section of fractal soot aggregates and its impact on LII modelling*. Journal of Quantitative Spectroscopy and Radiative Transfer, 2010. **111**(2): p. 302-308.
54. Snelling, D.R., O. Link, K.A. Thomson, and G.J. Smallwood, *Measurement of soot morphology by integrated LII and elastic light scattering*. Applied Physics B, 2011. **104**(2): p. 385-397.
55. Bladh, H., J. Johnsson, J. Rissler, H. Abdulhamid, N.E. Olofsson, M. Sanati, J. Pagels, and P.E. Bengtsson, *Influence of soot particle aggregation on time-resolved laser-induced incandescence signals*. Applied Physics B, 2011. **104**(2): p. 331-341.
56. Johnsson, J., H. Bladh, N.E. Olofsson, and P.E. Bengtsson, *Influence of soot aggregate structure on particle sizing using laser-induced incandescence: importance of bridging between primary particles*. Applied Physics B, 2013. **112**(3): p. 321-332.
57. Yon, J., E. Therssen, F. Liu, S. Bejaoui, and D. Hebert, *Influence of soot aggregate size and internal multiple scattering on LII signal and the absorption function variation with wavelength determined by the TEW-LII method*. Applied Physics B, 2015. **119**(4): p. 643-655.
58. Kempema, N.J. and M.B. Long, *Combined optical and TEM investigations for a detailed characterization of soot aggregate properties in a laminar coflow diffusion flame*. Combustion and Flame, 2016. **164**: p. 373-385.
59. Lemaire, R. and M. Mobtil, *Modeling laser-induced incandescence of soot: a new approach based on the use of inverse techniques*. Applied Physics B, 2015. **119**(4): p. 577-606.
60. Mitrani, J.M., M.N. Shneider, B.C. Stratton, and Y. Raitses, *Modeling thermionic emission from laser-heated nanoparticles*. Applied Physics Letters, 2016. **108**(5): p. 054101.
61. Michelsen, H.A., M.A. Linne, B.F. Kock, M. Hofmann, B. Tribalet, and C. Schulz, *Modeling laser-induced incandescence of soot: enthalpy changes during sublimation, conduction, and oxidation*. Applied Physics B, 2008. **93**(2-3): p. 645-656.
62. Michelsen, H.A., *Understanding and predicting the temporal response of laser-induced incandescence from carbonaceous particles*. The Journal of Chemical Physics, 2003. **118**(15): p. 7012-7045.
63. Liu, F., B.J. Stagg, D.R. Snelling, and G.J. Smallwood, *Effects of primary soot particle size distribution on the temperature of soot particles heated by a nanosecond pulsed laser in an atmospheric laminar diffusion flame*. International Journal of Heat and Mass Transfer, 2006. **49**(3-4): p. 777-788.

64. Liu, F. and G.J. Smallwood, *Relationship between soot volume fraction and LII signal in AC-LII: effect of primary soot particle diameter polydispersity*. Applied Physics B, 2013. **112**(3): p. 307-319.
65. Cenker, E., G. Bruneaux, T. Dreier, and C. Schulz, *Determination of small soot particles in the presence of large ones from time-resolved laser-induced incandescence*. Applied Physics B, 2014. **118**(2): p. 169-183.
66. Kuhlmann, S.A., J. Reimann, and S. Will, *On heat conduction between laser-heated nanoparticles and a surrounding gas*. Journal of Aerosol Science, 2006. **37**(12): p. 1696-1716.
67. Liu, F., S. Rogak, D.R. Snelling, M. Saffaripour, K.A. Thomson, and G.J. Smallwood, *Effects of laser fluence non-uniformity on ambient-temperature soot measurements using the auto-compensating laser-induced incandescence technique*. Applied Physics B, 2016. **122**(11): p. 286.
68. Bladh, H., J. Johnsson, and P.E. Bengtsson, *Influence of spatial laser energy distribution on evaluated soot particle sizes using two-colour laser-induced incandescence in a flat premixed ethylene/air flame*. Applied Physics B, 2009. **96**(4): p. 645-656.
69. Hadwin, P.J., T.A. Sipkens, K.A. Thomson, F. Liu, and K.J. Daun, *Quantifying uncertainty in auto-compensating laser-induced incandescence parameters due to multiple nuisance parameters*. Applied Physics B, 2017. **123**(4): p. 114.
70. Delhay, J., Y. Bouvier, E. Therssen, J.D. Black, and P. Desgroux, *2D imaging of laser wing effects and of soot sublimation in laser-induced incandescence measurements*. Applied Physics B, 2005. **81**(2-3): p. 181-186.
71. Yon, J., R. Lemaire, E. Therssen, P. Desgroux, A. Coppalle, and K.F. Ren, *Examination of wavelength dependent soot optical properties of diesel and diesel/rapeseed methyl ester mixture by extinction spectra analysis and LII measurements*. Applied Physics B, 2011. **104**(2): p. 253-271.
72. Bejaoui, S., R. Lemaire, P. Desgroux, and E. Therssen, *Experimental study of the $E(m, \lambda)/E(m, 1064)$ ratio as a function of wavelength, fuel type, height above the burner and temperature*. Applied Physics B, 2013. **116**(2): p. 313-323.
73. Cléon, G., T. Amodeo, A. Faccinetto, and P. Desgroux, *Laser induced incandescence determination of the ratio of the soot absorption functions at 532 nm and 1064 nm in the nucleation zone of a low pressure premixed sooting flame*. Applied Physics B, 2011. **104**(2): p. 297-305.
74. López-Yglesias, X., P.E. Schrader, and H.A. Michelsen, *Soot maturity and absorption cross sections*. Journal of Aerosol Science, 2014. **75**: p. 43-64.
75. Simonsson, J., N.-E. Olofsson, S. Török, P.-E. Bengtsson, and H. Bladh, *Wavelength dependence of extinction in sooting flat premixed flames in the visible and near-infrared regimes*. Applied Physics B, 2015. **119**(4): p. 657-667.
76. Tait, N.P. and D.A. Greenhalgh, *PLIF Imaging of Fuel Fraction in Practical Devices and LII Imaging of Soot*. Berichte der Bunsengesellschaft für physikalische Chemie, 1993. **97**(12): p. 1619-1624.
77. Hofmann, M., W.G. Bessler, C. Schulz, and H. Jander, *Laser-induced incandescence for soot diagnostics at high pressures*. Applied Optics, 2003. **42**(12): p. 2052-2062.
78. Liu, F., D.R. Snelling, K.A. Thomson, and G.J. Smallwood, *Sensitivity and relative error analyses of soot temperature and volume fraction determined by two-color LII*. Applied Physics B, 2009. **96**(4): p. 623-636.
79. Bengtsson, P.-E. and M. Alden, *C₂ Production and Excitation in Sooting Flames using Visible Laser Radiation: Implications for Diagnostics in Sooting Flames*. Combustion Science and Technology, 1991. **77**(4-6): p. 307-318.

80. Goulay, F., P.E. Schrader, L. Nemes, M.A. Dansson, and H.A. Michelsen, *Photochemical interferences for laser-induced incandescence of flame-generated soot*. Proceedings of the Combustion Institute, 2009. **32**(1): p. 963-970.
81. Goulay, F., L. Nemes, P.E. Schrader, and H.A. Michelsen, *Spontaneous emission from C²(d³Π_g) and C³(A¹Π_u) during laser irradiation of soot particles*. Molecular Physics, 2010. **108**(7-9): p. 1013-1025.
82. Vander Wal, R.L., T.M. Ticich, and J.R. West, *Laser-induced incandescence applied to metal nanostructures*. Applied Optics, 1999. **38**(27): p. 5867-5879.
83. Murakami, Y., T. Sugatani, and Y. Nosaka, *Laser-Induced Incandescence Study on the Metal Aerosol Particles as the Effect of the Surrounding Gas Medium*. The Journal of Physical Chemistry A, 2005. **109**(40): p. 8994-9000.
84. Maffi, S., F. Cignoli, C. Bellomunno, S. De Iuliis, and G. Zizak, *Spectral effects in laser induced incandescence application to flame-made titania nanoparticles*. Spectrochimica Acta Part B: Atomic Spectroscopy, 2008. **63**(2): p. 202-209.
85. Flügel, A., J. Kiefer, S. Will, and A. Leipertz, *Broadband Two-Color Laser-Induced Incandescence Pyrometry Approach for Nanoparticle Characterization with Improved Sensitivity*. Applied Spectroscopy, 2013. **67**(9): p. 1098-1100.
86. Shaddix, C.R. and K.C. Smyth, *Laser-induced incandescence measurements of soot production in steady and flickering methane, propane, and ethylene diffusion flames*. Combustion and Flame, 1996. **107**(4): p. 418-452.
87. Schraml, S., S. Dankers, K. Bader, S. Will, and A. Leipertz, *Soot temperature measurements and implications for time-resolved laser-induced incandescence (TIRE-LII)*. Combustion and Flame, 2000. **120**(4): p. 439-450.
88. Bryce, D.J., N. Ladommato, and H. Zhao, *Quantitative investigation of soot distribution by laser-induced incandescence*. Applied Optics, 2000. **39**(27): p. 5012-5022.
89. Witze, P.O., S. Hochgreb, D. Kayes, H.A. Michelsen, and C.R. Shaddix, *Time-resolved laser-induced incandescence and laser elastic-scattering measurements in a propane diffusion flame*. Applied Optics, 2001. **40**(15): p. 2443-2452.
90. Appel, J., B. Jungfleisch, M. Marquardt, R. Suntz, and H. Bockhorn, *Assessment of soot volume fractions from laser-induced incandescence by comparison with extinction measurements in laminar, premixed, flat flames*. Symposium (International) on Combustion, 1996. **26**(2): p. 2387-2395.
91. Axelsson, B., R. Collin, and P.-E. Bengtsson, *Laser-induced incandescence for soot particle size measurements in premixed flat flames*. Applied Optics, 2000. **39**(21): p. 3683-3690.
92. Axelsson, B., R. Collin, and P.E. Bengtsson, *Laser-induced incandescence for soot particle size and volume fraction measurements using on-line extinction calibration*. Applied Physics B, 2001. **72**(3): p. 367-372.
93. Geigle, K.P., Y. Schneider-Kühnle, M.S. Tsurikov, R. Hadef, R. Lütterath, V. Krüger, W. Stricker, and M. Aigner, *Investigation of laminar pressurized flames for soot model validation using SV-CARS and LII*. Proceedings of the Combustion Institute, 2005. **30**(1): p. 1645-1653.
94. Hofmann, M., B.F. Kock, T. Dreier, H. Jander, and C. Schulz, *Laser-induced incandescence for soot-particle sizing at elevated pressure*. Applied Physics B, 2007. **90**(3-4): p. 629-639.
95. Hadef, R., K.P. Geigle, W. Meier, and M. Aigner, *Soot characterization with laser-induced incandescence applied to a laminar premixed ethylene-air flame*. International Journal of Thermal Sciences, 2010. **49**(8): p. 1457-1467.

96. Leschowski, M., *Ruß-Diagnostik in laminaren vorgemischten Hochdruckflammen: Kombination von laserinduzierter Inkandeszenz (LII) mit optischen und konventionellen diagnostischen Methoden*. 2016, University of Duisburg-Essen.
97. Geitlinger, H., T.H. Streibel, R. Suntz, and H. Bockhorn, *Statistical Analysis of Soot Volume Fractions, Particle Number Densities and Particle Radii in a Turbulent Diffusion Flame*. Combustion Science and Technology, 1999. **149**(1-6): p. 115-134.
98. Sun, Z.W., Z.T. Alwahabi, D.H. Gu, S.M. Mahmoud, G.J. Nathan, and B.B. Dally, *Planar laser-induced incandescence of turbulent sooting flames: the influence of beam steering and signal trapping*. Applied Physics B, 2015. **119**(4): p. 731-743.
99. Vander Wal, R.L. and D.L. Dietrich, *Laser-induced incandescence applied to droplet combustion*. Applied Optics, 1995. **34**(6): p. 1103-1107.
100. Case, M.K. and D.L. Hofeldt, *Soot Mass Concentration Measurements in Diesel Engine Exhaust Using Laser-Induced Incandescence*. Aerosol Science and Technology, 1996. **25**(1): p. 46-60.
101. Kock, B., B. Tribalet, C. Schulz, and P. Roth, *Two-color time-resolved LII applied to soot particle sizing in the cylinder of a Diesel engine*. Combustion and Flame, 2006. **147**(1-2): p. 79-92.
102. Kock, B.F., *Zeitaufgelöste Laserinduzierte Inkandeszenz (TR-LII): Partikelgrößenmessung in einem Dieselmotor und einem Gasphasenreaktor*. 2006, Cuvillier Verlag.
103. Woiki, D., A. Giesen, and P. Roth, *Time-resolved laser-induced incandescence for soot particle sizing during acetylene pyrolysis behind shock waves*. Proceedings of the Combustion Institute, 2000. **28**(2): p. 2531-2537.
104. Chan, T.W., J.R. Brook, G.J. Smallwood, and G. Lu, *Time-resolved measurements of black carbon light absorption enhancement in urban and near-urban locations of southern Ontario, Canada*. Atmospheric Chemistry and Physics, 2011. **11**(20): p. 10407-10432.
105. Liggio, J., M. Gordon, G. Smallwood, S.-M. Li, C. Stroud, R. Staebler, G. Lu, P. Lee, B. Taylor, and J.R. Brook, *Are Emissions of Black Carbon from Gasoline Vehicles Underestimated? Insights from Near and On-Road Measurements*. Environmental Science & Technology, 2012. **46**(9): p. 4819-4828.
106. Yatom, S., J. Bak, A. Khrabryi, and Y. Raitses, *Detection of nanoparticles in carbon arc discharge with laser-induced incandescence*. Carbon, 2017. **117**: p. 154-162.
107. Gurentsov, E.V., A.V. Eremin, and E.Y. Mikheyeva, *Study of thermodynamic properties of carbon nanoparticles by the laser heating method*. High Temperature, 2017. **55**(5): p. 723-730.
108. Dankers, S., A. Leipertz, S. Will, J. Arndt, K. Vogel, S. Schraml, and A. Hemm, *In-situ Measurement of Primary Particle Sizes during Carbon Black Production*. Chemical Engineering & Technology, 2003. **26**(9): p. 966-969.
109. Leipertz, A. and S. Dankers, *Characterization of Nano-Particles Using Laser-Induced Incandescence*. Particle & Particle Systems Characterization, 2003. **20**(2): p. 81-93.
110. Vander Wal, R.L., G.M. Berger, T.M. Ticich, and P.D. Patel, *Application of laser-induced incandescence to the detection of carbon nanotubes and carbon nanofibers*. Applied Optics, 2002. **41**(27): p. 5678-5690.
111. Mitrani, J.M. and M.N. Shneider, *Time-resolved laser-induced incandescence from multiwalled carbon nanotubes in air*. Applied Physics Letters, 2015. **106**(4): p. 043102.
112. Sommer, R. and A. Leipertz, *Application of laser-induced incandescence to suspended carbon black particles*. Optics Letters, 2007. **32**(13): p. 1947-1949.

113. Sipkens, T.A., P.J. Hadwin, S.J. Grauer, and K.J. Daun, *Predicting the heat of vaporization of iron at high temperatures using time-resolved laser-induced incandescence and Bayesian model selection*. Journal of Applied Physics, 2018. **123**(9): p. 095103.
114. Eremin, A.V., E.V. Gurentsov, and S.A. Musikhin, *Diagnostics of carbon-encapsulated iron nanoparticles by laser heating*. Journal of Physics: Conference Series, 2018. **946**: p. 012068.
115. Eremin, A., E. Gurentsov, E. Mikheyeva, and K. Priemchenko, *Experimental study of carbon and iron nanoparticle vaporisation under pulse laser heating*. Applied Physics B, 2013. **112**(3): p. 421-432.
116. Sipkens, T.A., N.R. Singh, and K.J. Daun, *Time-resolved laser-induced incandescence characterization of metal nanoparticles*. Applied Physics B, 2017. **123**(1): p. 14.
117. Eremin, A.V., E.V. Gurentsov, and S.A. Musikhin, *Molybdenum atoms yield in pulse ultraviolet laser photolysis of Mo(CO)₆*. Journal of Physics: Conference Series, 2015. **653**: p. 012029.
118. Sipkens, T., G. Joshi, K.J. Daun, and Y. Murakami, *Sizing of Molybdenum Nanoparticles Using Time-Resolved Laser-Induced Incandescence*. Journal of Heat Transfer, 2013. **135**(5): p. 052401.
119. Eremin, A.V. and E.V. Gurentsov, *Sizing of Mo nanoparticles synthesised by Kr-F laser pulse photo-dissociation of Mo(CO)₆*. Applied Physics A, 2015. **119**(2): p. 615-622.
120. Allen, D., H. Krier, and N. Glumac, *Nano-Alumina Accommodation Coefficient Measurement Using Time-Resolved Laser-Induced Incandescence*. Journal of Heat Transfer, 2016. **138**(11): p. 112401.
121. Filippov, A.V., M.W. Markus, and P. Roth, *In-situ characterization of ultrafine particles by laser-induced incandescence: sizing and particle structure determination*. Journal of Aerosol Science, 1999. **30**(1): p. 71-87.
122. Cignoli, F., C. Bellomunno, S. Maffi, and G. Zizak, *Laser-induced incandescence of titania nanoparticles synthesized in a flame*. Applied Physics B, 2009. **96**(4): p. 593-599.
123. Schulz, C., T. Dreier, M. Fikri, and H. Wiggers, *Gas-phase synthesis of functional nanomaterials: Challenges to kinetics, diagnostics, and process development*. Proceedings of the Combustion Institute, 2018, <https://doi.org/10.1016/j.proci.2018.06.231>.
124. Sipkens, T.A., R. Mansmann, K.J. Daun, N. Petermann, J.T. Titantah, M. Karttunen, H. Wiggers, T. Dreier, and C. Schulz, *In situ nanoparticle size measurements of gas-borne silicon nanoparticles by time-resolved laser-induced incandescence*. Applied Physics B, 2014. **116**(3): p. 623-636.
125. Eom, G.S., C.W. Park, Y.H. Shin, K.H. Chung, S. Park, W. Choe, and J.W. Hahn, *Size determination of nanoparticles in low-pressure plasma with laser-induced incandescence technique*. Applied Physics Letters, 2003. **83**(6): p. 1261-1263.
126. Eom, G.S., S. Park, C.W. Park, W. Choe, Y.-H. Shin, K.H. Chung, and J.W. Hahn, *Size Monitoring of Nanoparticles Growing in Low-Pressure Plasma using Laser-Induced Incandescence Technique*. Japanese Journal of Applied Physics, 2004. **43**(9A): p. 6494-6498.
127. Petermann, N., N. Stein, G. Schierning, R. Theissmann, B. Stoib, M.S. Brandt, C. Hecht, C. Schulz, and H. Wiggers, *Plasma synthesis of nanostructures for improved thermoelectric properties*. Journal of Physics D: Applied Physics, 2011. **44**(17): p. 174034.
128. Daun, K.J., B.J. Stagg, F. Liu, G.J. Smallwood, and D.R. Snelling, *Determining aerosol particle size distributions using time-resolved laser-induced incandescence*. Applied Physics B, 2007. **87**(2): p. 363-372.
129. Hakamata, T. and Editorial Committee, *Hamamatsu Photonics - PHOTOMULTIPLIER TUBES - Basics and Applications (Edition 3a)*. 2007.

130. Flyckt, S.O. and C. Marmonier, *PHOTOMULTIPLIER TUBES principles & applications*. Photonis, Brive, France, 2002.
131. Wainner, R.T., J.M. Seitzman, and S.R. Martin, *Soot Measurements in a Simulated Engine Exhaust Using Laser-Induced Incandescence*. AIAA Journal, 1999. **37**(6): p. 738-743.
132. Hartman, D.H., *Pulse mode saturation properties of photomultiplier tubes*. Rev Sci Instrum, 1978. **49**(8): p. 1130.
133. Knappe, C., J. Linden, F. Abou Nada, M. Richter, and M. Alden, *Investigation and compensation of the nonlinear response in photomultiplier tubes for quantitative single-shot measurements*. Rev Sci Instrum, 2012. **83**(3): p. 034901.
134. Keene, J.P., *Fatigue and Saturation in Photomultipliers*. Review of Scientific Instruments, 1963. **34**(11): p. 1220-1222.
135. Riboldi, S., N. Blasi, S. Brambilla, F. Camera, A. Giaz, and B. Million, *Phototube non-linearity correction technique*. Journal of Physics: Conference Series, 2015. **620**: p. 012007.
136. Schip, L.J.B., B.P. Buzelatto, F.R. Batista, C.J.d. Cunha, L.C. Dias Jr., and J.B.M. Novo, *Photomultiplier nonlinear response in time-domain laser-induced luminescence spectroscopy*. Química Nova, 2007. **30**: p. 214-218.
137. Bristow, M.P., *Lidar-signal compression by photomultiplier gain modulation: influence of detector nonlinearity*. Applied Optics, 1998. **37**(27): p. 6468-6479.
138. Bristow, M.P., D.H. Bundy, and A.G. Wright, *Signal linearity, gain stability, and gating in photomultipliers: application to differential absorption lidars*. Applied Optics, 1995. **34**(21): p. 4437-4452.
139. Vićić, M., L.G. Sobotka, J.F. Williamson, R.J. Charity, and J.M. Elson, *Fast pulsed UV light source and calibration of non-linear photomultiplier response*. Nuclear Instruments and Methods in Physics Research Section A: Accelerators, Spectrometers, Detectors and Associated Equipment, 2003. **507**(3): p. 636-642.
140. Lee, H.S., G.K. Schwemmer, C.L. Korb, M. Dombrowski, and C. Prasad, *Gated photomultiplier response characterization for DIAL measurements*. Applied Optics, 1990. **29**(22): p. 3303-3315.
141. Willert, C., B. Stasicki, J. Klinner, and S. Moessner, *Pulsed operation of high-power light emitting diodes for imaging flow velocimetry*. Measurement Science and Technology, 2010. **21**(7): p. 075402.
142. Dreier, T. and C. Schulz, *Laser-based diagnostics in the gas-phase synthesis of inorganic nanoparticles*. Powder Technology, 2016. **287**: p. 226-238.
143. Eremin, A., E. Gurentsov, and C. Schulz, *Influence of the bath gas on the condensation of supersaturated iron atom vapour at room temperature*. Journal of Physics D: Applied Physics, 2008. **41**(5): p. 055203.
144. Cignoli, F., S. De Iuliis, V. Manta, and G. Zizak, *Two-dimensional two-wavelength emission technique for soot diagnostics*. Applied Optics, 2001. **40**(30): p. 5370-5378.
145. Mansmann, R., T. Terheiden, P. Schmidt, J. Menser, T. Dreier, T. Endres, and C. Schulz, *LiISim: a modular signal processing toolbox for laser-induced incandescence measurements*. Applied Physics B, 2018. **124**(4): p. 69.
146. Schulz, C., *Laser-induced Incandescence: Quantitative Interpretation, Modelling, Application*, in *Proceedings International Bunsen Discussion Meeting and Workshop*. 2005: Duisburg, Germany.

147. Suntz, R. and H. Bockhorn, *Laser-induced Incandescence: Quantitative Interpretation, Modelling, Applications*, in *Proceedings 2nd International Discussion Meeting and Workshop*. 2006: Bad Herrenalb, Germany.
148. Desgroux, P., *Laser-induced Incandescence 2012*, in *Proceedings 5th International Workshop on Laser-induced Incandescence*. 2012: Le Touquet, France.
149. Mansmann, R., T. Dreier, and C. Schulz, *Performance of photomultipliers in the context of laser-induced incandescence*. Applied Optics, 2017. **56**(28): p. 7849-7860.
150. Vander Wal, R.L., T.M. Ticich, and A.B. Stephens, *Optical and microscopy investigations of soot structure alterations by laser-induced incandescence*. Applied Physics B, 1998. **67**(1): p. 115-123.
151. Mansmann, R., K. Thomson, G. Smallwood, T. Dreier, and C. Schulz, *Sequential signal detection for high dynamic range time-resolved laser-induced incandescence*. Optics Express, 2017. **25**(3): p. 2413.
152. Luo, F.-J.H., Yue-Kun; Wang, Zhi-Min; Wang, Pei-Liang; Qin, Zhong-Hua; Xu, Mei-Hang; Liao, Dong-Hao; Zhang, Hai-Qiong; Huang, Yong-Bo; Lei, Xiang-Cui; Qian, Sen; Liu, Shu-Lin; Chen, Yuan-Bo; Wang, Yi-Fang, *PMT overshoot study for the JUNO prototype detector*. Chinese Physics C, 2016. **40**(9): p. 096002.
153. Snelling, D.R., K.A. Thomson, G.J. Smallwood, Oslash, L. G-uacute, Ider, E.J. Weckman, and R.A. Fraser, *Spectrally Resolved Measurement of Flame Radiation to Determine Soot Temperature and Concentration*. AIAA Journal, 2002. **40**(9): p. 1789-1795.
154. Will, S., S. Schraml, K. Bader, and A. Leipertz, *Performance characteristics of soot primary particle size measurements by time-resolved laser-induced incandescence*. Applied Optics, 1998. **37**(24): p. 5647-5658.
155. Bass, M., *Handbook of optics. 2. Devices, measurements, and properties*. 2. ed. ed. 1995, New York [u.a.]: McGraw-Hill.
156. Eberhardt, E.H., *Gain model for microchannel plates*. Applied Optics, 1979. **18**(9): p. 1418-1423.
157. Pastor, J.V., J.M. García, J.M. Pastor, and J.E. Buitrago, *Analysis of calibration techniques for laser-induced incandescence measurements in flames*. Measurement Science and Technology, 2006. **17**(12): p. 3279-3288.
158. Vander Wal, R.L., Z. Zhou, and M.Y. Choi, *Laser-induced incandescence calibration via gravimetric sampling*. Combustion and Flame, 1996. **105**(4): p. 462-470.
159. Snelling, D.R., G.J. Smallwood, R.A. Sawchuk, W.S. Neill, D. Gareau, W.L. Chippior, F. Liu, Ö.L. Gülder, and W.D. Bachalo, *Particulate Matter Measurements in a Diesel Engine Exhaust by Laser-Induced Incandescence and the Standard Gravimetric Procedure*. SAE Technical Paper 1999-01-3653, 1999.
160. Huber, F.J., M. Altenhoff, and S. Will, *A mobile system for a comprehensive online-characterization of nanoparticle aggregates based on wide-angle light scattering and laser-induced incandescence*. Rev Sci Instrum, 2016. **87**(5): p. 053102.
161. Yon, J., F.-X. Ouf, D. Hebert, J.B. Mitchell, N. Teuscher, J.-L.L. Garrec, A. Bescond, W. Baumann, D. Ourdani, T. Bizien, and J. Perez, *Investigation of soot oxidation by coupling LII, SAXS and scattering measurements*. Combustion and Flame, 2018. **190**: p. 441-453.
162. Singh, M., J.P. Abrahamson, and R.L. Vander Wal, *Informing TiRe-LII assumptions for soot nanostructure and optical properties for estimation of soot primary particle diameter*. Applied Physics B, 2018. **124**(7): p. 130.

163. Ryser, R., T. Gerber, and T. Dreier, *Soot particle sizing during high-pressure Diesel spray combustion via time-resolved laser-induced incandescence*. Combustion and Flame, 2009. **156**(1): p. 120-129.
164. Johnsson, J., *Laser-Induced Incandescence for Soot Diagnostics: Theoretical Investigation and Experimental Development*. 2012.
165. Cenker, E. and W.L. Roberts, *Quantitative effects of rapid heating on soot-particle sizing through analysis of two-pulse LII*. Applied Physics B, 2017. **123**(3): p. 74.
166. Ku, H.H., *Notes on the use of propagation of error formulas*. Journal of Research of the National Bureau of Standards, 1966. **70**(4): p. 263-273.
167. Sipkens, T.A., P.J. Hadwin, S.J. Grauer, and K.J. Daun, *General error model for analysis of laser-induced incandescence signals*. Applied Optics, 2017. **56**(30): p. 8436-8445.
168. Hadwin, P.J., T.A. Sipkens, K.A. Thomson, F. Liu, and K.J. Daun, *Quantifying uncertainty in soot volume fraction estimates using Bayesian inference of auto-correlated laser-induced incandescence measurements*. Applied Physics B, 2016. **122**(1): p. 1.
169. von Toussaint, U., *Bayesian inference in physics*. Reviews of Modern Physics, 2011. **83**(3): p. 943-999.
170. Fry, E.S., J. Musser, G.W. Kattawar, and P.-W. Zhai, *Integrating cavities: temporal response*. Applied Optics, 2006. **45**(36): p. 9053-9065.
171. Gülder, Ö.L., D.R. Snelling, and R.A. Sawchuk, *Influence of hydrogen addition to fuel on temperature field and soot formation in diffusion flames*. Symposium (International) on Combustion, 1996. **26**(2): p. 2351-2358.
172. Nordström, E., N.-E. Olofsson, J. Simonsson, J. Johnsson, H. Bladh, and P.-E. Bengtsson, *Local gas heating in sooting flames by heat transfer from laser-heated particles investigated using rotational CARS and LII*. Proceedings of the Combustion Institute, 2015. **35**(3): p. 3707-3713.
173. Bauer, R.K. and A. Balter, *A method of avoiding wavelength-dependent errors in decay-time measurements*. Optics Communications, 1979. **28**(1): p. 91-96.
174. Wahl, P., J.C. Auchet, and B. Donzel, *The wavelength dependence of the response of a pulse fluorometer using the single photoelectron counting method*. Review of Scientific Instruments, 1974. **45**(1): p. 28-32.
175. Sipp, B., J.A. Miehe, and R. Lopez-Delgado, *Wavelength dependence of the time resolution of high-speed photomultipliers used in single-photon timing experiments*. Optics Communications, 1976. **16**(1): p. 202-204.
176. Lehre, T., B. Jungfleisch, R. Suntz, and H. Bockhorn, *Size distributions of nanoscaled particles and gas temperatures from time-resolved laser-induced-incandescence measurements*. Applied Optics, 2003. **42**(12): p. 2021-2030.
177. Nanthaamornphong, A., K. Morris, D.W.I. Rouson, and H.A. Michelsen, *A case study: Agile development in the community laser-induced incandescence modeling environment (CLiiME)*. in *2013 5th International Workshop on Software Engineering for Computational Science and Engineering (SE-CSE)*. 2013.
178. Nanthaamornphong, A., J.C. Carver, K. Morris, H.A. Michelsen, and D.W.I. Rouson, *Building CLiiME via Test-Driven Development: A Case Study*. Computing in Science & Engineering, 2014. **16**(3): p. 36-46.

179. Cenker, E., G. Bruneaux, T. Dreier, and C. Schulz, *Sensitivity analysis for soot particle size imaging with laser-induced incandescence at high pressure*. Applied Physics B, 2015. **119**(4): p. 745-763.
180. S. De Iuliis, M. Urciuolo, A. Cammarota, S. Maffi, R. Chirone, and G. Zizak, *LII measurements of soot particles produced by fluidized bed combustion of wood pellets*. XXXIV Meeting of the Italian Section of the Combustion Institute, 2011.
181. *The Qt Framework*. July 2015; Available from: <http://www.qt.io>.
182. *Boost C++ Libraries*. November 2013; Available from: <http://www.boost.org/>.
183. *Qwt library*. June 2016; Available from: <http://qwt.sourceforge.net/>.
184. Moré, J.J. *The Levenberg-Marquardt algorithm: Implementation and theory*. 1978. Berlin, Heidelberg: Springer Berlin Heidelberg.
185. Press, W.H., S.A. Teukolsky, W.T. Vetterling, and B.P. Flannery, *Numerical Recipes 3rd Edition: The Art of Scientific Computing*. 2007: Cambridge University Press. 1256.
186. Dormand, J.R. and P.J. Prince, *A family of embedded Runge-Kutta formulae*. Journal of Computational and Applied Mathematics, 1980. **6**(1): p. 19-26.
187. Snelling, D.R., K.A. Thomson, F. Liu, and G.J. Smallwood, *Comparison of LII derived soot temperature measurements with LII model predictions for soot in a laminar diffusion flame*. Applied Physics B, 2009. **96**(4): p. 657-669.
188. Tosi, A., A.D. Mora, F. Zappa, A. Gulinatti, D. Contini, A. Pifferi, L. Spinelli, A. Torricelli, and R. Cubeddu, *Fast-gated single-photon counting technique widens dynamic range and speeds up acquisition time in time-resolved measurements*. Optics Express, 2011. **19**(11): p. 10735-10746.
189. Jenkins, T.P. and R.K. Hanson, *Soot pyrometry using modulated absorption/emission*. Combustion and Flame, 2001. **126**(3): p. 1669-1679.
190. Menser, J., K. Daun, T. Dreier, and C. Schulz, *Laser-induced atomic emission of silicon nanoparticles during laser-induced heating*. Appl Opt, 2017. **56**(11): p. E50-E57.
191. Huber, F.J.T., S. Will, and K.J. Daun, *Sizing aerosolized fractal nanoparticle aggregates through Bayesian analysis of wide-angle light scattering (WALS) data*. Journal of Quantitative Spectroscopy and Radiative Transfer, 2016. **184**: p. 27-39.
192. Sipkens, T.A. and K.J. Daun, *Defining regimes and analytical expressions for fluence curves in pulsed laser heating of aerosolized nanoparticles*. Opt Express, 2017. **25**(5): p. 5684-5696.
193. Sipkens, T.A., P.J. Hadwin, S. Grauer, and K.J. Daun. *Applying model selection to laser-induced incandescence*. in *9th International Conference on Inverse Problems in Engineering*. 2017. Waterloo, ON.
194. Candy, B.H., *Photomultiplier characteristics and practice relevant to photon counting*. Review of Scientific Instruments, 1985. **56**(2): p. 183-193.
195. Knappe, C., F. Abou Nada, M. Richter, and M. Alden, *Comparison of photo detectors and operating conditions for decay time determination in phosphor thermometry*. Rev Sci Instrum, 2012. **83**(9): p. 094901.
196. Aster, R.C., B. Borchers, and C.H. Thurber, *Parameter estimation and inverse problems*. International geophysics series. 2005, Amsterdam: Elsevier Acad. Press.
197. Liu, F., K.J. Daun, D.R. Snelling, and G.J. Smallwood, *Heat conduction from a spherical nanoparticle: status of modeling heat conduction in laser-induced incandescence*. Applied Physics B, 2006. **83**(3): p. 355-382.

PUBLICATIONS

Submitted journal articles

- R. Mansmann, T.A. Sipkens, J. Menser, K. J. Daun, T. Dreier, C. Schulz, “*Detector calibration and measurement issues in multi-color time-resolved laser-induced incandescence*”, Applied Physics B, submitted (2018).
- T. A. Sipkens, J. Menser, R. Mansmann, C. Schulz, K. J. Daun, “*Apparent temporal variation in calibration factors used for time-resolved laser-induced incandescence*”, Applied Physics B, submitted (2018).

Peer-reviewed journal articles

- R. Mansmann, T. Terheiden, P. Schmidt, J. Menser, T. Dreier, T. Endres, C. Schulz, “*LII-Sim: a modular signal processing toolbox for laser-induced incandescence measurements*”, Applied Physics B **124**(4), p. 69 (2018).
- R. Mansmann, T. Dreier, C. Schulz, “*Performance of photomultipliers in the context of laser-induced incandescence*”, Applied Optics **56**(28), pp. 7849-7860 (2017).
- R. Mansmann, K. Thomson, G. Smallwood, T. Dreier, C. Schulz, “*Sequential signal detection for high dynamic range time-resolved laser-induced incandescence*”, Optics Express **25**(3), p. 2413 (2017).
- K. J. Daun, J. Menser, R. Mansmann, S. T. Moghaddam, T. Dreier, C. Schulz, “*Spectroscopic models for laser-heated silicon and copper nanoparticles*”, Journal of Quantitative Spectroscopy and Radiative Transfer **197**, pp. 3-11 (2017).
- T. A. Sipkens, R. Mansmann, K. J. Daun, N. Petermann, J. T. Titantah, M. Karttunen, H. Wiggers, T. Dreier, C. Schulz, “*In situ nanoparticle size measurements of gas-borne silicon nanoparticles by time-resolved laser-induced incandescence*”, Applied Physics B **116**(3), pp. 623-636 (2014).

Conference proceedings

- T. A. Sipkens, K. J. Daun, R. Mansmann, J. Menser, T. Dreier, C. Schulz, “*Simultaneous inference of temperature and intensity scaling factor in laser-induced incandescence*”, Proceedings of Combustion Institute – Canadian Section, Spring Technical Meeting, McGill University, Montréal, Canada, May 15-18, 2017.
- K. J. Daun, J. Menser, R. Mansmann, T. Dreier, C. Schulz, “*Laser-Induced Incandescence Measurements of Silicon and Copper Nanoparticles: Spectroscopic Model*”, Proceedings of the 8th International Symposium on Radiative Transfer (ISRT), Cappadocia, Turkey, Jun 6-10, 2016.
- R. Mansmann, T. Dreier, C. Schulz, “*Laser-Induced Incandescence (LII) Measurements on Gas-Borne Silicon Nanoparticles*”, Laser Applications to Chemical, Security and Environmental Analysis (LACSEA), Seattle, WA, USA, Jul 13-17, 2014.

Conference contributions

- 8th International Workshop and Meeting on Laser-Induced Incandescence
Jun 10-13, Tutzing, Germany
 - **Invited discussion session leader:** “*Pulsed and CW LII: modeling, evaluation and unresolved questions*”
 - R. Mansmann, K. J. Daun, “*How to compare data between research groups?*”. (Talk/Discussion)
 - R. Mansmann, T. Terheiden, P. Schmidt, J. Menser, T. Dreier, T. Endres, C. Schulz, “*LIISim: a modular signal processing toolbox for laser-induced incandescence measurements*”. (Poster)
 - S. Musikhin, R. Mansmann, J. Menser, T. Dreier, C. Schulz, „*Temporally- and spectrally-resolved LII measurements on a standard flame using a streak camera and multi-color PMT setup*”. (Poster)
 - T. A. Sipkens, J. Menser, R. Mansmann, C. Schulz, K. J. Daun, “*What is hiding in the intensity scaling factor and what can be gained from analyzing its temporal variation?*”. (Poster)
- Gordon Research Conference: Laser Diagnostics in Combustion
Aug 6-11, 2017, Mount Snow, West Dover, VT, USA
 - R. Mansmann, T. Terheiden, P. Schmidt, J. Menser, T. Dreier, T. Endres, C. Schulz, “*LIISim: a modular signal processing toolbox for laser-induced incandescence measurements*”. (Poster)
- 7th International Workshop and Meeting on Laser-Induced Incandescence
Jun 19-22, 2016, Lake Tahoe, CA, USA
 - R. Mansmann, T. Terheiden, P. Schmidt, J. Menser, T. Dreier, C. Schulz, “*LIISim: a modular signal processing toolbox for laser-induced incandescence measurements*”. (Poster)
 - R. Mansmann, T. Dreier, C. Schulz, „*Light-emitting diodes as gain calibration light source for photomultiplier tubes*”. (Poster)
 - R. Mansmann, K. Thomson, G. Smallwood, T. Dreier, C. Schulz, “*Sequential signal detection for high-dynamic-range time-resolved laser-induced incandescence*”. (Poster)
 - K. J. Daun, R. Mansmann, J. Menser, C. Schulz, “*LII Characterization of Copper Nanoparticles*”. (Talk presented by K. J. Daun)
- Gordon Research Conference: Laser Diagnostics in Combustion
Aug 9-14, 2015, Waterville Valley, NH, USA
 - R. Mansmann, K. Thomson, G. Smallwood, T. Dreier, C. Schulz, “*Scanning technique for high-dynamic-range time-resolved laser-induced incandescence*”. (Poster)

- Materials Research Society Fall Meeting
Nov 30 - Dec 5, 2014, Boston, MA, USA
 - R. Mansmann, J. Menser, T. Dreier, H. Wiggers, C. Schulz, "*In situ size measurements of gas-borne silicon nanoparticles with laser-induced incandescence (LII)*". (Talk)
(MRS Symposium HH – Best Early PhD Presentation Award)
- Aerosol Technology 2014
Jun 16-18, 2014, Karlsruhe, Germany
 - R. Mansmann, T. Dreier, H. Wiggers, C. Schulz, "*Laser-induced incandescence (LII) measurements on gas-borne silicon nanoparticles*". (Talk)
- 6th International Workshop and Meeting on Laser-Induced Incandescence
Jun 8-11, 2014, Hven, Sweden
 - R. Mansmann, T. Dreier, H. Wiggers, C. Schulz, "*Laser-induced incandescence (LII) measurements on gas-borne silicon nanoparticles*". (Talk/Poster)
- Gordon Research Conference: Laser Diagnostics in Combustion
Aug 11-16, 2013, Waterville Valley, NH, USA
 - R. Mansmann, N. Petermann, T. Dreier, H. Wiggers, C. Schulz, "*Laser-induced incandescence (LII) measurements on gas-borne silicon nanoparticles*". (Poster)

ACKNOWLEDGMENTS

The research presented in this thesis was influenced by many individuals to whom I would like to express my gratitude and appreciation:

First, I want to especially thank my supervisor and mentor Prof. Christof Schulz for the continuous support, for the many fruitful discussions and feedback, and for introducing me to the scientific community. You were always supporting my new and immature ideas and giving me the freedom to try new things. Your appreciation of my research motivated me to push further and higher. It has been an honor and pleasure working with you.

I would also like to thank Prof. Kyle Daun from the University of Waterloo for being my co-supervisor during my PhD and during the ongoing collaboration between Canada and Germany. I thank you for the numerous profound discussions about Bayesian statistics, LII modeling and the many powerful numeric tools that helped shaping my research. These discussions have significantly influenced my scientific way of thinking. Thank you for everything!

For sharing his broad experience, I want to thank Prof. Thomas Dreier. Your guidance contributed to various solutions and helped me to master technical challenges in the lab. I really appreciated working with you, and in your group.

My fellows, Jan Menser and Timothy Sipkens, I would like to thank you for the intense collaboration over the past years. Working with you have always been motivating, productive and exciting! Not only the many, many fruitful discussions, the problem solving in the lab and the elaboration of new ideas have been a great pleasure, but also the joint journeys to the many conferences and the beer tastings at so many places in the world. Thank you guys for the great time!

I want to especially thank my two students Tobias Terheiden and Philip Schmidt, who worked with me for several years and helped to make the LIISim software a success. Thanks also to my successor, Stanislav Musikhin, who caught up so quickly on my research. The many discussions and follow-up of my work showed me that everything I have done comes to fruition. I wish you guys all the best on your way!

A special role during my PhD plays Prof. Greg Smallwood, who invited me twice to work at the National Research Council (NRC) Canada. These research stays had a significant influence on my research direction. I would like to thank you for the continuous collaboration over the last years and for the many helpful discussions during your visits.

It has been an honor and pleasure working with Robert Sawchuk from NRC, who gave me detailed trainings on laser-system alignment, calibration, and troubleshooting. You left a significant impact on how I work in the lab. Thank you so much!

I would like to extend the thanks to my other colleagues from NRC, including Kevin Thomson, Dave Snelling, Fengshan Liu, Dan Clavel, Brett Smith, Simon-Alexandre Lussier from the Black Carbon Metrology group for welcoming and helping me during that time, as well as Andrew Todd and Donald Woods from the Photometry and Radiometry group, who gave me the special opportunity for the calibration measurements on the blackbody standard.

Many thanks go to two people who helped me making my research much more efficient: Barbara Nota, who has an impressive talent in eliminating so many bureaucratic obstacles. Without your help, I would still be sitting in my office and fill out forms. Erdal Akyildiz, you helped me in so many ways in the lab to establish quick and robust technical solutions so that projects could be finished in time.

I also want to thank all my other colleagues from IVG for the great working atmosphere, the beautiful working trips and the barbecues. I really appreciated the helpfulness and the team-minded work environment. Thank you for the great time!

Finally, I want to thank my family and friends who have always been there for me whenever I needed them. I owe you so much!